THE UNIVERSITY OF
WARWICK

AUTHOR: **Daniel Thomas O'Flynn** DEGREE: **Ph.D.**

TITLE: **Multiferroic properties of rare earth manganites**

DATE OF DEPOSIT: .....

I agree that this thesis shall be available in accordance with the regulations governing the University of Warwick theses.

I agree that the summary of this thesis may be submitted for publication.

I **agree** that the thesis may be photocopied (single copies for study purposes only).

Theses with no restriction on photocopying will also be made available to the British Library for microfilming. The British Library may supply copies to individuals or libraries. subject to a statement from them that the copy is supplied for non-publishing purposes. All copies supplied by the British Library will carry the following statement:

> "Attention is drawn to the fact that the copyright of this thesis rests with its author. This copy of the thesis has been supplied on the condition that anyone who consults it is understood to recognise that its copyright rests with its author and that no quotation from the thesis and no information derived from it may be published without the author's written consent."

AUTHOR'S SIGNATURE: .....

USER'S DECLARATION

1. I undertake not to quote or make use of any information from this thesis without making acknowledgement to the author.
2. I further undertake to allow no-one else to use this thesis while it is in my care.

DATE SIGNATURE ADDRESS

.....

.....

.....

.....

.....

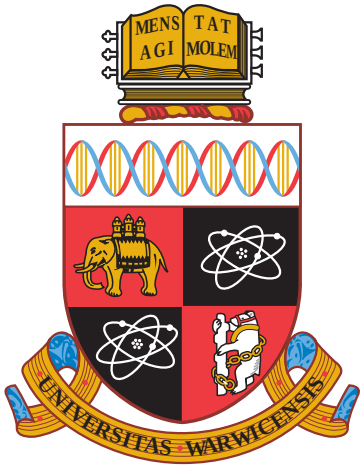

Multiferroic properties of rare earth manganites

by

Daniel Thomas O'Flynn

Thesis

Submitted to the University of Warwick

for the degree of

Doctor of Philosophy

Department of Physics

September 2010

THE UNIVERSITY OF WARWICK

Contents

Acknowledgments

I would firstly like to thank my supervisor, Geetha Balakrishnan, for continual guidance and assistance throughout the duration of my Ph.D., and without whom this work would not have been possible. I am extremely grateful to Martin Lees for his help with taking laboratory measurements and understanding the results, C. V. Tomy for building the electric properties measurement system, and initiating our work in this exciting new area, and Pam Thomas for much help with X-ray diffraction and crystallography issues, and for introducing me to the subject of ferroics as an undergraduate student. My thanks also go to Oleg Petrenko, Don M^{c}K. Paul, Le Duc Tung, Stefano Agrestini, Da-qian Liao, Tom Hase, Tom Orton (a constant ray of sunshine), Sue Burrows, Steve York and Dean Keeble.

Experiments conducted at central facilities - as well as the following data analysis and interpretation - relied upon the invaluable help of Pascale Deen, Devashibhai Adroja, Peter Normile, Jason Gardner, Carlos Giles, Winfried Kockelmann and Aziz Daoud-Aladine.

I gratefully acknowledge the financial support received from the Engineering and Physical Sciences Research Council (EPSRC), and the Science City Advanced Materials Project, supported by Advantage West Midlands (AWM) and part funded by the European Regional Development Fund (ERDF).

A massive thank you to all my friends who have made the last 4 years so enjoyable: Jenny Wooldridge, Nic Wilson, Andy Crichton, Tom Hayes, Catherine Fleck, Pabitra Biswas and Olga Young, for making the P130 mezzanine a great place to work; Dan Baker for a pleasant game of croquet, and for setting up *that* goal; Jimothy "James" Cook for making sure my belaying was up to scratch by falling every five minutes; Andy Barker for my first pair of Anasazis, and for teaching me trad at a deserted, snow-covered Bamford; and the members of Warwick University Climbing Club for many great experiences.

I am indebted to my parents, Christina and Seán O'Flynn, for their constant support and encouragement throughout all of my studies. Finally, I would like to thank Lettuce, for always being there.

Declaration and published work

The work presented in this thesis was carried out by me, except where explicitly stated. The sample preparation and data collection detailed in Chapters 2-6 took place between September 2006 and June 2010 at the University of Warwick Physics Department, the ISIS facility at the Rutherford-Appleton Laboratory, and the European Synchrotron Radiation Facility (ESRF). Experiments at central facilities were performed with the assistance of a local contact. I was the sole experimentalist for the experiment at GEM, ISIS, and principal investigator for the experiment at XMaS, ESRF. Analysis of the data from these experiments was conducted under the guidance of Dr. Aziz Daoud-Aladine and Dr. Peter Normile, respectively. No part of this thesis has been submitted for examination at any other institute.

I have presented the work described in this thesis at the following meetings:

- D. O'Flynn, M. R. Lees and G. Balakrishnan. Magnetic properties of $TbMnO_3$ single crystals. *European School on Multiferroics*, Grenoble Institute of Technology, 2-6 July 2007 (Poster presentation)

- D. O'Flynn, C. V. Tomy, M. R. Lees and G. Balakrishnan. Multiferroic properties of $Sm_{1-x}Y_xMnO_3$. *X-ray & Neutron Scattering in Multiferroics Research*, National Physical Laboratory, 17 June 2009 (Poster presentation)

- D. O'Flynn, C. V. Tomy, M. R. Lees and G. Balakrishnan. Multiferroic behaviour in $Sm_{1-x}Y_xMnO_3$. *International Conference on Magnetism*, Karlsruhe, 26-31 July, 2009 (Poster presentation)

- D. O'Flynn, C. V. Tomy, M. R. Lees and G. Balakrishnan. Studies of the new multiferroic crystals: $Sm_{1-x}Y_xMnO_3$. *Condensed Matter and Materials Physics*, University of Warwick, 15-17 December 2009 (Oral presentation)

Publications

- D. O'Flynn, C. V. Tomy, M. R. Lees and G. Balakrishnan, Multiferroic behaviour in $Sm_{1-x}Y_xMnO_3$ *Journal of Physics: Conference Series* **200**, 012149 (2010)

- D. O'Flynn, C. V. Tomy, M. R. Lees and G. Balakrishnan, Multiferroic properties of single crystal $Sm_{1-x}Y_xMnO_3$ ($x = 0.4$, 0.5) [submitted for publication]

- D. O'Flynn, A. Daoud-Aladine and G. Balakrishnan, Neutron powder diffraction study of multiferroic $Sm_{0.6}Y_{0.4}MnO_3$ [submitted for publication]

- D. O'Flynn, J. S. Gardner, P. Normile, C. Giles and G. Balakrishnan, X-ray resonant scattering study of $Sm_{0.5}Y_{0.5}MnO_3$ [in preparation]

- D. O'Flynn, M. R. Lees and G. Balakrishnan, Heat capacity of $TbMnO_3$ under an applied magnetic field [in preparation]

Abstract

Well known multiferroic compounds $TbMnO_3$ and $DyMnO_3$ show a strong coupling between antiferromagnetism and ferroelectricity. Magnetic susceptibility data for both compounds have been taken, showing large magnetic anisotropy, and providing strong evidence for the existence of crystal field effects up to 150 K above T_N ($\sim$40 K). Further evidence for crystal field effects is given by a measurement of the magnetic heat capacity of $TbMnO_3$.

A new group of multiferroic compounds, of the form $Sm_{1-x}Y_xMnO_3$, were discovered as part of this work. The parent compound, $SmMnO_3$, is not ferroelectric and exhibits commensurate A-type antiferromagnetic order below $T_N\sim$58 K. By doping with Y on the Sm site, significant changes are seen in the magnetic properties, with a feature seen in the susceptibility data at $\sim$24 K for $x = 0.4, 0.5$ corresponding with a peak in the dielectric constant and the onset of an electric polarisation ($\sim$275 μC m^{-2} for $Sm_{0.5}Y_{0.5}MnO_3$) along the crystallographic c-axis. The magnetoelectric coupling seen in $Sm_{0.6}Y_{0.4}MnO_3$ and $Sm_{0.5}Y_{0.5}MnO_3$ is linked to alterations in the local structure of the Mn-O octahedra, and in particular to the Mn-O-Mn bond angle, which can be tuned by Y doping.

The zero-field electric properties of $Sm_{1-x}Y_xMnO_3$ ($x = 0.4$, 0.5) are very similar to those of $TbMnO_3$, but show markedly different magnetic field dependence. Neutron diffraction and X-ray resonant scattering experiments were performed on $Sm_{1-x}Y_xMnO_3$ ($x = 0$, 0.4, 0.5) in order to attempt to determine the magnetic structure of the Y doped compounds. Evidence was found for a sinusoidally modulated collinear order of the Mn moments along the b-axis below $T_{N1}\sim$47 K, and cycloidal Mn order in the b-c plane below $T_{N2}\sim$24 K. This magnetic model is similar to that of $TbMnO_3$, and it is proposed that the difference in the magnetic field dependence of the electric properties seen in $TbMnO_3$ is due to coupling of the Mn moments with the strongly anisotropic Tb moments.

The studies of Y doping were extended to the $GdMnO_3$ system. Preliminary measurements show a similar magnetoelectric coupling in polycrystalline $Gd_{1-x}Y_xMnO_3$ ($x = 0.1$-0.4). Further research has been carried out on this group of compounds as a consequence of this work.

Chapter 1

Introduction

This thesis details work carried out on rare earth manganite materials (of the form $R\mathrm{MnO}_3$ or $R_{1-x}\mathrm{Y}_x\mathrm{MnO}_3$, with R representing the rare earth element) which show multiferroic properties. As an introduction, the underlying physics relevant to these compounds will be discussed. A summary of the research in the field of multiferroics is then presented, leading into an outline of the current challenges faced by researchers, and the motivation for this work.

The term 'multiferroic' was initially coined by Schmid [1] to define a material possessing two or more primary ferroic properties (ferroelectricity, ferromagnetism, ferroelasticity) which occur in the same phase. Such materials can exhibit cross-coupling between these different properties (Figure 1.1), making the field of multiferroics very attractive for research from both a fundamental and technological point of view [2–6].

Research activity into multiferroics has been steadily increasing since several major breakthroughs in 2003-4 (Figure 1.2) [7–9]. In the vast majority of cases, the term "multiferroic" refers to the coexistence of (anti)ferroelectricity and (anti)ferromagnetism.

Ferroic materials are defined as possessing spontaneous order, the direction of which can be switched by an external field. A ferromagnet has a spontaneous magnetisation $\mathbf{M}$ and shows hysteresis under an applied magnetic field $\mathbf{H}$. A ferroelectric has a spontaneous polarisation $\mathbf{P}$ and shows hysteresis under an applied electric field $\mathbf{E}$. A ferroelastic has a spontaneous strain ε and shows hysteresis under an applied stress σ. Such spontaneous order typically occurs as a result of a

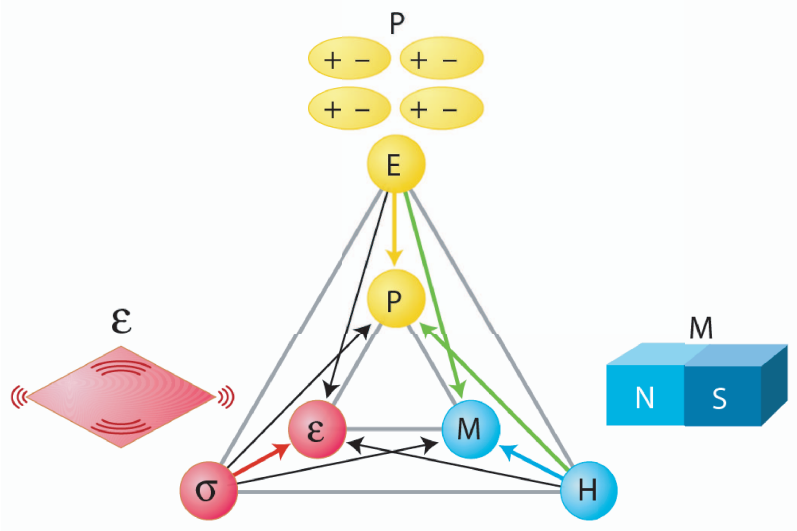

Figure 1.1: Multiferroics can show coupling between ferroelectric, ferromagnetic and ferroelastic properties. Figure from Ref. [3]

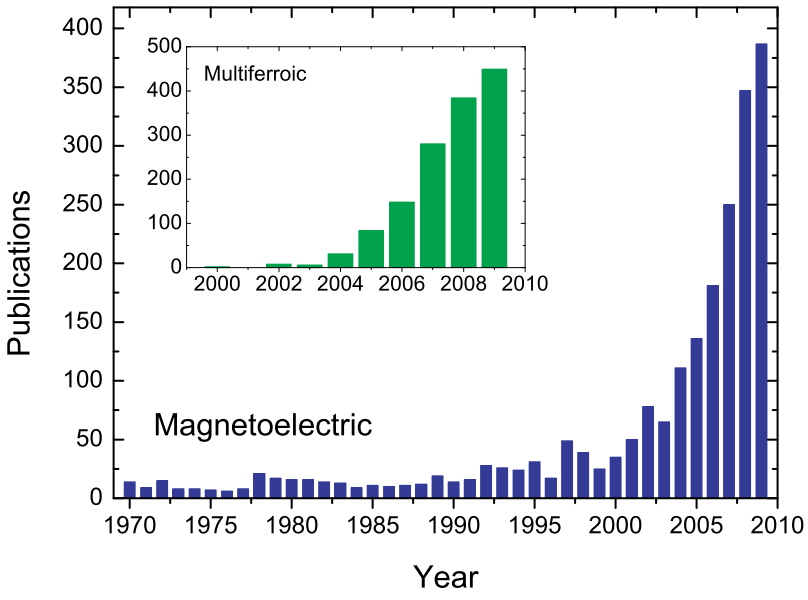

Figure 1.2: Publication history found for a Web of Science search for "magnetoelectric" (inset: results for "multiferroic").

phase transition, when the material is cooled below a particular temperature. The following sections provide a brief description of ferroelectricity and the magnetic order most relevant to the studies in this thesis.

1.1 Ferroelectricity

A (proper) ferroelectric possesses a spontaneous polarisation of the electric dipole which can be switched by the application of an electric field. This polarisation is due to a lack of inversion symmetry within the crystal structure. For example, consider the classic perovskite of the form ABO_3, in which a central positive B-ion (a transition metal element) is surrounded by an octahedron of negatively charged oxygen ions (Figure 1.3). A shift in the position of the B-site ion would break the inversion symmetry and cause the induction of a dipole moment, giving rise to ferroelectric order. Such shifts can occur during structural phase transitions, in which the system moves from a high to low symmetry state (e.g. cubic to tetragonal). One of the best known examples of a proper ferroelectric is $BaTiO_3$ [10, 11]. In the majority of ferroelectric perovskites, the B-site atom has an empty d electron shell, which allows covalent bonding with the full p orbitals of the the oxygen atoms. Ferroelectricity can also occur due to the existence of lone pairs of electrons on the outer shell of the A-site atom, which are highly susceptible to polarisation. This is the cause of ferroelectricity in $BiFeO_3$ (Section 1.4.1), for example.

In an improper ferroelectric, the spontaneous polarisation is not due to a polar

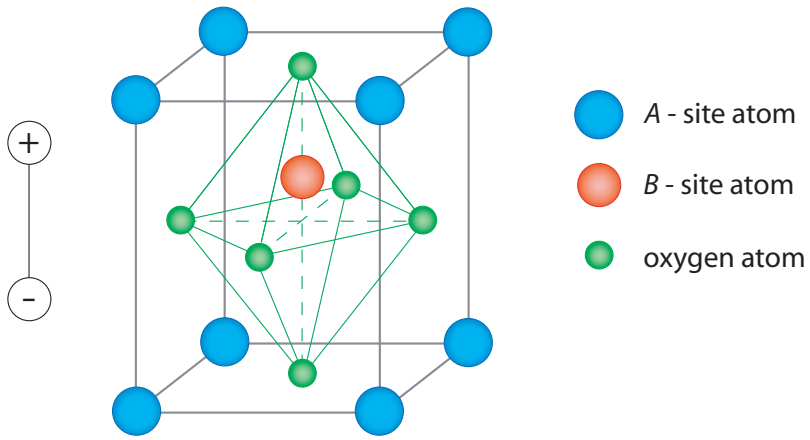

Figure 1.3: Perovskite crystal structure, showing a dipole moment generated by a displaced B-site atom

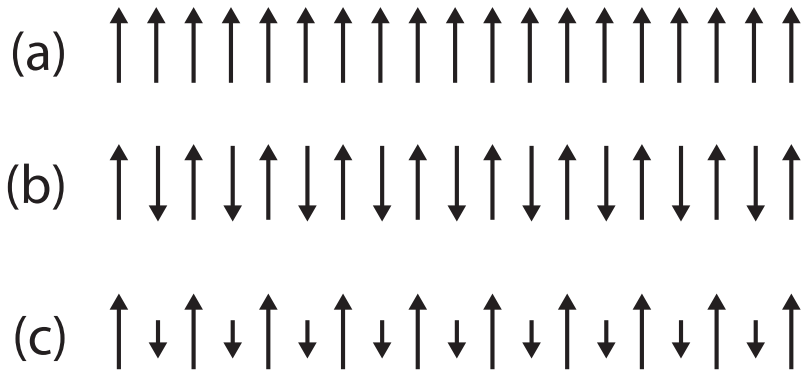

Figure 1.4: Magnetic order: (a) ferromagnetism, (b) antiferromagnetism, (c) ferrimagnetism

displacement of the ions, but occurs as a result of some other effect within the material. In a geometric ferroelectric, the dipole moment occurs due to non-polar lattice distortions, due to e.g. electrostatic forces rather than changes in chemical bonding. An example of this is in $YMnO_3$, where a ferroelectric state is due to a buckling of the rigid MnO_5 bipyramids [12]. In charge ordered ferroelectrics, the spontaneous polarisation is dependent on electron correlations in the material [13]. Such charge ordered ferroelectricity is observed in $LuFe_2O_4$ [14]. Improper ferroelectricity can also occur due to magnetic order, a topic which will be covered in more detail in the following sections.

1.2 Magnetism

1.2.1 Magnetic order

Magnetic order in a material occurs due to the interactions between magnetic moments. The interactions between neighbouring spins $\mathbf{S}_i$ and $\mathbf{S}_j$ are described by the Heisenberg model, with the Hamiltonian given by

$$\hat{\mathscr{H}} = -\sum_{ij} J_{ij}\, \mathbf{S}_i \cdot \mathbf{S}_j \tag{1.1}$$

The value J_{ij} is called the exchange constant, and describes the nature of the interaction between $\mathbf{S}_i$ and $\mathbf{S}_j$. If J_{ij} is positive, neighbouring spins favour a parallel alignment, and the system is ferromagnetic. If J_{ij} is negative, neighbouring spins favour an antiparallel alignment, and the system is antiferromagnetic. Antiferromagnetism can exist in many forms, with the common theme of sublattices of

moments arranged so as to cancel each other out, and give no net magnetisation in the absence of an applied magnetic field. If the sublattices are not equally opposed (such that a net magnetisation is present), the system is called ferrimagnetic. These different configurations are illustrated in Figure 1.4.

Antiferromagnetic order can be described as commensurate (i.e. the periodicity of the spins is linked to the crystal structure), or incommensurate. Examples of commensurate antiferromagnetic order are A-type and G-type order, as shown in Figure 1.5. Examples of incommensurate antiferromagnetic order are sinusoidally modulated spin density waves, and cycloidal order, in which the spins change orientation along the propagation direction inside a circular or ellipsoidal envelope (Figure 1.6).

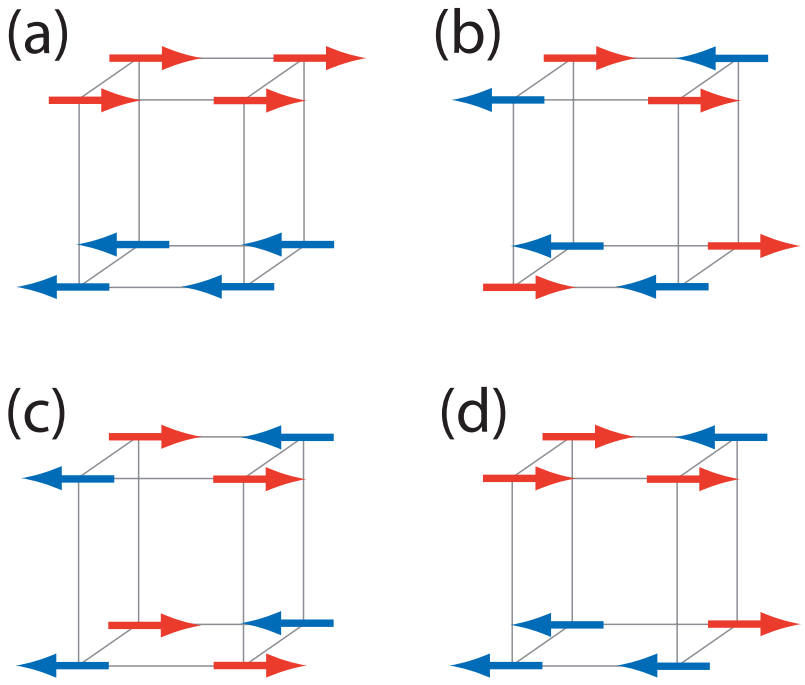

Figure 1.5: (a) A-type, (b) G-type, (c) C-type and (d) E-type commensurate antiferromagnetic order

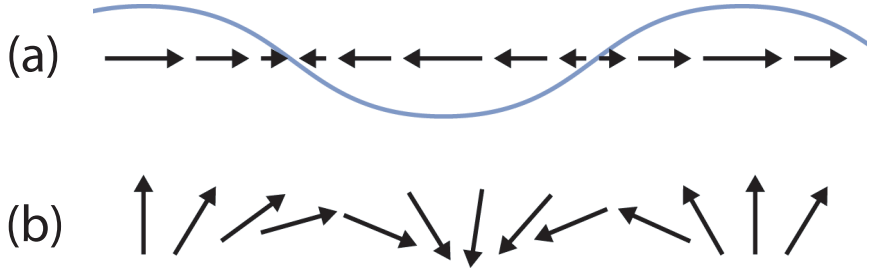

Figure 1.6: (a) sinusoidal and (b) cycloidal incommensurate antiferromagnetic order

1.2.2 Local environments

1.2.2.1 Crystal fields

The anions and cations in a crystal will generally arrange themselves in such a way as to minimise the effects of electrostatic repulsion. This arrangement is dependent on the atomic orbitals, and can have a significant influence on the magnetic properties which are exhibited.

The compounds central to this thesis have perovskite crystal structures (Section 1.1), with a central Mn^{3+} ion surrounded by an octahedron of O^{2-} ions. Electrostatic forces in this case occur between the d orbital of the Mn ion and the p orbitals of the oxygen ions. The d orbitals, such as those in the Mn^{3+} ($3d^4$) ions, can take five different forms: the e_g levels (d_{z^2} and $d_{x^2-y^2}$), defined with the orbitals pointing along the x-, y- and z-axes; and the t_{2g} levels (d_{xy}, d_{xz} and d_{yz}) in which the orbitals point between the axes. The three p orbital types, p_x, p_y and p_z, point along each respective axis. Therefore, in the octahedral environment the e_g orbitals will be in a higher energy configuration than the t_{2g} orbitals [15]. There is a corresponding splitting of the d orbital energy levels, as shown in Figure 1.7. The amount of splitting, Δ, is dependent on such factors as the geometry of the octahedra, the repulsion between the ions, and the effects of Jahn-Teller distortion, as discussed below.

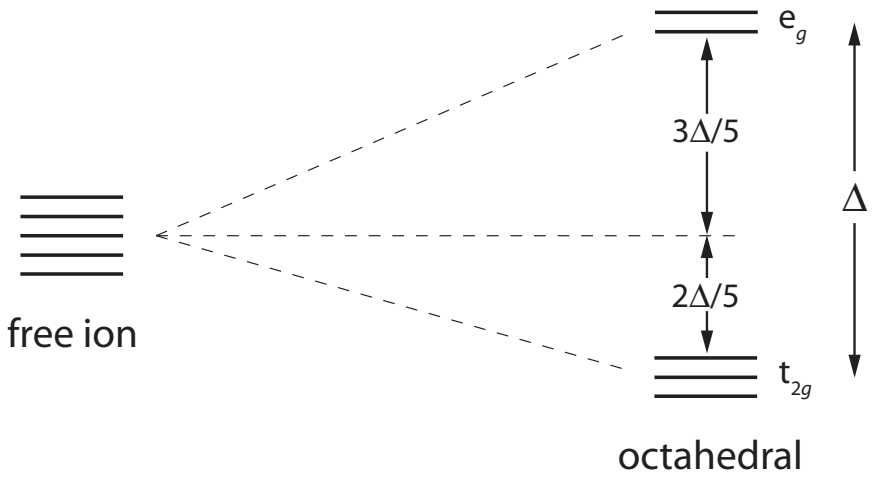

Figure 1.7: Crystal field splitting of the d orbital in an octahedral crystal environment [15].

1.2.2.2 Jahn-Teller distortion

Distortions of the crystal structure can occur in magnetic systems, which have the result of lowering the overall energy. An example of Jahn-Teller distortion is found for the magnetic Mn^{3+} ion, which has 4 electrons in the partially filled $3d$ shell, in an octahedral system. The preferred spin configuration in this case (according to Hund's first rule) is for the spins to all align parallel, which would give three electrons in the lower energy t_{2g} levels and the remaining electron in the higher energy e_g level. By distorting the octahedra via a stretch along the z-axis and a contraction along the x- and y-axes, the e_g and t_{2g} levels are split in energy such that the lone electron in the e_g state can now occupy a lower energy level (Figure 1.8).

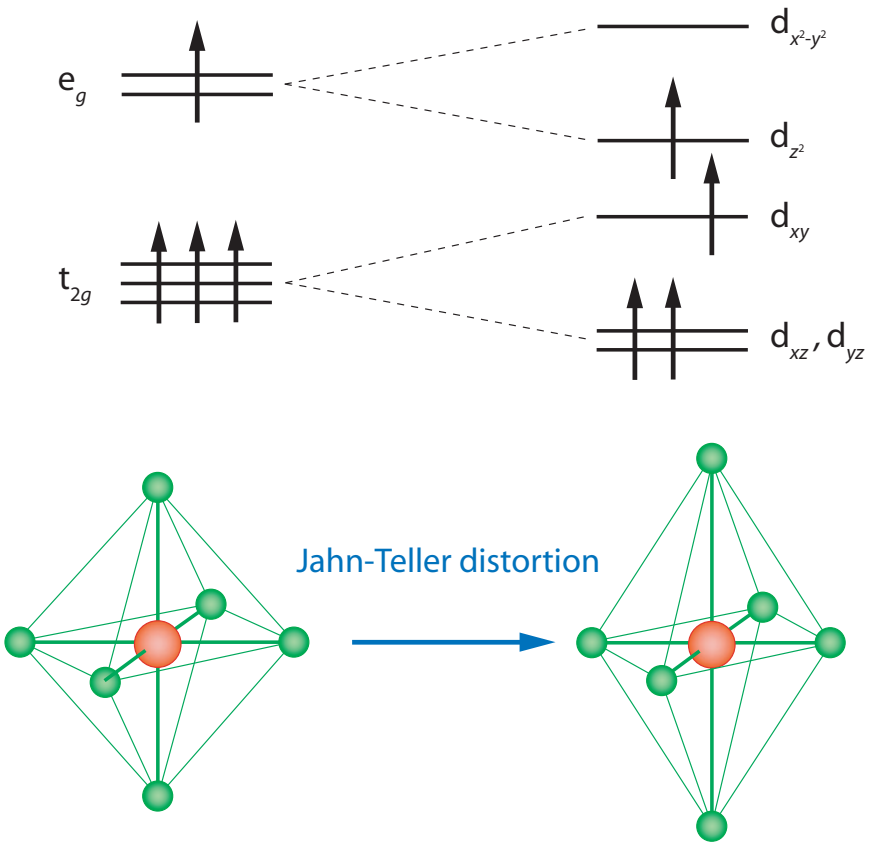

Figure 1.8: Jahn-Teller distortion for a Mn^{3+} ion in an octahedral environment [15].

1.2.3 Magnetic interactions

1.2.3.1 Superexchange

Long range magnetic order occurs due to the exchange interaction between magnetic moments. Direct exchange refers to the interaction between neighbouring moments, but if the process occurs via some intermediate process it is termed indirect exchange or superexchange. For example, consider a system with two magnetic atoms, each with a single d-orbital electron, separated by an oxygen atom. In an ionically bonded system, the oxygen ion will have two electrons in its p-orbital which will overlap with the d-orbitals of the magnetic atoms (Figure 1.9). The energy of the system is lowered if the magnetic atoms order antiferromagnetically, since the electrons are then free to move from the oxygen ion to either magnetic ion. Conversely, if the magnetic ions order ferromagnetically, the oxygen electrons will not be able to move due to the Pauli exclusion principle.

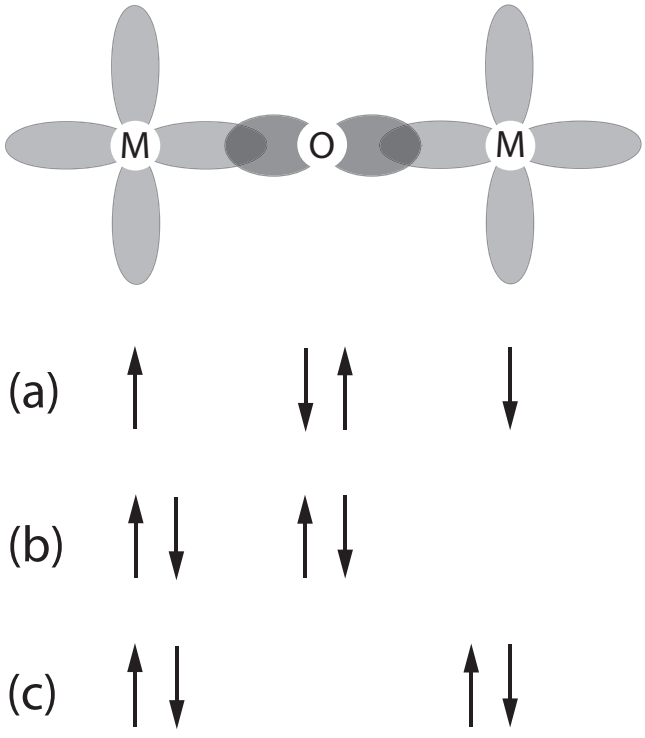

Figure 1.9: Two magnetic atoms, M, separated by an oxygen atom, O. (a) Antiferromagnetic alignment of the magnetic atoms is favoured due to superexchange, since this gives the electrons on the oxygen atom freedom to move, as shown in (b) and (c) [15].

1.2.3.2 Dzyaloshinskii-Moriya interaction

The Dzyaloshinskii-Moriya (DM) interaction is a process similar to superexchange, where the intermediate process is via spin-orbit interaction rather than an oxygen ion. An exchange interaction occurs between the excited state of a magnetic ion and the ground state of the neighbouring ion. For spins $\mathbf{S}_i$ and $\mathbf{S}_j$, a new term in the Hamiltonian is then given by

$$\hat{\mathscr{H}} = \mathbf{D} \cdot (\mathbf{S}_i \times \mathbf{S}_j) \tag{1.2}$$

The Dzyaloshinskii-Moriya vector $\mathbf{D}$ is finite when the crystal field does not have inversion symmetry with respect to the centre between $\mathbf{S}_i$ and $\mathbf{S}_j$. The effect of the DM interaction is often to provide a small canting of the moments in an antiferromagnetic structure, resulting in weak ferromagnetism. The DM interaction favours non-collinear spin ordering, which has important implications for multiferroic properties (Section 1.6)

1.3 The magnetoelectric effect

The relation for the free energy of a material in an electric field $\mathbf{E}$ and/or a magnetic field $\mathbf{H}$ can be expanded as follows [2]:

$$\begin{aligned} F(\mathbf{E},\mathbf{H}) = F_0 &- P_i^S E_i - M_i^S H_i \\ &- \frac{1}{2}\epsilon_0\epsilon_{ij}E_iE_j - \frac{1}{2}\mu_0\mu_{ij}H_iH_j - \alpha_{ij}E_iH_j \\ &- \frac{1}{2}\beta_{ijk}E_iH_jH_k - \frac{1}{2}\gamma_{ijk}H_iE_jE_k - ... \end{aligned}$$

where ϵ is the permittivity, μ is the permeability, and α is a second rank tensor known as the magnetoelectric susceptibility tensor. This equation can be differentiated to give the electric polarisation $\mathbf{P}$ and the magnetisation $\mathbf{M}$ of the material (with the superscript S denoting spontaneous components):

$$P_i(\mathbf{E},\mathbf{H}) = -\frac{\partial F}{\partial E_i} = P_i^S + \epsilon_0\epsilon_{ij}E_j + \alpha_{ij}H_j + \frac{1}{2}\beta_{ijk}H_jH_k + \gamma_{ijk}H_iE_j - ... \tag{1.3}$$

$$M_i(\mathbf{E},\mathbf{H}) = -\frac{\partial F}{\partial H_i} = M_i^S + \mu_0\mu_{ij}H_j + \alpha_{ij}E_i + \beta_{ijk}E_iH_j + \frac{1}{2}\gamma_{ijk}E_jE_k - ... \tag{1.4}$$

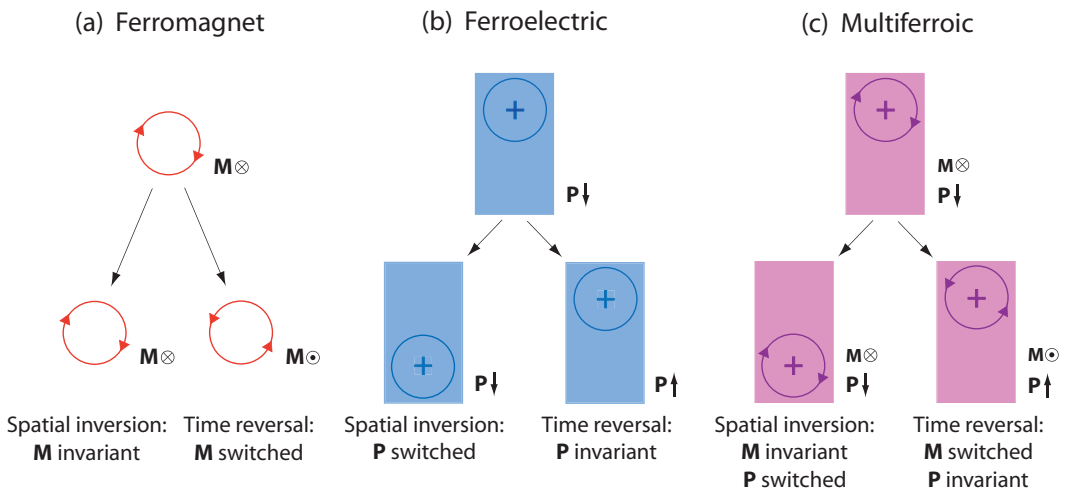

Figure 1.10: The effect of spatial inversion and time reversal on (a) ferromagnets, (b) ferroelectrics and (c) multiferroics. Adapted from Eerenstein *et al.* [16]

It can be seen from Equations 1.3 and 1.4 that α describes a cross-coupling between the electric polarisation and magnetic field, and the magnetisation and electric field, respectively. This coupling is the so-called linear magnetoelectric effect. The terms β and γ describe higher order coupling, which shall be omitted from the following discussion.

For the majority of materials there is no cross-coupling between electric and magnetic properties. This can be explained by examining the effect of time and spatial inversion operations on the system. The electric polarisation and electric field change sign under spatial inversion, and are invariant under time reversal. Conversely, the magnetisation and magnetic field are invariant under spatial inversion and change sign upon time reversal. The magnetoelectric susceptibility tensor is invariant for a material with inversion symmetry. If we take the example of the electric polarisation (just looking at the cross-coupling term), $\mathbf{P} = \alpha\mathbf{H}$, applying spatial inversion gives $-\mathbf{P} = \alpha\mathbf{H}$. This can only be consistent with the original state if $\alpha = 0$. The same result is reached if time or spatial inversion operations are applied to either the polarisation or the magnetisation, meaning that no magnetoelectric coupling can exist in such a material. A non-zero value for α can only occur for a material which breaks both time and spatial inversion symmetry (Figure 1.10).

In 1961, experiments confirmed that a magnetoelectric coupling was present

in antiferromagnetic Cr_2O_3, which shows an electric field induced magnetisation and a magnetic field induced electric polarisation (Figure 1.11) [17, 18]. These discoveries initiated a great deal of research into magnetoelectrics over the next decade. However, the weak magnetoelectric coupling observed meant that the potential technological applications for such materials were limited. In 1968, Brown *et al*. [19] proposed that the magnetoelectric coefficient of a material was restricted by its electric susceptibility χ^e, and magnetic susceptibility χ^m:

$$\alpha_{ij}^2 < \chi_{ii}^e \chi_{jj}^m \tag{1.5}$$

Therefore, a material can only show a strong magnetoelectric coupling if it has a high electric and/or magnetic susceptibility, i.e. it is ferroelectric and/or ferromagnetic. Few compounds were found to show both magnetic and ferroelectric properties, and so the research on the subject of magnetoelectrics largely declined by the mid 1970s.

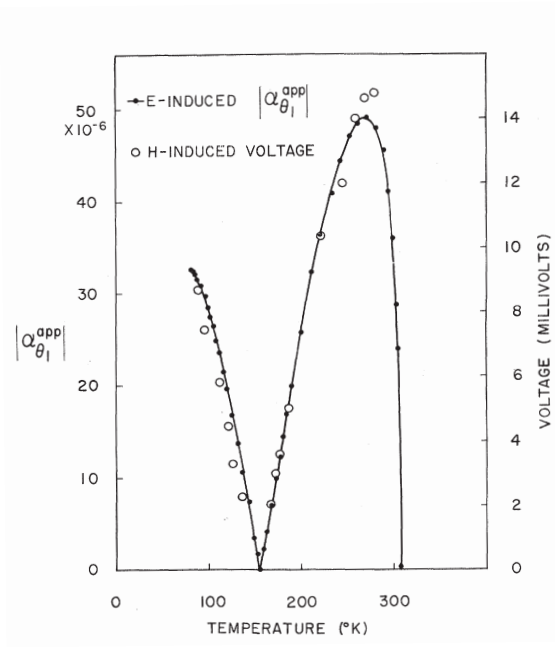

Figure 1.11: Temperature dependence of the magnetoelectric effect in Cr_2O_3 (filled circles: electric field induced, open circles: magnetic field induced ME effect). Taken from Folen *et al*. [17].

1.4 Multiferroics - the revival of magnetoelectric research

Research into the magnetoelectric effect remained at a low level until as recently as 2003. A combination of events at the start of the decade led to the renewed interest in the field. Hill examined the question 'Why are there so few magnetic ferroelectrics?' from a theoretical viewpoint in 2000 [20]. In most ferroelectric materials, such as the classic example of $BaTiO_3$ [10, 11], the ferroelectricity is caused by hybridisation of empty d orbitals of the B-site ions with the occupied p orbitals of the surrounding octahedra of oxygen atoms [21]. Magnetic order, however, requires a partially filled d electron shell, and so the two properties are seemingly incompatible. Hill, however, also showed that this was not a steadfast rule, and went on to suggest materials which could be studied in order to find strong magnetoelectric properties with the aim of prompting further research.

Three major experimental breakthroughs in multiferroics research occurred in 2003-4: the discovery of enhanced magnetoelectric coupling in thin films of $BiFeO_3$ by Wang *et al.*; [8] and the magnetic control of electric polarisation in $TbMnO_3$ by Kimura *et al.* [7], and in $TbMn_2O_5$ by Hur *et al.* [9]. Since then, several new multiferroic materials have been discovered and studied. Highlighted below are some of the most well studied examples of multiferroics.

1.4.1 $BiFeO_3$

$BiFeO_3$ shows ferroelectric order at T_C ~1100 K, and antiferromagnetic order at T_N = 643 K [22]. The bulk spontaneous polarisation in single crystals of $BiFeO_3$ is ~6.1 μC cm^{-2}, rather small for a ferroelectric compound with such a high Curie temperature [23]. By comparison, the room temperature spontaneous polarisation values of well known ferroelectrics $BaTiO_3$ (T_C = 381 K) and $PbTiO_3$ (T_C = 763 K) are ~26 μC cm^{-2} and ~60 μC cm^{-2}, respectively [11, 24]. Wang *et al.* discovered that the polarisation magnitude was greatly increased in thin films of $BiFeO_3$ grown onto a $SrTiO_3$ (100) substrate. The crystal structure of $BiFeO_3$ was found to change from rhombohedral in bulk form to pseudo-tetragonal (with a slight monoclinic distortion) in the thin film form. For a film of ~200 nm thickness,

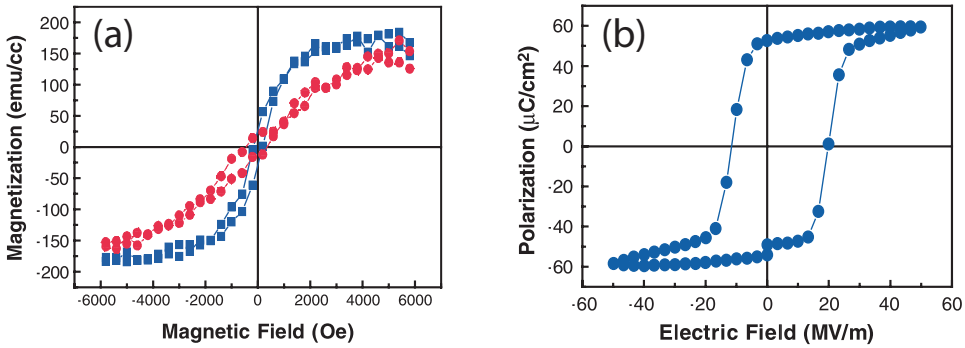

Figure 1.12: (a) Magnetic hysteresis loop for a $BiFeO_3$ film of 70 nm thickness (blue data is in plane, red data is out of plane of film), and (b) electric hysteresis loop for a $BiFeO_3$ film of 200 nm thickness, measured at a frequency of 15 kHz. All data was measured at room temperature. Adapted from Wang *et al.* [8].

the polarisation was measured to be ∼55 μC cm^{-2} at room temperature, an increase of nearly an order of magnitude from that in the bulk form (Figure 1.12).

The antiferromagnetic domains in $BiFeO_3$ were found to change orientation under an applied electric field by Zhao *et al.* [25]. This property occurs at room temperature, and so makes $BiFeO_3$ desirable for use as a data storage media (since data could be written using less energy than using applied magnetic fields). Much of the recent work on $BiFeO_3$ has focused on potential technological applications of the thin film compounds, with work detailing the electric (and magnetic) domain structures and properties of $BiFeO_3$ thin films, or doped/composite variant materials [25–27].

1.4.2 $TbMnO_3$

$TbMnO_3$ was found to be ferroelectric by Kimura *et al.* in 2003, with a spontaneous electric polarisation along the *c*-axis developing at the same temperature as a magnetic phase transition (Figure 1.13) [7]. Heat capacity and magnetisation data for $TbMnO_3$ clearly show three transitions, occurring at 41 K, 27 K and 7 K (Figure 1.13(a)). The magnetic properties of $TbMnO_3$ were first reported by Quezel *et al.* in 1977, where the transition at 41 K was attributed to an ordering of the Mn^{3+} moments and the transition at ∼7 K was found to be due to the ordering of the Tb^{3+} moments [28]. The transition at 41 K was further described by Kimura *et al.* to be a sinusoidally modulated antiferromagnetic order with the

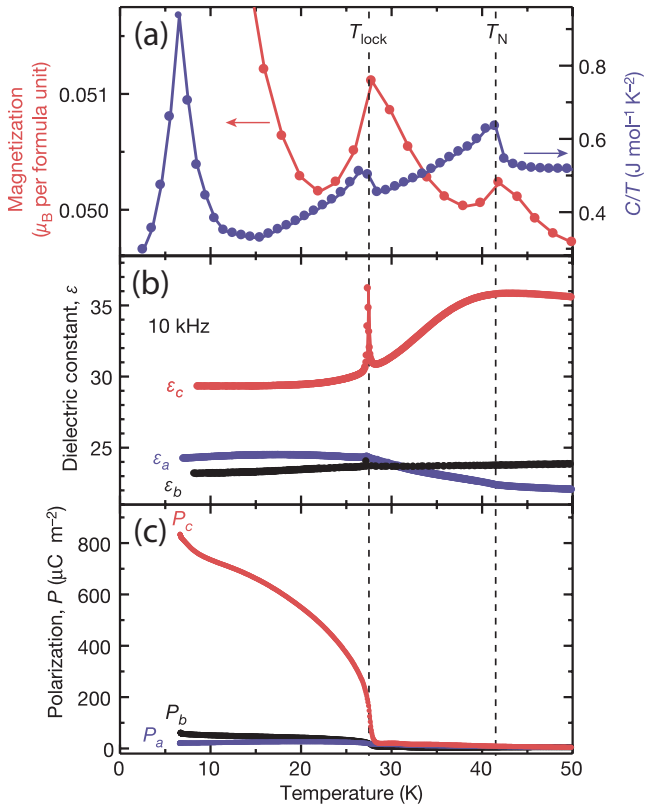

Figure 1.13: Temperature dependences of (a) magnetisation and heat capacity, (b) dielectric constant and (c) electric polarisation for single crystal $TbMnO_3$, illustrating the correlation between electric and magnetic properties. Taken from Kimura *et al.* [7]

spins aligned along the *b*-axis [29], but the exact nature of the transition at 27 K - which coincides with the onset of the spontaneous polarisation - was still unclear. The most significant result from the paper of Kimura *et al.*, however, is the giant magnetoelectric coupling found in $TbMnO_3$. This coupling is demonstrated by the application of a magnetic field along the *b*-axis resulting in a change in the electric polarisation direction from the *c*- to the *a*-axis, a so-called polarisation flop (Figure 1.14). Observation of the magnetisation versus magnetic field along the *b*-axis (Figure 1.14(c)) shows a metamagnetic transition at ∼4.5 T - the same applied field as that which causes the polarisation flop.

1.4.3 $TbMn_2O_5$

Shortly after the discovery of multiferroic properties in $TbMnO_3$, Hur *et al.* found that $TbMn_2O_5$ also shows a very interesting magnetoelectric coupling. [9] Due to the existence of Tb^{3+}, Mn^{3+} and Mn^{4+} moments, the magnetic interactions are not quite the same as those found in $TbMnO_3$. $TbMn_2O_5$ shows 3 magnetic tran-

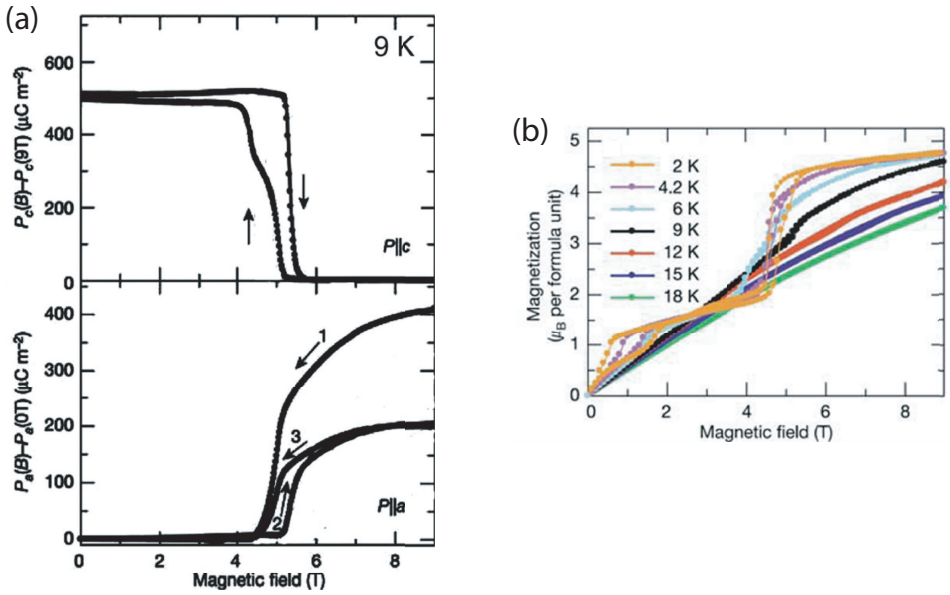

Figure 1.14: (a) Magnetic field induced change in the electric polarisation direction in $TbMnO_3$, with the magnetic field applied parallel to the *b*-axis. (b) The polarisation flop occurs at the same magnetic field as a metamagnetic transition along the *b*-axis [7].

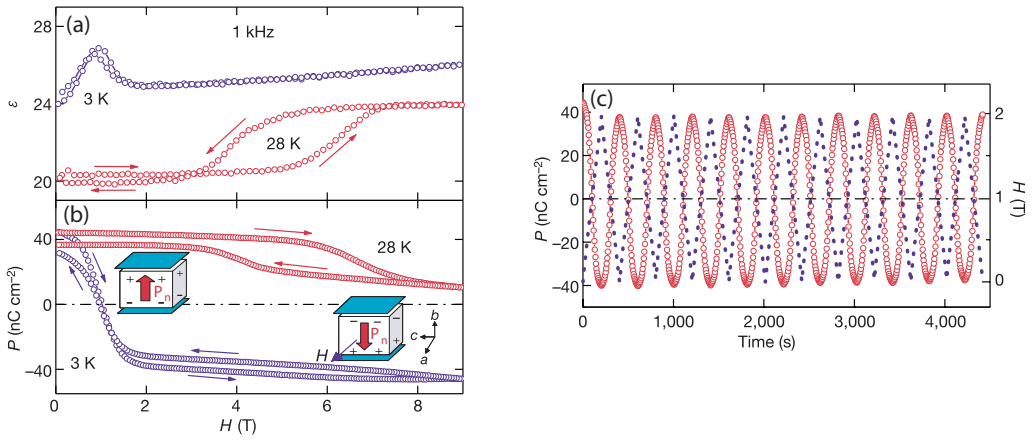

Figure 1.15: (a) Dielectric constant and (b) electric polarisation along the *b*-axis of $TbMn_2O_5$. (c) The polarisation can be flipped multiple times without loss of magnitude. Taken from Hur *et al.* [9]

sitions, with long range antiferromagnetic order of the Mn^{3+} and Mn^{4+} moments at ∼43 K, Mn spin reorientation at ∼24 K, and a further transition at ∼38 K which coincides with a ferroelectric polarisation along the *b*-axis.

The application of a magnetic field along the *a*-axis has a significant effect on the electric polarisation. At 3 K, a magnetic field of ∼2 T causes the polarisation to completely change direction - i.e. from +*b* to -*b* (Figure 1.15(b)). This polarisation flipping was demonstrated multiple times with no apparent loss in magnitude (Figure 1.15(c)). This behaviour has clear implications for the realms of data storage, where media would need to be erasable and rewritable.

1.4.4 $DyMnO_3$

Shortly after the giant magnetoelectric effect was discovered in $TbMnO_3$, similar properties were found by the same group in $DyMnO_3$ [30]. The magnitude of the spontaneous polarisation that develops below the cycloidal ordering temperature is significantly larger in $DyMnO_3$ than $TbMnO_3$ in zero magnetic field (Figure 1.16). As with $TbMnO_3$, the polarisation develops along the *c*-axis, and can be switched to the *a*-axis with a magnetic field applied parallel to *b*.

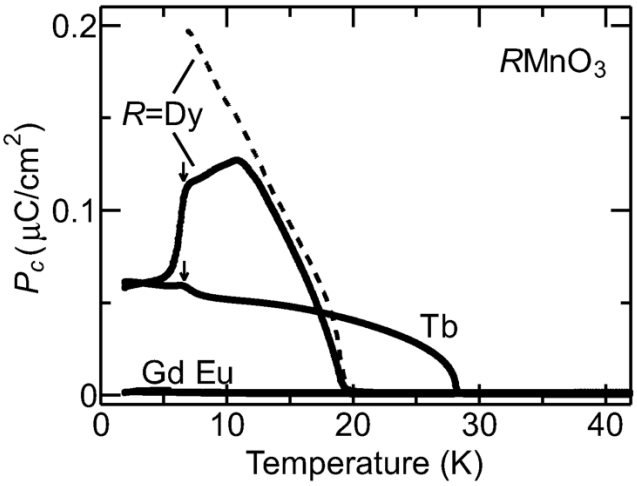

Figure 1.16: Electric polarisation along the *c*-axis of single crystal $R\mathrm{MnO_3}$ (R = Eu, Gd, Tb, Dy). Note: the magnitude of the polarisation is given in μC cm^{-2}, rather than μC m^{-2}. Solid line: sample pre-cooled to 2 K, dashed line: pre-cooled to 7 K. The arrows signify the magnetic ordering temperatures of the R moments. Taken from Goto *et al*. [30]

1.4.5 $GdMnO_3$

Goto *et al*. also reported data on $GdMnO_3$, and found that no (or only extremely small) spontaneous polarisation was seen along the *c*-axis at zero applied magnetic field. Kimura *et al*. later reported that similar properties are seen along the *a*-axis, with only a very small polarisation ($\sim$35 μC m^{-2}) appearing below 10 K [31]. However, it was found that applying a magnetic field parallel to *b* induces a much larger electric polarisation, with $\sim$540 μC m^{-2} measured at 6 T (Figure 1.17). There was no observed change in the direction of the electric polarisation with a magnetic field applied along any of the principal crystallographic axes.

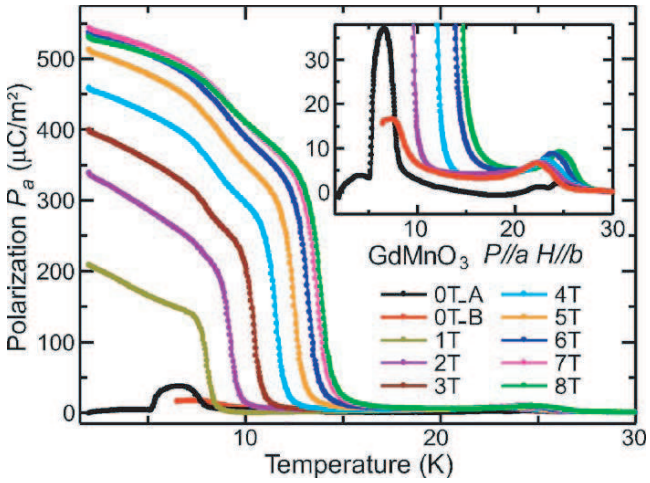

Figure 1.17: Electric polarisation along the *a*-axis of $GdMnO_3$, with the magnetic field applied parallel to *b*. Taken from Kimura *et al*. [31]

1.5 Classification of multiferroics

Since the discovery of the materials highlighted above, Schmid's definition of a multiferroic [1] has evolved. Multiferroics are now put into one of two main classes [6]:

1.5.1 Type-I multiferroics

In type-I multiferroics the magnetic and ferroelectric ordering occur at different temperatures, and due to different processes. The result of this is that there is a weak coupling between them. The ferroelectric state generally arises at a higher temperature, with the spontaneous polarisation being of order 10-100 μC cm^{-2}. An example of a widely studied type-I multiferroic is $BiFeO_3$ (Section 1.4.1).

1.5.2 Type-II multiferroics

In a type-II multiferroic the ferroelectricity is directly caused by magnetic order. This implicitly means that a strong coupling must exist between the two orders. The most well known example of a type-II multiferroic is $TbMnO_3$, in which a cycloidal antiferromagnetic ordering induces a spontaneous electric polarisation at $\sim$27 K (Section 1.4.2). Due to the strong coupling that exists in such a material, it is often possible to alter the ferroelectric polarisation of a type-II multiferroic with an applied magnetic field, or vice versa. The practical drawback of this class of multiferroic is that the magnitude of the polarisation is much lower than that of a type-I multiferroic (of order 10^{-2} μC cm^{-2}).

One of the major current challenges facing researchers in the field of multiferroics is to find a material which has both the electric polarisation magnitude of a type-I multiferroic and the strong magnetoelectric coupling of a type-II multiferroic.

1.6 Understanding the magnetoelectric effect in $TbMnO_3$

By 2005, strong magnetoelectric coupling had been discovered in $TbMnO_3$ and $DyMnO_3$ with $GdMnO_3$ also showing an electric polarisation under an applied magnetic field [30, 31]. Research then began to focus on understanding the nature of the magnetic phase which induced the ferroelectricity in these compounds.

Kenzelmann *et al*. [32] carried out neutron diffraction experiments on $TbMnO_3$ single crystals. Below 41 K, data corresponding to a sinusoidal magnetic order of the Mn^{3+} moments were found (Figure 1.18(a)), in agreement with the model proposed by Kimura *et al*. [7]. However, the magnetic phase below 27 K was not found to be commensurate as previously thought, therefore discounting an incommensurate-commensurate "lock-in" transition as the cause of ferroelectricity. Instead, the phase was proposed to be cycloidal, with the Mn^{3+} moments in the form of an ellipsoidal spiral in the *b*-*c* plane (Figure 1.18(b)).

The appearance of a ferroelectric order in $TbMnO_3$ was described by Kenzelmann *et al*. by analogy with the description for a similar effect in $Ni_3V_2O_8$ [33].

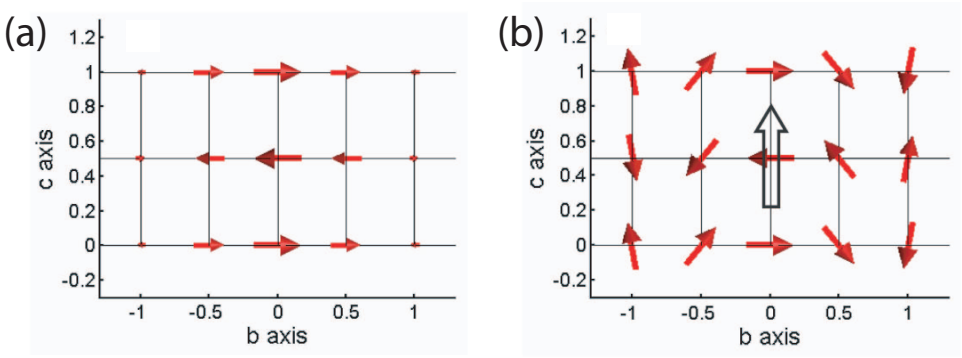

Figure 1.18: (a) The sinusoidal magnetic order of the Mn spins below 41 K, and (b) the cycloidal magnetic order below 27 K in $TbMnO_3$. The black arrow in (b) represents the electric polarisation. Adapted from Kenzelmann *et al.* [32].

The spontaneous polarisation was proposed to be due to the cycloidal order of the Mn^{3+} moments breaking the magnetic spatial inversion symmetry and thus allowing a coupling between the magnetic and electric order parameters (see Section 1.3). Using symmetry arguments, the direction of the electric polarisation was correctly predicted for $Ni_3V_2O_8$ and $TbMnO_3$.

A microscopic model for describing the magnetoelectric coupling in non-collinear magnets such as $TbMnO_3$ was presented by Katsura *et al.* [34]. It was proposed that the electric polarisation is induced by a spin current, $\mathbf{j}_S \propto \mathbf{S}_i \times \mathbf{S}_j$, for neighbouring spins $\mathbf{S}_i$ and $\mathbf{S}_j$ separated by a vector $\mathbf{r}_{ij}$:

$$\mathbf{P} \propto \mathbf{r}_{ij} \times (\mathbf{S}_i \times \mathbf{S}_j) \tag{1.6}$$

In $TbMnO_3$, the magnetic Mn atoms are connected by non-magnetic oxygen atoms, with Mn-O-Mn bond angle ϕ (Figure 1.19). The spins propagate along the b-axis and spirally ordered in the b-c plane (i.e. $(\mathbf{S}_i \times \mathbf{S}_j)$ is parallel to a). According to equation 1.6, the induced polarisation will be proportional to $(b \times a)$ and will therefore point along the c-axis, as confirmed by experiment (Figure 1.13). A similar result was also found by Mostovoy, using a phenomenological approach [35]. As shown in Figure 1.14, the electric polarisation switches from the c- to the a-axis under an applied magnetic field along the b-axis. According to Equation 1.6, a cycloid in the a-b plane, propagating along the b-axis would be expected in this state (such that $\mathbf{r}_{ij}//b$, $\mathbf{j}_S//c$, $\mathbf{P}//a$). This spin configuration was experimentally confirmed by Aliouane *et al.* [36].

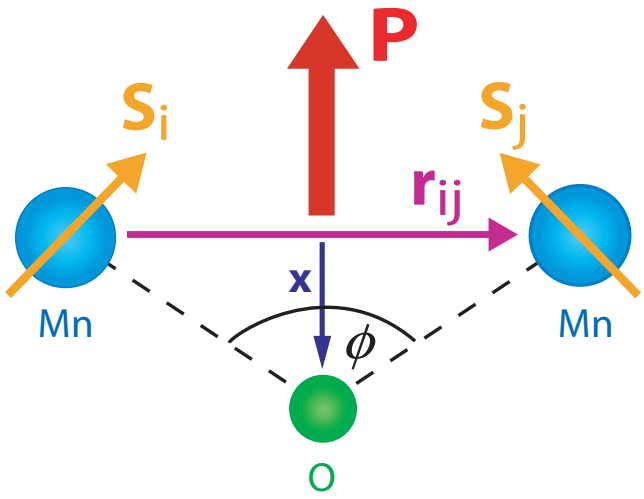

Figure 1.19: Electric polarisation induced by cycloidal magnetic order in $TbMnO_3$.

Sergienko *et al*. proposed a link between the Dzyaloshinskii-Moriya (DM) interaction and the onset of ferroelectricity in systems which show non-collinear spin order [37, 38]. The DM vector $\mathbf{D}$ shown in Equation 1.2 is proportional to $\mathbf{x} \times \mathbf{r}_{ij}$, where $\mathbf{x}$ is the displacement of the oxygen atom (Figure 1.19). The DM interaction energy is therefore increased by pushing the negative O ions away from the positive Mn ions, resulting in an electric polarisation. Supporting this theory is the fact that the electric polarisation is found to be perpendicular to the direction of magnetic propagation for all incommensurate multiferroics, as would be expected by Equation 1.2.

As the displacement $\mathbf{x}$ of the oxygen atoms increases, the Mn-O-Mn bond angle ϕ decreases, suggesting an important link between ϕ and the existence of multiferroic properties.Goto *et al*. suggested a link between the multiferroic properties seen in $TbMnO_3$ and $DyMnO_3$ and ϕ in 2004 (Figure 1.20) [30]. It was apparent that the cycloidal magnetic order was only seen for ϕ in the range $144.5° \lesssim \phi \lesssim 145.8°$, implying a strong link between the relative positions of neighbouring Mn atoms and the magnetic frustration they experience. It has also been proposed that the magnetic ordering of the rare earth moments plays a part in inducing the cycloidal Mn^{3+} phase [39].

Recent X-ray scattering experiments on $TbMnO_3$ have confirmed that the Tb^{3+} moments order as well as the Mn^{3+} moments at the ferroelectric transition temperature, with a component along the b-axis [40, 41]. This result confirmed previous

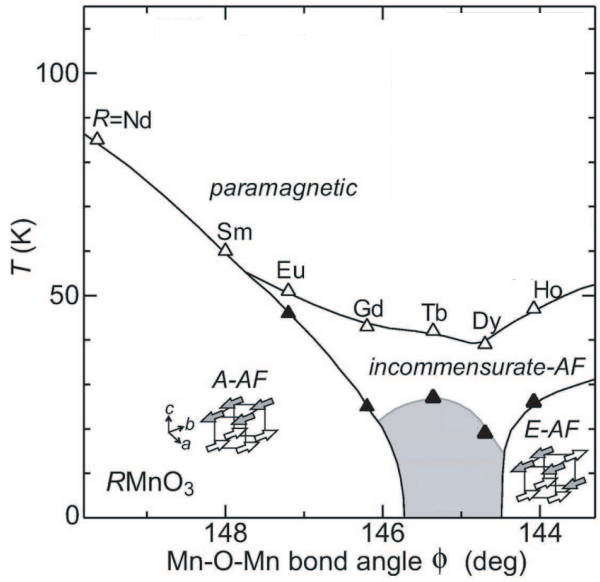

Figure 1.20: Magnetic phase diagram for RMnO$_3$ (AF = antiferromagnetic), taken from Goto *et al*. [30]. The grey area indicates the region in the phase diagram where a cycloidal Mn order and strong magnetoelectric coupling is observed.

predictions [32], and has potentially important implications for understanding the nature of the magnetoelectric effect in TbMnO$_3$. The description of the magnetic structure of TbMnO$_3$ was also modified by Wilkins *et al*. to include a slight canting of the of the Mn^{3+} moments in the c-direction in the sinusoidal magnetic phase, and an out of plane canting in the cycloidal phase.

1.7 Recent research and motivation for this work

In the past 5 years, research into the multiferroics has branched into several different areas. The use of multiferroics for technology is currently a widely researched field, and the fundamental physics governing the strong magnetoelectric coupling seen in multiferroics is still not fully understood.

1.7.1 Technological applications

In the field of spintronics the spin of an electron, rather than (or in addition to) its charge is used to carry information. Spintronic devices, therefore, can retain information without an applied electric current (i.e. are non-volatile) and so have a much lower power consumption than typical charge-based devices. Spintronics could theoretically be used for magnetic random access memory (MRAM). The

ability to change the magnetisation state of a sample with an applied electric field would mean that less power is used, and so multiferroic materials could prove to be very important to this field. Papers on multiferroic thin films frequently cite potential use in spintronics as a motivation for research.

A problem with using multiferroics in the field of spintronics is that they typically show antiferromagnetic order, and therefore have little or no overall magnetisation. One way of overcoming this is the synthesis of composite materials of antiferromagnetic multiferroics and ferromagnets. The magnetisation of the ferromagnet is linked to the antiferromagnet due to exchange bias. In principle, applying an electric field to the material would change the ferroelectric polarisation of the multiferroic antiferromagnet and thus the direction of the antiferromagnetic order. This, in turn, would flip the magnetisation direction of the ferromagnet. This process is illustrated in Figure 1.21, taken from Ramesh & Spaldin [4]. This process does not strictly require a multiferroic material, rather one with a strong magnetoelectric response. A similar effect was found by Zavaliche *et al*. for a composite thin film consisting of $CoFe_2O_4$ nanopillars inside a $BiFeO_3$ matrix [42], and research is currently focusing on producing a technologically viable thin film material.

Another proposed practical application for multiferroic materials is as read heads for magnetic storage devices [43, 44]. Presently, read heads make use of magnetoresistance effects, with the resistance experienced by the device being dependent on the magnetic orientation of the domains in the storage media. Measuring this resistance requires a test current to be supplied to the read head, but a multiferroic device could generate an output voltage in the absence of an external current. This would then lead to reduced power consumption of the device, which is particularly valuable for battery powered handheld devices.

1.7.2 $R_{1-x}\mathbf{Y}_x\mathbf{MnO}_3$

Now that the causes of multiferroic behaviour are better understood, it has been possible for new multiferroics to be synthesized. One such branch of research has concentrated on composite multiferroics, which are made up of 2 (or more)

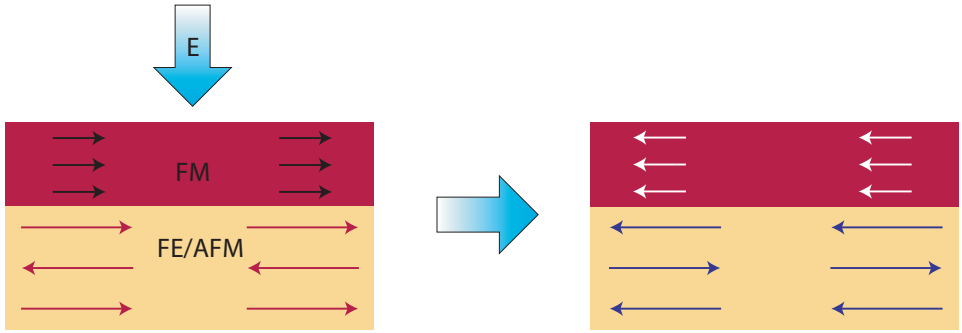

Figure 1.21: A theoretical picture of an applied electric field changing the ferromagnetic alignment of a material due to exchange bias. The material is made up of a ferromagnetic (FM) layer on top of a ferroelectric antiferromagnet (FE/AFM). Taken from Ramesh & Spaldin [4]

compounds that have respective ferroelectric and ferromagnetic properties. The magnetoelectric response in such materials can be very large, and can occur at room temperature. Examples of well studied composite multiferroics are PbTiO3-$CoFe_2O_4$, $x CoFe_2O_4$-(1-x)$PbZr_{0.52}Ti_{0.48}O_3$ and $BaTiO_3$-$CoFe_2O_4$ [45–47].

From a fundamental point of view, composite multiferroics do not help us to understand the physics which causes the magnetoelectric coupling in single phase compounds. A relatively new area of research with explores this theme involves developing new multiferroics based on doping non-multiferroic materials. Such research makes up a substantial part of this thesis.

The rare earth manganite ($R MnO_3$) series shows various different magnetic states as the lanthanide atom is changed. The $R MnO_3$ compounds (R = La, Ce, Pr, Nd, Pm, Sm, Eu, Gd, Tb, Dy) form as orthorhombically distorted perovskite structures, space group Pbnm. For R = La-Eu, the compounds have A-type antiferromagnetic order (Figure 1.5) [48].

As discussed in Sections 1.4.2, 1.4.4, $TbMnO_3$ and $DyMnO_3$ are multiferroic, with frustrated magnetism in the form of cycloidal ordering of the Mn^{3+} moments inducing ferroelectricity. $GdMnO_3$ also shows an electric polarisation under an applied field (Section 1.4.5).

The $R MnO_3$ compounds (R = Ho, Er, Tm, Yb, Lu, Y) form as hexagonal structures, but can be prepared as orthorhombic with high pressure synthesis. These compounds have been found to show type-I multiferroic behaviour, with antiferromagnetic order occurring at low temperature (<100 K), and ferroelectric

order at high temperature (>500 K) [49–55]. The R-site moments typically order at low temperatures ($\lesssim$10 K) across the RMnO$_3$ series.

Based on the phase diagram of the RMnO$_3$ series (Section 1.6), Ivanov *et al.* doped EuMnO$_3$ and GdMnO$_3$ with non-magnetic Y, with the aim of reducing the Mn-O-Mn bond angle and inducing multiferroic properties [56]. A spontaneous electric polarisation was found for both $Eu_{1-x}Y_xMnO_3$ and $Gd_{1-x}Y_xMnO_3$ at x = 0.2 and 0.1, respectively. The magnitude of the spontaneous polarisation in $Eu_{0.8}Y_{0.2}MnO_3$ is ~700 μC m^{-2} at 0 T, a similar value to that found in TbMnO$_3$, but pointing along the a-axis rather than the c-axis. The application of a magnetic field along the c-axis causes a suppression of the polarisation along a at ~5 T. A smaller electric polarisation of ~75 μC m^{-2} is also seen along the c-axis in zero field (Figure 1.22). $Gd_{1-x}Y_xMnO_3$ was found to show a relatively small polarisation along the c-axis of ~20 μC m^{-2}, which could also be suppressed by an applied magnetic field along the c-axis [56]. The results for $Eu_{1-x}Y_xMnO_3$ were expanded upon by the same group in the following year for Y-doping up to a concentration of x=0.5 [57]. An increase in the electric polarisation magnitude to ~1200 μC m^{-2} was found for $Eu_{0.595}Y_{0.405}MnO_3$ by Noda *et al.* [58] and Yamasaki *et al.* for $Eu_{0.6}Y_{0.4}MnO_3$ [59]. Both papers reported a polarisation flop from the a-axis to the c-axis with a magnetic field applied along the a-axis of ~4 T. The magnitude of the electric polarisation that developed along the c-axis was approximately 3-4 times smaller than that along the a-axis. Up to the present date (April 2010), papers have continued to be published trying to further understand the multiferroic properties of $Eu_{1-x}Y_xMnO_3$ [60–62]. The papers on $Eu_{1-x}Y_xMnO_3$ often state that there is no magnetic moment contribution from the Eu^{3+} ions, since the free ion has a total angular momentum $J = 0$ [57–59]. They therefore infer that the strong rare earth moments of Tb^{3+} and Dy^{3+} ions are not necessary for the magnetic frustration of the Mn^{3+} moments in the RMnO$_3$ compounds. However, it is still possible that rare earth-Mn interactions can enhance multiferroic properties, as proposed for DyMnO$_3$ by Prokhnenko *et al.* [63]. An electric polarisation flop where similar values of polarisation are seen along the initial and flop directions could also be linked to a strong coupling between the rare earth

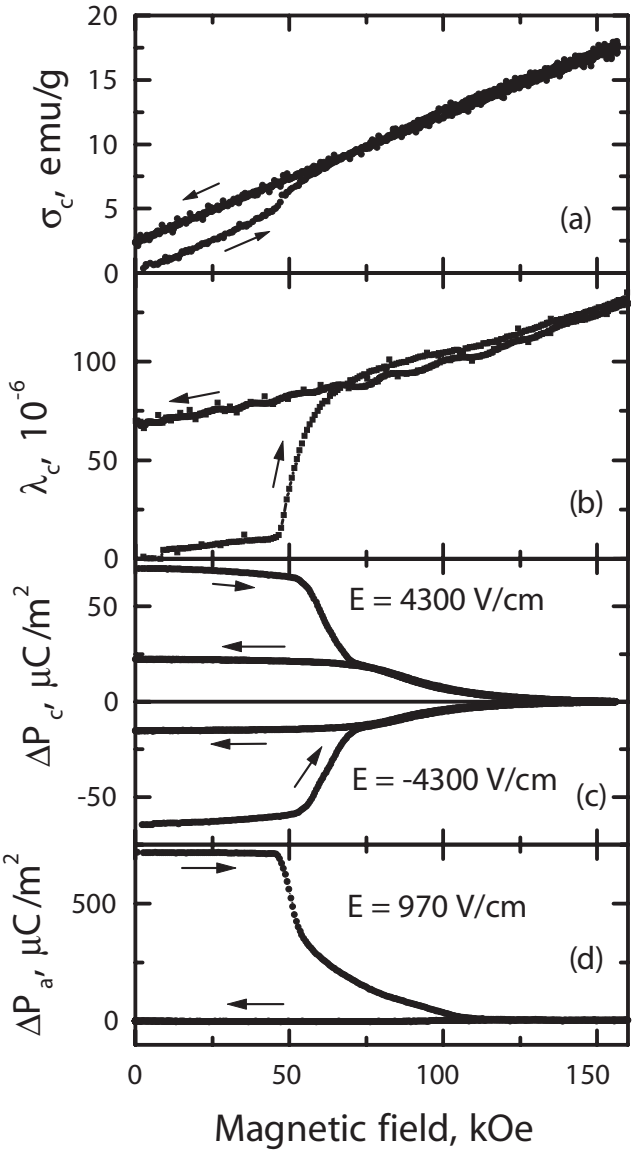

Figure 1.22: Magnetic field dependence of (a) magnetisation, (b) longitudinal magnetostriction, and electric polarisation along the (c) c- and (d) a-axis for $Eu_{0.8}Y_{0.2}MnO_3$. The magnetic field is applied parallel to the c-axis at 4.5 K. Taken from Ivanov *et al.* [56]

and Mn^{3+} ions.

The Mn-O-Mn bond angle has been found to decrease with increasing Y concentration in $Nd_{1-x}Y_xMnO_3$, with an associated change in the magnetic properties [64]. Ferroelectric properties have subsequently been found for this group of compounds with $x = 0.4 - 0.55$ [65].

The compounds studied in this thesis are the rare earth manganites of the form $RMnO_3$ (R = Sm, Tb, Dy) and $R_{1-x}Y_xMnO_3$ (R = Sm, Gd). $TbMnO_3$ and $DyMnO_3$ are well studied compounds, and were chosen as a starting point for the project. The procedure for single crystal growth was refined using these compounds, and measurements of magnetic and electric properties were made, as detailed in Chapter 3. The magnetic susceptibility data along the three principal crystallographic axes of $TbMnO_3$ and $DyMnO_3$, the heat capacity of $TbMnO_3$ in an applied magnetic field, and the magnetisation data for $DyMnO_3$ are unpublished elsewhere at the time of writing. Similar data for a new group of multiferroic compounds, $Sm_{1-x}Y_xMnO_3$ ($x = 0.4, 0.5$) are presented in Chapter 4. The production of $Sm_{1-x}Y_xMnO_3$ (both polycrystalline and single crystal samples), and the measurements of magnetoelectric properties were carried out for the first time as part of this project. This work was prompted by the research discussed in Section 1.7.2, with the aim of further understanding the fundamental physics which leads to multiferroic properties. The following chapter presents results of neutron diffraction and X-ray resonant scattering experiments, conducted as an attempt to determine the magnetic structure of $Sm_{1-x}Y_xMnO_3$. Initial work on compounds of the form $Gd_{1-x}Y_xMnO_3$ and $Gd_{1-x}Lu_xMnO_3$ is detailed in Chapter 6, which were studied as a follow-up to $Sm_{1-x}Y_xMnO_3$.

Chapter 2

Experimental methods

Several different experimental techniques were utilised for the investigations described in this thesis. This chapter details these techniques, covering sample preparation and characterisation, laboratory measurements of magnetic and electric properties, and the underlying physics of neutron scattering and X-ray resonant scattering experiments carried out at central facilities.

2.1 Sample preparation

All samples used for the experiments detailed in this thesis were made at the University of Warwick. Polycrystalline samples were synthesised by solid state reaction. This was carried out by mixing and grinding together stoichiometric ratios of the required metal oxide powders, followed by furnace heating. Typically, powders were heated 3-4 times for 12 hours at temperatures up to 1400−1500°C. Hygroscopic starting compounds (those which absorb moisture from the air) such as Nd_2O_3 and Y_2O_3 were pre-heated for 4 hours at 1100°C to remove impurities before reacting with other oxides.

2.2 X-ray diffraction

Powder X-ray diffraction was used to check phase formation and determine the crystal structure of synthesised samples. Incident X-rays are scattered by a polycrystalline sample according to Bragg's law

$$n\lambda = 2d \sin \theta \tag{2.1}$$

where λ is the wavelength of the X-ray beam, θ is the incident angle, and d is the distance between crystal planes. The value for d is dependent on the Miller indices h, k and l. Two different X-ray machines were used to record the diffraction patterns presented in this thesis: a Philips PW1720 X-ray generator, which uses Cu K_α radiation ($\lambda \sim 1.54$Å); and a (more advanced) Panalytical X'Pert Pro multipurpose X-ray diffraction system (MPD), with monochromated Cu $K_{\alpha 1}$ radiation.

2.3 Single crystal growth

Single crystal samples are vital to understand the physics exhibited by samples which have high magnetic/ferroelectric anisotropy (i.e. significantly different behaviour is seen along different crystallographic directions). This is especially the case in multiferroic compounds, where the application of a magnetic field along one crystallographic direction could affect the electric properties seen along another direction, and vice versa. Single crystals are also necessary in order to observe local magnetic behaviour (such as domains and short-range correlations) using neutron diffraction or X-ray scattering.

The single crystal specimens used for the measurements presented in this thesis were grown using the floating zone method. Samples need to be in the form of polycrystalline rods before crystal growth can be carried out. Polycrystalline materials were made into rods by compacting the powder into a waterproof balloon before compressing isostatically by submerging in water and applying high pressure (>150 kg cm^{-2}). The resulting rod was sintered again for 12 hr at ∼1400°C to make it less likely to crumble upon handling.

The resultant rod (the feed rod) is then suspended using platinum wire (which is non-reactive and has a high melting point) inside the optical floating zone furnace, as shown in Figure 2.1. Inside a sealed quartz tube, the rod is suspended from a shaft above a crystal of either the same compound, or one with similar lattice parameters (the seed). The shafts are then counter-rotated and the feed and seed are brought close to each other at the centre of the furnace. At this point, light from halogen (or xenon) bulbs is focused by using ellipsoidal mirrors

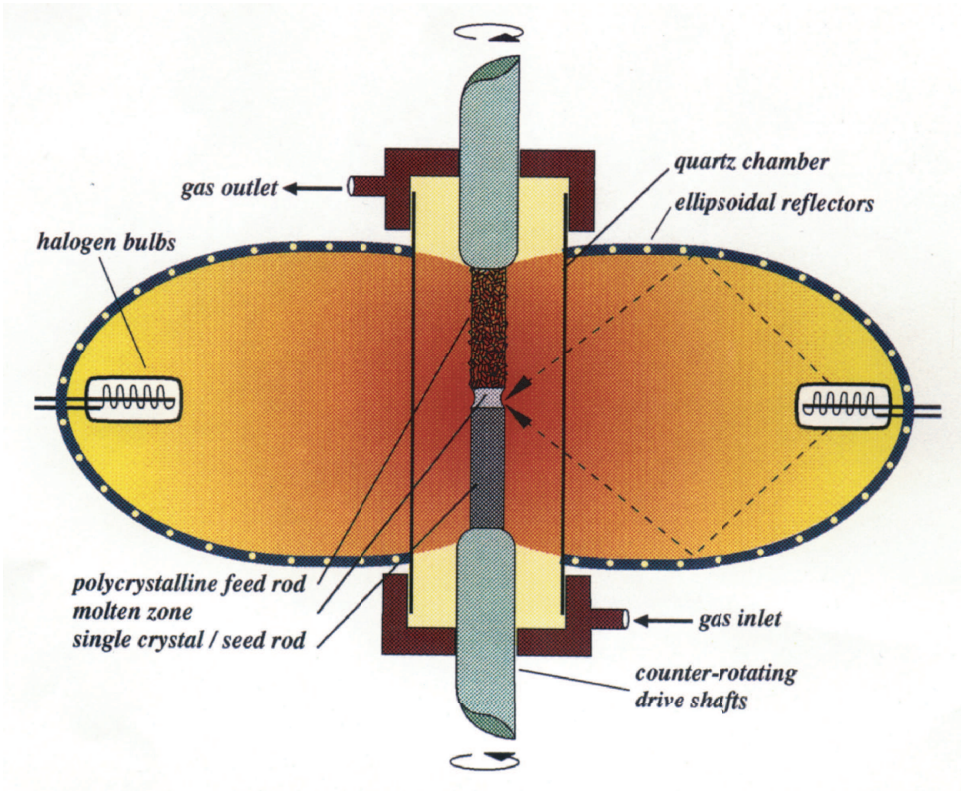

Figure 2.1: Schematic of a two-mirror floating zone image furnace

inside the furnace, creating a region of high temperature. The temperature in this region is gradually increased until both rods reach their melting points, at which point they are brought together to make a molten zone, held together by the surface tension of the material. The counter-rotation helps to homogenise both the temperature and the composition in this region. The rods are then both lowered through the hot region such that the length of the feed rod is transformed from polycrystalline to a molten state, and then into a single crystal as it leaves the high temperature zone and resolidifies upon slow cooling.

The stability of the molten zone can be maintained by remotely controlling the power to the bulbs to raise/lower the temperature in the zone, and by controlling the individual rate at which each shaft is lowered, as well as making small adjustments to their positions if necessary. Crystal growth can be carried out in an atmosphere of air, oxygen, argon or a combination of these gases (an argon atmosphere could be used for a compound that is particularly reactive with oxygen, for example). The crystal growth rates for samples described in this thesis have ranged from 5-10 mm/h. The furnaces used for crystal growth were the

NEC SC-N35HD and Canon Machinery SC1-MDH 11020 two mirror furnaces, and the Crystal Systems Inc. F-ZT-10000-H-IV-VPS and FZ-T-12000-X-VI-VP four mirror furnaces.

Using the floating zone method, crystals up to 80 mm in length and 8 mm in diameter were grown. Large crystal sizes are particularly useful for neutron scattering experiments (Section 2.9), where signals are small. There is no contamination of samples with the floating zone method, since growths are carried out in a closed atmosphere without the need for a crucible (unlike the Bridgman and Czochralski methods). Compositions of dopants tend to be uniform in the grown boules, and are representative of the composition of the feed rod. However, the gravity-based nature of the crystal growth means that there is a limitation on the size of the crystals grown compared to, for example, the Czochralski method.

2.4 X-ray Laue method

Single crystal quality and orientation are determined using the X-ray Laue technique. A "white" beam of X-rays is used for this technique, i.e. the beam is not single wavelength. The range of X-ray wavelengths gives a range of Ewald spheres of different radii, meaning that a large portion of reciprocal space is diffracted simultaneously. The setup is such that the incident X-ray beam is fired from the centre of a scintillator screen, and is backscattered towards the screen by the crystal (Figure 2.2. Images are recorded using a charge-coupled device (CCD) connected to a computer. The peak emission of the (GdOS:Tb) scintillator screen is at 500nm, which matches the quantum efficiency response of the CCD. Image-Pro Express software[1] allows control over the data collection, including exposure times and number of images recorded. Samples were mounted on a triple-axis goniometer which allowed rotation and translation in each axis/direction to be remotely controlled from a computer. This allowed samples to be checked and aligned without having to shut down the X-ray power supply to access the sample area.

[1] http://www.mediacy.com/

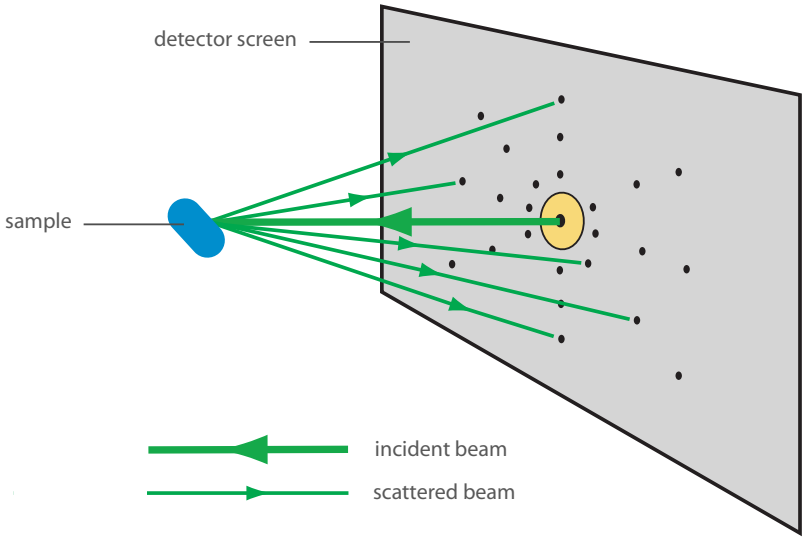

Figure 2.2: The X-ray Laue technique

Using OrientExpress software,[2] Laue patterns for single crystals can be simulated, provided that information is known on the crystal space group and lattice parameters. These patterns can then be used to orient single crystal samples. Typically, oriented single crystals are cut using a low speed diamond saw, such that the crystallographic directions of interest are normal to the cut surface. The crystal pieces used for the measurements presented in this thesis were parallelepipeds, with each face perpendicular to a principal crystallographic direction (the *a*-, *b*- and *c*-axes for orthorhombic systems). The dimensions of these samples were $\sim 3 \times 2 \times 2$ mm^2 or smaller.

2.5 Magnetic properties

2.5.1 Superconducting QUantum Interference Device (SQUID)

The SQUID magnetometer is an instrument which is very sensitive to magnetic fields, making it ideal for measuring subtle changes in the magnetic behaviour of a sample when it is subjected to different temperatures, magnetic fields or pressures. The magnetometer comprises a SQUID attached to pick up coils which sit inside a superconducting magnet. Samples are fixed to non-magnetic tufnol holders with GE (General Electric) varnish, and then placed on the end of a non-magnetic sample rod between the pick up coils. Liquid helium and liquid nitrogen are used

[2] http://www.ccp14.ac.uk/ccp/web-mirrors/lmgp-laugier-bochu/

to cool the magnet and control the temperature inside the sample space. To take measurements, a magnetic field is applied to the sample as it is slowly moved through the coils in a series of 32 steps. The magnetic response of the sample generates a current in the pick-up coils which in turn is detected by the SQUID. The SQUID is shielded from the magnetic fields so as to detect only the current from the pick-up coils. After the sample has been moved through the specified range (typically 4 cm), the measured signal is fitted and then converted into a magnetic moment value in electromagnetic units (emu). A schematic diagram of the SQUID is shown in Figure 2.3. Two different SQUID magnetometers were used to take the measurements presented in this thesis - a Quantum Design MPMS-5S and MPMS-XL. The MPMS-5S can be used to take magnetisation measurements over a temperature range of $1.8 - 400$ K and applied magnetic field range of up to ± 5 T. The MPMS-XL is able to reach ± 7 T.

Typical measurements carried out with the SQUID were of magnetic susceptibility versus temperature at a rate of $\sim$1 K/min when measuring around magnetic transitions, or 2-5 K/min if measuring the paramagnetic behaviour over a large temperature range. Magnetic susceptibility can be measured in both zero-field cooled (ZFC) and field cooled (FC) situations. A zero-field cooled measurement involves the sample being cooled from the high temperature paramagnetic state to base temperature before a magnetic field is applied to the sample, and in a field cooled measurement the field is applied beforehand. There can be a significant difference between the ZFC and FC data depending on the nature of the magnetic order present in a material.

2.5.1.1 Interpreting susceptibility data

In the paramagnetic state of a material, the susceptibility is expected to behave according to the Curie-Weiss law. For a ferromagnet with Curie temperature T_{C}, this law is given as

$$\chi = \frac{C}{T - T_{\mathrm{C}}} \tag{2.2}$$

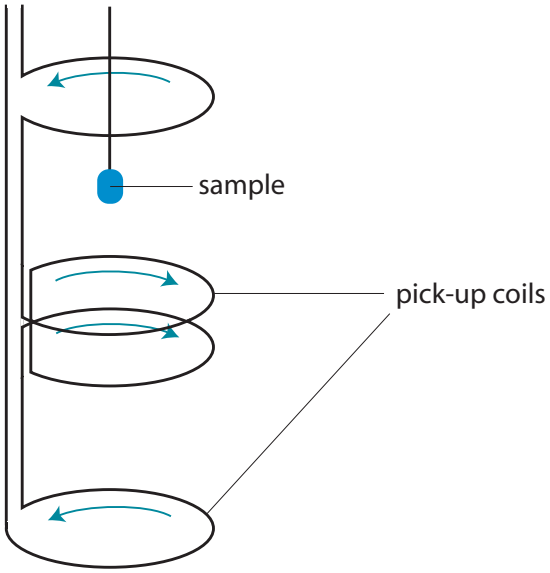

Figure 2.3: Schematic of a SQUID magnetometer

where C is the Curie constant, a value which is dependent on the material under study. For a general magnetic system, this law is rewritten as

$$\chi = \frac{C}{T - \theta} \tag{2.3}$$

where θ is the Weiss temperature. The value of θ can be determined by plotting $^1/_\chi$ (Figure 2.4), and gives information on the nature of the magnetic properties of a material. For a material which is paramagnetic down to 0 K, $\theta = 0$. A positive value of θ indicates a ferromagnetic material, with $\theta = T_C$ expected. A negative value of θ indicates an antiferromagnetic material, with $\theta = -T_N$ expected. This relation assumes that, for antiferromagnets, the molecular field on a magnetic sublattice is purely dependent on the magnetisation of the other sublattice, and discrepancies between the values of θ and -T_N are common in practice [15].

The value of C can be used to calculate the effective magnetic moment, μ_{eff} present in a sample, according to

$$C = \frac{\mu_B^2 p_{eff}^2 N_A}{3k_B} \tag{2.4}$$

where μ_B is the Bohr magneton, k_B is the Boltzmann constant (both in c.g.s. units), N_A is Avogadro's number and $p_{eff} = {}^{\mu_{eff}}/_{\mu_B}$. The magnetic moment of an ion can be theoretically calculated from the orbital (L), spin (S) and total (J) angular momentum values:

$$p_{eff} = g_J \sqrt{J(J+1)} \tag{2.5}$$

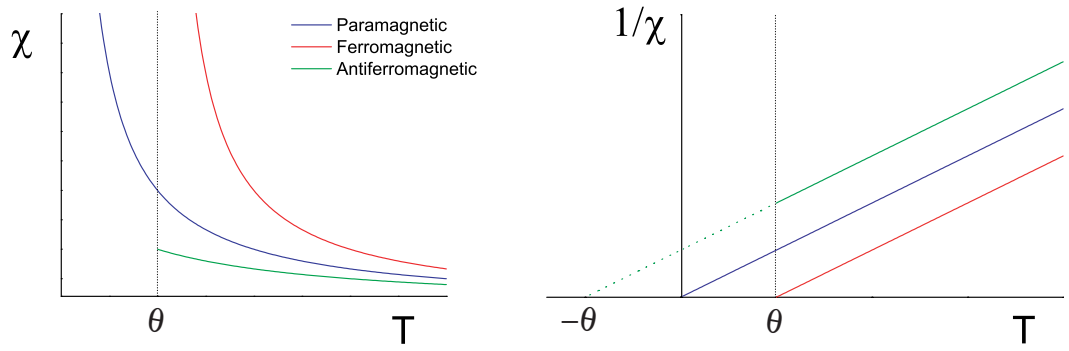

Figure 2.4: (a) Curie-Weiss behaviour of the magnetic susceptibility of different magnetic systems, above the magnetic ordering temperature, θ. (b) Plotting the inverse susceptibility gives straight line data, with θ given by the intercept with the temperature axis. $\theta = 0$ for a paramagnet, $\theta > 0$ for a ferromagnet, and $\theta < 0$ for an antiferromagnet.

where g_J is the Landé g-value, given by

$$g_J = \frac{3}{2} + \frac{S(S+1) - L(L+1)}{2J(J+1)} \tag{2.6}$$

2.5.2 Vibrating Sample Magnetometer (VSM)

The Oxford Instruments VSM is an instrument that is suited to smoothly varying the applied magnetic field, up to ±12 T. This makes it a more suitable instrument than a SQUID magnetometer for measuring the field dependence of the magnetisation of a sample (although the SQUID has greater sensitivity). As with the SQUID magnetometer, a current is induced in the pick-up coils due to the motion of a magnetic sample between them. The motion is given by a vibration of the sample at a constant frequency of 55 Hz. Measuring the magnetisation of a sample along different crystallographic directions gives information on its magnetic anisotropy, and the size of the magnetisation can be related to the magnetic order present. The VSM can also be used to observe sample hysteresis and metamagnetic transitions.

The size of the magnetisation observed under an applied magnetic field can be compared with theoretical values to further understand the behaviour of a magnetic system. If an applied magnetic field is sufficient to saturate the magnetic moments in a sample, the expected saturation magnetisation is given by

$$M_S = nJg_J\mu_B \tag{2.7}$$

where n is the number of atoms per unit volume.

2.5.3 Physical Properties Measurement System (PPMS)

The PPMS is used to measure the heat capacity of a sample, usually as a function of temperature, but also as a function of applied magnetic field. The sample is placed on a 3×3 mm^2 platform in the middle of a "puck" (Figure 2.5). The platform is suspended by wires, which isolate the platform from thermal contact with the system, and are also used for platform heating and temperature measurement. The sample is attached to the platform using Apiezon grease (N-grease for low temperature measurements and H-grease for measurements above room temperature). This puck is then placed inside a superconducting magnet which has a temperature range of 2-400 K, and is capable of applying magnetic fields up to ±9 T. The heat capacity is then determined at a particular temperature by applying a small increase in temperature (typically ∼5% of the current temperature) and measuring how long the sample takes to return to the initial temperature. Because both the sample platform and the Apiezon grease will contribute to this relaxation time, it is necessary to initially take an addenda measurement, where the heat capacity of just the puck and the grease is measured over the temperature range required for the sample measurement. This addenda is then subtracted from the subsequent measurement with the sample present. Samples for heat capacity measurements can be either polycrystalline or single crystal for zero field measurements, since the heat capacity is a bulk value. However, if a magnetic field is to be applied along a certain crystallographic direction, a single crystal is necessary. The sample should be relatively thin (ideally less than 1 mm) to avoid the effects of a thermal gradient between the platform and the top of the sample, and should have a large surface area to improve the accuracy of the measurement (a larger sample will have a larger relaxation time upon a change in temperature).

2.5.3.1 Interpreting heat capacity data

The heat capacity, C, of a sample at a particular temperature gives information on the entropy, S, present in the system. At constant pressure, this relationship is given by

$$C_P = T\left(\frac{\partial S}{\partial T}\right)_P \tag{2.8}$$

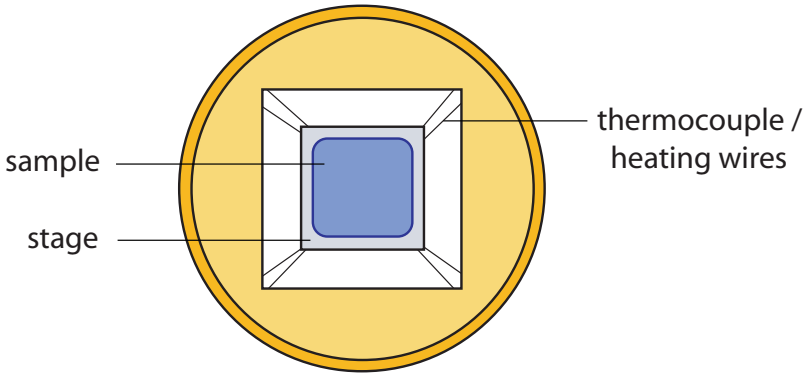

Figure 2.5: Sample puck, inserted into PPMS for heat capacity measurements

The entropy of a system is given by the following equation for a fixed volume, V and magnetic field, B:

$$S = -\left(\frac{\partial F}{\partial T}\right)_{V,B} \tag{2.9}$$

where F is the Helmholtz free energy, a portion of the total internal energy, E of the system defined as

$$F = U - TS \tag{2.10}$$

From equation 2.9, it can be seen that a change in the energy of the system will have an associated entropy change, and so measurements of the heat capacity are useful for observing phase transitions, which appear as sharp peaks as a function of temperature. Determining the magnetic entropy also gives quantitative information on the magnetic order present in the sample:

$$S = R\ln(2J+1) \tag{2.11}$$

where R is the molar gas constant (8.314 $\mathrm{m^2\ kg\ s^{-2}\ K^{-1}\ mol^{-1}}$) and J is the total angular momentum of the magnetic ion.

In order to extract the magnetic entropy from the total entropy, phonon contributions need to be subtracted. This can be achieved by measuring the heat capacity of a non-magnetic analogue of the sample, and then subtracting its heat capacity. This non-magnetic compound is known as a phonon blank, and is chosen to have a molecular weight and crystal structure as close as possible to the magnetic compound in order to have an accurate representation of its lattice contribution to the heat capacity.

2.6 Dielectric constant measurements

A material is referred to as a dielectric if it can be electrically polarised upon the application of an electric field. This polarisation occurs due to electric dipoles orienting themselves in response to the applied field. An internal electric field within the dielectric is generated (the electric displacement field), and acts to compensate the external field. The electric susceptibility of a dielectric, χ_e is a measure of how strongly the polarisation, $\mathbf{P}$, is dependent on the applied field, $\mathbf{E}$:

$$\mathbf{P} = \chi_e \varepsilon_0 \mathbf{E} \tag{2.12}$$

where ε_0 is the permittivity of free space (8.854×10^{-12} Fm^{-1}). The electric susceptibility is a dimensionless quantity, and is related to the permittivity, ε. For a material with a relative permittivity, ε_r:

$$\varepsilon = \varepsilon_0 \varepsilon_r = (1 + \chi_e)\varepsilon_0 \tag{2.13}$$

The relative electric permittivity is also referred to as the dielectric constant. The electric displacement field, $\mathbf{D}$ is also directly linked to the electric polarisation and the dielectric constant:

$$\mathbf{D} = \varepsilon_0 \mathbf{E} + \mathbf{P} \tag{2.14}$$

Referring to Equations 2.12 and 2.13, this relation can be expressed as

$$\mathbf{D} = \varepsilon_0 \varepsilon_r \mathbf{E} \tag{2.15}$$

The behaviour of dielectric materials in response to external electric field is well illustrated in the case of the parallel plate capacitor. For two electrodes of area A, separated by a distance d across a vacuum (Figure 2.6), a capacitance develops when an electric field is applied:

$$C = \frac{\varepsilon_0 A}{d} \tag{2.16}$$

If a dielectric material is then inserted between the two electrodes (Figure 2.6), the electric field is reduced, and the capacitance increases:

$$C = \frac{\varepsilon_0 \varepsilon_r A}{d} \tag{2.17}$$

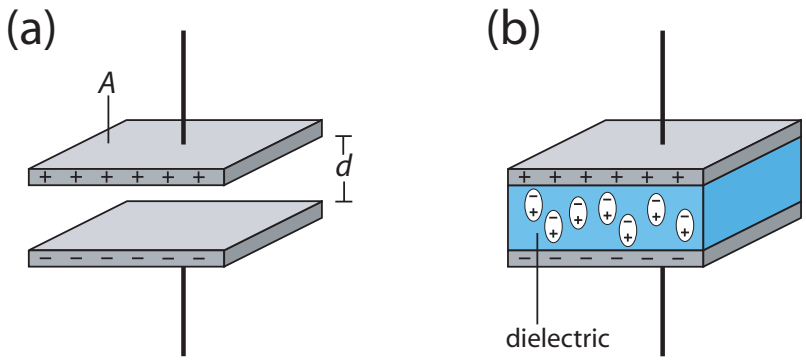

Figure 2.6: A parallel plate capacitor, where the electrodes are separated by (a) a vacuum, and (b) a dielectric material

Experimentally, the dielectric constant of a material can be determined by measuring its capacitance, assuming its dimensions are well known.

In order to measure the electric properties of multiferroic materials, a new PPMS sample insert was made by Professor C.V. Tomy (EPSRC Visiting Fellow, 2008-09). This insert allowed the sample to be placed inside a superconducting magnet for measurements to be made from 400 K to 2 K, and in magnetic fields up to 9 T. The application of a magnetic field whilst measuring electrical properties is very important for demonstrating the existence of multiferroic properties. The sample insert could be connected to an impedance analyser, an electrometer or a high voltage power supply as required. A schematic diagram and photograph of the sample insert can be seen in Figure 2.7. A LabVIEW program was developed (by C.V. Tomy and summer student Ashley Chapman), enabling computer control of the PPMS operations and communication with the impedance analyser, electrometer and voltage supply. Part of the work carried out for this Ph.D. was helping to set up this electric measurement system, and performing trial experiments in order to standardise results(Section 2.8).

Samples used for electric properties measurements need to have two flat, opposite faces (i.e. of the form of a parallel plate capacitor) and are attached to the insert using GE varnish. Electrical contacts are made by coating the flat faces with silver paste (Du Pont 4929N conductor paste) and attaching wires. During the course of testing this new system, it was discovered that to reduce noise in the measurements it was best to use a thin sample (<1 mm thick) with a relatively large surface area (>5 mm^2). It was also found that silver paint alone did not give

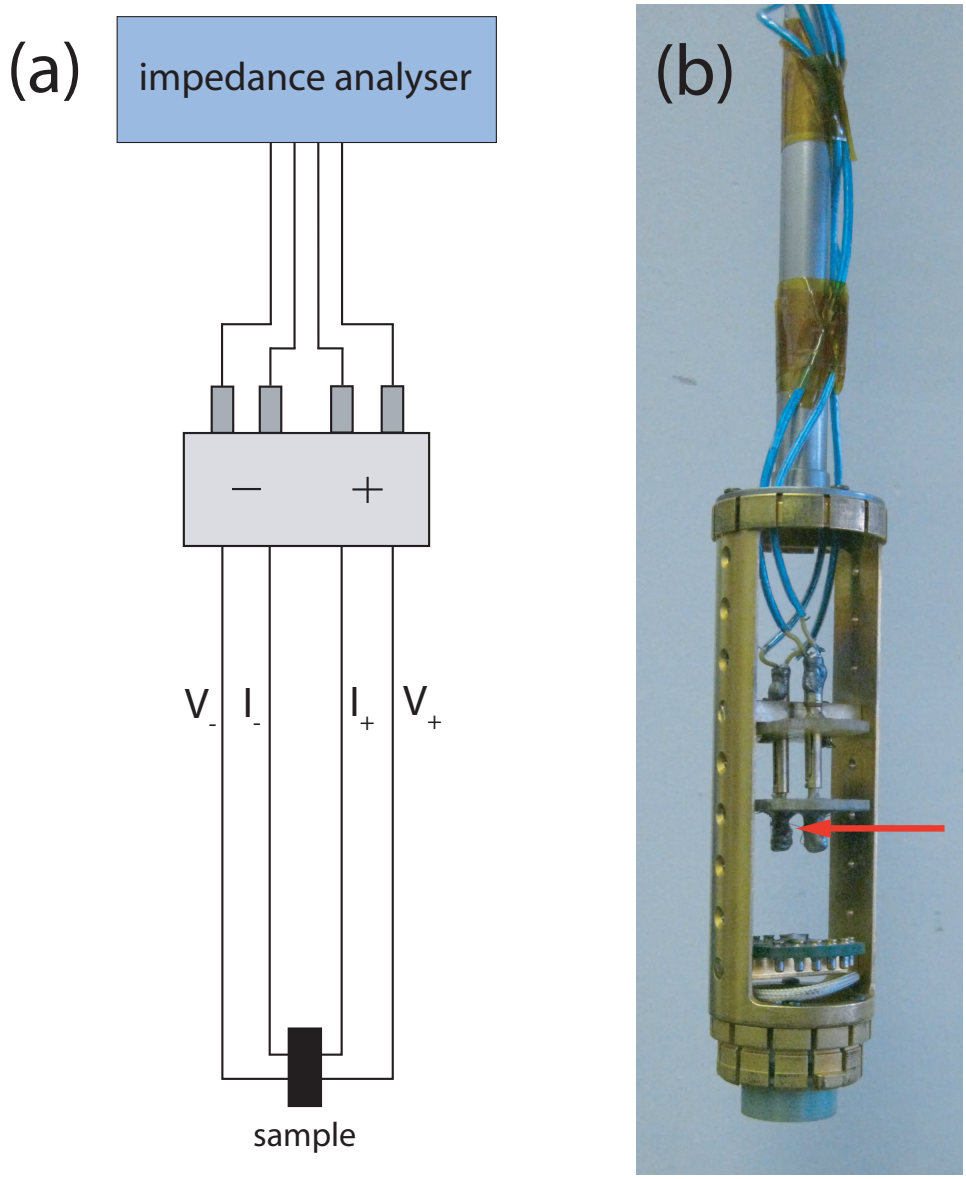

Figure 2.7: (a) Schematic diagram of the sample insert for electric properties measurements. (b) Close up of the sample connection point (the arrow indicates the point where the sample is attached)

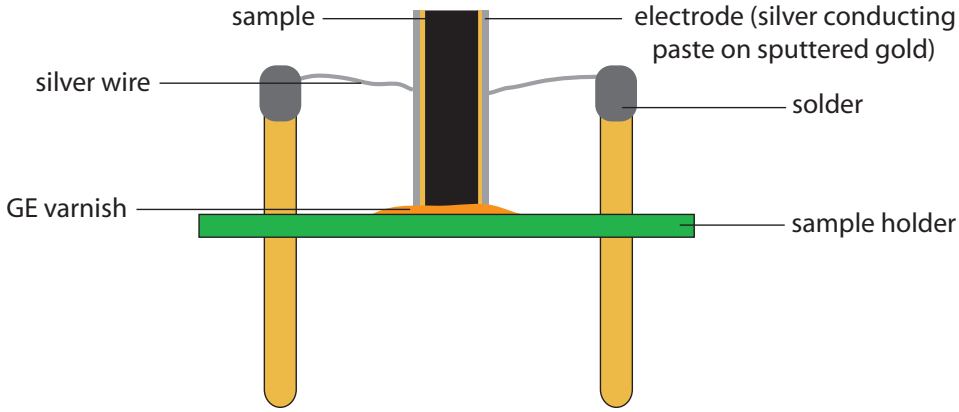

Figure 2.8: Illustration of sample mounting and connection for dielectric measurements

sufficient electrical contact with the surface of the sample, and so gold sputtering was used as a base before silver paint was used to attach the wires (Figure 2.8).

For measurements of the dielectric constant, an Agilent 4294A impedance analyser was connected to the PPMS sample insert. The sample capacitance was then measured as a function of temperature, and used to calculate the dielectric constant using Equation 2.17.

2.7 Polarisation measurements

Measurements of the electric polarisation were conducted by detecting the pyroelectric current as a function of temperature. This method is commonly used for multiferroics [7, 66], where the polarisation magnitudes are small compared with those of standard ferroelectrics. Samples were prepared in a similar manner as for capacitance measurements, with electrodes sputtered on opposite faces of the crystal. The sample insert was first connected to a high voltage power supply (Stanford Research Systems PS310). A voltage of 150-200 V mm^{-1} was applied across the sample, at some temperature far above the ferroelectric transition temperature (T_C). Keeping the voltage applied, the sample was then cooled through T_C to a low temperature value (2-10 K). At this point, the high voltage was removed from the sample.

Since polarisation measurements are concerned with the bulk polarisation within the sample, it was important to remove the effect of surface charges which had built up due to the application of an electric field. A bleed resistor box was built

for this purpose (Section 2.8.3), which dissipated the surface charge when the voltage supply was disconnected. It was found that it was necessary to leave samples connected to the bleed resistor for 30-60 min for sufficient removal of surface charge. The sample was then connected to a Keithley 6517A electrometer, and the temperature of the sample was increased (at a rate of 1-5 K min^{-1}) whilst measuring the pyroelectric current. The electrometer has a very high sensitivity, essential for measuring the small pyroelectric current which is of the order of 1 pA $= 10^{-12}$ A. This sensitivity introduces the practical problem of making sure the measured signal is not influenced by ground loops, or stray electric fields from equipment connected to the mains power supply - or even movement of people near the equipment.

The temperature dependence of the pyroelectric current will typically show a finite signal in the ferroelectric phase, with a sharp anomaly at T_{C}. Above T_{C}, the signal becomes flat, showing that electric polarisation no longer exists in the system. In order to convert the data into a measure of the polarisation (in Cm^{-2}), the following relationship is used:

$$P = \int \frac{I \, \mathrm{d}t}{A} \tag{2.18}$$

The pyroelectric current data is measured as a function of temperature and time by the LabVIEW program. The data is integrated with respect to time, from the final time to start time. This integration method ensures that zero polarisation is calculated in the temperature range where the pyroelectric current is zero (i.e. above T_{C}). The integral of the current is divided by the sample area (electrode area) to give the polarisation, which can be plotted against temperature. This process is shown in Figure 2.9. In order to determine the crystallographic axis along which the polarisation develops, single crystal specimens are required.

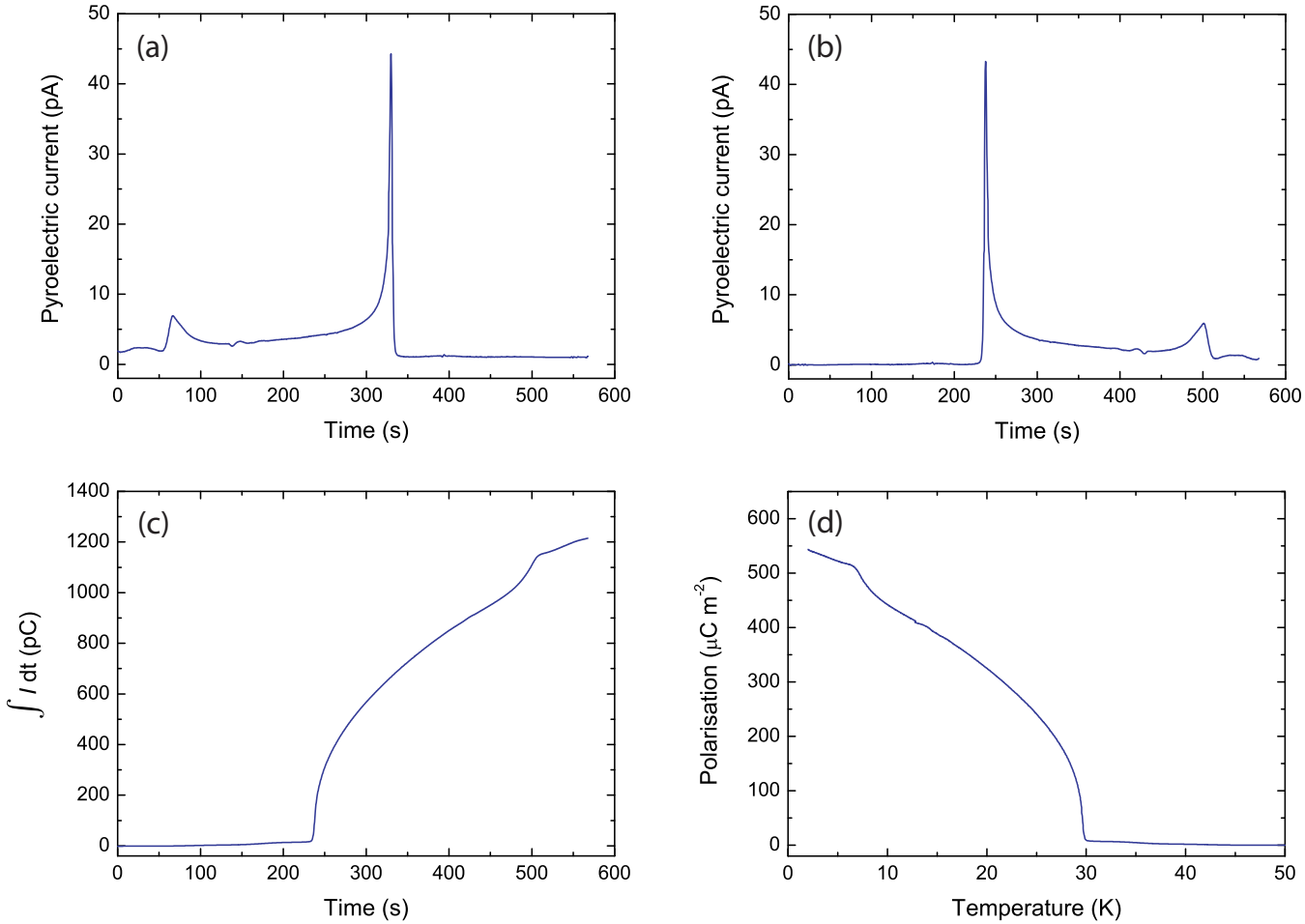

Figure 2.9: Procedure for converting pyroelectric current to polarisation: (a) Plot of initial current versus time data. (b) Time axis reversed, and current background set to zero. (c) Current integrated with respect to time. (d) Integrated current divided by sample electrode area, then plotted versus temperature. Data taken from a $TbMnO_3$ crystal - more detail in Section 2.8

2.8 Standardisation of polarisation measurements

The electric polarisation measurements in this thesis utilised the method of measuring the pyroelectric current, as described in Section 2.7. Since this technique used a new setup at the time, it was important to standardise the results prior to making measurements on new, untested compounds. Since the polarisation data for $TbMnO_3$ are well reported, a single crystal of this compound was used as a control sample to allow standardisation of measurements. The pyroelectric current that develops in these systems is extremely small (of the order of 10 pA), and so measurements were found to be very sensitive to external effects. It was also found that the sample preparation and measurement procedure have a significant impact on the quality and reliability of the data. Initially, there were problems with obtaining reproducible results for the polarisation, and the magnitudes measured were a lot smaller than expected. Alterations to the experimental method drastically improved these results, and resulted in much better data being taken first for $TbMnO_3$, and then for $Sm_{0.5}Y_{0.5}MnO_3$ (as shown in Section 4.2.6).

2.8.1 Electrical contacts

The sample under test was electrically connected to the PPMS insert by attaching wires from the sample to a removable mount, as shown in Figure 2.8. Fine silver wire (⌀ 0.125 mm or 0.05 mm) was used for this connection, with silver paste (Du Pont 4929N conductor paste) joining the wires to the opposing crystal faces, and solder connecting the wires to the mount. Initially, the opposing sample faces were coated with just a layer of silver paste, but it was discovered that this resulted in insufficient surface contact between the wires and the sample. This problem was overcome by first sputtering gold contacts onto the sample faces, giving a fine base layer covering as much of the surface as possible. Silver paste was then used on top of this layer to connect the wires to the sample mount. Gold sputtering was carried out using a Polaron range sputter coater. Electrical contacts were checked before inserting the sample into the PPMS by using a standard multimeter.

2.8.2 Sample thickness

In order to electrically pole the sample under test, a high voltage was applied. According to published methods, a suitable voltage for this purpose was generally $\sim$150 V mm$-$1 [7, 66]. The initial $TbMnO_3$ single crystal sample was cuboid in form, with dimensions $l_a = 1.19$ mm, $l_b = 1.89$ mm and $l_c = 2.70$ mm, where l_a is the length of the crystal parallel to the a-axis, etc. Since the electric polarisation direction in $TbMnO_3$ is along the c-axis (in zero magnetic field), this meant that a very high voltage needed to be applied in order to pole the crystal (405 V). This introduced two problems into the experiment, before any measurements were taken. Firstly, a result of applying such a high voltage was that the current often tripped when cooling, resulting in an inconsistency in the amount of poling of the sample. The high voltage also generated a significant amount of heat, making it difficult to cool the sample to 2 K, and degrading the electrical contacts with repeated application of the electric field. The solution to this problem was to use 3 different crystals of $TbMnO_3$, in the form of plates with the surface normal parallel to each principal crystallographic axis. These plates had typical dimensions of $\sim 2 \times 2 \times < 1$ mm^3, meaning that a much lower voltage could be applied to satisfy 150 V mm^{-1}, and (in certain situations) the electrode area could be calculated more accurately.

2.8.3 Removal of surface charge

Once the sample is cooled to the starting temperature for measurement, a surface charge is present due to the application of a high voltage. Since the pyroelectric current measurement is concerned with purely bulk polarisation, this charge needs to be removed. Initial attempts to remove surface charge involved connecting the sample to earth, by touching the wires connected to the sample to an earth point. This was quite a crude method, with varying lengths of time (in the region of 15 s) for earthing introducing inconsistencies into the experimental method. Human contact was also a potential issue, since there could be some significant charge transfer associated. It was discovered that samples needed to be short-circuited for a much longer time than we had been doing previously, up to 90 min [66].

A bleeder resistor box, consisting of three 330 kΩ resistors, was incorporated into the circuit in order to accomplish the removal of surface charge. When the high voltage was turned off, the resistors acted to dissipate any current left in the circuit (i.e. from the surface charge). The system was left connected to the bleeder resistor for 60 min before connecting the electrometer and beginning the pyroelectric current measurement. The pyroelectric current, by definition, arises due to a change in temperature of the sample, so should not be affected by the draining of the surface charge.

2.8.4 Measurement procedure

The high voltage is applied to the sample in the paraelectric phase, so that when the sample is cooled through the ferroelectric transition there is as much poling of the crystal as possible. Initially, the voltage was applied at 90 K (the ferroelectric transition temperatures, T_{N2}, for $Sm_{1-x}Y_xMnO_3$ and $TbMnO_3$ compounds lie between 25-30 K). To be certain that no error was occurring due to some remnant ferroelectric polarisation above T_{N2}, later measurements on $Sm_{0.5}Y_{0.5}MnO_3$ were taken after applying the high voltage at 300 K. The sample was always cooled to 10 K at a rate of 10 K min^{-1}. If the sample was further cooled down to 5 K or 2 K, this was set at a rate of 1-2 K min^{-1}. Cooling was always slower than expected from the set rate; this was likely due to heating effects from the high voltage through sample wires and across the sample. When the sample was warmed or cooled to a particular temperature, the system was set to wait for 5-10 min to ensure the temperature was stable before removing the high voltage.

Measurements of the pyroelectric current were taken at a rate of 5 K min^{-1} for $TbMnO_3$ and $Sm_{0.6}Y_{0.4}MnO_3$ samples, and at 1 K min^{-1} for $Sm_{0.5}Y_{0.5}MnO_3$. The slower method was eventually used in order to obtain more data points around the ferroelectric transition temperature. This can be important due to the sharp nature of the peak (over a range of ∼1 K) in the pyroelectric current measured around transition temperatures. Due to the extremely sensitive nature of the experiment, the static fields of people walking past the PPMS can cause significant spikes in the pyroelectric current. This is especially problematic when measuring

around electric phase transitions.

2.8.5 Pyroelectric current and polarisation for $TbMnO_3$

The result of refining the pyroelectric current measurement procedure can be seen in Figure 2.10. The sample was a cuboid single crystal, with dimensions l_a = 1.17 mm, l_b = 1.91 mm and l_c = 0.92 mm. The pyroelectric current was measured along the c-axis (where polarisation is expected in zero magnetic field), such that the electrodes covered an area of ∼2.24 mm^2 and were separated by 0.92 mm. Five sets of data were taken, to make sure that the results were reproducible. Each test was taken under the same conditions: The high voltage (150 V mm^{-1} = 138 V) was applied at 90 K, and the sample was cooled to 10 K at 10 K min^{-1}, and then to 2 K at 1 K min^{-1}. The voltage was then removed, and the bleed resistor drained the surface charge for ∼10 s. The electrometer was then connected, and the pyroelectric current was measured whilst increasing the temperature at 5 K min^{-1}. These results were a significant improvement on previous data, both in terms of consistency and magnitude of polarisation measured. The installation of the bleed resistor box seems to have been an important factor, but the time taken to remove surface charge was still very short (the charge removal time of 90 min reported in Ref. [66] was discovered after these data were taken, and was applied to the measurements of $Sm_{0.5}Y_{0.5}MnO_3$ presented in Section 4.2.6).

It can be seen from Figure 2.10(a) that the values measured for the pyroelectric current have a good degree of consistency, especially when considering the size of the variations between different data sets is ∼1 pA. The largest differences between the data sets seems to be the magnitude of the peak seen at T_C, this is possibly due to the short amount of time taken to pass through the transition at 5 K min^{-1}. Figure 2.10(b) shows that even small differences in the pyroelectric current can have relatively large effects on the value of the polarisation calculated. This is due to the cumulative effect of integration over time that is made when converting to P. The sensitivity of the polarisation to the pyrocurrent seems to be a common issue, and is a possible reason for the discrepancies between the reported values for the polarisation along the c-axis in $TbMnO_3$ [7, 31].

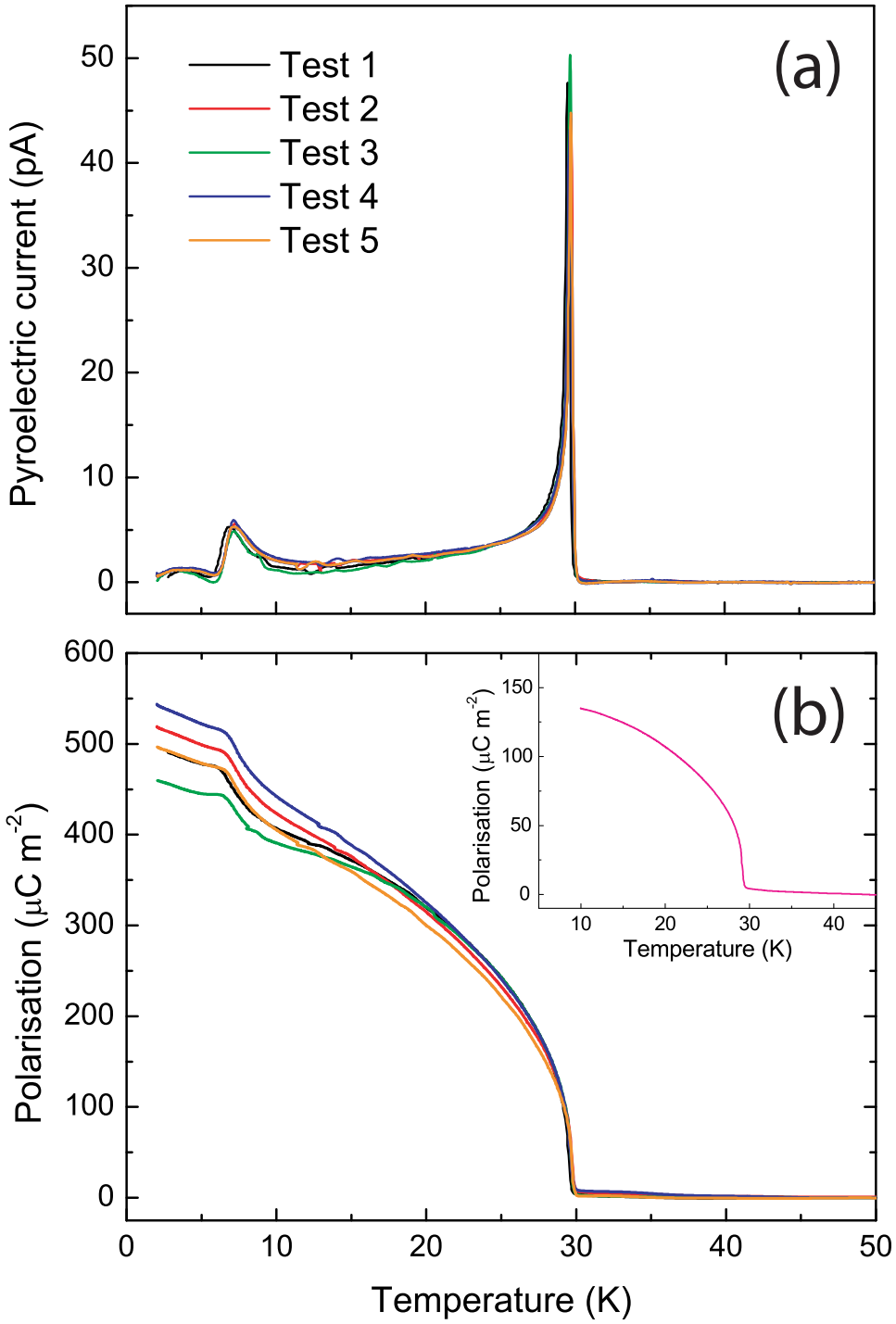

Figure 2.10: (a) Pyroelectric current and (b) polarisation versus temperature for $TbMnO_3$. Tests 1-5 were taken under the same conditions, to test the reproducibility of the data. The inset for (b) shows the results of a typical polarisation measurement before the refined technique was applied.

The polarisation data shown in Figure 2.10 are in good agreement with those reported by Kimura *et al.* in the comprehensive study of the magnetoelectric properties along all three crystal axes [31], albeit with polarisation magnitudes slightly smaller ($\sim$500 μC m^{-2} at 2 K for the measurements shown in Figure 2.10, compared with 600 μC m^{-2} Kimura *et al.*). The sharp peak in the pyroelectric current corresponds to the cycloidal ordering of the Mn moments, but is 2-3 K higher in temperature than expected. This is possibly due to a lag between the environment temperature measured by the PPMS (which is the recorded value), and the actual sample temperature, due to the fast heating rate. The feature in the data seen at low temperatures corresponds to the ordering of the Tb moments. This result is also seen in Ref. [31], and illustrates the clear effect that the Tb magnetic order has on the electric polarisation.

2.8.6 Summary of polarisation measurements

In conclusion, a measurement of the pyroelectric current is a good technique for measuring a small electric polarisation, and so is particularly useful to Type-II multiferroics such as $TbMnO_3$. To summarise the optimum conditions determined for measurements of the pyroelectric current:

- a base electrical contact made by gold sputtering, onto which wires can be connected with conducting paste
- the sample under test must be thin (no thicker than 1 mm)
- 150 V mm^{-1} is a sufficient applied voltage for poling the sample
- the voltage should be applied high above the ferroelectric transition temperature, and should not be removed until the sample has been cooled to base temperature
- the sample should be left connected to the bleed resistor for a minimum of 1 hr to remove the surface charge
- measurement of the pyroelectric current should be carried out at 1-5 K min^{-1}

- people must not walk past the experimental setup whilst measurements are being taken, since they will introduce significant electrical noise

Using this method, the polarisation was measured for $TbMnO_3$, and found to agree with previously published data. Measurements of the polarisation of $Sm_{0.5}Y_{0.5}MnO_3$ were carried out using the above method (Section 4.2.6).

2.9 Neutron scattering

The following theory of neutron scattering covers the diffraction process, i.e. elastically scattered waves, from both crystal (nuclear) and magnetic structures. This theory is applicable to the experiment conducted at GEM (ISIS), as presented in Chapter 5.

Neutron scattering is a tool which allows both the nuclear and the magnetic structure of a material to be examined. Unlike X-rays, neutrons have no electrical charge, and so do not strongly interact with the electron cloud of an atom. The result of this is that neutrons can probe deeper into a material than X-rays, and the effect of absorption does not increase with the size of the atom. These properties are particularly useful for defining the crystal structure of a compound, since the positions of relatively light atoms (e.g. oxygen) can be determined even when alongside much heavier rare earth atoms and transition metal ions.

Importantly, neutrons have a spin value of $1/2$, allowing them to interact with the magnetic moments present in a sample. The interaction between the intrinsic magnetic moment of the neutron, μ_N, and the atomic magnetic field, $\mathbf{B}$ (which is due to the resultant spin and orbital angular momenta of the atom [67]) is described by a potential of the form $-\boldsymbol{\mu}_N \cdot \mathbf{B}$. Neutron scattering can therefore be used to determine the magnetic structure of a compound, as well as its crystal structure. It is typical for neutron scattering experiments to complement laboratory measurements of the bulk magnetic properties of samples to give a more detailed picture of the magnetic properties of a system.

A disadvantage of using neutrons is that scattering is weak - only a small fraction of the incident neutron beam is scattered by the nuclei in the sample. This, combined with the fact that the incident neutron flux produced by a neutron source will be orders of magnitude smaller than the photon flux from an X-ray source means that, generally, much longer counting times are required in neutron scattering experiments than in X-ray scattering experiments. Also, samples are generally required to be large for magnetic measurements using neutrons, providing a practical problem for single crystal work (ideally, crystals should be of the

order of 1-5 cm^3).

It is necessary to go to central facilities to conduct neutron scattering experiments. At the Institute Laue-Langevin (Grenoble, France) neutrons are produced by a reactor source, by the nuclear fission of uranium. At ISIS (Oxfordshire, UK), a proton beam is accelerated to high energy before it collides with a heavy metal target, causing neutrons to be produced by spallation. The neutrons at ISIS are produced in bursts rather than in the continuous flow at the Institute Laue-Langevin. Experiments are generally carried out in evacuated conditions, to reduce/remove the effect of neutrons scattering with air particles.

2.9.1 Nuclear neutron scattering

In a neutron diffraction experiment, neutrons fired upon a sample have an incident wavevector $\mathbf{k}_i$, and scattered wavevector $\mathbf{k}_f$. The scattering vector, $\mathbf{Q}$, is then defined as (assuming elastic scattering)

$$\mathbf{Q} = \mathbf{k}_i - \mathbf{k}_f \tag{2.19}$$

The effective cross section, σ, seen by the neutron beam is related to the nuclear scattering length, b, an atom (and isotope) dependent quantity:

$$\sigma = 4\pi b^2 \tag{2.20}$$

The differential cross section, $\frac{\mathrm{d}\sigma}{\mathrm{d}\Omega}$, is defined as the number of neutrons scattered into a solid angle $\mathrm{d}\Omega$ per second, as a fraction of the incident flux (It is assumed that the distance between the sample and detector is large compared with the dimensions of the sample and detector, such that $\mathrm{d}\Omega$ is well defined [67]). This value represents the probability of detecting a neutron over a solid angle range, and is dependent on the values of $\mathbf{Q}$ and b. For a neutron beam elastically scattered by an array of n atoms, the differential cross section is given by

$$\frac{\mathrm{d}\sigma}{\mathrm{d}\Omega} = \left| \sum_n b_n \exp\left(\mathrm{i}\mathbf{Q}\cdot\mathbf{r}_n\right) \right|^2 \tag{2.21}$$

where $\mathbf{r}$ is the vector describing the position of the nucleus the neutron interacts with. For a crystal with lattice parameters $\mathbf{a}$, $\mathbf{b}$ and $\mathbf{c}$:

$$\mathbf{r} = x\mathbf{a} + y\mathbf{b} + z\mathbf{c} \tag{2.22}$$

Scattering from a crystal occurs when the Laue condition is satisfied:

$$\mathbf{Q} = \mathbf{G} = h\mathbf{a}^* + k\mathbf{b}^* + l\mathbf{c}^* \tag{2.23}$$

where $\mathbf{a}^*$, $\mathbf{b}^*$ and $\mathbf{c}^*$ are the reciprocal space lattice parameters ($\mathbf{a}^* = 2\pi/\mathbf{a}$, etc), and h, k and l are the crystal Miller indices. The differential cross section in this case is given by

$$\frac{\mathrm{d}\sigma}{\mathrm{d}\Omega} = N^2 \left|\mathrm{F}_{hkl}\right|^2 \tag{2.24}$$

where N is the number of unit cells in the crystal. F_{hkl} is the nuclear structure factor, and is given by

$$\mathrm{F}_{hkl} = \sum_n b_n \exp\left[2\pi \mathrm{i}\left(hx_n + ky_n + lz_n\right)\right] \tag{2.25}$$

The intensity, I, of the scattered beam is related to to the nuclear structure factor [67]:

$$I \propto \left|\mathrm{F}_{hkl}\right|^2 \tag{2.26}$$

2.9.2 Magnetic neutron scattering

As mentioned above, neutrons are also scattered by the magnetic moments in a crystal. Magnetic scattering only occurs from components of the magnetisation which are perpendicular to the scattering vector $\mathbf{Q}$. The magnetic structure factor, F_M, is given by

$$\mathrm{F}_M = \sum_j f_j(\mathbf{Q})\mu_j \exp\left(\mathrm{i}\mathbf{Q}\cdot\mathbf{r}_j\right) \tag{2.27}$$

where μ_j is the magnetic moment at the jth site, and $f_j(\mathbf{Q})$ is the magnetic form factor (as given by the dipole approximation), which gives the $\mathbf{Q}$-dependence of the magnetic scattering from an atom. The magnetic scattering intensity is dependent on F_M, as with the nuclear scattering case [67]:

$$I_M \propto \left|\mathrm{F}_M\right|^2 \tag{2.28}$$

If a neutron powder diffraction experiment utilises measurements of the scattered intensity as a function of the scattering vector, $\mathbf{Q}$ or the crystal d-spacing, any

peaks found can then be related to the magnetic or crystal structure of the compound. In order to distinguish between nuclear peaks and magnetic peaks, measurements can be taken at temperatures in the paramagnetic phase, where no magnetic order (and thus no magnetic Bragg peaks) are expected. Models of the magnetic structure can then be determined by using Rietveld refinement of the data. The analysis of results in Chapter 5 was carried out using the Fullprof suite of programs [68, 69].

2.10 X-ray resonant magnetic scattering

2.10.1 Introduction

X-ray resonant scattering (XRS) is a complementary technique to neutron scattering for the study of magnetic materials. As discussed in Section 2.9, neutrons are able to probe the magnetic moment of an atom via an interaction between the intrinsic magnetic moment of the neutron, μ_N, and the atomic magnetic field, $\mathbf{B}$ (which is due to the resultant spin and orbital angular momenta of the atom [67]). This interaction is described by a potential of the form $-\boldsymbol{\mu}_N \cdot \mathbf{B}$. XRS, on the other hand, does not involve a direct interaction with the net magnetic moments in a sample. The scattering in this case is electric in nature, and is element and electron shell specific with respect to the magnetism of a sample [70]. Such scattering occurs when the incident X-ray photon energy is tuned close to an atomic absorption edge, as shown in Figure 2.11. The photon transfers energy to an electron in the *core* shell corresponding to the absorption edge (photon absorption), exciting the electron from its energy shell. The excited electron subsequently decays back into the core level (over a timescale of 10^{-16}-10^{-15} s [71]), with the emission of the scattered photon. The incident and scattered photon energies are equal, such that the scattering can be thought of as an elastic process. The overall scattering event is a two-step process: photon-absorption followed by emission.

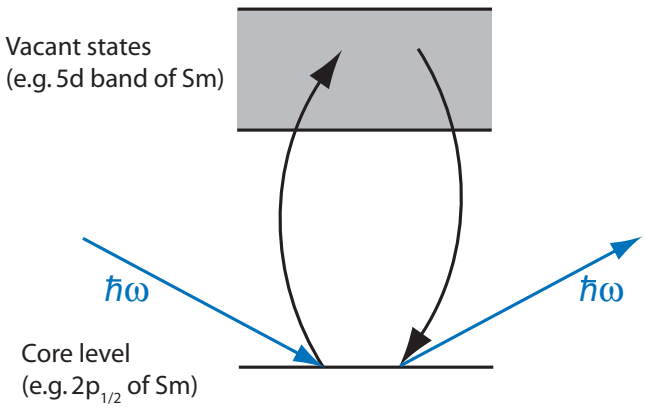

Figure 2.11: The two-step process which leads to X-ray resonant scattering (XRS) from a magnetic ion. The incident photon (left) excites a core electron into a vacant state in a shell possessing magnetic polarisation. The excited electron subsequently decays into the core hole, with the emission of a scattered photon (right). Since the incident and scattered photons have equal energy ($\hbar\omega$), XRS is an elastic process.

The vacant state occupied by the excited electron in the scattering event may be a partially filled atomic orbital in a magnetic moment carrying shell (e.g. the $4f$ shell of a rare-earth ion), or an empty state in a band which is exchange split by the presence of local magnetic moments (e.g. the $5d$ shell of a rare-earth ion) [70]. The presence of such vacant states indicates the presence of localised magnetic moments. Since the excitation of an electron must obey the Pauli exclusion principal, XRS is therefore an element and atomic shell specific probe of local magnetisation [70]. This attribute makes XRS a very useful complementary technique to neutron scattering, alongside the following factors:

- Since the incident X-ray energy needs to be tuned to probe specific absorption edges, the use of synchrotron radiation facilities is required for XRS experiments. Synchrotrons have much higher fluxes than neutron sources, meaning that although magnetic scattering cross sections for XRS can be weaker than for neutron scattering, magnetic scattering intensities tend to be much higher in XRS experiments. This allows data to be collected more quickly in XRS experiments, and also means that far smaller samples (a surface area as small as 2×2 mm^2) can be used compared with neutron scattering studies.

- Detecting changes in probe polarisation due to scattering is easier for XRS than for neutron scattering. This is because synchrotron X-rays are intrinsically highly polarised, and detection of the scattered beam polarisation is more straightforward for X-ray scattering experiments.

- The resolution in the scattering vector $\mathbf{Q}$ is usually much better in XRS experiments, giving more accurate determination of, for example, the antiferromagnetic wavevector and magnetic correlation lengths.

- XRS can be used to study the magnetic properties of elements which are strongly neutron-absorbing. An example pertinent to this work is the natural isotope abundance of Sm.

In the following subsections, the concepts of XRS discussed above will be expanded upon, before a description of the synchrotron beamline and experimental setup

used for the XRS study of $Sm_{0.5}Y_{0.5}MnO_3$ (the results of which are presented in Section 5.2.4).

2.10.2 X-ray photoelectric absorption

X-ray photoelectron absorption (Figure 2.12) is the first step in the process of XRS, and takes place when the incident photon energy is matched to an *atomic absorption edge* (or *binding energy*) of an element within the sample under study. The absorption edge of an element represents the minimum energy required to excite a core electron, such that it overcomes its binding to the nucleus. Since the core shells occupied by electrons are discrete, quantised levels of energies that vary from element to element, absorption edges are element-specific quantities. The result of this is that XRS is an element-specific scattering probe. (As discussed later in this chapter, the technique is also an electron shell specific scattering probe of magnetism, meaning that it is possible to determine the shell corresponding to the magnetic polarisation giving rise to the scattering. This point relates to the electric multipole nature of XRS, and its associated polarisation dependence.).

By convention, the absorption edges of an element are denoted by the letters K, L, M and N, which refer to the binding energies of electrons in levels with principal quantum number $n = 1$, 2, 3 and 4, respectively. A subscript number distinguishes the non-degenerate shells in the $n \geq 2$ levels, which have different angular momentum values. This notation is illustrated in Figure 2.12, which shows the ejection of an electron from the $2p_{1/2}$ sub-level. This process occurs when the $2p_{1/2}$ electron absorbs an X-ray photon of energy greater than or equal to the L_2 absorption edge of the atom. The K and L absorption edges of the $(3d)$ transition metal and $(4f)$ rare earth elements are probed by so-called *hard* X-rays, with photon energies greater than ~ 3 keV.

X-ray photoelectric absorption occurs in several processes, and is not exclusive to XRS. The promotion and subsequent decay of an electron from its core shell can be either elastic or inelastic in nature. In an elastic process, such as XRS, no energy is transferred to the sample. Inelastic processes involve, for example, the emission of a fluorescence photon or Auger electron, with energy lower than that of the

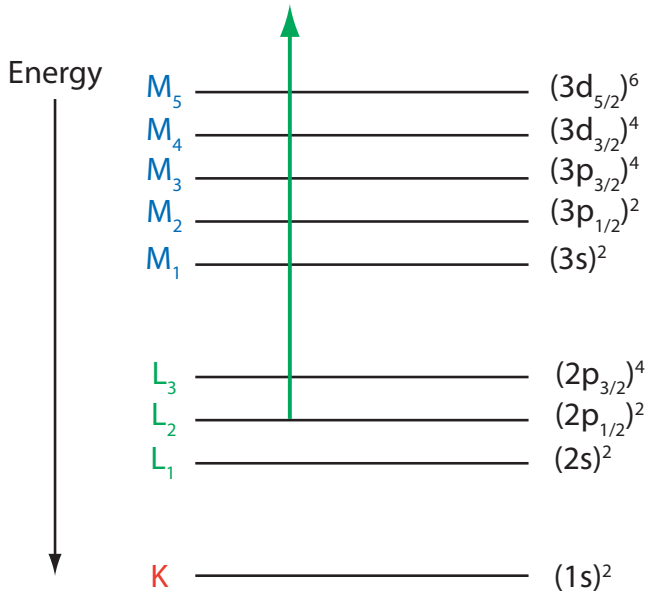

Figure 2.12: Atomic energy shells, with labels of the form $(nl_j)^{2j+1}$, where n, l and j are the principal, orbital angular momentum and total angular momentum quantum numbers, respectively. The value of $2j+1$ represents the degeneracy of the shell. The green arrow represents the example of an L_2 edge excitation, where an electron in the $2p_{1/2}$ sub-level absorbs a photon of sufficient energy to be ejected from the atom.

incident photon. Significant XRS only occurs when the incident energy is tuned within a window of width $\sim$ a few eV, centered on an absorption edge, whereas inelastic processes (such as those mentioned above) will continue to occur for energies far (i.e. many eV) greater than the absorption edge. Inelastic scattering processes give the largest contribution to the linear X-ray absorption coefficient, μ, of a material. A typical plot of μ versus incident photon energy exhibits distinct increases at points where the photon energy passes through an absorption edge of any one of the constituent elements (Figure 2.13).

2.10.3 Scattering amplitudes and their polarisation dependence

As discussed in Section 2.10.1, XRS involves the absorption of an X-ray photon by an electron, which is then excited into a different energy level. The available energy levels for the electron to move in to are determined by the atom's electronic configuration, as are the magnetic properties of the material. XRS is therefore sensitive to element and shell specific magnetisation in a sample by probing the vacant states associated with these magnetic moments.

In this subsection, the scattering amplitudes associated with XRS due to a

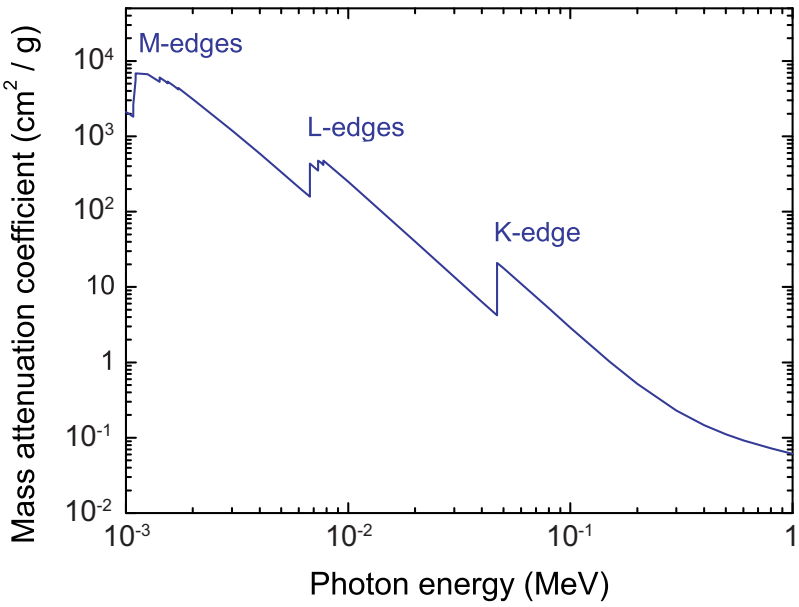

Figure 2.13: X-ray attenuation versus incident photon energy for Sm. Sharp increases in attenuation occur when the energy is tuned through the M, L and K edges of the element. Data taken from the Lawrence Berkeley National Laboratory website - http://henke.lbl.gov/optical_constants

magnetic moment will be quoted from the literature. The polarisation aspects of these amplitudes allow determination of the electron shell to which a core electron is excited in XRS. Initially, a brief introduction to the polarisation dependence of Thomson scattering will be given. The purpose for this is to provide the simplest example of a polarisation factor (and its origin) in X-ray scattering, before moving on to the more complex case of XRS, where the polarisation factors will be quoted directly from the literature. In Chapter 5, the scattering amplitudes for the latter case will be used to interpret the data from an XRS experiment on $Sm_{0.5}Y_{0.5}MnO_3$.

Thomson scattering can be classically described as the elastic scattering of an X-ray beam by electrons present in a sample. The incident X-ray beam has a time-oscillating electric field component, oriented perpendicular to the wavevector **k** (the magnetic field component of the beam is neglected for Thomson scattering). This electric field interacts with the electrons in a material, causing them to oscillate in the direction of the field, with the acceleration of the electrons resulting in the radiation of scattered X-rays of the same frequency (therefore same energy) as the incident beam. The intensity of the scattered X-rays is dependent on the direction of view towards the material with respect to the incident electric

polarisation, $\mathbf{e}$. For example, if an observer is looking along the direction parallel to $\mathbf{e}$, they will also be viewing along the direction of oscillation of the electrons. In this direction, the amplitude of oscillation will appear to be zero, and thus no scattering will be seen in this direction.

The polarisation dependence of Thomson scattering is represented by the term $\hat{\mathbf{e}}' \cdot \hat{\mathbf{e}}$ in the Thomson scattering amplitude (scattered *intensity* $\propto |\text{amplitude}|^2$), where $\hat{\mathbf{e}}'$ is the electric polarisation of the scattered wave - which is perpendicular to the scattered wavevector, $\mathbf{k}'$ - and the $\hat{}$ symbol denotes a unit vector. As well as having a polarisation dependence of the form $\hat{\mathbf{e}}' \cdot \hat{\mathbf{e}}$, the amplitude of Thomson scattering from an atom also depends on the atomic form factor (which comprises a Fourier transform of the atom's electronic charge distribution, $\rho(\mathbf{r})$). The Thomson scattering amplitude is therefore given by $f^0(\mathbf{Q}) \propto \hat{\mathbf{e}}' \cdot \hat{\mathbf{e}} \int \rho(\mathbf{r}) e^{-i\mathbf{Q}\cdot\mathbf{r}} d\mathbf{r}$, where $\mathbf{Q}$ is the scattering vector, given by $\mathbf{Q} = \mathbf{k}' - \mathbf{k}$.

At X-ray energies far from an absorption edge, the total elastic scattering amplitude associated with an element is given solely by the Thomson scattering amplitude term. When the incident X-ray energy is tuned close to an absorption edge, additional terms appear in the total scattering amplitude. For X-rays of photon energy $\hbar\omega$ incident upon a material, the total scattering amplitude for a given element in the material is given by [72]

$$f_{\text{tot}}(\mathbf{Q}, \omega) = f^0(\mathbf{Q}) + f'(\omega) + if''(\omega) \tag{2.29}$$

where $f'(\omega)$ and $f''(\omega)$ are the so-called resonant (or anomalous) scattering terms, which are found for both magnetic and non-magnetic materials. At an elemental absorption edge, the increase in the absorption cross-section, σ_{a}, for that element gives an increase in $if''(\omega)$ according to

$$f''(\omega) = -\left(\frac{\omega}{4\pi r_0 c}\right)\sigma_{\text{a}} \tag{2.30}$$

In practice, $f'(\omega)$ can then be derived from $if''(\omega)$ using a Kramers-Kronig transform [72]. Thus, in principle, the resonant scattering terms can be determined from the absorption coefficient of a material, demonstrating the intrinsic link between X-ray scattering and absorption.

l	0	1	2	3	4
	s	p	d	f	g

Table 2.1: Labeling convention for orbital angular momentum values

One of the first observations of resonant scattering due to magnetic order in a sample was made by Gibbs *et al.* during synchrotron X-ray studies of Ho metal. The team discovered a large increase in the intensities of peaks at magnetic satellite positions when tuning the incident X-ray energy through the L_3 absorption edge [73]. Satellite positions are points in reciprocal space at which diffraction is forbidden by the crystal structure, but allowed by some other order (e.g. antiferromagnetism); the positions are "satellites " of the structural Bragg positions. This discovery helped to initiate research into XRS of magnetic materials. Hannon *et al.* explained the resonant signal reported by Gibbs *et al.* at the $L_{2,3}$ edges of Ho in terms of electric multipole (EL) processes [70]. The E1 (or electric dipole) process involves the excitation of a core ($2p$) electron to a vacant state in the $5d$ band. The change in the orbital angular momentum, l, between these energy shells is 1 unit of momentum, since the l values for the p and d states are 1 and 2, respectively (Table 2.1). The E2 (or electric quadrupole) process involves the excitation of a core ($2p$) electron to a vacant state in the $4f$ shell, the change in l in this case being 2 units. The total scattering amplitude for E1 processes was determined by Hannon *et al.* [70] to be

$$f_{E1} = (\hat{\mathbf{e}}' \cdot \hat{\mathbf{e}})\, F^{(0)} - i\,(\hat{\mathbf{e}}' \times \hat{\mathbf{e}}) \cdot \hat{\mathbf{z}}_n F^{(1)} + (\hat{\mathbf{e}}' \cdot \hat{\mathbf{z}}_n)\,(\hat{\mathbf{e}} \cdot \hat{\mathbf{z}}_n)\, F^{(2)} \tag{2.31}$$

where $\hat{\mathbf{z}}_n$ is the unit vector of the magnetic moment on the nth resonant ion. The first term (the term in $F^{(0)}$) is not dependent on magnetic order - since it has no z dependence - but describes resonant charge scattering of the X-ray beam, i.e. it gives a resonant correction to Thomson scattering. This term shows a similar polarisation dependence to Thomson scattering $(\hat{\mathbf{e}}' \cdot \hat{\mathbf{e}})$. The second term (the term in $F^{(1)}$) is linear in $\hat{\mathbf{z}}_n$, and when entered in a structure factor,[3] will give rise to first harmonic satellite reflections from an antiferromagnetic sample. This term explains the observations by Gibbs *et al.* of a resonant signal at antiferromagnetic

[3]The intensity of X-ray diffraction due to scattering from a crystal or magnetic structure is determined as the modulus squared of the sum of scattering amplitudes (multiplied by phase factors) of the atoms in the corresponding (crystal or magnetic) unit cell. This sum is called the structure factor.

satellite positions in Ho, and will be used to explain the XRS signals observed for $Sm_{0.5}Y_{0.5}MnO_3$ later in this thesis (Chapter 5). The third term (in $F^{(2)}$) relates to second harmonic satellite reflections, and is beyond the scope of this thesis.

Each of the terms in Equation 2.31 gives a separate contribution to the resonant $f'(\omega)$ and $f''(\omega)$ terms for a magnetic atom. The real and imaginary components of each term arise due to terms of the form $F^{(n)}$. Each $F^{(n)}$ is composed of a different combination of terms denoted by F_{LM}, which describe the probability of transitions between electron shells in the ion. A given F_{LM} term describes the probability for a given two-step process as shown in Figure 2.11. The subscripts L and M represent the change in orbital angular momentum, l ($L = \Delta l = 1$ for an electric dipole (E1) interaction, and 2 for an electric quadrupole (E2) interaction), and angular momentum value, m_j, respectively, between the core and excited state. The energy dependence of the XRS intensity ($\propto |F_{LM}|^2$) has a Lorentzian-like form, which is due to the general form of the denominator of F_{LM}.

As stated above, the second term in Equation 2.31 will later be used to explain the XRS measurements on $Sm_{0.5}Y_{0.5}MnO_3$. This term is given by Hannon *et al.* [70] as

$$F^{(1)} = \left(\frac{3}{4}k\right)[F_{11} - F_{1-1}] \tag{2.32}$$

where k is the X-ray wavevector. This term vanishes ($F^{(1)} = 0$) when $F_{11} = F_{1-1}$. So in order to have a finite value for this scattering term, there must be an asymmetry in the states available for the excited electron to move to, such that the probability of a transition $L = +1$, $M = +1$ is not equal to that of a transition $L = +1$, $M = -1$. As well as being key to XRS from antiferromagnetic systems, such asymmetry is the origin of the phenomenon of *X-ray Magnetic Circular Dichroism*, which is observed in absorption experiments on ferromagnetic materials [71].

The factor $(\hat{\mathbf{e}}' \times \hat{\mathbf{e}}) \cdot \hat{\mathbf{z}}_n$ in the second term in Equation 2.31 indicates that the strength of the scattering depends, in a complex way, on the orientations of the polarisation vectors of the incident and scattered photons with respect to the magnetic moment (magnetic polarisation) that is probed at the resonance. This factor is expressed by Hill and McMorrow in terms of the possible changes in the *linear* polarisation of the X-ray beam occurring during the XRS process [74]. The

four possible changes between linear polarised states of the incident and scattered photon are given in the form of a 2 × 2 matrix:

$$\begin{pmatrix} \sigma \rightarrow \sigma' & \pi \rightarrow \sigma' \\ \sigma \rightarrow \pi' & \pi \rightarrow \pi' \end{pmatrix} \tag{2.33}$$

where σ and π denote polarisation components perpendicular and parallel to the scattering plane, respectively.

By writing the general (unit) magnetic moment $\hat{\mathbf{z}}_n$ from Equation 2.31 in the form of components with respect to an experimental vector basis $\hat{\mathrm{U}}_{1,2,3}$ (as defined in the next section), Hill and McMorrow expressed the 2 × 2 matrix for E1 scattering due to $F^{(1)}$ as

$$f^{(1)}{}_{E1} = -iF^1 \begin{pmatrix} 0 & z_1 \cos\theta + z_3 \sin\theta \\ z_3 \sin\theta + z_1 \cos\theta & -z_2 \sin 2\theta \end{pmatrix} \tag{2.34}$$

where θ denotes the Bragg angle (equal to half of the scattering angle) [74].

2.10.4 Scattering geometry and nomenclature in XRS experiments

An example of the setup in a XRS experiment can be seen in Figure 2.14. The scattering plane is defined by the incident, $\mathbf{k}$, and scattered, $\mathbf{k}'$, wave-vectors and contains the scattering vector $\mathbf{Q} = \mathbf{k}' - \mathbf{k}$. In this example the scattering plane is vertical and normal to the sample surface. The incident and scattered beams make the same angle, θ, with the sample surface, which is the case of a *specular* scattering condition (diffracting planes parallel to the sample surface). Consequently the scattering vector is normal to the sample surface. A rotation about the scattering vector is called an azimuthal rotation, with an angle defined by ψ. U_1, U_2 and U_3 are a set of orthogonal axes in the laboratory frame onto which the scattering is projected. U_3 is defined as pointing antiparallel to $\mathbf{Q}$, and U_2 is perpendicular to the scattering plane, pointing in the direction parallel to $\mathbf{k} \times \mathbf{k}'$. U_1 lies in the scattering plane, and orthogonal to U_3.

Another consideration of the experimental geometry concerns the polarisation of the incident and scattered X-ray beams. As mentioned above, the incident X-ray is σ polarised if the electric field component of the beam, $\hat{\mathbf{e}}$ is perpendicular to the scattering plane and π polarised if $\hat{\mathbf{e}}$ lies within the scattering plane. Depending on

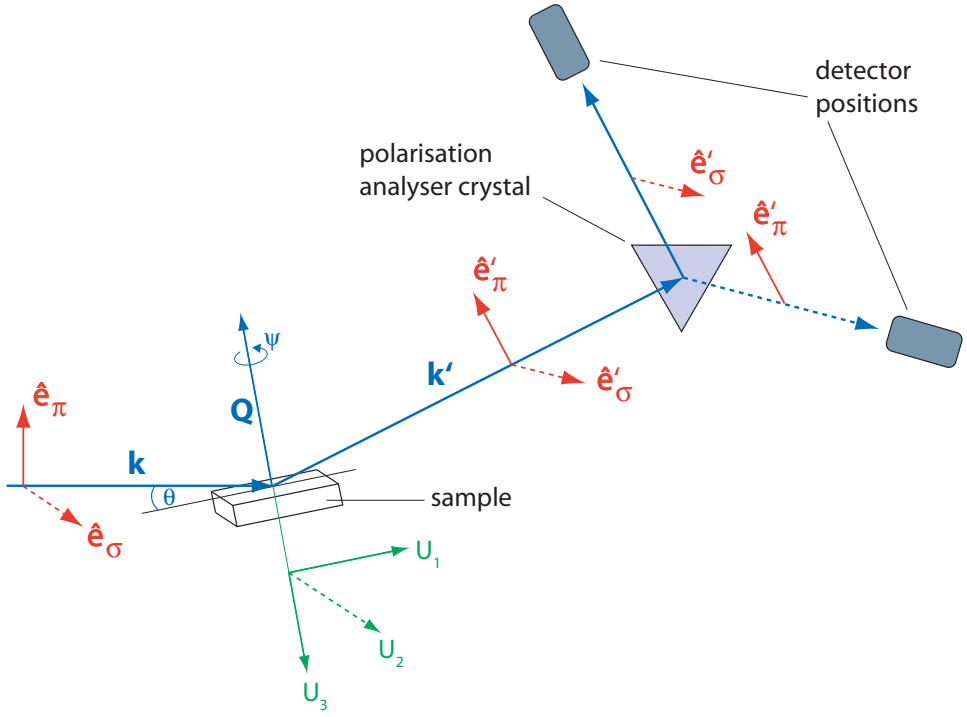

Figure 2.14: An example of the scattering geometry in a XRS experiment. The polarisation analyser allows separation of the σ and π components of the scattered beam. The orthonormal vectors U_i are defined as U_3//-$\mathbf{Q}$ and U_2//$\mathbf{k} \times \mathbf{k}'$ Dashed lines refer to the direction perpendicular to the page.

the interaction cross-section, the polarisation of the scattered beam can be different from the initial beam. If the electric field component of the incident X-ray beam is polarised perpendicular to the scattering plane (i.e. in the σ configuration) and no change in polarisation is observed, the scattering process is referred to as $\sigma \rightarrow \sigma'$. Conversely, a change in polarisation after scattering from the sample is known as $\sigma \rightarrow \pi'$.

The final component in the experimental geometry is the polarisation analyser crystal. The choice of analyser crystal is dependent on the X-ray energy at which the XRS measurement is performed. A crystal is selected which has a specular reflection of Bragg angle (θ_{CA}) very close to 45° (the approximate Brewster's angle of solids in the X-ray wavelength range) at the given X-ray energy of the measurement. The crystal analyser is used to separate the $\sigma \rightarrow \sigma'$ and $\sigma \rightarrow \pi'$ channels by rotation about an axis parallel to $\mathbf{k}'$. The $\sigma \rightarrow \pi'$ setting corresponds to the analyser surface lying at an angle of θ_{CA} to $\mathbf{k}'$, and its surface normal perpendicular to $\hat{\mathbf{e}}'_\pi$. In contrast, the $\sigma \rightarrow \sigma'$ setting has the surface normal of the

crystal analyser perpendicular to $\hat{\mathbf{e}}'_\sigma$.

In practice, there is some finite leakage of the unwanted component (σ or π) of the scattered beam, due to the nature of the analyser crystal which separates the two polarisation states. As stated, a crystal is picked which has a Bragg angle as close to 45° as possible for the energy that the X-ray is tuned to, giving a scattering angle at the analyser of ∼90°. The detector therefore points toward the analyser in a direction almost exactly parallel to the unwanted polarisation direction. However, any deviation of the (analyser) Bragg angle from 45° will result in some leakage of unwanted polarisation, as will the finite mosaic spread of the crystal. An often more significant factor than the analyser leakage is a non-perfect linear polarisation of the incident X-ray beam - e.g., rather than being 100% σ polarised, only 95% of the incident photons are σ and the other 5% are elliptically polarised. This is an issue particularly for bending magnetic beamlines, such as the XMaS beamline at the ESRF, Grenoble (the beamline used for the XRS results in this thesis).

The effects that lead to a leakage between the two channels are collectively described by a *leakage factor*. Experimentally, this factor is determined by comparing the diffraction signal at a normal Bragg position between the rotated and unrotated polarisation channels. The factor is then given as a percentage, e.g. [(signal in $\sigma \rightarrow \pi'$)]/[(signal in $\sigma \rightarrow \sigma'$)] $\times$ 100. For normal Bragg scattering the polarisation factor is that of Thomson (charge) scattering, as described above, i.e. $\hat{\mathbf{e}}' \cdot \hat{\mathbf{e}}$. In the case of a perfectly linearly polarised incident beam, the 2×2 matrix (as above) corresponding to Thomson scattering is

$$\hat{\mathbf{e}}' \cdot \hat{\mathbf{e}} = \begin{pmatrix} 1 & 0 \\ 0 & \cos 2\theta \end{pmatrix} \tag{2.35}$$

Thus, for an ideally operating polarisation analyser crystal, the leakage factor would be zero.

Chapter 3

Magnetoelectric properties of $TbMnO_3$ and $DyMnO_3$

$TbMnO_3$ is a well studied multiferroic compound, as discussed in Section 1.4.2. However, there are several properties which remain unreported in the literature, particularly with regards to the magnetic susceptibility and the heat capacity data. $DyMnO_3$ is known to exhibit similar multiferroic properties to $TbMnO_3$, but much less information has been published on the bulk magnetic properties of this compound. The principal aim of the work presented in this chapter was to address some of the incomplete areas of research for these compounds, in order to further understand the nature of the magnetoelectric coupling. The results presented in this chapter represent the initial study of such compounds by the research group at the University of Warwick. Therefore, it was also beneficial to begin the research with well studied compounds, such that the method of sample preparation and single crystal growth could be refined for future studies. Another important use of $TbMnO_3$ was in standardising the results of pyroelectric current measurements, as detailed in Section 2.8.

There are three magnetic ordering temperatures for $TbMnO_3$ ($DyMnO_3$). At T_{N1}~41 K (39 K), the Mn moments show a sinusoidal antiferromagnetic order along the *b*-axis [7]. At T_{N2}~27 K (19 K), the Mn moments order in a *b*-*c* cycloid [32]. It is known that the Tb moments also order at this temperature, with modulation along the *b*-axis [40], but it is not currently known if a similar order of the Dy ions is present in $DyMnO_3$. The ferroelectric polarisation for $TbMnO_3$

and $DyMnO_3$ also occurs at T_{N2}. At T_{N3}∼7 K (9 K), the rare earth moments order independently of the Mn moments. The nature of the coupling between the magnetic and electric order in $TbMnO_3$ is discussed in more detail in Section 1.6.

3.1 Sample preparation

Polycrystalline $TbMnO_3$ and $DyMnO_3$ were synthesised by reacting stoichiometric quantities of Tb_4O_7 (99.9%), Dy_2O_3 (99.99%) and MnO_2 (99+%). The procedure used for heating the powders is given in Table 3.1. The powder mixture was thoroughly ground between each heating. Approximately 30 g of material was produced for each batch, from which two feed rods of each compound were prepared as described in Section 2.3. Single crystal growths of $TbMnO_3$ and $DyMnO_3$ were then carried out by the floating zone method.

Four attempts were made to grow a single crystal of $TbMnO_3$. The best quality crystal was grown using a Crystal Systems Inc. F-ZT-10000-H-IV-VPS four mirror furnace, in an atmosphere of Ar and with a growth rate of 10 mm/hr (following the procedure in Ref. [31]). The resultant boule broke into pieces upon removal from the image furnace (Figure 3.1). It is possible that the boule broke due to the a large thermal gradient inside the furnace (i.e. the hottest region in the centre of the furnace, with much lower temperatures within centimetres of this point). A single crystal of $DyMnO_3$ was grown in an atmosphere of air, at a rate of 5 mm/hr (an Ar flow was reported to result in hexagonal, rather than orthorhombic, $DyMnO_3$ [31]).

Several pieces of the $TbMnO_3$ boule were found to be of high crystal quality using the X-ray Laue technique. Using published information on the crystal space group (P*bnm*) and lattice parameters of $TbMnO_3$, simulated Laue patterns were generated using the OrientExpress program. By comparison with the simulated

Heating	Temperature (°C)	Duration (hours)	Comments
1	1300 (1200)	12	Tb_4O_7 (Dy_2O_3) + MnO_2
2	1300 (1200)	12	Tb_4O_7 (Dy_2O_3) + MnO_2
3	1400	12	feed rods + powder

Table 3.1: Sample heating procedure for $TbMnO_3$ ($DyMnO_3$)

Figure 3.1: Pieces of a grown boule of $TbMnO_3$, which broke upon removal from the image furnace.

images, it was possible to orient the crystal with respect to the three principal crystallographic axes (i.e. the *a*-, *b*- and *c*-axes), as shown in Figure 3.2. The crystal was then cut for magnetic/electric properties measurements using a low speed diamond saw, as described in Section 2.4. The $DyMnO_3$ boule was found to be not single crystal along most of its length, but small single crystal volumes were isolated.

$TbMnO_3$ is a much more actively studied compound than $DyMnO_3$, and its magnetic properties are better understood. The larger amount of single crystal material available for $TbMnO_3$ compared with $DyMnO_3$ made it a more straightforward task to isolate $TbMnO_3$ crystal pieces for laboratory measurements. Therefore, the majority of the results presented below are from measurements on $TbMnO_3$.

3.2 Magnetic susceptibility

At present, the only magnetic susceptibility data for $TbMnO_3$ in the literature consists of measurements on polycrystalline samples, and the limited single crystal data given by Kimura *et al.* (which covers a temperature range of 10-50 K for an unknown orientation) [7]. The following DC susceptibility data were measured along the *a*-, *b*- and *c*-axes of $TbMnO_3$ with an MPMS SQUID magnetometer (Figure 3.3). It can be seen that the magnetic properties in $TbMnO_3$ are highly anisotropic, with the magnitude and temperature dependence of the susceptibility being significantly different along each axis. A quantitative analysis of the

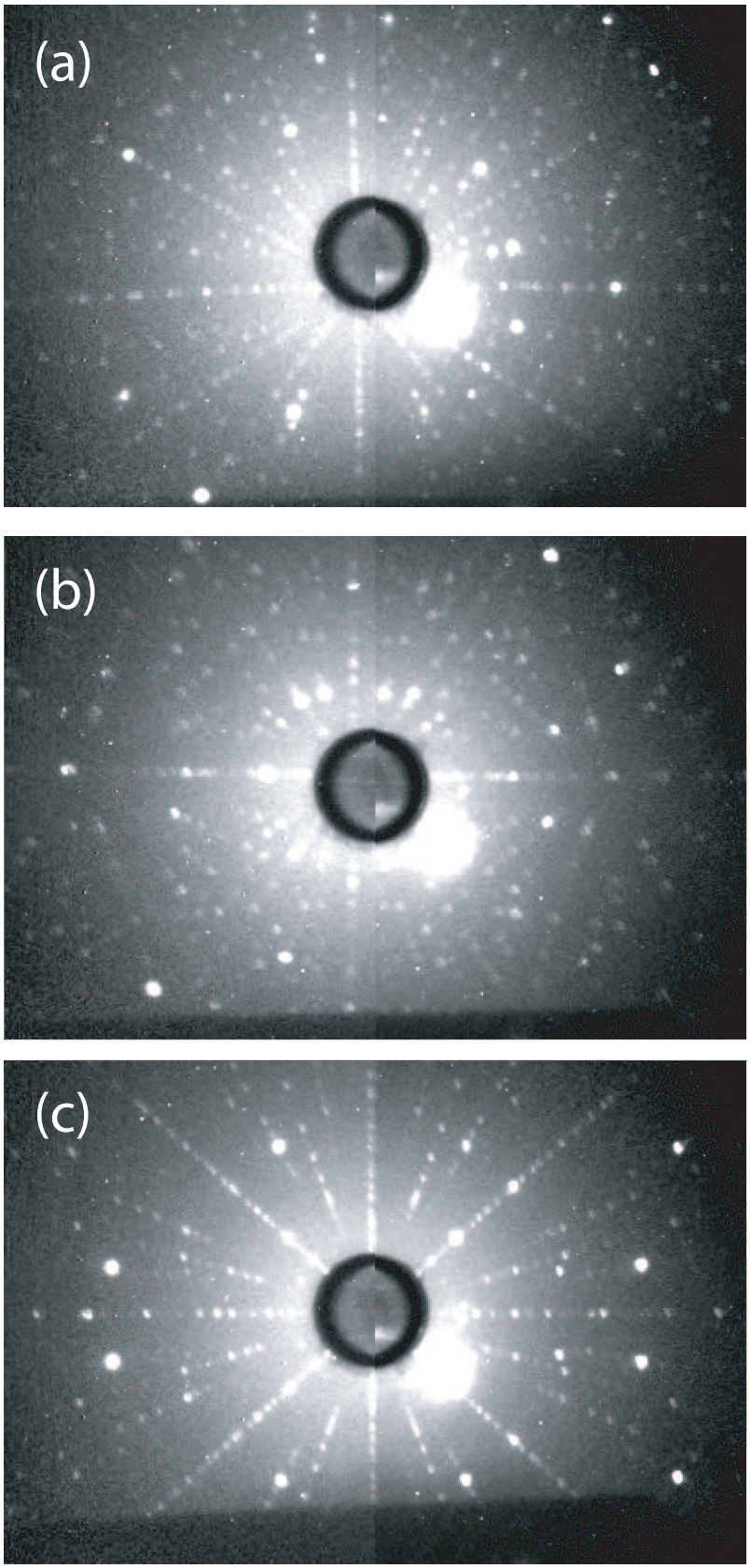

Figure 3.2: X-ray diffraction patterns along the (a) *a*-, (b) *b*- and (c) *c*-axes of a single crystal of $TbMnO_3$, taken using the Laue technique (The overexposed area below and right of the centre of each image is due to damage to the detector screen, and is not related to the crystal quality).

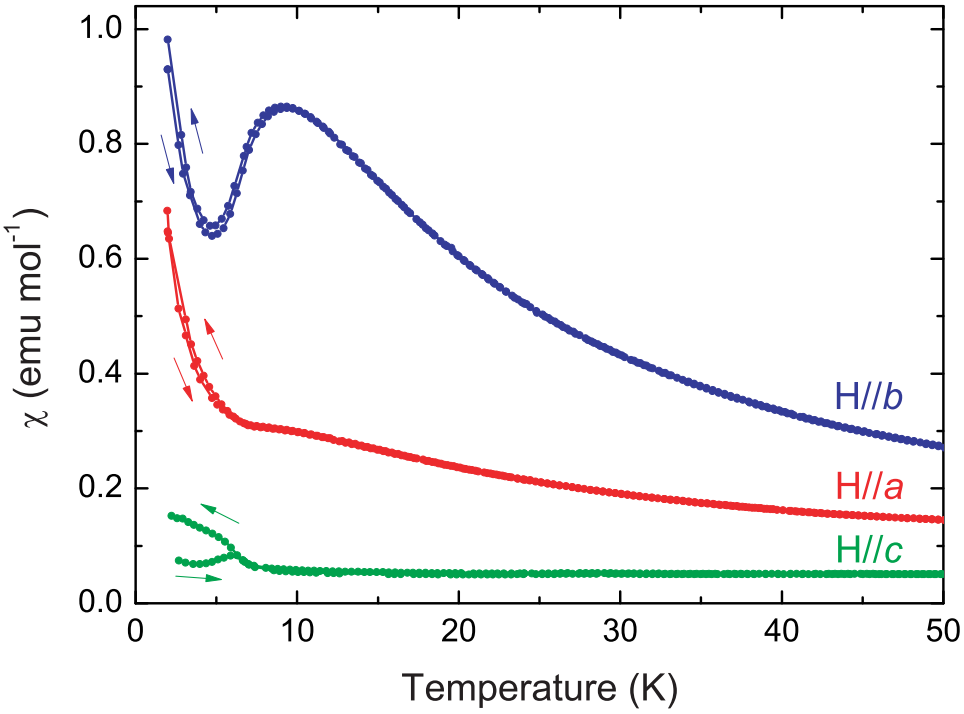

Figure 3.3: Magnetic DC susceptibility along the principal crystallographic axes of a $TbMnO_3$ single crystal as a function of temperature. Measured in an applied magnetic field of 0.1 T

susceptibility data was carried out by calculating the effective magnetic moment, p_{eff}, found along each axis (Section 2.5.1.1). Since there are two magnetic ions present in $TbMnO_3$, Tb^{3+} and Mn^{3+}, only an overall moment for $TbMnO_3$ can be determined. This moment is given by

$$p^2_{\text{eff}}(\text{TbMnO}_3) = p^2(\text{Tb}) + p^2(\text{Mn}) \tag{3.1}$$

The Curie constant, C, was determined by the method described in Section 2.5.1.1. The inverse susceptibility data along each principal axis of $TbMnO_3$ are shown in Figure 3.4. Due to the anisotropic nature of the magnetism in $TbMnO_3$, the $1/\chi$ values along each axis show significant differences. Also, a Curie-Weiss dependence is not seen until temperatures much higher than $T_{\text{N1}} = 41$ K along any direction. The results of the Curie-Weiss fits are shown in Table 3.2.[1] The theoretical effective moment of $TbMnO_3$ was calculated by adapting Equation 2.5:

$$p_{\text{eff}}(Th.) = g_{J_{\text{Tb}}}\sqrt{J_{\text{Tb}}(J_{\text{Tb}}+1)} + g_{J_{\text{Mn}}}\sqrt{J_{\text{Mn}}(J_{\text{Mn}}+1)} \tag{3.2}$$

[1]It should be noted that the errors given for the values of C, θ and p_{eff} are from the fit to the data, and do not account for errors in the sample mass, external sources of magnetism or the calculated values of the magnetic susceptibilities from the data recording program.

	C (emu K mol^{-1})	θ (K)	p_{eff}	Fit range (K)
H // a	15.15(2)	-9.3(5)	11.002(7)	200-400
H // b	13.33(1)	+17.6(2)	10.320(4)	100-400
H // c	16.75(5)	-128(1)	11.57(2)	250-400
Crystal average	14.784(4)	-30.8(1)	10.869(1)	250-400
Polycrystalline	14.376(3)	-21.87(4)	10.718(1)	60-400

Table 3.2: Curie constant, C, Weiss temperature, θ, and effective magnetic moment, p_{eff}, for $TbMnO_3$ (T_N=41 K). Obtained from Curie-Weiss fits to inverse susceptibility data for a single crystal, a crystal average calculated as $(\chi_a + \chi_b + \chi_c)/3$, and powder from a crushed crystal piece. The expected p_{eff} value for $TbMnO_3$ is 10.93.

The angular momentum values were taken for the ions Tb^{3+} (L = 3, S = 3, J = 6) and Mn^{3+} (L = 0, S = 2, J = 2, assuming orbital quenching) and give a theoretical effective moment of 10.89 μ_B. A slightly different value for p is found by using the experimentally determined values of p for Tb^{3+} (9.77) and Mn^{3+} (4.82) in Ref. [15]. Putting these numbers into Equation 3.1 gives an expected p for $TbMnO_3$ of 10.93.

Moderate agreement with the expected value of p is found from the data along the a-, b- and c-axes. The values of θ are all far from $-T_N = -41$ K. However, the average value of θ over the three axes is -40 K. A possible explanation for the θ discrepancy is the existence of another source of magnetic susceptibility (e.g. the sample holder, the varnish attaching the sample to the holder) acting to shift the data. To test this, fits to the data were made adding on a further term in the susceptibility, χ_0:

$$\chi = \frac{C}{T - \theta} + \chi_0 \tag{3.3}$$

Values of χ_0 found from fits to this equation were all very small (no larger than 0.008 emu mol^{-1}), implying that there was no significant contribution to the susceptibility from another source.

The susceptibility along the c-axis does not follow Curie-Weiss behaviour, with a straight line not seen in $1/\chi$ up to 250 K. It is possible that this behaviour is a result of additional short range magnetic correlations still present in the system up to high temperatures, or crystal field effects. The broad feature seen in the χ versus temperature data along the c-axis could result from changes in the spin

state of the system occurring as electrons have enough energy to move between different energy levels, which are split by the local crystal environment of the magnetic ion (Section 1.2.2.1). A detailed evaluation of the crystalline electric field levels would be required to test this suggestion.

At the time of writing, there was no published high temperature magnetic susceptibility data for single crystal $TbMnO_3$. However, Blasco *et al.* [75] carried out such a study on polycrystalline $TbMnO_3$, with Curie-Weiss analysis. For comparison with the results of Blasco *et al.*, a piece of $TbMnO_3$ crystal was crushed into powder for magnetic susceptibility measurements. The temperature dependence of the susceptibility and its inverse are shown in Figure 3.5. An effective moment of 10.718 $\pm$ 0.001 μ_B was found for this sample, in good agreement with the theoretical value, and the value of 10.68 μ_B reported by Blasco *et al.*. The $1/\chi$ data were also found to be linear over a similar temperature range (from 60 K upwards), much closer to T_{N1}. The value for θ was calculated as -21.9 K for the polycrystalline sample, which is closer to -T_{N1} than the values obtained from the single crystal data. An average of the susceptibility data along the three principal crystallographic axes - i.e. $(\chi_a + \chi_b + \chi_c)/3$ - gives similar results to the polycrystalline data, as shown in Figure 3.6. Analysing these data gives $\theta = -30.8(1)$ K and $p_{eff} = 10.869(1)$, which is very close to the expected value of 10.93 calculated above.[2]

The fact that the polycrystalline inverse susceptibility shows Curie-Weiss behaviour close to T_{N1} suggests that magnetic correlations are not present in the system above 60 K. This argument is also supported by the calculated value of p_{eff} - a value close to the full expected magnetic moment is expected in the paramagnetic regime. The close agreement between the crystal average and polycrystalline susceptibility data suggests that the behaviour seen for the $H//a, b, c$ data are real, and that the Curie-Weiss law is not sufficient to model the behaviour along specific crystal directions for $TbMnO_3$. Instead, the deviation from Curie-Weiss behaviour in the single crystal sample is likely due to crystal field effects, especially the broad feature in the data seen for $H//c$. A literature search showed

[2]Changing the fit range for crystal average data to 60 – 400 K does not significantly affect the fit, with $\theta = -31.67(3)$ K and $p_{eff} = 10.883(1)$ in this case.

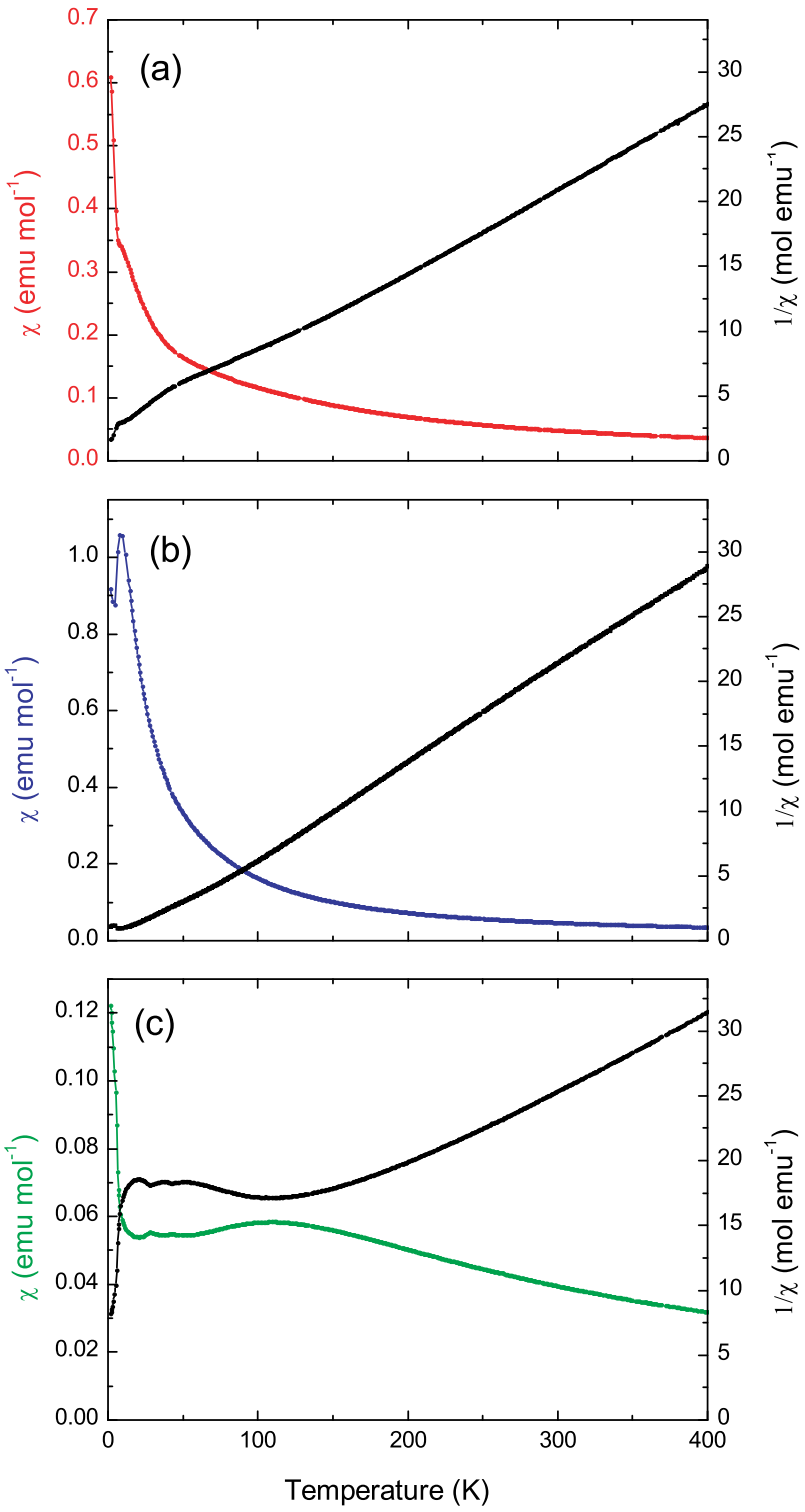

Figure 3.4: Magnetic DC susceptibility and inverse susceptibility for $TbMnO_3$, along the (a) *a*-axis, (b) *b*-axis, and (c) *c*-axis. Measured in an applied magnetic field of 0.5 T

no information on the crystal field excitations in $TbMnO_3$, making it difficult to conclusively interpret the susceptibility results above.

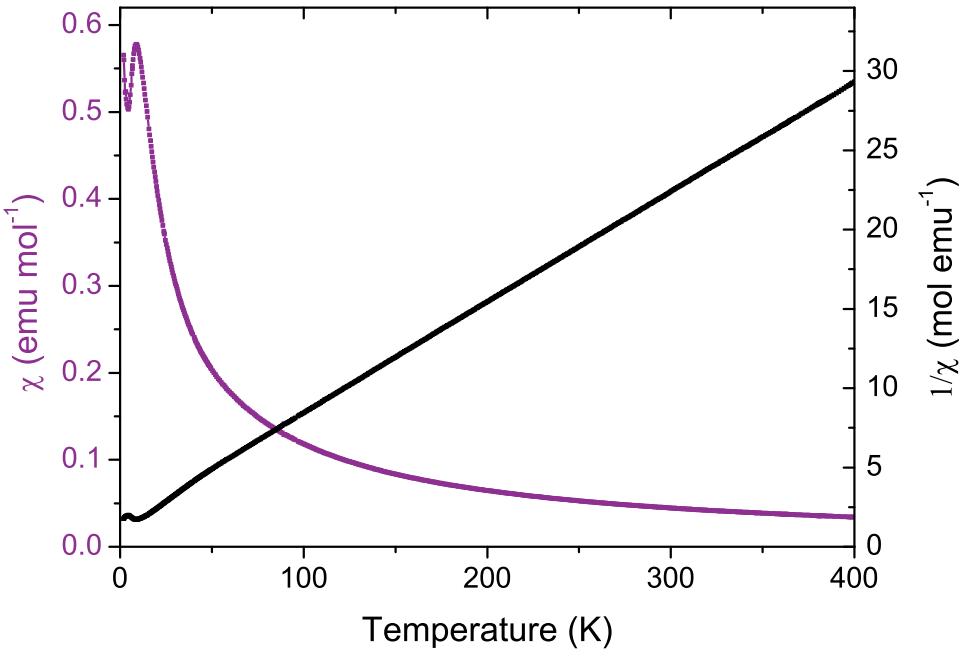

Figure 3.5: Magnetic DC susceptibility and inverse susceptibility for a crushed single crystal of $TbMnO_3$. Measured in an applied magnetic field of 0.5 T

3.3 Magnetisation

The magnetisation data for $TbMnO_3$ has been previously published [7, 28, 31], and was repeated as part of this project in order to look for any new features for the single crystal samples grown at the University of Warwick, and to test the reproducibility of the data in advance of work on new multiferroic compounds. The magnetisation of $TbMnO_3$ was measured using a vibrating sample magnetometer (VSM) along the three principal crystallographic directions (Figure 3.7). The data presented below are in very good agreement with those published by Kimura *et al*. [31].

As with the magnetic susceptibility temperature profiles, the magnetisation as a function of applied magnetic field shows large anisotropy. The *a*-axis is clearly the "easy" magnetic axis, with a field of approximately 2 T causing a near-saturation of the signal at 2 K and 1.45 K (Figure 3.8(a)). The magnetisation continues to slowly increase above this field, reaching a value of $\sim$6 μ_B/formula

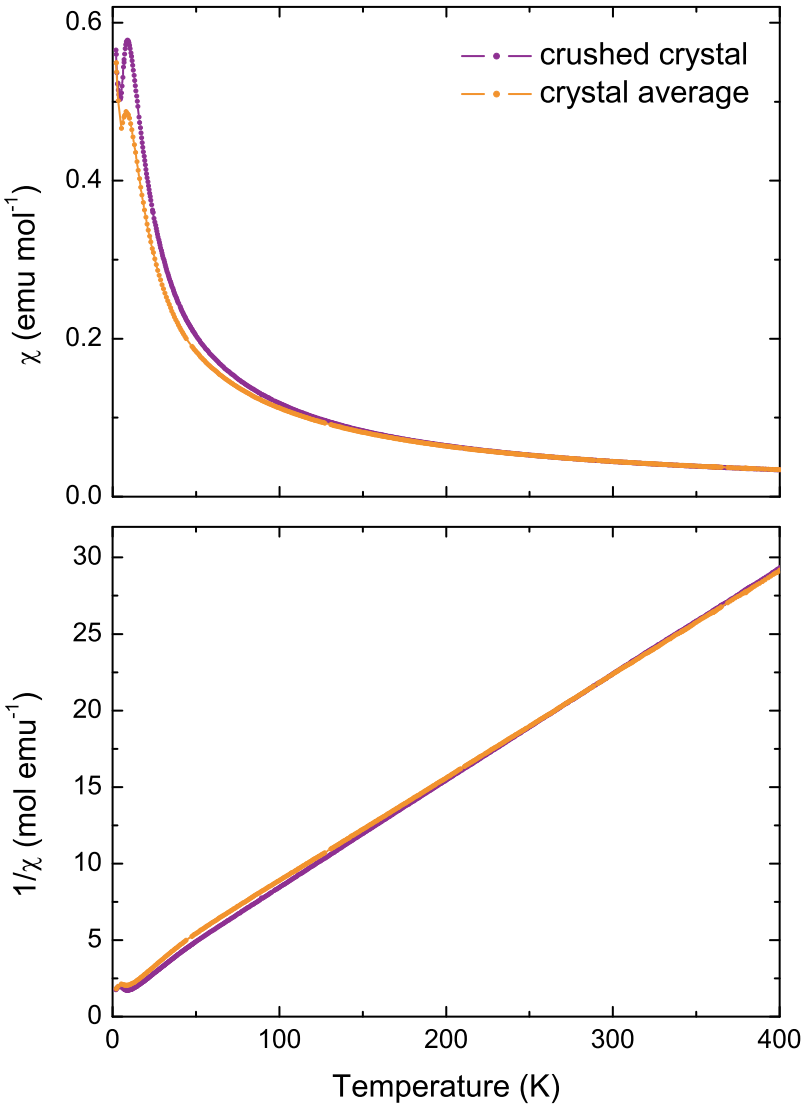

Figure 3.6: (a) Magnetic DC susceptibility and (b) inverse susceptibility for polycrystalline $TbMnO_3$, and an average of the data along the *a*-, *b*- and *c*-axes. Measured in an applied magnetic field of 0.5 T

unit at 10 T for temperatures of 12 K and below. A small amount of hysteresis is seen upon returning the applied field to zero in this direction. Kimura *et al.* proposed that the saturation with $H//a$ was linked to the Tb moments [31], as discussed further below.

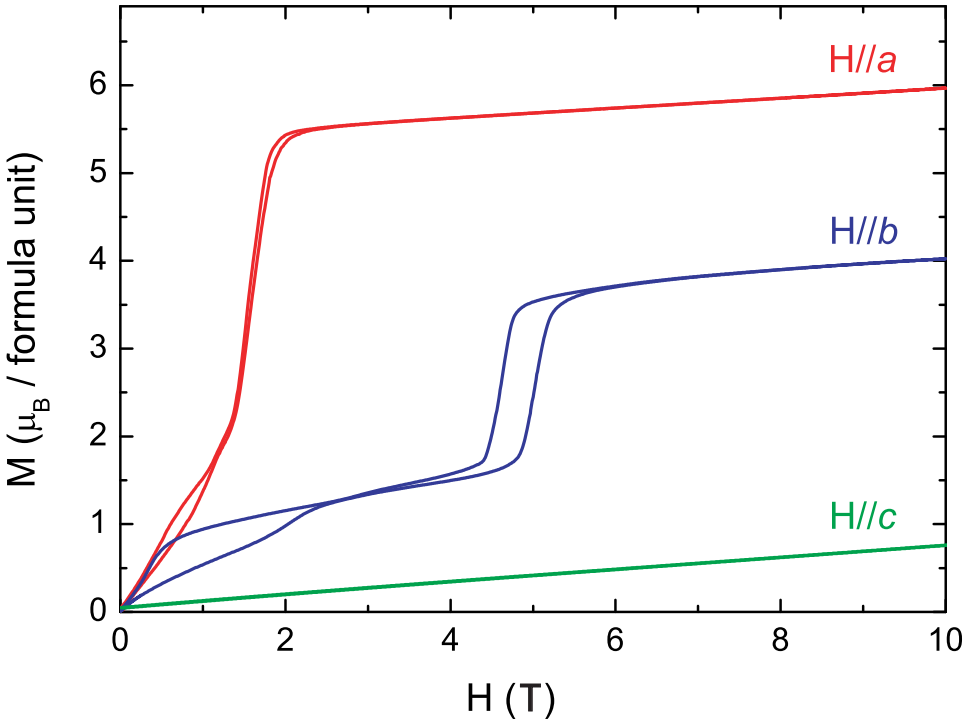

Figure 3.7: Magnetisation of a single crystal of $TbMnO_3$ versus applied magnetic field along the principal crystallographic axes, taken at 1.45 K

The most interesting magnetic behaviour occurs when a magnetic field is applied along the *b*-axis (Figure 3.8(b)), with 2 distinct metamagnetic transitions seen below 9 K. The metamagnetic transitions for $H//a$ and $H//b$ were described by Kimura *et al.* by analogy with $TbFeO_3$ [31]. It was proposed that the Tb moments lie in along two Ising axes in the *a*-*b* plane, as shown in Figure 3.9. The application of a magnetic field parallel to the *a*-axis causes the moments labelled 1 and 2 to change direction in a one-step process, resulting in the observed large increase in magnetisation (Figure 3.9(a)). A different situation occurs when a magnetic field is applied parallel to the *b*-axis, with a two-step spin reversal (Figure 3.9(b)). The metamagnetic transition of the Tb moments with $H//b{\sim}5$ T coincides with a change in the orientation of the Mn moments from a *b*-*c* cycloid to an *a*-*b* cycloid [36], and corresponds to the point at which the ferroelectric polarisation flops from the *c*- to the *a*-axis (Section 1.6). The Tb moments were initially

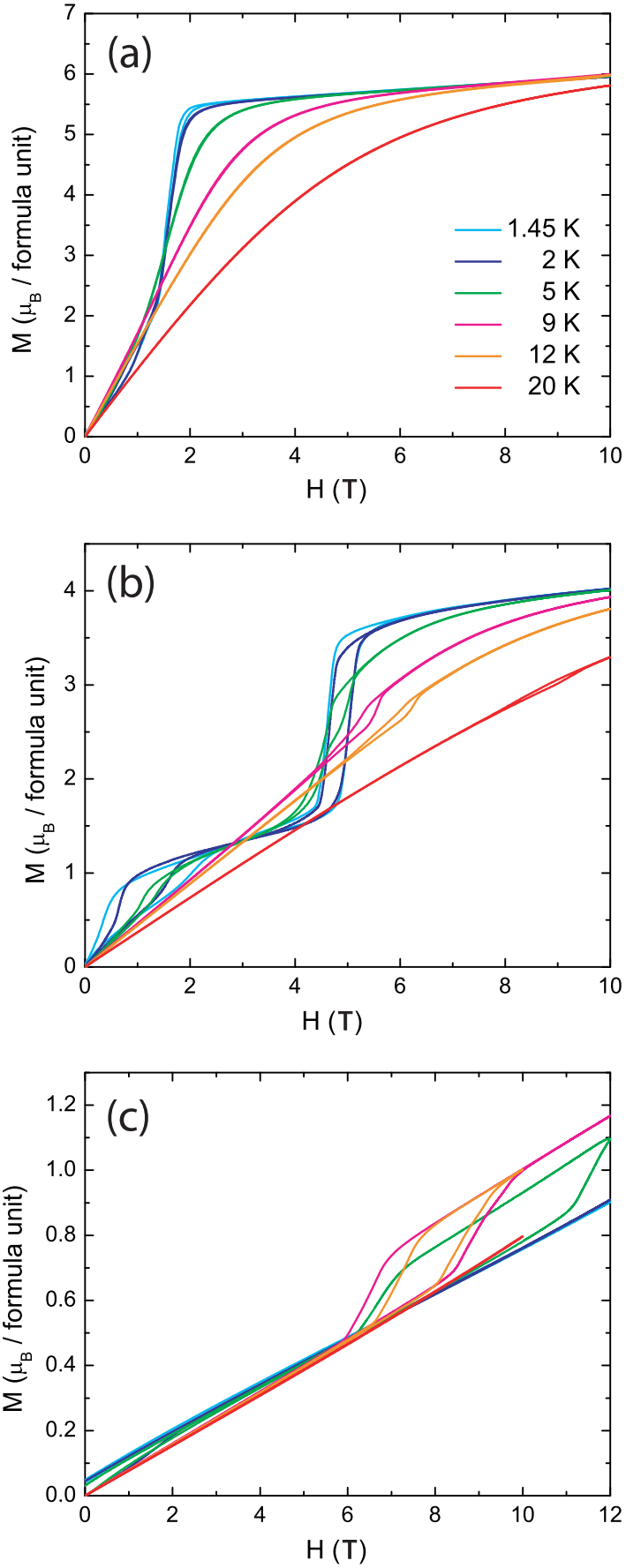

Figure 3.8: Magnetisation of a single crystal of $TbMnO_3$ versus applied magnetic field along the (a) *a*-, (b) *b*-, (c) *c*-axis.

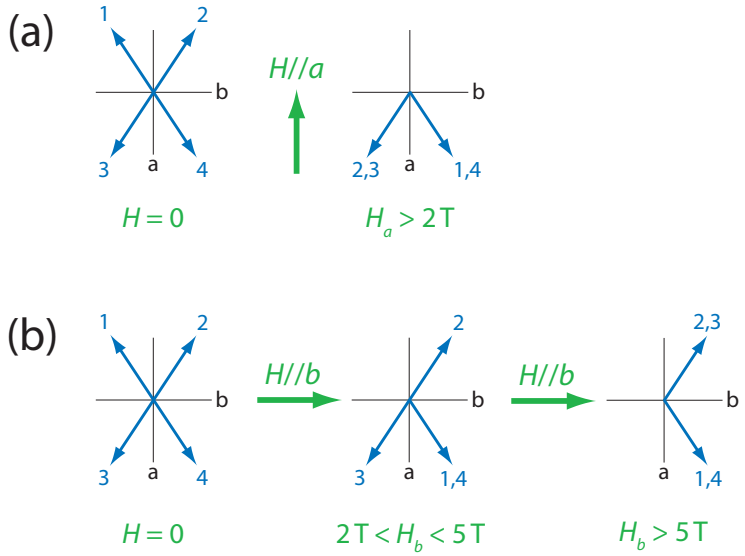

Figure 3.9: Tb moment configuration in $TbMnO_3$, showing spin reversal under a magnetic field applied along (a) the a-axis, and (b) the b-axis. Magnetic field values given correspond to measurements taken at 1.45 K. Adapted from Kimura *et al.* [31]

thought to order at ∼8 K, which seems to be reflected by the rapid smearing out of the metamagnetic transitions with $H//b$ above this temperature. However, there are still transitions visible in this configuration up to 20 K. It has now been confirmed that the Tb moments also order along the b-axis at the Mn cycloidal transition temperature ∼27 K [40, 41], which is a possible explanation for this behaviour.

From Equation 2.7, the expected saturation magnetisation of the Tb^{3+} ions was calculated as 9 μ_B. It is known that the behaviour of the Tb moments and the Mn moments are strongly coupled, with Aliouane *et al.* confirming that the application of a magnetic field parallel to the b-axis results in a change in the orientation of the Mn cycloid from the b-c plane to the a-b plane [36]. It is possible that a similar coupling is found for $H//a$, and the plateau in the magnetisation is at a value lower than the saturation magnetisation of the Tb^{3+} moments due to some antiparallel arrangement of the Mn magnetic sublattice.

The features in the magnetisation with $H//b$ are more pronounced with lower temperature, with the low field transition disappearing above 5 K, and the transition at ∼5 T becoming smeared out and shifted toward higher magnetic field with increasing temperature. Less hysteresis is also seen at higher temperatures. This behaviour also suggests that the metamagnetic transitions are linked to the

the additional ordering of the Tb moments at ∼7 K. No data appear to have been published confirming the exact nature of the low temperature magnetic order of the Tb moments in $TbMnO_3$, with reports usually focusing on the ferroelectricity-inducing Mn order.

The *c*-axis of $TbMnO_3$ is the "hard" magnetic axis, with magnetisation of no more than 1.2 μ_B/formula unit found for magnetic fields of 12 T in temperatures up to 20 K (Figure 3.8(c)). The small magnetisation along this axis agrees with the susceptibility data shown in 3.2. A magnetic transition develops at 11 T when the sample temperature is 5 K, with a large amount of hysteresis seen (the width of the loop being greater than 5 T). This behaviour was proposed by Kimura *et al.* as being due to a magnetic transition of the Mn moments to a canted antiferromagnetic (paraelectric) state [31].

3.4 Specific heat

The heat capacity data on $TbMnO_3$ in the literature are currently limited to zero magnetic field data taken over the range 2-50 K [7]. The data presented below greatly expand on this, with zero field data taken over a larger temperature range ($0.6 - 400$ K), and measurements of the heat capacity taken in applied magnetic fields up to 9 T. The magnetic field dependence of the heat capacity is also shown at two fixed temperatures, and the heat capacity data of a non-magnetic analogue compound are subtracted to separate out the magnetic contributions of the heat capacity.

The specific heat of $TbMnO_3$ was measured as a function of temperature in several magnetic fields using a Quantum Design PPMS (Section 2.5.3). The results are shown in Figure 3.10. As reported by Kimura *et al.*, there are 3 distinct peaks in the specific heat, corresponding to the sinusoidal order of the Mn^{3+} moments at ∼41 K, the cycloidal order of the Mn^{3+} moments at ∼28 K, and the ordering of the Tb^{3+} moments at ∼7 K [7]. Magnetic fields were only applied along the *a*-axis of the crystal piece for practical reasons - since this is the magnetic easy axis, it meant that there would be minimal torque on the sample due to moments re-aligning, and therefore there would be no damage to the wires supporting the

sample stage in the puck.

For successively higher applied magnetic fields, there is a gradual smearing out of the low temperature peak corresponding to the ordering of the Tb^{3+} moments until it has nearly completely disappeared at 9 T (the highest field the PPMS is capable of achieving). This implies that the magnetic field is sufficient to force the Tb^{3+} moments into the saturated paramagnetic state. This is further confirmed by inspection of the magnetisation data for $H//a$, which show a near-saturation above 8 T for $T \leq 9$ K.

Another change that is seen due to an applied magnetic field is the shift of the Mn^{3+} ordering peak at ∼41 K towards higher temperature, with an overall change of ∼1.5 K in 9 T. This behaviour was also reported in the phase diagram of $TbMnO_3$ by Kimura *et al.*, from measurements of the dielectric constant [31]. To more closely observe the changes due to an applied magnetic field, scans of the specific heat as a function of field were also carried out at 3 K and 60 K. These scans are shown in Figure 3.11. The sharp peak seen at 3 K corresponds to the saturation of the Tb moments, as seen in Figures 3.8(a) and 3.10. The gradual rise in the specific heat as a function of field at 60 K (in the paramagnetic phase) is as expected from the general trend shown in Figure 3.10.

In order to infer purely magnetic specific heat data for $TbMnO_3$, a non-magnetic analogue of $LaGaO_3$ was also measured as a function of temperature, giving the lattice contribution to the specific heat. Polycrystalline $LaGaO_3$ was prepared by reacting together stoichiometric ratios of La_2O_3 and Ga_2O_3, and the heat capacity of a piece of a $LaGaO_3$ pellet was then used for measurements of specific heat. This lattice contribution was then subtracted from the specific heat data of $TbMnO_3$ (Figure 3.12). Since the $LaGaO_3$ and $TbMnO_3$ compounds have different molecular masses, the temperature values of $LaGaO_3$ were normalised by multiplying by the ratio of the effective Debye temperatures of the two compounds, with the method used by Bouvier *et al.* [76]. For a general magnetic compound $R_mX_nZ_p$ and non-magnetic compound $R'_mX'_nZ_p$, this ratio is given by

$$\frac{\Theta_D(R_mX_nZ_p)}{\Theta_D(R'_mX_nZ_p)} = \left[\frac{m(M_{R'})^{\frac{3}{2}} + n(M_{X'})^{\frac{3}{2}} + p(M_Z)^{\frac{3}{2}}}{m(M_R)^{\frac{3}{2}} + n(M_X)^{\frac{3}{2}} + p(M_Z)^{\frac{3}{2}}}\right]^{\frac{1}{3}} \tag{3.4}$$

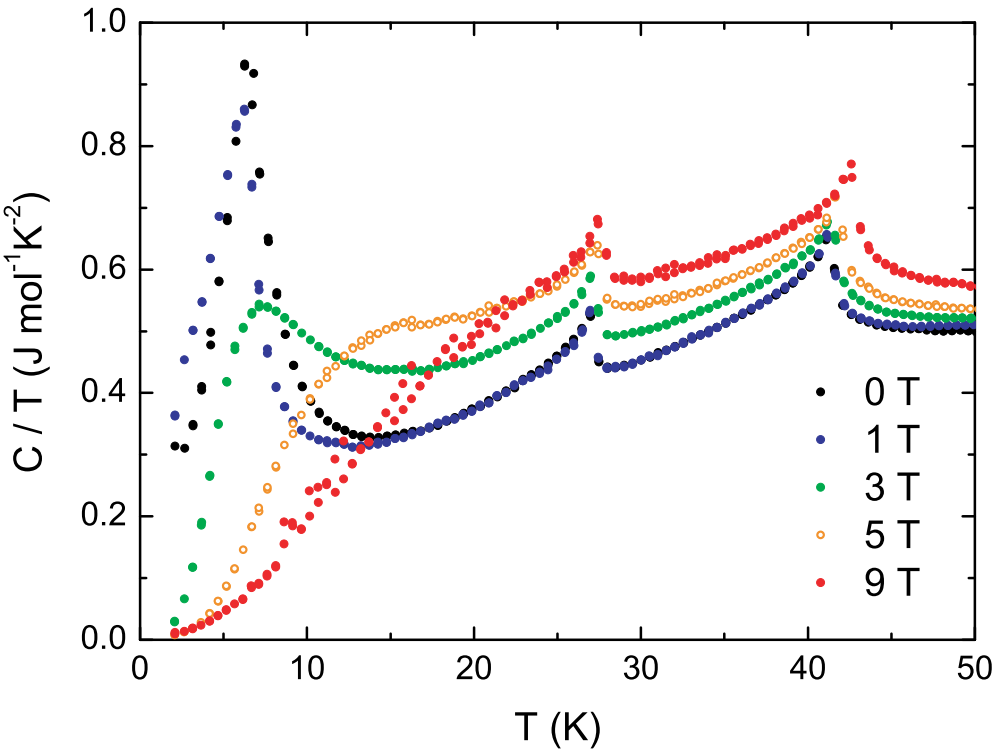

Figure 3.10: Specific heat/temperature versus temperature for a single crystal of $TbMnO_3$, with magnetic fields applied along the a-axis

where Θ_D is the Debye temperature and M is the molecular mass of each atom. This relationship was adapted for $TbMnO_3$ and $LaGaO_3$ as follows:

$$\frac{\Theta_D(TbMnO_3)}{\Theta_D(LaGaO_3)} = \left[\frac{(M_{La})^{\frac{3}{2}} + (M_{Ga})^{\frac{3}{2}} + 3(M_O)^{\frac{3}{2}}}{(M_{Tb})^{\frac{3}{2}} + (M_{Mn})^{\frac{3}{2}} + 3(M_O)^{\frac{3}{2}}}\right]^{\frac{1}{3}} = 0.975 \qquad (3.5)$$

Equation 3.4 is most accurate for low temperatures, where the Debye model predicts that the heat capacity is proportional to T^3. The heat capacity data for $TbMnO_3$ and the Debye corrected $LaGaO_3$ are shown in Figure 3.12. It can be seen that there is a non-zero value for the phonon-subtracted specific heat - and therefore still entropy in the system - up to ~200 K, over 150 K higher than the magnetic ordering temperature $T_{N1} = 41$ K. This entropy is possibly due to short-range correlations in the system persisting well into the paramagnetic state, or the existence of crystal field effects. The presence of apparent magnetic order above T_{N1} was also found in the magnetic susceptibility data (Section 3.2).

The difference in heat capacity between $TbMnO_3$ and $LaGaO_3$, C_{diff}, was integrated to find the magnetic entropy, S_{mag}, as shown in Figure 3.13. A point was added to the data before integration, at zero temperature and zero heat capac-

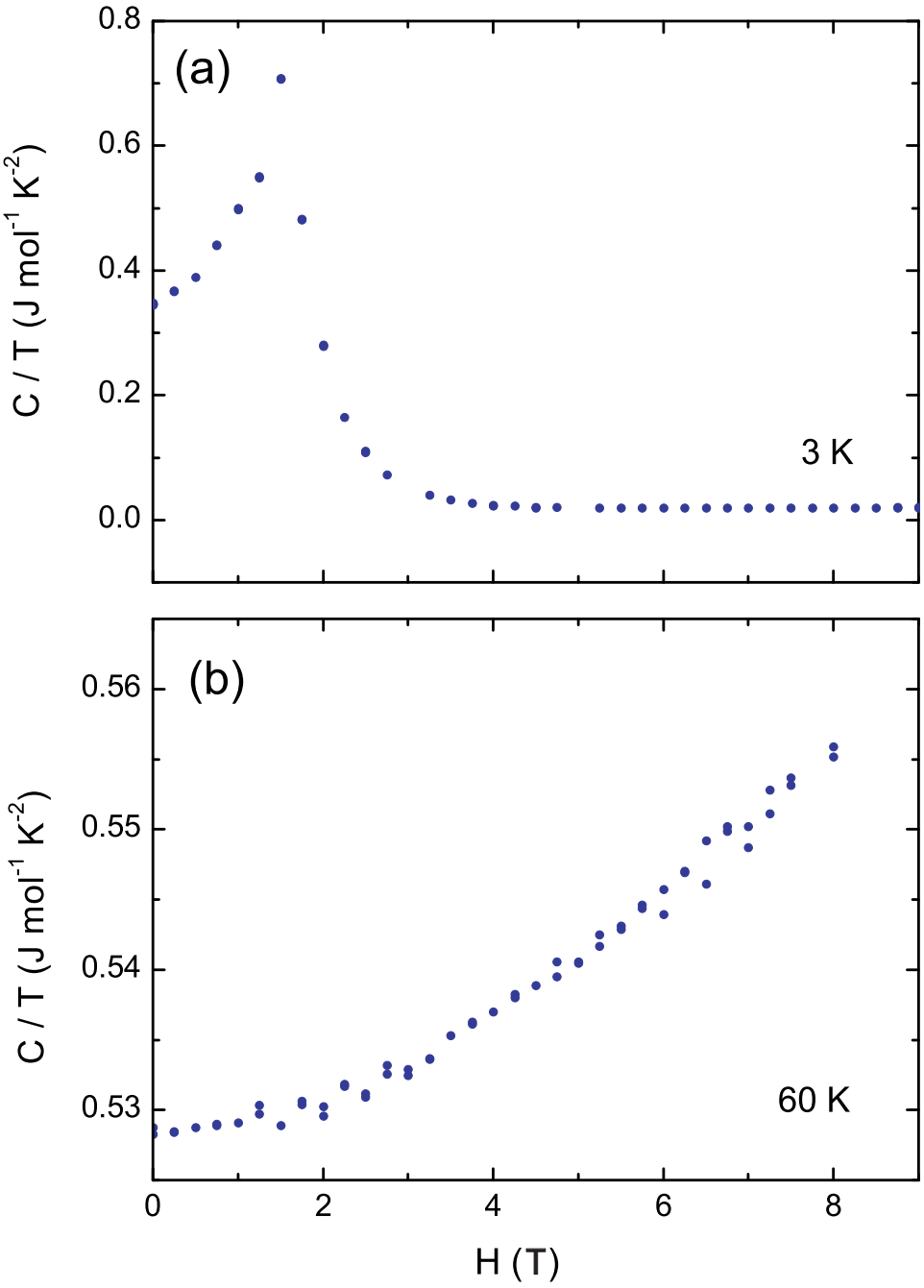

Figure 3.11: Specific heat/temperature versus magnetic field along the a-axis for a single crystal of $TbMnO_3$, at (a) 3 K and (b) 60 K

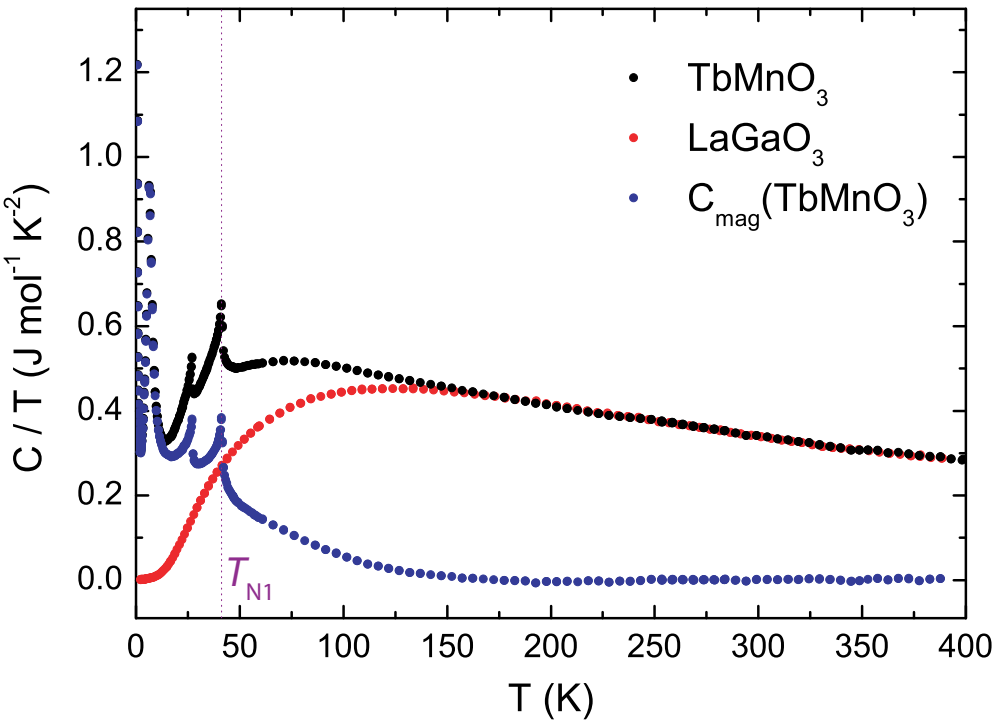

Figure 3.12: Specific heat data for a single crystal of $TbMnO_3$ and a phonon blank of $LaGaO_3$ in zero applied magnetic field. The blue data shows the purely magnetic specific heat, calculated as C($TbMnO_3$)-C($LaGaO_3$)

ity. This allowed extrapolation of the maximum entropy, since 2 K was the lowest point at which measurements were initially made. To prevent the slightly negative C_{diff} values above 177 K affecting the integration, these data were set to zero. A theoretical maximum entropy of 34.7 J mol^{-1} K^{-1} was calculated for $TbMnO_3$ by adapting Equation 2.11,

$$S_{\text{mag}}(\text{TbMnO}_3) = R\ln(2J_{\text{Tb}^{3+}} + 1) + R\ln(2J_{\text{Mn}^{3+}} + 1) \tag{3.6}$$

with the total angular momentum values $J_{\text{Tb}^{3+}} = 6$ and $J_{\text{Mn}^{3+}} = 2$. The measured magnetic entropy reached a saturation at ~23.4 J mol^{-1} K^{-1}. A large discrepancy therefore was found between the expected maximum entropy and the experimentally observed entropy.

3.4.1 Low temperature specific heat

Two possible reasons for the lower than expected value of S_{mag} are the lattice contribution derived from $LaGaO_3$, or the existence of a large amount of entropy below 2 K which was not measured. To test the for heat capacity contributions below 2 K, a helium-3 insert was used to lower the sample temperature to 0.6 K.

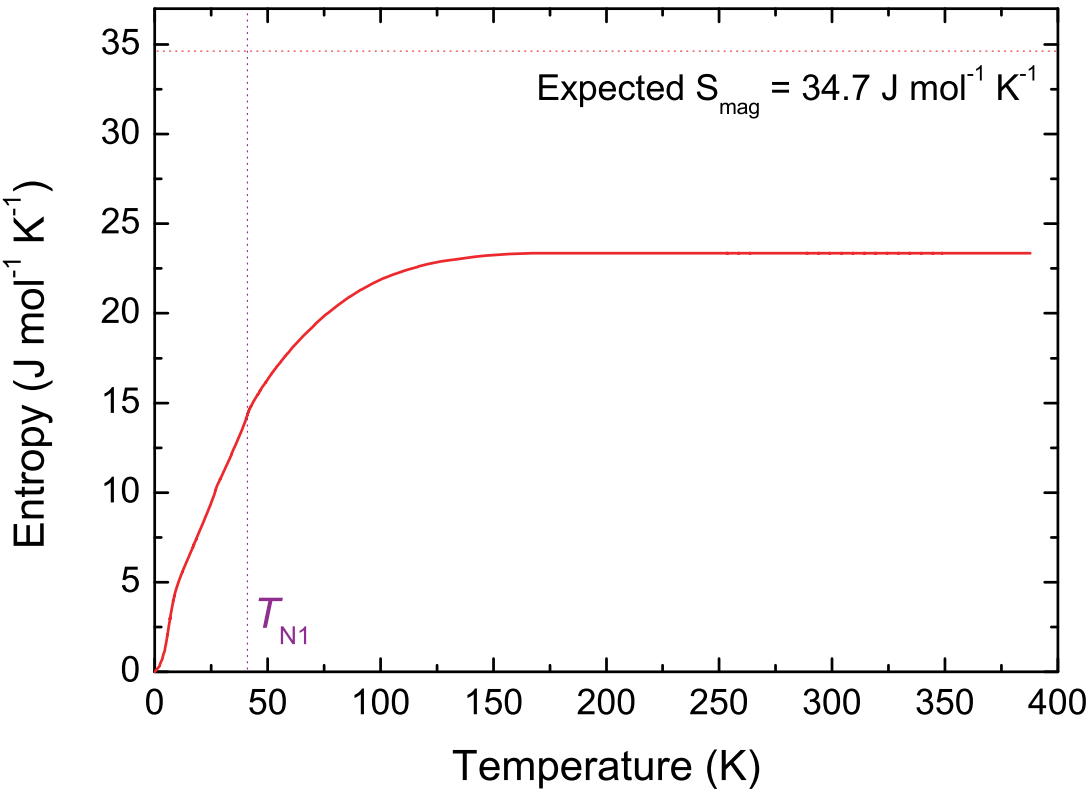

Figure 3.13: Magnetic entropy for $TbMnO_3$. The red dotted line shows the expected maximum entropy, calculated from Equation 3.6

Measurements of the specific heat were then taken in zero field, and with fields of 3 T and 5 T applied along the a-axis (Figure 3.14).

A large increase in the heat capacity is seen below 2 K, which appears to be the tail of a peak located below the range of measurement. Peaks in low temperature heat capacity data are characteristic of hyperfine transitions. These peaks occur due to transitions between energy levels split by the magnetic contribution from the nucleus of an atom, and provide a much smaller contribution to the heat capacity than lattice effects (which scale as T^3) at higher temperatures. The hyperfine contribution to the heat capacity is expected to scale as AT^{-2} at temperatures above the hyperfine transition of an ion, with the coefficient A being related to the ion's hyperfine field, H_{hf}:

$$A = \frac{\mu_{\mathrm{I}}^2 \mu_{\mathrm{N}}^2 R}{3k_{\mathrm{B}}^2} \left(\frac{I+1}{I}\right) H_{\mathrm{hf}}^2 \tag{3.7}$$

where I and μ_{I} are the nuclear spin quantum number and the nuclear magnetic moment of the ion, respectively, R is the molar gas constant (8.315 J mol^{-1} K^{-1}) and μ_{N} is the nuclear magneton (5.051×10^{-27} J T^{-1}) [77]. Applying the method

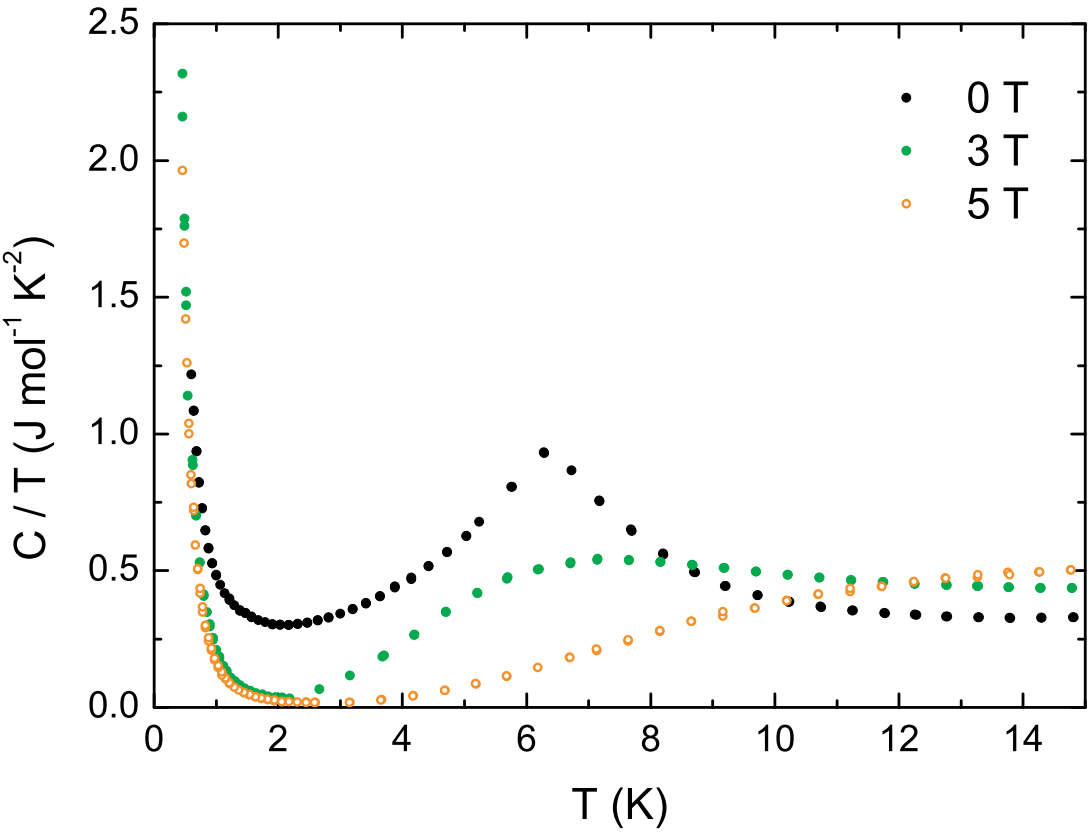

Figure 3.14: Low temperature specific heat data for a single crystal of $TbMnO_3$, with magnetic fields applied along the a-axis

of Scurlock and Stevens [78], a fit was made to the zero field low temperature heat capacity data, giving a value for A of 0.2027(7) J K mol^{-1}. For Tb, $I = 3/2$ and $\mu_I = 1.5$. Putting these values into Equation 3.7 gives $H_{hf} = 382(1)$ T, in reasonable agreement with the value of 312(2) T given by Li *et al.* [79]. If instead the hyperfine transition is assumed to be due to the Mn ions, with $I = 5/2$ and $\mu_I = 3.461$ (Ref. [80]), the hyperfine field is calculated as 181(1) T, over an order of magnitude larger than the values of ~9 T for Mn quoted in the literature [78, 81]. The feature in the low temperature heat capacity data is therefore assumed to be the tail of a Tb hyperfine peak.

Since no additional magnetic contribution is present in the low temperature heat capacity data, it is proposed that an incorrect lattice contribution from $LaGaO_3$ is the main factor in the measured magnetic entropy being lower than expected.

By separating the heat capacity data for the peaks corresponding to the Tb order and the Mn order, a rough estimate of the contribution of each ion can be

made. From Equation 3.6, the total expected entropy for $TbMnO_3$ is made up of 21.3 J mol^{-1} K^{-1} from Tb and 13.4 J mol^{-1} K^{-1} from Mn. The Tb peak was integrated between zero temperature and 17 K (at which point the peak corresponding to the Mn cycloidal order begins), showing an entropy contribution of ∼7.7 J mol^{-1} K^{-1}, far below the expected value. A possible reason for this low value is that the complete magnetic entropy of Tb is not contained in this temperature range, i.e. there is still a Tb magnetic contribution to the heat capacity above 7 K. This is supported by the results of Wilkins *et al.*, which show the existence a finite Tb order at T_{N2} = 27 K [41]. The entropy found by integrating over the two Mn ordering peaks (between 17 K and 50 K) was ∼9.1 J mol^{-1} K^{-1}, which is also lower than expected - even if possible contributions from Tb are neglected. A further entropy contribution of ∼7.0 J mol^{-1} K^{-1} is calculated in the paramagnetic state. This result again seems to point to an incorrect lattice contribution, since there is an underestimate of the magnetic entropy across the temperature range of the experiment. Due to time constraints, no further work was carried out trialing different potential phonon blanks for $TbMnO_3$.

3.5 Dielectric constant

Extensive information on the dielectric constant and electric polarisation of $TbMnO_3$ exists in the literature [7, 31]. As discussed in Section 2.8, this made $TbMnO_3$ an ideal compound for standardising the results of the new electric properties measurement system, developed as part of this project. Presented below are data from measurements on $TbMnO_3$ which illustrate the link between magnetic and electric order.

The dielectric constant of $TbMnO_3$ was measured along the *c*-axis, using the method detailed in Section 2.6. This is the crystallographic direction along which the electric polarisation develops at $T_{N2}\sim$ 28 K. The dielectric constant data are shown in Figure 3.15. The trend seen is the same as reported for $TbMnO_3$ [7], with a sharp peak seen at T_{N2}. The magnitude of the measured dielectric constant is ∼ 28, which is lower than the previously reported value of ∼37. Also, there is some noise visible in the data. These problems are most likely due to a poor electrical

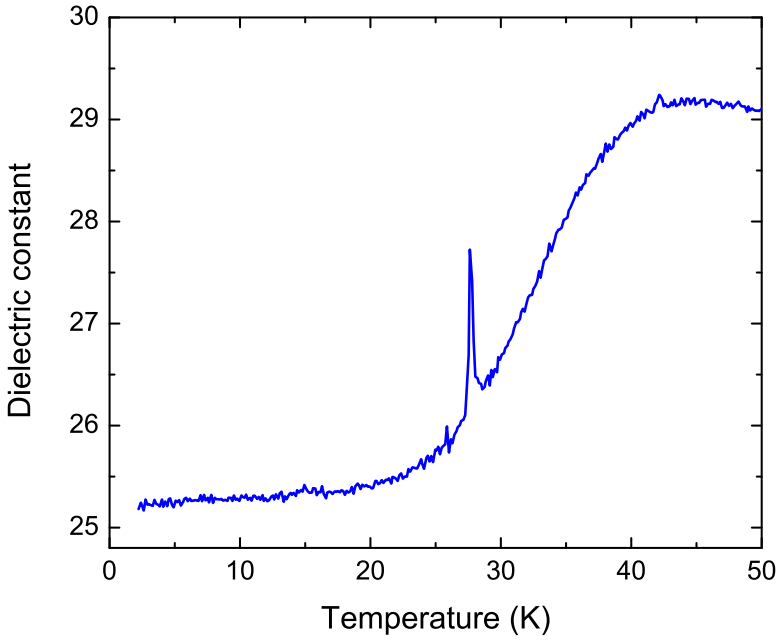

Figure 3.15: Temperature dependence of the dielectric constant along the *c*-axis for $TbMnO_3$, measured at 10 kHz

contact with the sample, since only a layer of silver conducting paste was used on each face (as discussed in Section 2.8).

3.6 Electric polarisation

The electric polarisation of $TbMnO_3$ was measured using the refined method as described in Section 2.8. Figure 3.16 shows the polarisation along the *c*-axis in zero applied magnetic field (the field dependence of the electric polarisation as reported by Kimura *et al.* is detailed in Section 1.4.2 [31]). As with the peak in the dielectric constant seen along this crystallographic direction, the electric polarisation develops at approximately the same temperature as the peak in the magnetic susceptibility and heat capacity data corresponding to the cycloidal order of the Mn moments. The value of the electric polarisation measured at 2 K is $\sim$550 μC m^{-2}, which is slightly lower than the value of $\sim$600 μC m^{-2} reported by Kimura *et al.* [31], but there is a strong agreement with the temperature dependence of the polarisation.

A comparison of the temperature dependences of the magnetic and electric

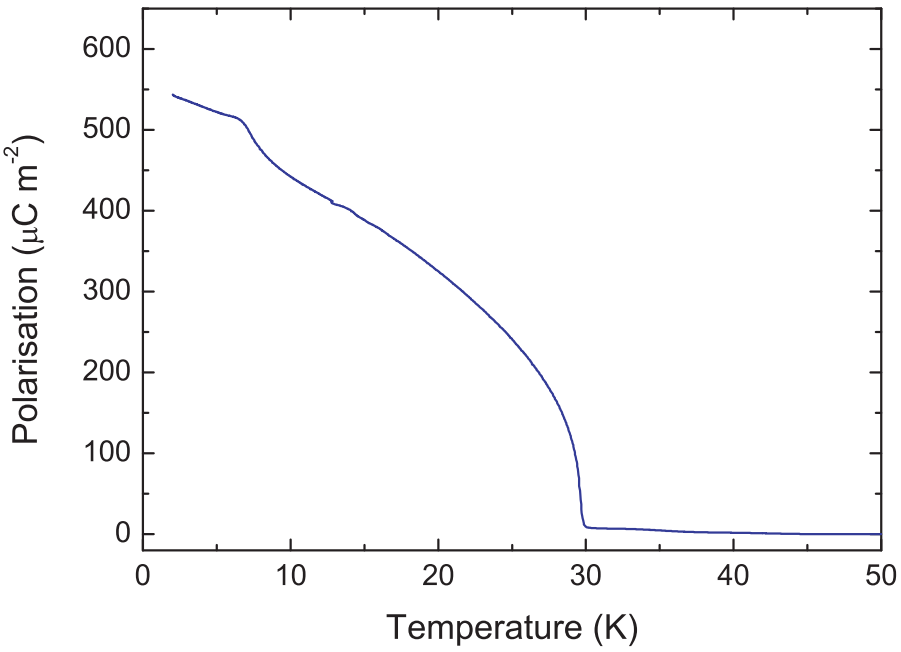

Figure 3.16: Temperature dependence of the electric polarisation along the *c*-axis of $TbMnO_3$, calculated from a measurement of the pyroelectric current.

properties of $TbMnO_3$ is shown in Figure 3.17, illustrating the strong coupling between the two properties. The slight temperature discrepancy for the polarisation data is believed to be due to thermal lag, as the measurement was carried out at 5 K/min (as opposed to 1-2 K/min for the susceptibility and dielectric constant measurements, and a much slower rate for heat capacity measurements).

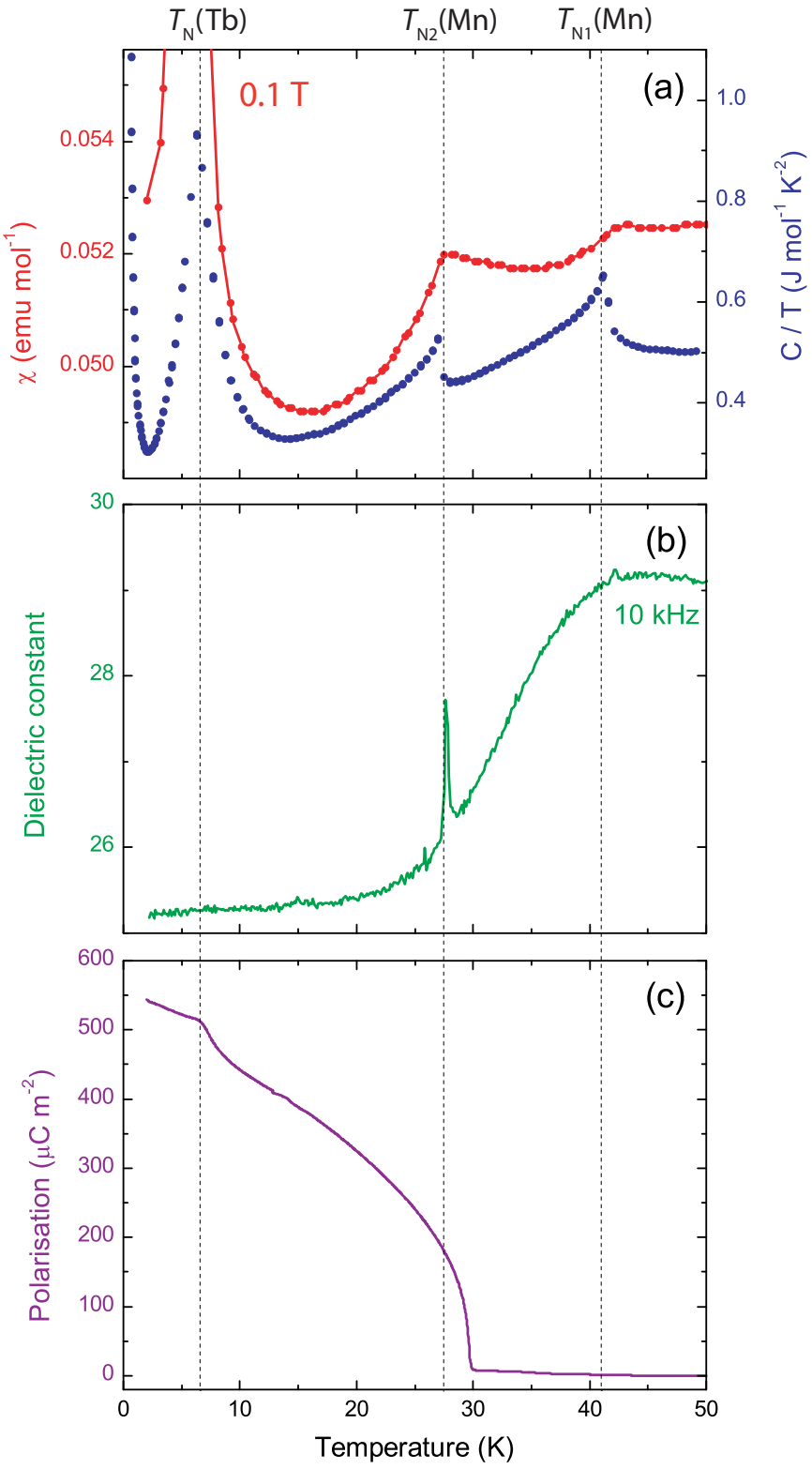

Figure 3.17: Temperature dependence of (a) magnetic susceptibility and specific heat, (b) dielectric constant, and (c) electric polarisation for single crystal $TbMnO_3$. All data except specific heat measured along the *c*-axis. The apparent shift in T_{N2} observed in the polarisation measurement is a result of thermal lag, due to rapid sample heating (5 K min^{-1} rather than 1-2 K min^{-1}).

3.7 $DyMnO_3$

$DyMnO_3$ shares many of the magnetoelectric properties seen in $TbMnO_3$ (Section 1.4.4), but much fewer data exist on this compound in the literature. It is interesting to measure the magnetic properties of $DyMnO_3$, to learn more about the nature of magnetoelectric coupling in the RMnO$_3$ compounds. As will be shown below, there are significant differences in the magnetic behaviour of $DyMnO_3$ and $TbMnO_3$, particularly in the susceptibility data. The single crystal magnetic susceptibility and magnetisation data presented below have not been reported in the literature.

3.7.1 Magnetic DC susceptibility

The magnetic susceptibility along the a- and b-axes of $DyMnO_3$ are shown in Figure 3.18. The susceptibility is anisotropic, with the susceptibility along the a-axis approximately 4 times greater than that along the b-axis. The susceptibility does not follow Curie-Weiss behaviour until above 200 K along the a- or the b-axis. There is also a slight deviation from linearity of the $1/\chi$ data above 300 K. This is not thought to be due to magnetic order so far above T_{N1} (∼39 K), and is possibly due to a crystal field effect, or some external source of magnetism (e.g. from the sample holder) which becomes apparent in this temperature range. The results of Curie-Weiss fits to the data are shown in Table 3.3. The expected effective moment was calculated as 11.71 μ_B, using Equation 2.5. The measured values for p_{eff} are in good agreement with the expected value, implying the moments are in the paramagnetic state above 200 K. The initial magnetic ordering temperature in $DyMnO_3$ is ∼39 K, where the Mn moments antiferromagnetically align. The measured value for θ along the b-axis is in moderate agreement with this value, but not so along the a-direction.

No single crystal magnetic susceptibility data with Curie-Weiss analysis were found in the literature for $DyMnO_3$, but a polycrystalline study was conducted by Chen *et al*. [82]. Similar behaviour is seen for the polycrystalline sample as for the single crystal presented here, with the magnitude of the polycrystalline suscepti-

bility lying in between the a-axis and b-axis data. As reported for $TbMnO_3$ [75], the susceptibility of polycrystalline $DyMnO_3$ shows Curie-Weiss behaviour close to the magnetic transition temperature, with $1/\chi$ being linear above 50 K. The effective moment calculated by Chen *et al.* was 11.19 μ_B, which is in reasonable agreement with the expected value of 11.71 μ_B, but not as close as the single crystal data. Chen *et al.* found θ = -25.3 K for polycrystalline $DyMnO_3$.

The features in the magnetic susceptibility data for $DyMnO_3$ are very different to those seen along the same axes in $TbMnO_3$, showing that the effect of rare earth magnetism plays a significant role in the magnetic properties of the $RMnO_3$ systems. The difference between the Néel temperature and the onset of Curie-Weiss behaviour, implies that a similar crystal field situation exists here as in $TbMnO_3$ (Section 3.2). This is also supported by the calculated values of θ for both $DyMnO_3$ and $TbMnO_3$ being significantly different to -T_N. The strong influence of crystal field effects on the magnetic properties of these compounds underlines the need to study single crystal (rather than polycrystalline) samples.

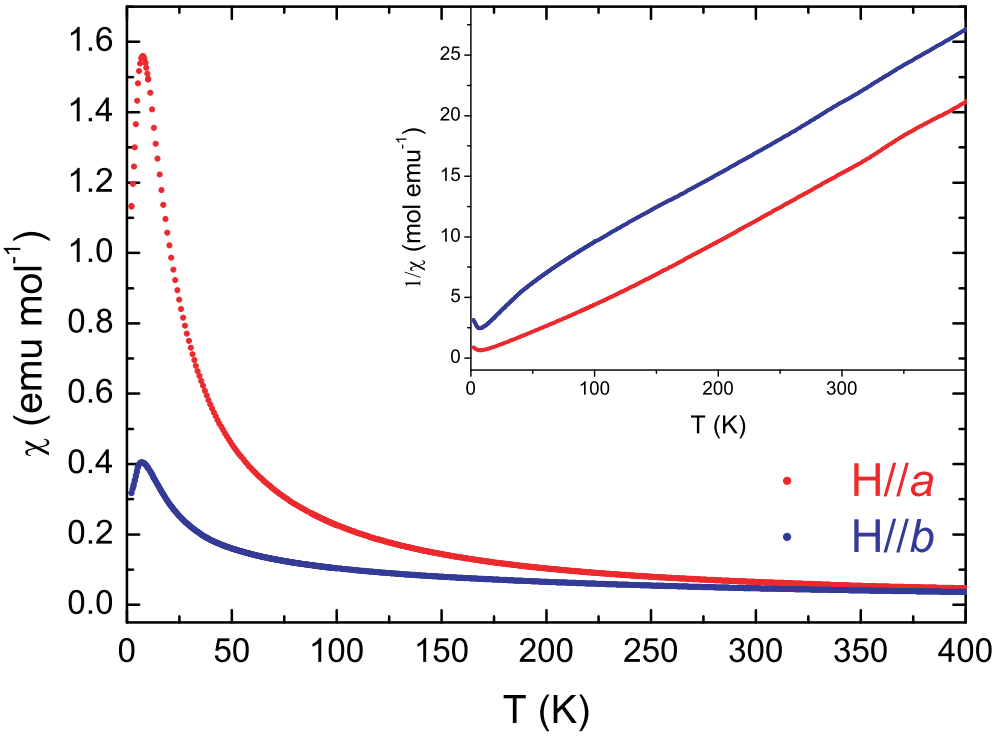

Figure 3.18: Magnetic susceptibility versus temperature for single crystal $DyMnO_3$. Measured in an applied magnetic field of 0.5 T along the a- and b-axes

Sample state	C (emu K mol^{-1})	θ (K)	p_{eff}	Fit range (K)
H // a	17.153(2)	-37.0(4)	11.707(1)	200-400
H // b	16.667(8)	+49.7(2)	11.540(3)	200-400

Table 3.3: Curie constant, C, Weiss temperature, θ, and effective magnetic moment, p_{eff}, for $DyMnO_3$. Derived from a Curie-Weiss fit to inverse susceptibility data for single crystal samples

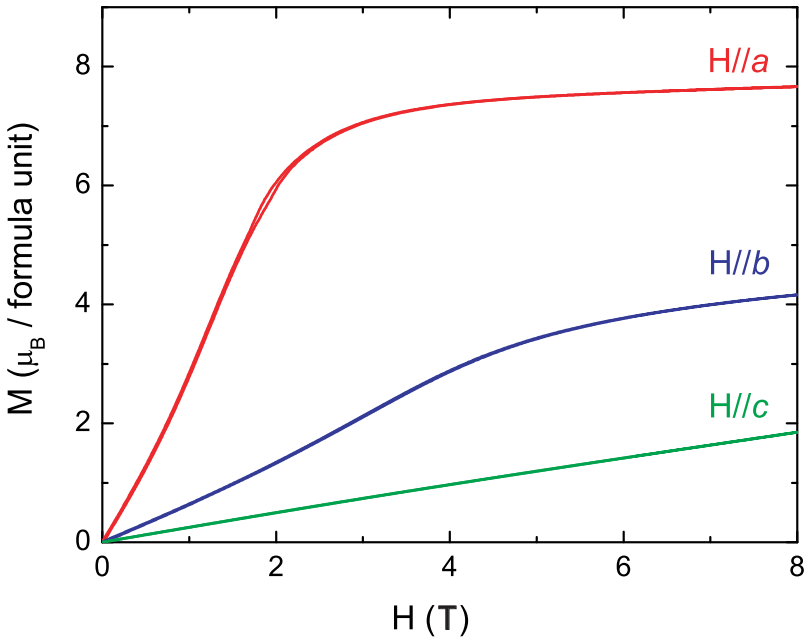

Figure 3.19: Magnetisation of a single crystal of $DyMnO_3$ versus applied magnetic field along the principal crystallographic axes, taken at 5 K

3.7.2 Magnetisation

The magnetic field dependence of the magnetisation along each axis is shown in Figures 3.19 and 3.20. The behaviour along the a-axis (Figure 3.20(a)) is similar to that seen for $TbMnO_3$, with the saturation above 2 T at 1.5 K most likely due to ordering of the Dy moments. The size of the saturated magnetisation along the a-axis is $\sim$8 μ_B/f.u., which is higher than the value of $\sim$6 μ_B/f.u. in $TbMnO_3$. The expected saturation moment for Dy^{3+} ions is 10 μ_B, compared with 9 μ_B for Tb^{3+} ions. It is also possible with $DyMnO_3$ that an antiparallel arrangement of the Mn magnetic sublattice is the cause of magnetisation along the a-axis, being lower than the saturation magnetisation of the Dy^{3+} moments. With a magnetic field applied along the b-axis (Figure 3.20(b)), metamagnetic transitions are seen below 10 K, although they are not as distinct as those found in $TbMnO_3$ (Figure 3.8(b)).

Kimura *et al*. report a change in the electric polarisation direction from the *c*- to *a*-axis with a field applied along the *b*-axis of $DyMnO_3$ [31]. No features are seen in the magnetisation along the *c*-axis (Figure 3.20(c)).

It is interesting to note that the behaviour of the magnetisation along the three principal axes is not equivalent at 50 K. The magnitude of the magnetisation along the *c*-axis is approximately one quarter of that along the *a*-axis at 6 T, implying that the moments are constrained from pointing along the *c*-axis as easily. Since this temperature is in the paramagnetic phase (T_{N1} for $DyMnO_3$ is $\sim$39 K), the difference between the data sets is likely due to crystal field effects.

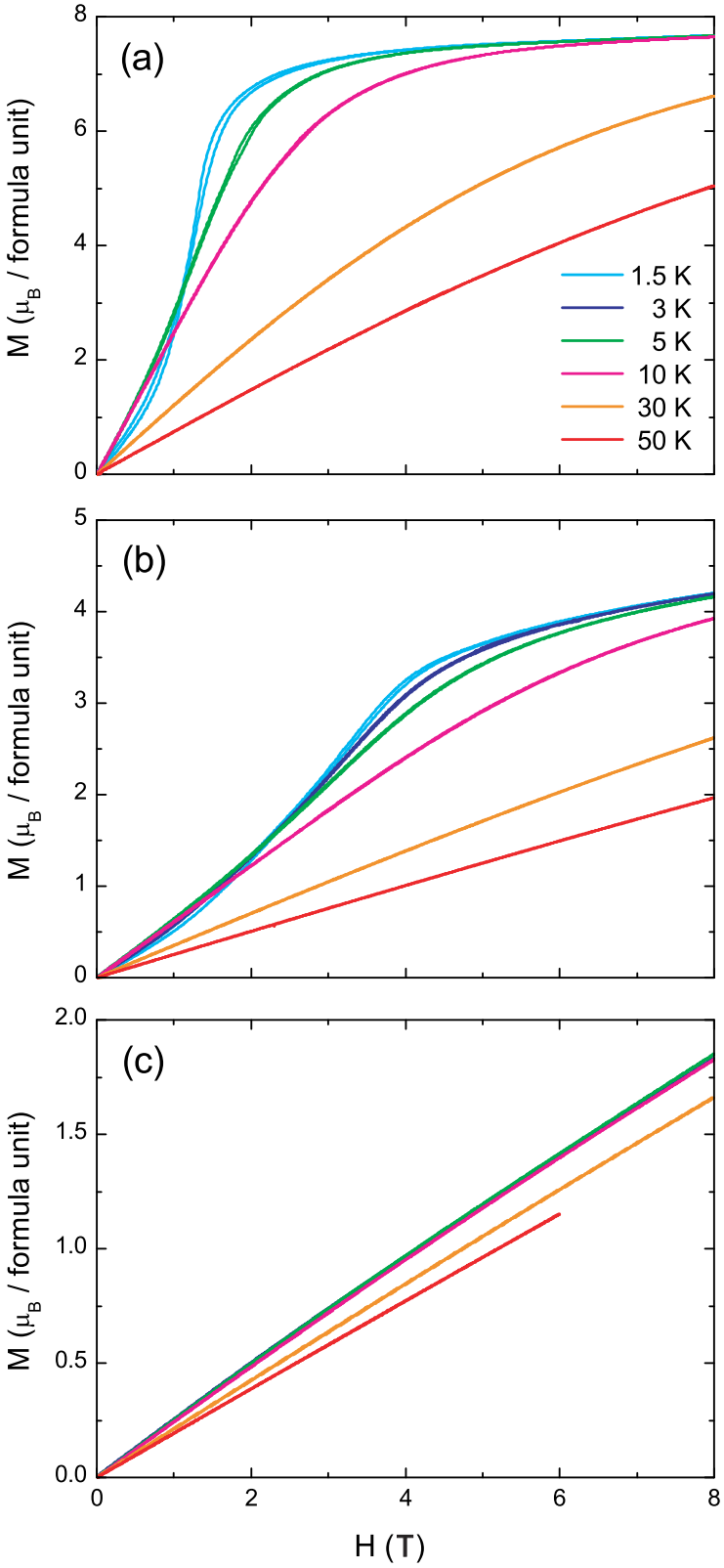

Figure 3.20: Magnetisation of a single crystal of $DyMnO_3$ versus applied magnetic field in different temperatures, measured along the (a) *a*-, (b) *b*-, and (c) *c*-axis

3.8 Conclusion

$TbMnO_3$ shows a clear link between magnetic and ferroelectric properties (Figure 3.17) Although $TbMnO_3$ is one of the most widely studied of the multiferroics, there are still unanswered questions raised by the properties presented above. Interesting new observations include the magnetic susceptibility not obeying Curie-Weiss behaviour until well above T_{N1}, alongside the existence of magnetic entropy in the system over a similar temperature range. These results point towards magnetic correlations in the system above T_{N1}, or crystal field effects. This behaviour is especially pronounced in the susceptibility measurement along the c-axis (Figure 3.4(c)), which shows a broad hump over a range of ∼200 K in the paramagnetic phase. The results of heat capacity measurements under an applied magnetic field confirmed the proposal that the magnetisation saturation seen for $H//a$ is due to the Tb moments [31]. These heat capacity data correspond with the magnetoelectric transitions presented by Kimura *et al.* in the phase diagram of $TbMnO_3$ (Figure 3.21). The metamagnetic transitions observed in Section 3.3 are also shown on these phase diagrams for $H//b$ and $H//c$. The metamagnetic transitions coincide with the magnetoelectric transitions along these directions, as expected.

The data presented also illustrate the contrast between the properties of $TbMnO_3$ and $DyMnO_3$. The magnetic susceptibility shown by the two compounds is markedly different, although similar crystal field effects also appear to be present in $DyMnO_3$. The magnetisation data for $DyMnO_3$ do not show the distinct metamagnetic transitions for $H//b$ seen for $TbMnO_3$, although they are still present. For both compounds, these transitions appear to be strongly linked to the rare earth magnetic order, being pronounced below the ordering temperatures for Tb and Dy, respectively. The importance of the Tb ions in $TbMnO_3$ is apparent when observing the magnetic field dependence of the electric polarisation [7, 31]. Since there is only a small amount of published data on the magnetic order of the Tb ions, it is currently difficult to further understand the magnetic interactions between the Tb and Mn ions.

The measurements of the dielectric constant and electric polarisation along the c-axis of $TbMnO_3$ gave results similar to those published by Kimura *et al.* [7, 31]. Although no new information was found from these results, they are important in that they serve to show the single crystal samples had been correctly synthesised, and to standardise the results of the electric properties measurement system (Section 2.8). This was a necessary step before conducting similar measurements on the new multiferroic compounds of the form $Sm_{1-x}Y_xMnO_3$, which will be discussed in the following chapters.

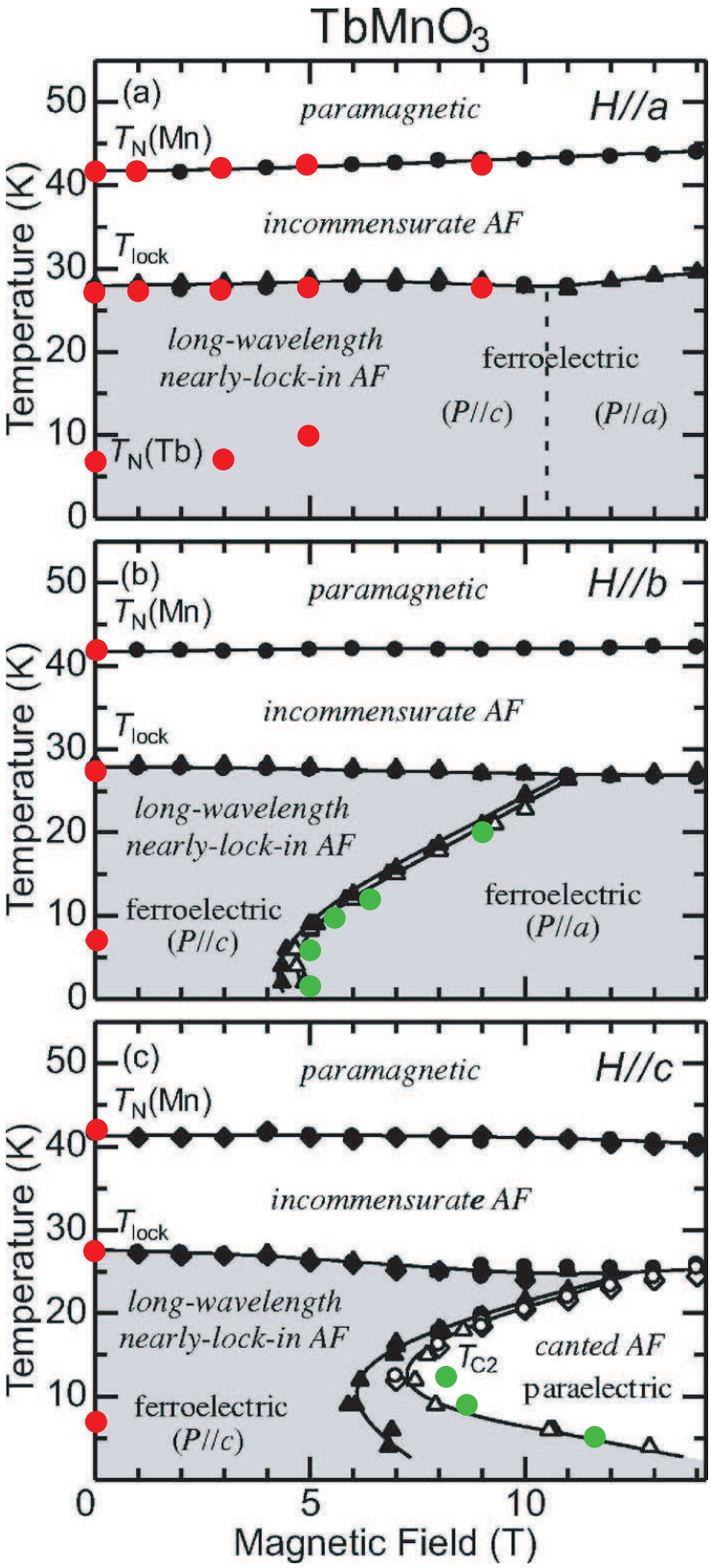

Figure 3.21: Magnetoelectric phase diagrams of $TbMnO_3$ for (a) $H//a$, (b) $H//b$ and (c) $H//c$, taken from Kimura *et al.* [31]. The black circles, triangles and diamonds represent data obtained by measurements in Ref. [31] of dielectric constant, pyroelectric (or magnetoelectric) current, and magnetisation, respectively. The red and green circles represent heat capacity and magnetisation data measured for this Thesis.

Chapter 4

Magnetoelectric properties of $Sm_{1-x}Y_xMnO_3$

In the multiferroic compounds $TbMnO_3$ and $DyMnO_3$, the ferroelectric properties are coincident with a cycloidal magnetic order of the Mn^{3+} moments (Section 1.6). It has been proposed that this magnetic order is dependent on the crystal structure [30] of the compounds, as well as the magnetic interaction between the rare earth moments and the Mn moments [32, 40, 41].

The RMnO$_3$ compounds for R = La–Ho have an orthorhombically distorted perovskite structure (space group Pbnm), with a central Mn atom surrounded by an octahedron of oxygen atoms (Figure 1.3). The Mn-O-Mn bond angle represents the degree of tilting between adjacent Mn-O octahedra, and describes the local distortions in the structure. The manganites with larger rare earth ionic radius (R = La, Sm, Eu) exhibit non-ferroelectric A-type antiferromagnetic order. As the Mn-O-Mn bond angle ϕ decreases with decreasing rare earth ionic radius [83], the magnetic frustration increases, resulting in the cycloidal magnetic ground state seen in $TbMnO_3$ and $DyMnO_3$ (Figure 1.20).

In order to understand the emergence of multiferroic behaviour in the RMnO$_3$ compounds, it is highly desirable to study the effects of altering the Mn-O-Mn bond angle in non-multiferroic/weakly multiferroic materials. As seen in Section 1.7.2, several groups have succeeded in discovering multiferroic properties in $EuMnO_3$ by doping with Y at the Eu site [56–59]. This result is evidence for the existence of a relationship between ϕ and the cycloidal magnetic order

of the Mn^{3+} moments. The electric polarisation develops along a different crystallographic direction in $Eu_{1-x}Y_xMnO_3$ to $TbMnO_3$ and $DyMnO_3$, suggesting a possible connection with the existence of rare earth magnetism [39]. At present, no data has been published explicitly confirming the magnetic structure of the $Eu_{1-x}Y_xMnO_3$ compounds.

The work presented in the following two chapters focuses on Y-doped $SmMnO_3$. This was a logical choice of compound in attempting to gain a fuller picture of the behaviour of the RMnO$_3$ series for two main reasons. $SmMnO_3$ is the neighbouring compound to $EuMnO_3$ in the RMnO$_3$ series (ionic radius values: Sm > Eu > Tb). Also, unlike Eu^{3+}, Sm^{3+} ions possess a finite magnetic moment, but with a magnitude of less than a fifth of those of Tb^{3+} and Dy^{3+}. The purpose of studying the $Sm_{1-x}Y_xMnO_3$ compounds was therefore to test if multiferroic properties could be induced by doping as with $Eu_{1-x}Y_xMnO_3$, to measure the change in ϕ with Y-doping, and to shed further light on the relationship between the rare earth magnetic order and the ferroelectricity-inducing Mn order. Y was used as a dopant for two principal reasons: the ionic radius of Y is smaller than that of Sm, and it is a non-magnetic element. It is important to not introduce further sources of magnetic interaction into the system when studying the effect of doping on the magnetic properties. Presented in this chapter are details of the sample preparation and characterisation of polycrystalline and single crystal $Sm_{1-x}Y_xMnO_3$, with bulk heat capacity, magnetic and electric properties measurements. The data are then summarised in a phase diagram (Figure 4.30).

4.1 Polycrystalline $Sm_{1-x}Y_xMnO_3$

As an initial study, small amounts (2-3 g) of polycrystalline $Sm_{1-x}Y_xMnO_3$ ($x = 0$, 0.25, 0.4, 0.5, 0.6) were synthesized in order to observe phase formation and any changes in the magnetic and/or electric properties.

4.1.1 Sample preparation

Polycrystalline samples were synthesized by heating stoichiometric ratios of Sm_2O_3 (99.9%), Y_2O_3 (99.99%) and MnO_2 (99+%) powders. The procedure used for

Heating	Temperature (°C)	Duration (hours)	Comments
1	1100	4	Y_2O_3 preheat
2	1100	12	Sm_2O_3 + Y_2O_3 + MnO_2
3	1400	24	Sm_2O_3 + Y_2O_3 + MnO_2
4	1400	12	pellets + powder

Table 4.1: Sample heating procedure for the preparation of $Sm_{1-x}Y_xMnO_3$ (x = 0-0.6)

heating the powders is given in Table 4.1. Since Y_2O_3 is hygroscopic (i.e. it absorbs moisture from the air), this powder was heated to remove impurities prior to mixing with the Sm_2O_3 and MnO_2 powders. Pellets of each composition were pressed before the final sintering, from which pieces were cut for magnetic and dielectric measurements. Electrical contacts were painted onto the flat surface of the pellets using silver paste, as described in Section 2.6.

4.1.2 X-ray diffraction

Preliminary powder X-ray diffraction patterns were taken with a Philips PW1720 X-ray generator, with 0.02° increments and a counting time of 2 s/step. These patterns show that the synthesized compounds are single phase for $0 \leq x \leq 0.5$, since no additional peaks are seen for this Y doping range (Figure 4.1). At $x = 0.6$, additional peaks were seen in the diffraction pattern (Figure 4.2). These peaks correspond to $YMnO_3$ [84], indicating that this doping level is above the solubility limit of the series. More detailed diffraction patterns of the $x = 0, 0.4$ compositions were taken with a Panalytical X'Pert Pro multipurpose X-ray diffraction system, and are shown in Figures 4.3 and 4.4. A Rietveld refinement of the latter data sets was performed with Topas Academic [85], giving the crystal structure information shown in Table 4.2.

There are two different Mn-O-Mn bond angles, ϕ_1 and ϕ_2, found for perovskite structures with corner-sharing oxygen octahedra, as shown in Figure 4.5. Since there are two ϕ_1 values and four ϕ_2 values, the mean bond angle presented is a weighted average of the two angles. It is important to note that powder X-ray diffraction is not an ideal method for determining the Mn-O-Mn bond angles for systems such as those in the RMnO$_3$ series. The relatively small atomic number of the oxygen atoms (8) compared with those of the rare earth (57-71), Y (39)

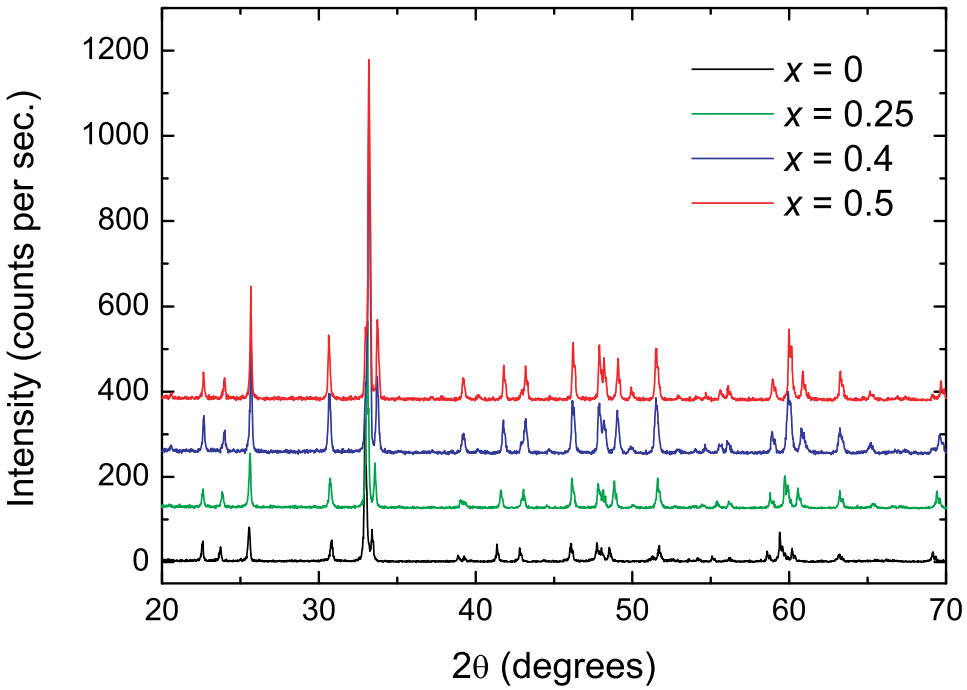

Figure 4.1: X-ray diffraction patterns for polycrystalline $Sm_{1-x}Y_xMnO_3$ (x = 0-0.5), taken with a Philips PW1720 X-ray generator (Cu K_α radiation).

and Mn (25) atoms makes them harder to see with X-rays, making it difficult to accurately determine oxygen atomic positions. A more suitable method for determining ϕ is to use neutron diffraction, as presented in Chapter 5.

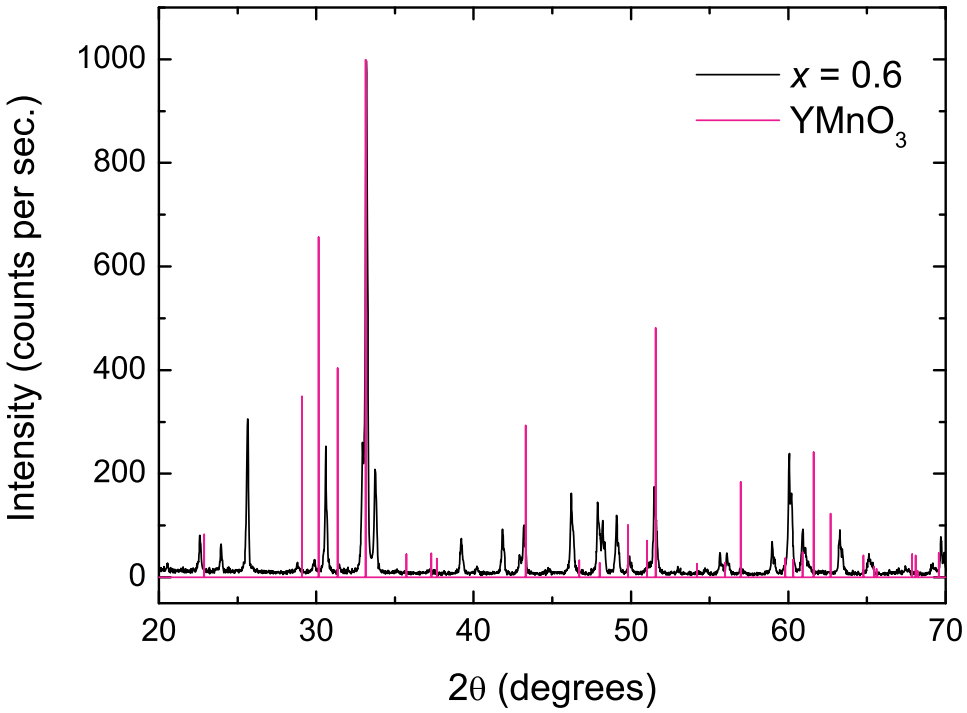

Figure 4.2: X-ray diffraction pattern for polycrystalline $Sm_{0.4}Y_{0.6}MnO_3$, taken with a Philips PW1720 X-ray generator (Cu K_α radiation). Peaks in the pattern not observed for $x = 0$-0.5 correspond to the X-ray diffraction data for $YMnO_3$ [84].

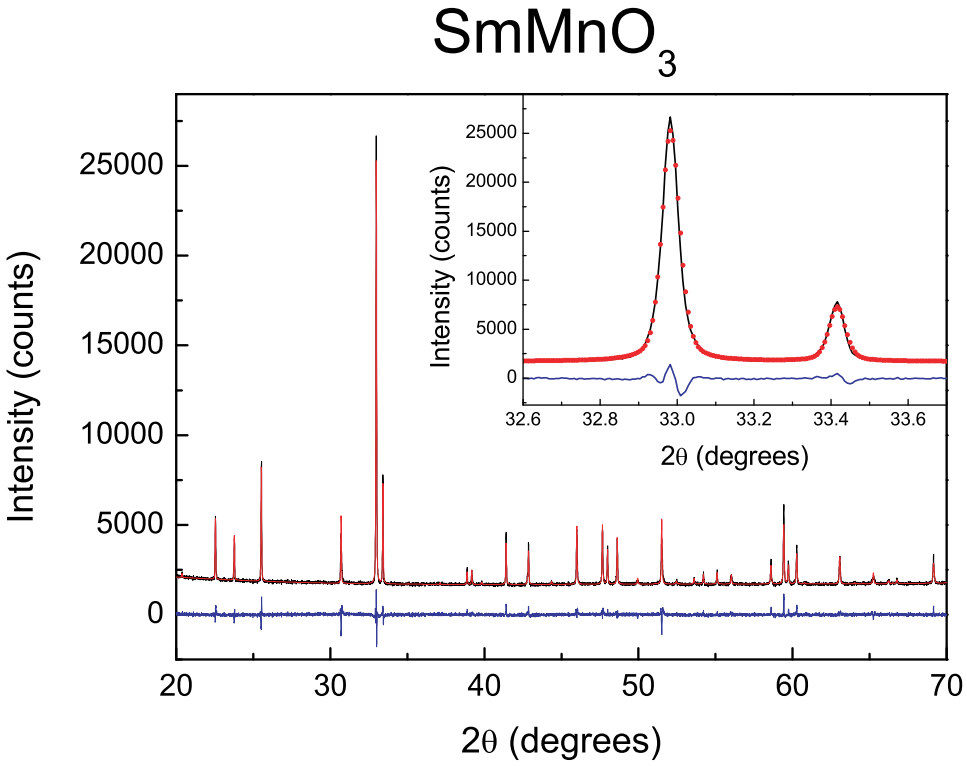

Figure 4.3: X-ray diffraction pattern for polycrystalline $SmMnO_3$, taken with a Panalytical X'Pert Pro multipurpose X-ray diffraction system (Cu $K_{\alpha 1}$ radiation). The red line shows the observed data, the black line is the fit to the data using Topas Academic, and the blue line is the difference between the two. Inset: close up of the fit in the region of the high intensity peaks, for detail.

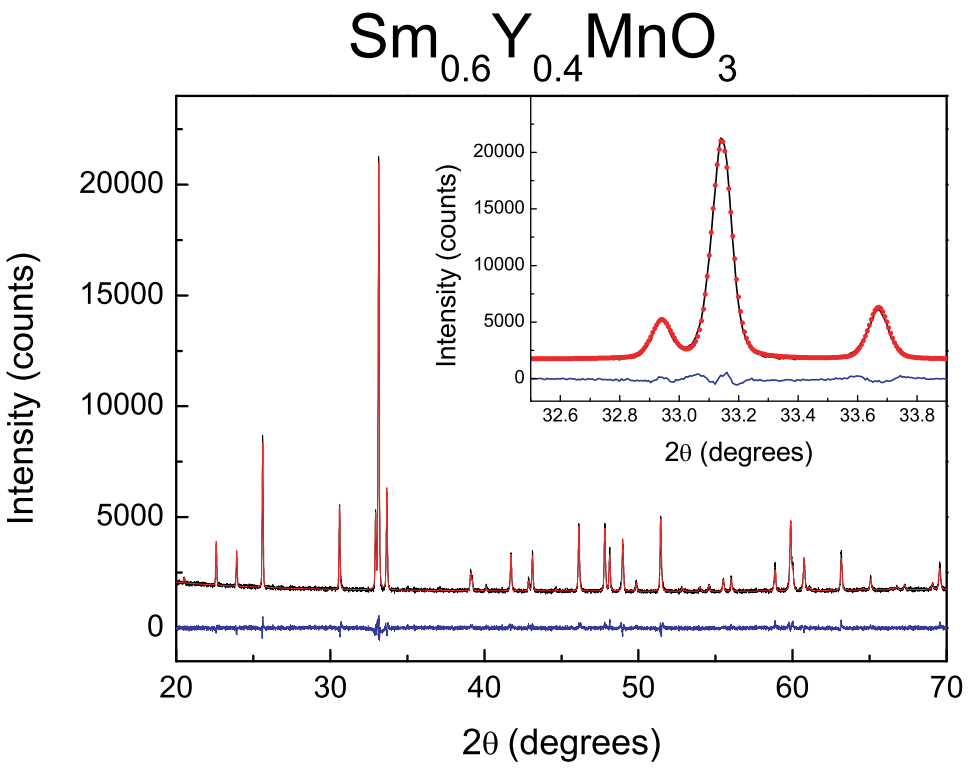

Figure 4.4: X-ray diffraction pattern for polycrystalline $Sm_{0.6}Y_{0.4}MnO_3$, taken with a Panalytical X'Pert Pro multipurpose X-ray diffraction system. The red line shows the observed data, the black line is the fit to the data using Topas Academic, and the blue line is the difference between the two. Inset: close up of the fit in the region of the high intensity peaks, for detail.

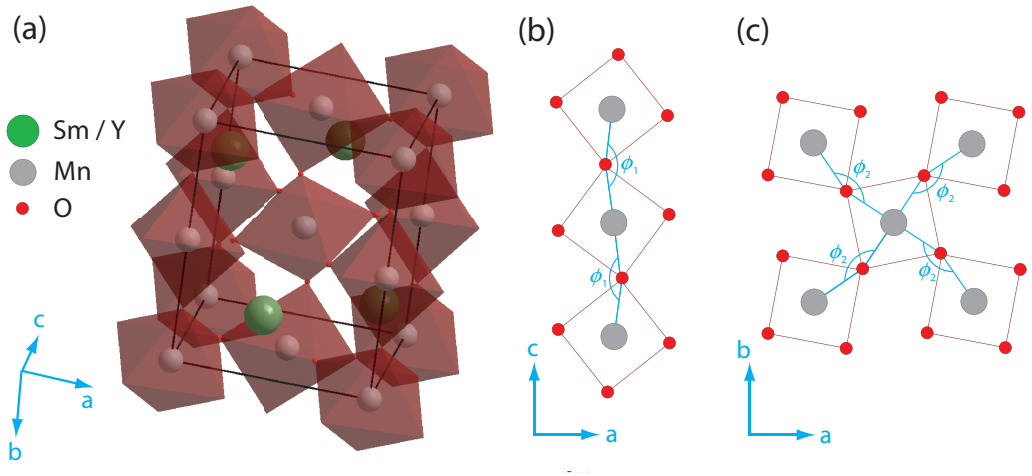

Figure 4.5: (a) Crystal structure of $Sm_{0.6}Y_{0.4}MnO_3$ (space group Pbnm), from refined powder X-ray diffraction data. Illustrations of the (b) a-c and (c) a-b planes indicate the different bond angles, ϕ_1 and ϕ_2.

	$SmMnO_3$	$Sm_{0.6}Y_{0.4}MnO_3$
a (Å)	5.36010(16)	5.31722(5)
b (Å)	5.79368(14)	5.83555(5)
c (Å)	7.4932(2)	7.42946(6)
V (Å^3)	232.70(6)	230.528(3)
Mn-O1-Mn, ϕ_1 (×2)	148.4(5)°	148.5(3)°
Mn-O2-Mn, ϕ_2 (×4)	148.5(5)°	142.1(3)°
$\langle\phi\rangle$	148.5(5)°	144.2(3)°
Reliability factors		
R_p(%)	2.572	2.338
R_{wp}(%)	3.722	3.070
R_{exp}(%)	2.311	2.302
χ^2	1.610	1.334

Table 4.2: Lattice parameters and Mn-O-Mn bond angles for $SmMnO_3$ and $Sm_{0.6}Y_{0.4}MnO_3$ (space group P*bnm* for both compounds), from refined powder X-ray diffraction data.

4.1.3 Magnetic properties

The magnetic properties of $Sm_{1-x}Y_xMnO_3$ ($x = 0 - 0.5$) are shown in Figure 4.6. Pure $SmMnO_3$ is known to exhibit a magnetic transition due to the ordering of the Mn^{3+} spins at T_N∼60 K [86], this is reflected by a sharp increase in the susceptibility at this temperature. No polycrystalline susceptibility data were found in the literature for $SmMnO_3$, but the behaviour is similar to that seen in the single crystal compound, discussed in Section 4.2.2.

The Néel temperature measured in the Y doped samples is lower than that found in $SmMnO_3$, with values of ∼48 K for $x = 0.4$ and ∼46 K for $x = 0.5$. The size of the observed magnetic susceptibility in the Y-doped samples is seen to decrease by two orders of magnitude from the parent compound. In $SmMnO_3$, there is a small canting of the Mn^{3+} moments, causing a weak ferromagnetic component of the magnetisation. By doping at the Sm site with non-magnetic Y, this ferromagnetic component is rapidly suppressed. Magnetic susceptibility versus temperature plots on the Y substituted compounds show an additional magnetic anomaly developing at T∼21 K as the doping is increased to $x = 0.4$, and at T∼19 K for $x = 0.5$ (Figure 4.6(b)). These temperatures are similar to those of the transitions seen in $TbMnO_3$ and $DyMnO_3$ where the Mn^{3+} moments

show a cycloidal ordering. The transition in $Sm_{1-x}Y_xMnO_3$ is subtle, and possibly appears smeared out due to the polycrystalline nature of the samples. It was clear that single crystal samples were required to gain a clearer picture of this feature in the susceptibility data.

4.1.4 Dielectric properties

A measurement of the temperature dependence of the dielectric constant of pure $SmMnO_3$ shows featureless data, which decrease smoothly with decreasing temperature (Figure 4.7). A well defined peak in the dielectric constant begins to develop as x is increased, being most pronounced for $x = 0.4$ and 0.5. This peak is observed at the same temperature at which the cusp in the magnetic susceptibility is seen for these compositions (Figure 4.8) - a clear indication of the coupling between magnetic and dielectric properties in the $Sm_{1-x}Y_xMnO_3$ compounds.

The results of the susceptibility and dielectric constant measurements on polycrystalline $Sm_{1-x}Y_xMnO_3$ are presented in a proposed phase diagram in Figure 4.9.

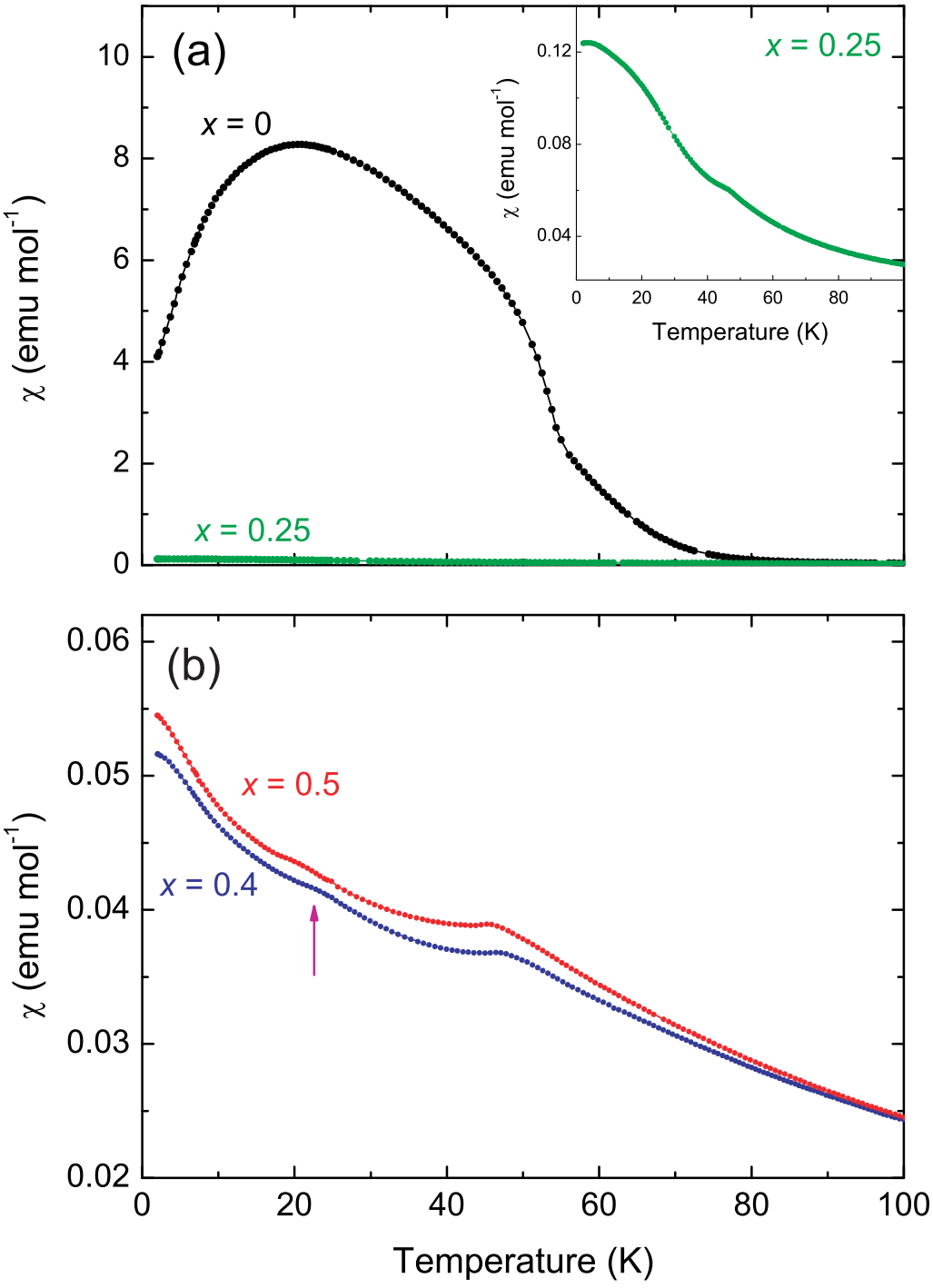

Figure 4.6: Magnetic DC susceptibility of polycrystalline $Sm_{1-x}Y_xMnO_3$ as a function of temperature, measured in an applied magnetic field of 0.01 T. The purple arrow points to the possible new magnetic transition seen in the Y-doped compounds

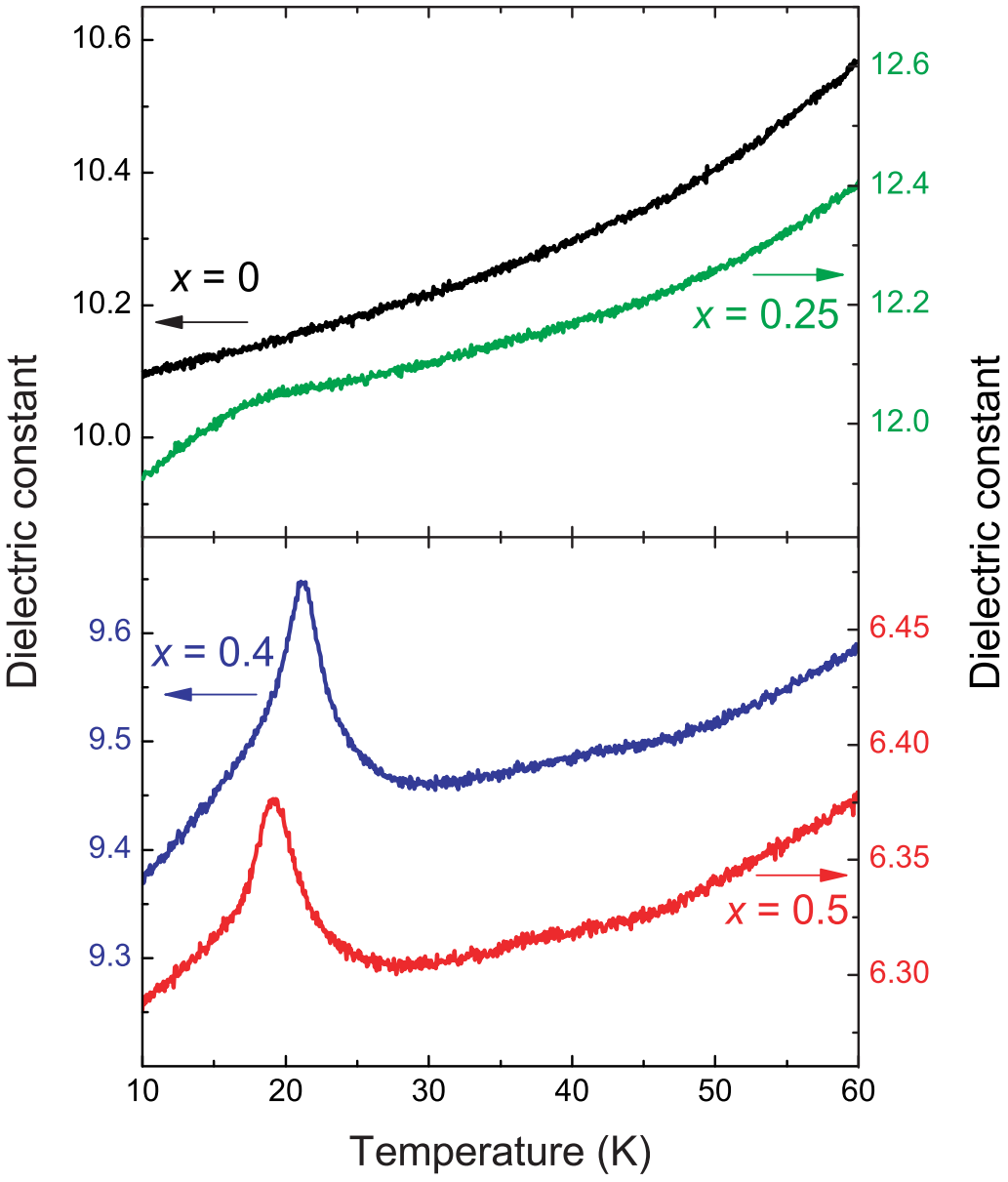

Figure 4.7: Dielectric constant of polycrystalline $Sm_{1-x}Y_xMnO_3$ as a function of temperature, measured at 10 kHz

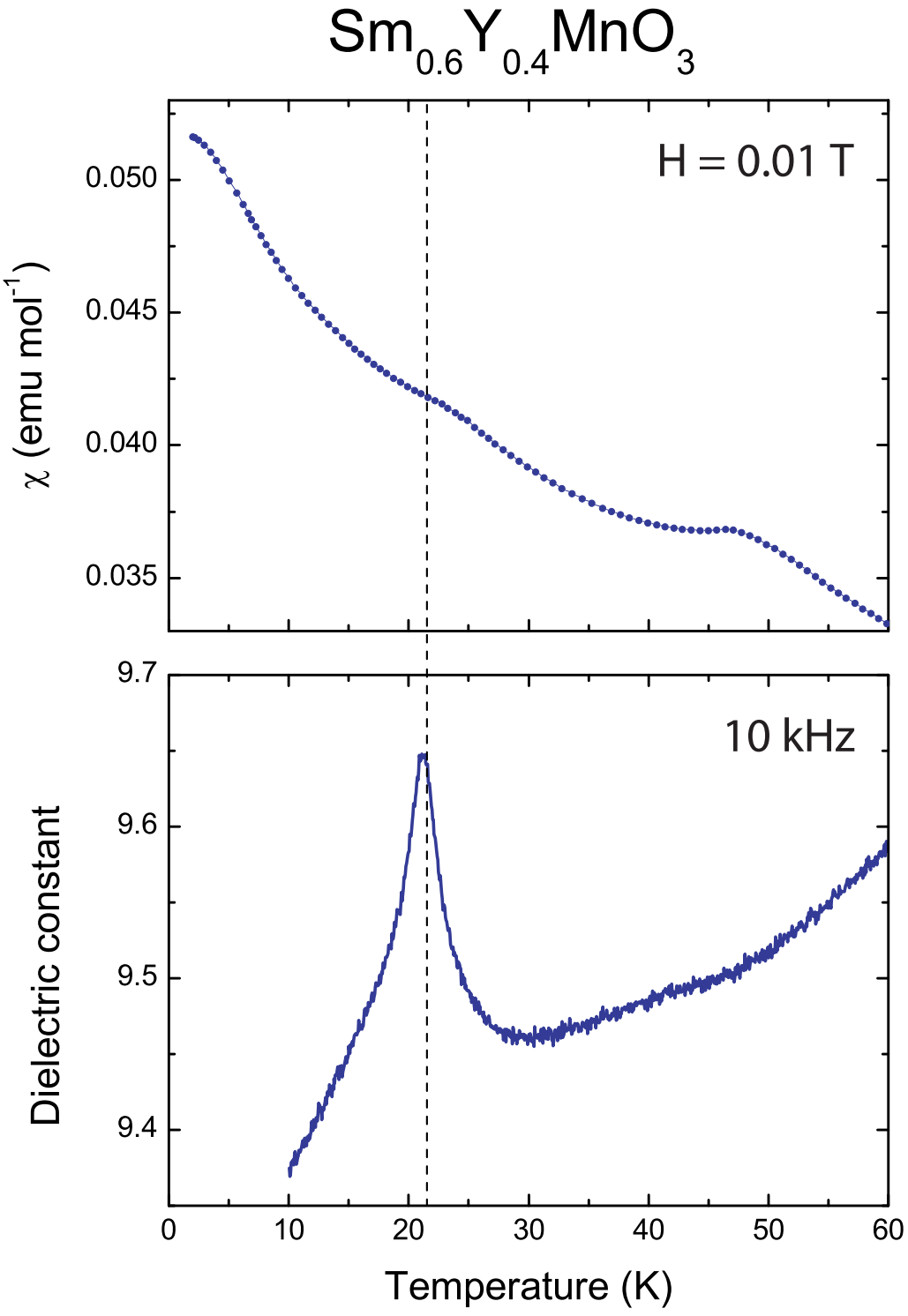

Figure 4.8: Comparison of magnetic and dielectric data of polycrystalline $Sm_{0.6}Y_{0.4}MnO_3$ as a function of temperature, showing a peak in the dielectric constant at the same temperature as a small change in the magnetic susceptibility

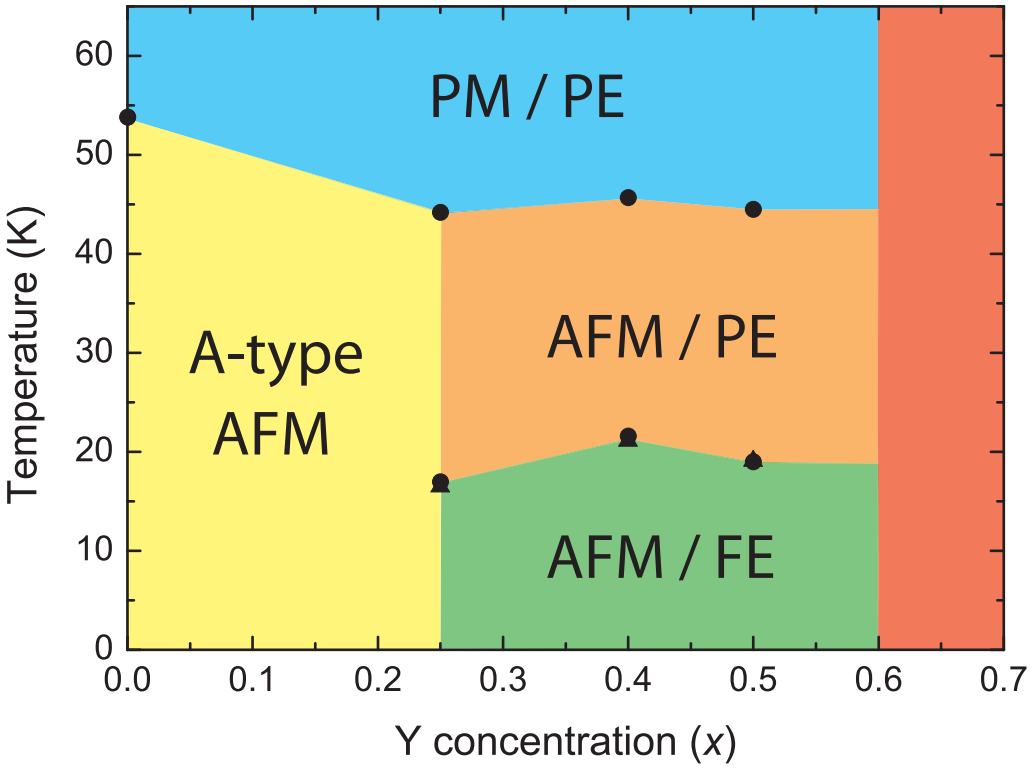

Figure 4.9: Proposed phase diagram for the $Sm_{1-x}Y_xMnO_3$ compounds as a function of Y concentration. Circles and triangles represent transitions observed in magnetic susceptibility and dielectric constant data, respectively. PM = paramagnetic, AFM = antiferromagnetic, PE = paraelectric, FE = ferroelectric. The red area represents multi-phase compounds.

4.2 Single crystal $Sm_{1-x}Y_xMnO_3$

4.2.1 Sample preparation

It is clear from the results on the polycrystalline $Sm_{1-x}Y_xMnO_3$ samples that the observed magnetic and dielectric transitions are coupled. Therefore, the next step was to produce single crystal samples for the $x = 0, 0.4, 0.5$ compositions using the floating zone method (Section 2.3). Crystals were grown at a rate of 6-8 mm/hr in an atmosphere of 50% Ar / 50% O_2. The boules were typically 7 mm in diameter, and 60-70 mm in length (Figure 4.10), but broke into pieces upon removal from the furnace, or shortly afterwards.

Crystal quality and orientation were determined using the X-ray Laue technique (Figure 4.11). For all three compositions, the boules had a polycrystalline or glassy surface, with single crystal beneath. Using published information on the crystal space group (P*bnm*) and lattice parameters of $SmMnO_3$, simulated Laue patterns were generated using the OrientExpress program. By comparison with the simulated images, it was possible to orient the crystal with respect to the three principal crystallographic axes (the *a*-, *b*- and *c*-axes), as shown in Figure 4.11. The lattice parameters of $SmMnO_3$ were sufficient for generating the simulated patterns since it was assumed that the Y doping did not result in large changes in these values (i.e. such that the principal axes became indistinguishable/incorrectly assigned). This assumption was subsequently confirmed by experiment (Table 5.2). The growth axis was generally close to the *c*-axis (within 5-10°). The single crystal portions of each boule were isolated, and then cut into 2-3 mm^3 parallelepipeds, such that each face had a principal crystallographic direction as the surface normal.

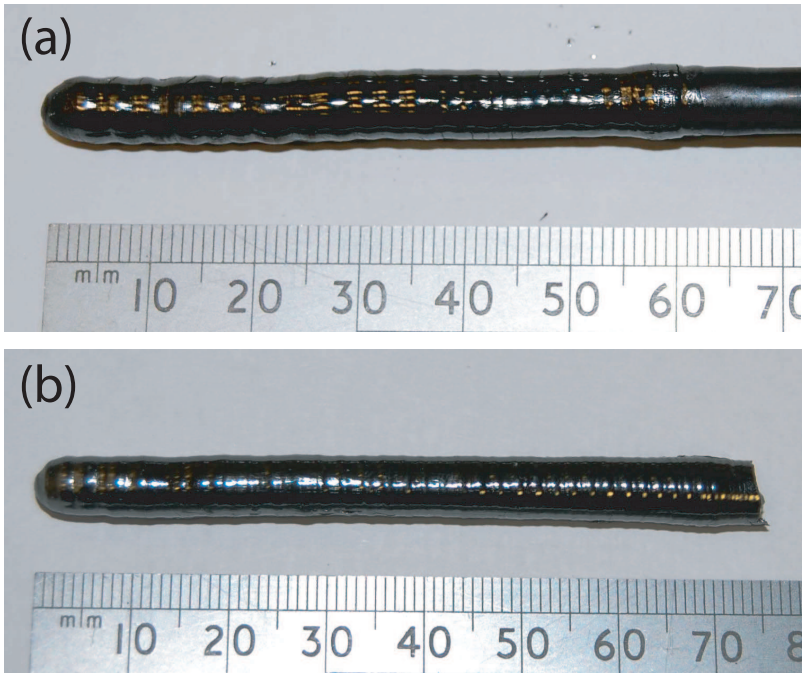

Figure 4.10: Boules of (a) $SmMnO_3$ and (b) $Sm_{0.6}Y_{0.4}MnO_3$ grown using the floating zone method.

4.2.2 Magnetic susceptibility

4.2.2.1 $SmMnO_3$

The temperature dependence of the magnetic DC susceptibility along the c-axis of $SmMnO_3$ is shown in Figure 4.12. The behaviour seen is in agreement with previously published data [29, 82, 87], with magnetic order developing at T_N ~58 K. As the sample is cooled, the susceptibility gradually increases until ~24 K, at which point χ drops sharply, becoming negative below 7 K. This behaviour is explained by Mukhin *et al.* [87] as being due to an antiparallel alignment of the weakly ferromagnetic Sm and Mn magnetic moments, due to a Sm-Mn exchange interaction. The magnetic susceptibility and inverse susceptibility up to 300 K are shown in Figure 4.13.

A quantitative analysis of the susceptibility data was carried out by calculating the effective magnetic moment, p_{eff}, as done for $TbMnO_3$ (Section 3.2). The inverse susceptibility data was found to be linear above 120 K, i.e. over 60 K above T_N (Figure 4.13). There is possibly a similar crystal field effect in $SmMnO_3$ to that found in $TbMnO_3$, but only limited crystal field analysis has been carried out on $SmMnO_3$ [88]. The results of the Curie-Weiss fits are shown in Table 4.3.

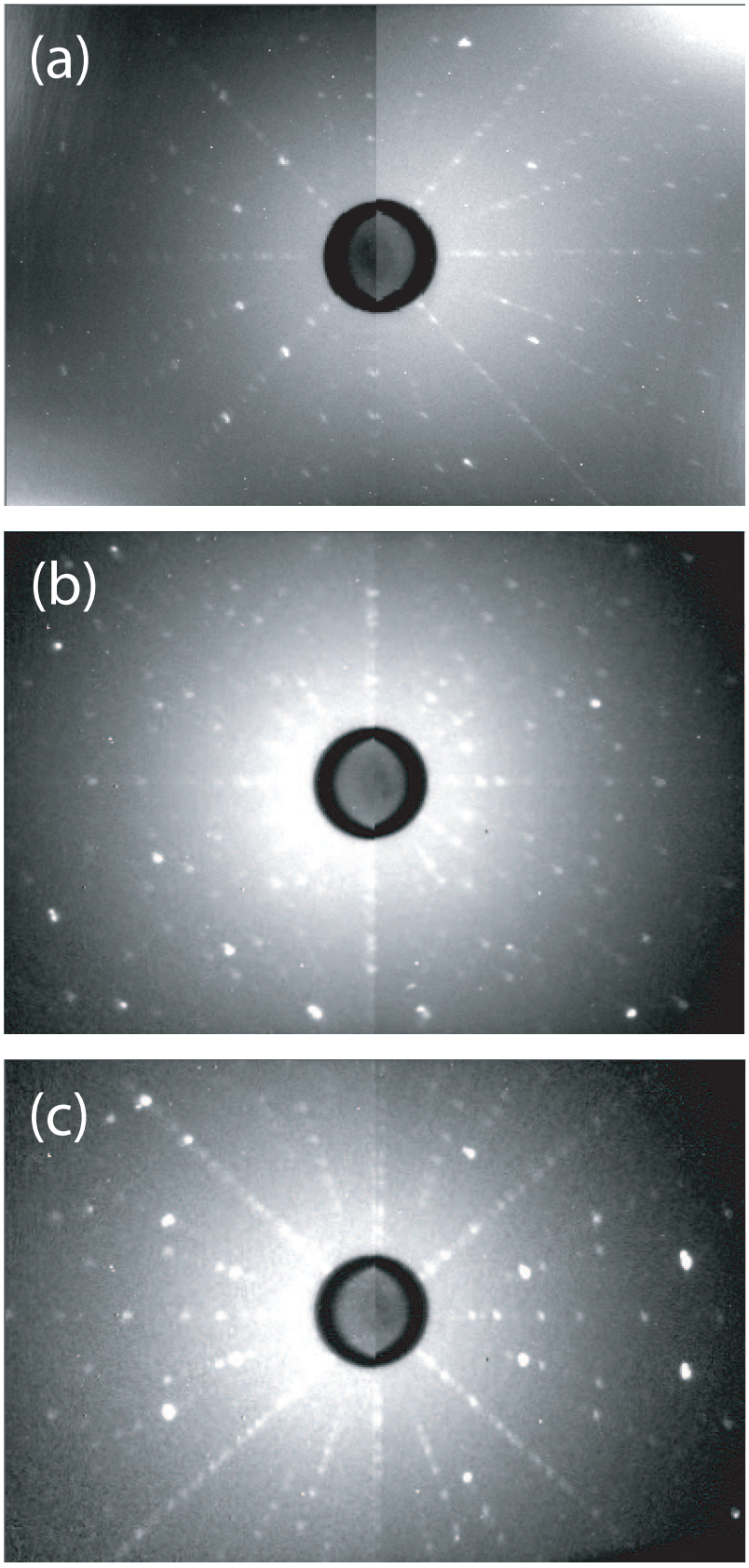

Figure 4.11: X-ray diffraction patterns along the (a) *a*-, (b) *b*- and (c) *c*-axes of a single crystal of $Sm_{0.6}Y_{0.4}MnO_3$, taken using the Laue technique.

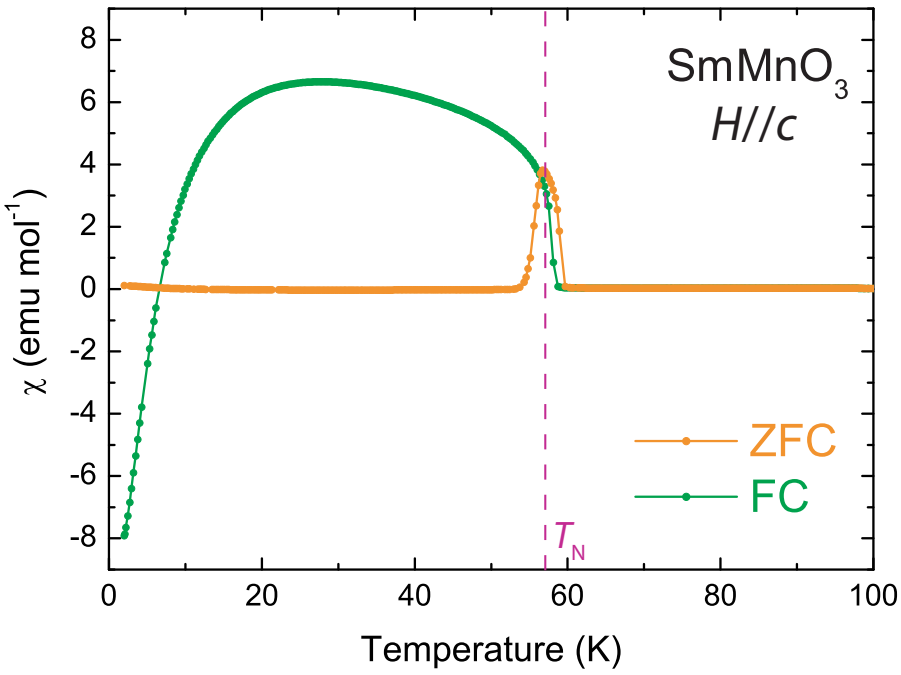

Figure 4.12: Zero field cooled and field cooled magnetic DC susceptibility along the c-axis of $SmMnO_3$, measured in an applied field of 0.01 T

Using Equation 2.5, the theoretical effective moment for $SmMnO_3$ is given as 4.97 μ_B. If, instead, the experimentally observed values of p for Sm^{3+} and Mn^{3+} are used [15], the expected value of p is calculated to be 5.12. The values for p_{eff} obtained along the a-, b- and c-axes of $SmMnO_3$ are in good agreement with the latter value of 5.12, with all axes agreeing to within 4%. The values of p_{eff} measured along each axis are consistent with each other to within 1%. As seen for $TbMnO_3$, the values of θ are far from -T_N= −59 K (Section 3.2).

4.2.2.2 $Sm_{1-x}Y_xMnO_3$

The temperature dependences of the magnetic DC susceptibility along the principal crystallographic axes of $Sm_{1-x}Y_xMnO_3$ ($x = 0.4, 0.5$) are shown in Figure 4.14.

	C (emu K mol^{-1})	θ (K)	p_{eff}	Fit range (K)
H // a	3.527(1)	-27.9(1)	5.309(1)	120-300
H // b	3.436(1)	-21.10(7)	5.240(1)	120-300
H // c	3.480(1)	-18.6(2)	5.273(3)	120-300

Table 4.3: Curie constant, C, Weiss temperature, θ, and effective magnetic moment, p_{eff}, for $SmMnO_3$. Obtained from a Curie-Weiss fit to inverse susceptibility data.

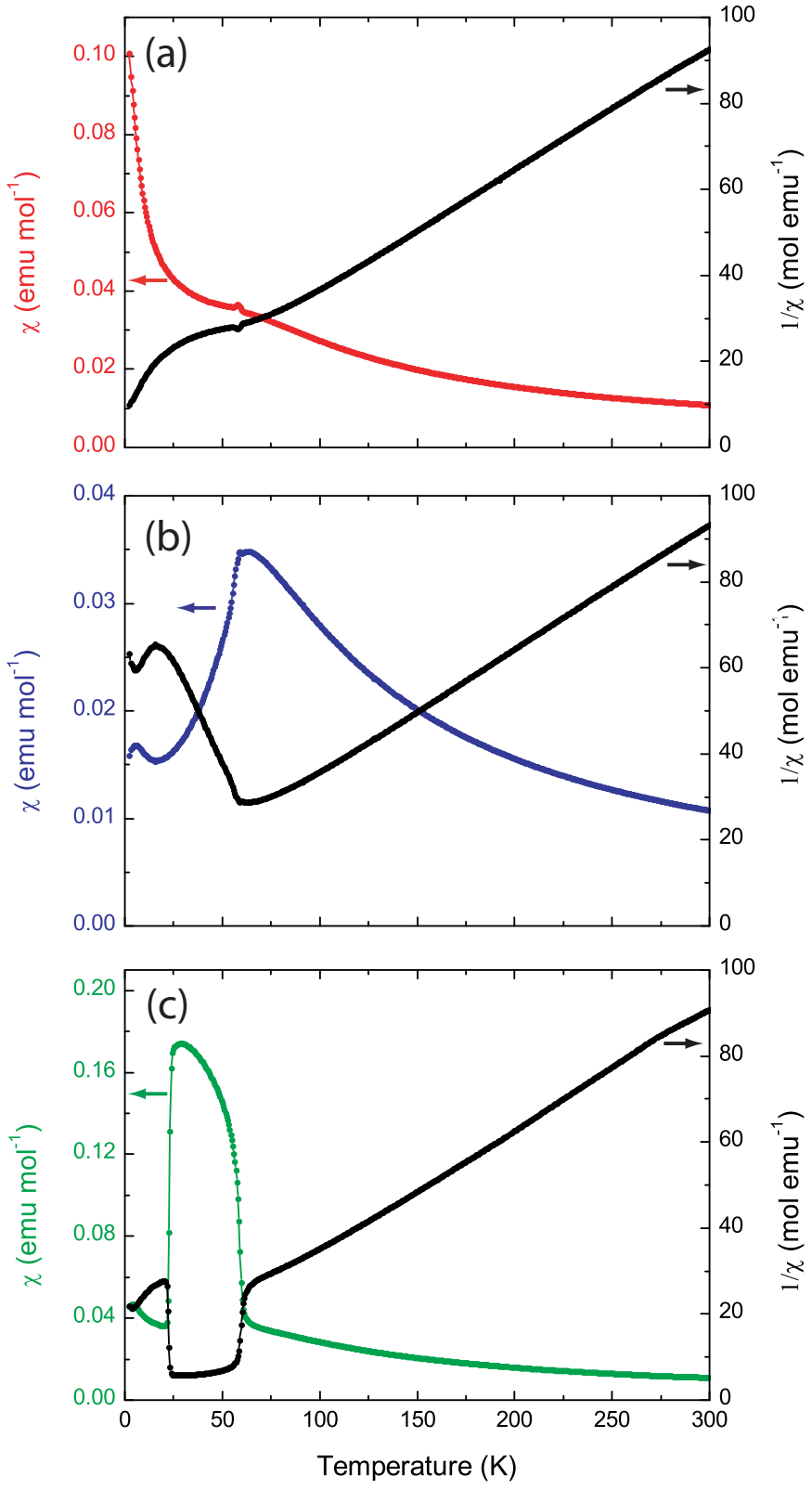

Figure 4.13: Field cooled magnetic susceptibility and inverse susceptibility for $SmMnO_3$, along the (a) *a*-, (b) *b*-, and (c) *c*-axis. Measured in an applied magnetic field of 0.5 T

The zero field cooled data have been omitted since there was negligible difference between ZFC and FC data along the three axes in both compounds. It can be seen that much smaller values of χ are seen as the doping level is increased. This is expected with decreasing Sm content, since the weak ferromagnetic Sm order is the cause of the high value of χ in pure $SmMnO_3$ [87]. The behaviour along the *a*-, *b*- and *c*-axes for $x = 0.4$ and 0.5 are reminiscent of those seen in $TbMnO_3$ (Figure 3.3), with the features in the data most pronounced along the *c*-axis. The small features seen in the polycrystalline susceptibility data are clear peaks in the single crystal data (albeit slightly shifted upwards in temperature), seen more clearly in Figure 4.24.

The magnetic susceptibility and inverse susceptibility data (up to 300 K) for $Sm_{0.6}Y_{0.4}MnO_3$ and $Sm_{0.5}Y_{0.5}MnO_3$ are shown in Figures 4.15 and 4.16. The results of Curie-Weiss fits to the data are shown in Table 4.4. The expected values of p for $Sm_{1-x}Y_xMnO_3$ were determined from the experimentally obtained values for Sm^{3+} and Mn^{3+} ions [15] using

$$p(Sm_{1-x}Y_xMnO_3) = \sqrt{(1-x)p(Sm^{3+})^2 + p(Mn^{3+})^2} \tag{4.1}$$

which gives $p(Sm_{0.6}Y_{0.4}MnO_3) = 5.00$, and $p(Sm_{0.5}Y_{0.5}MnO_3) = 4.97$. As with $SmMnO_3$, agreement is found to within a maximum of 4% for all values of p. A slight underestimate of p is seen along each axis for $SmMnO_3$ and $Sm_{1-x}Y_xMnO_3$, with the measured values systematically higher than expected.

	C (emu K mol^{-1})	θ (K)	p_{eff}	Fit range (K)
$Sm_{0.6}Y_{0.4}MnO_3$				
H // *a*	3.373(1)	-34.2(1)	5.191(1)	110-300
H // *b*	3.304(1)	-30.46(7)	5.138(1)	110-300
H // *c*	3.317(1)	-30.61(7)	5.148(1)	110-300
$Sm_{0.5}Y_{0.5}MnO_3$				
H // *a*	3.307(3)	-32.1(2)	5.140(2)	120-300
H // *b*	3.331(1)	-37.24(6)	5.159(1)	100-300
H // *c*	3.287(1)	-33.10(7)	5.125(1)	110-300

Table 4.4: Curie constant, C, Weiss temperature, θ, and effective magnetic moment, p_{eff}, for $Sm_{1-x}Y_xMnO_3$ ($x = 0.4$, 0.5). Obtained from a Curie-Weiss fit to inverse susceptibility data.

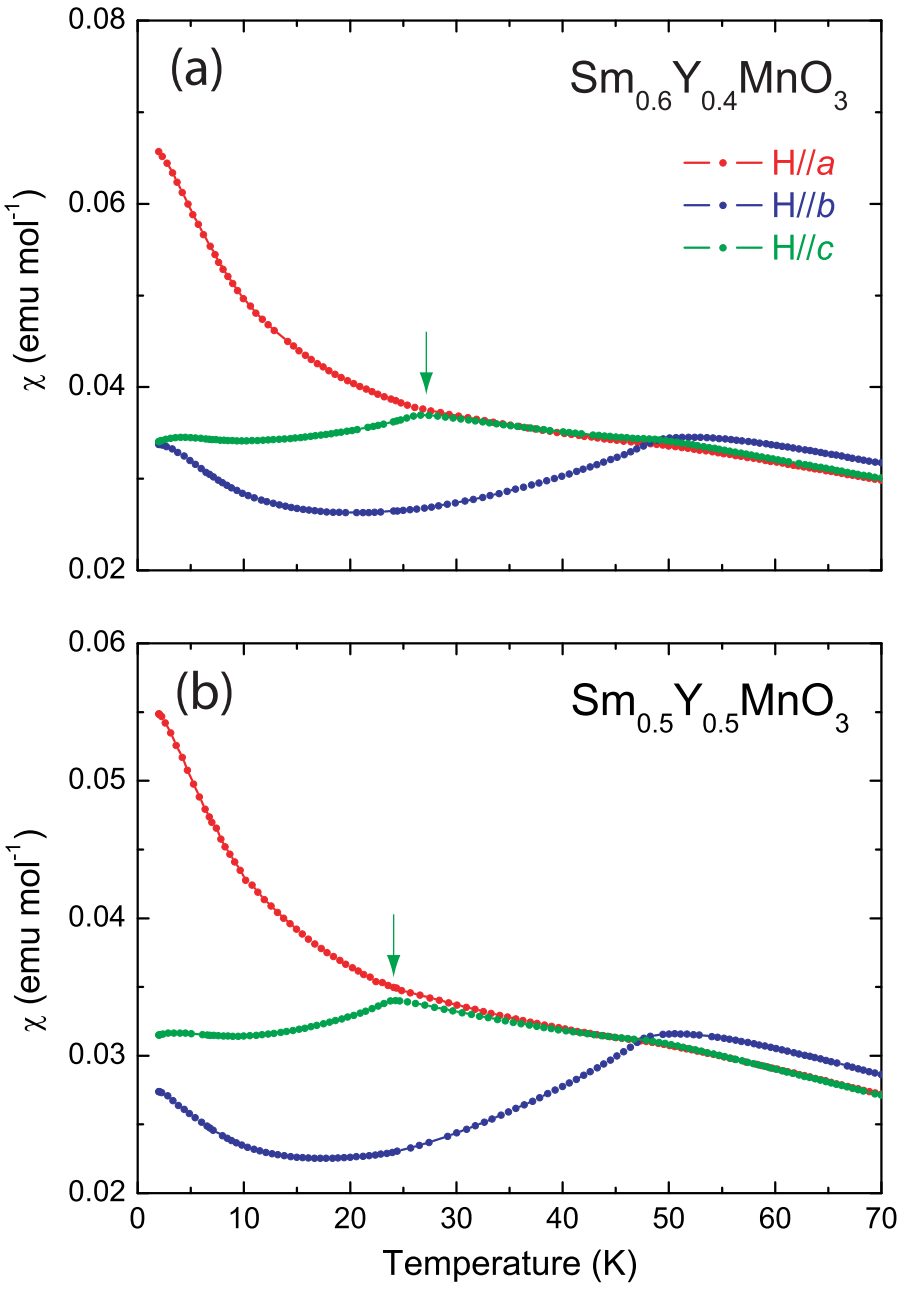

Figure 4.14: Magnetic DC susceptibility along the principal crystallographic axes of $Sm_{1-x}Y_xMnO_3$ ($x = 0.4$, 0.5) single crystals, measured in an applied magnetic field of 0.01 T. The green arrows indicate magnetic features along the c-axis which have arisen as a result of Y doping

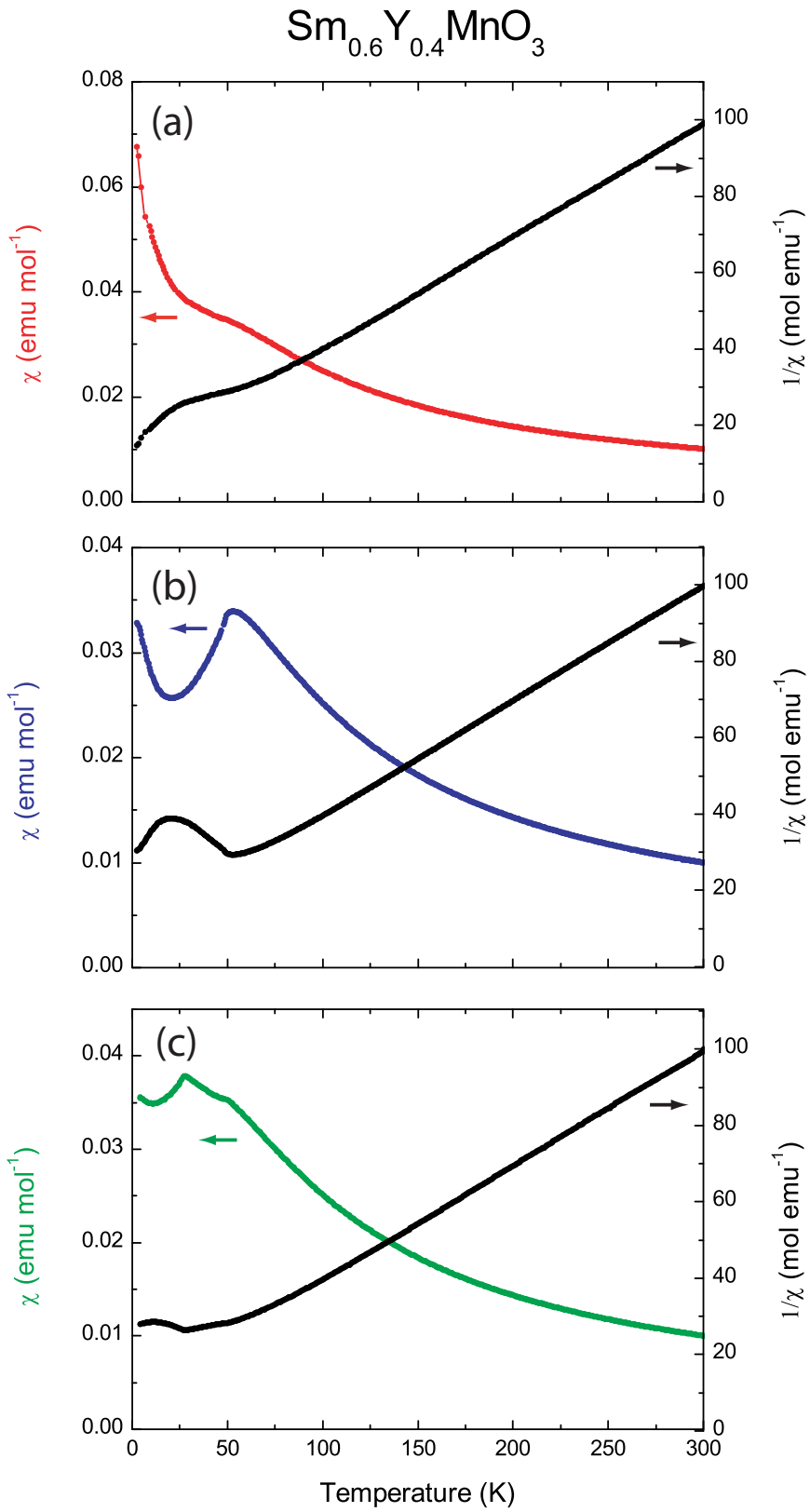

Figure 4.15: Field cooled magnetic susceptibility and inverse susceptibility for $Sm_{0.6}Y_{0.4}MnO_3$, along the (a) *a*-, (b) *b*-, and (c) *c*-axis. Measured in an applied magnetic field of 0.5 T

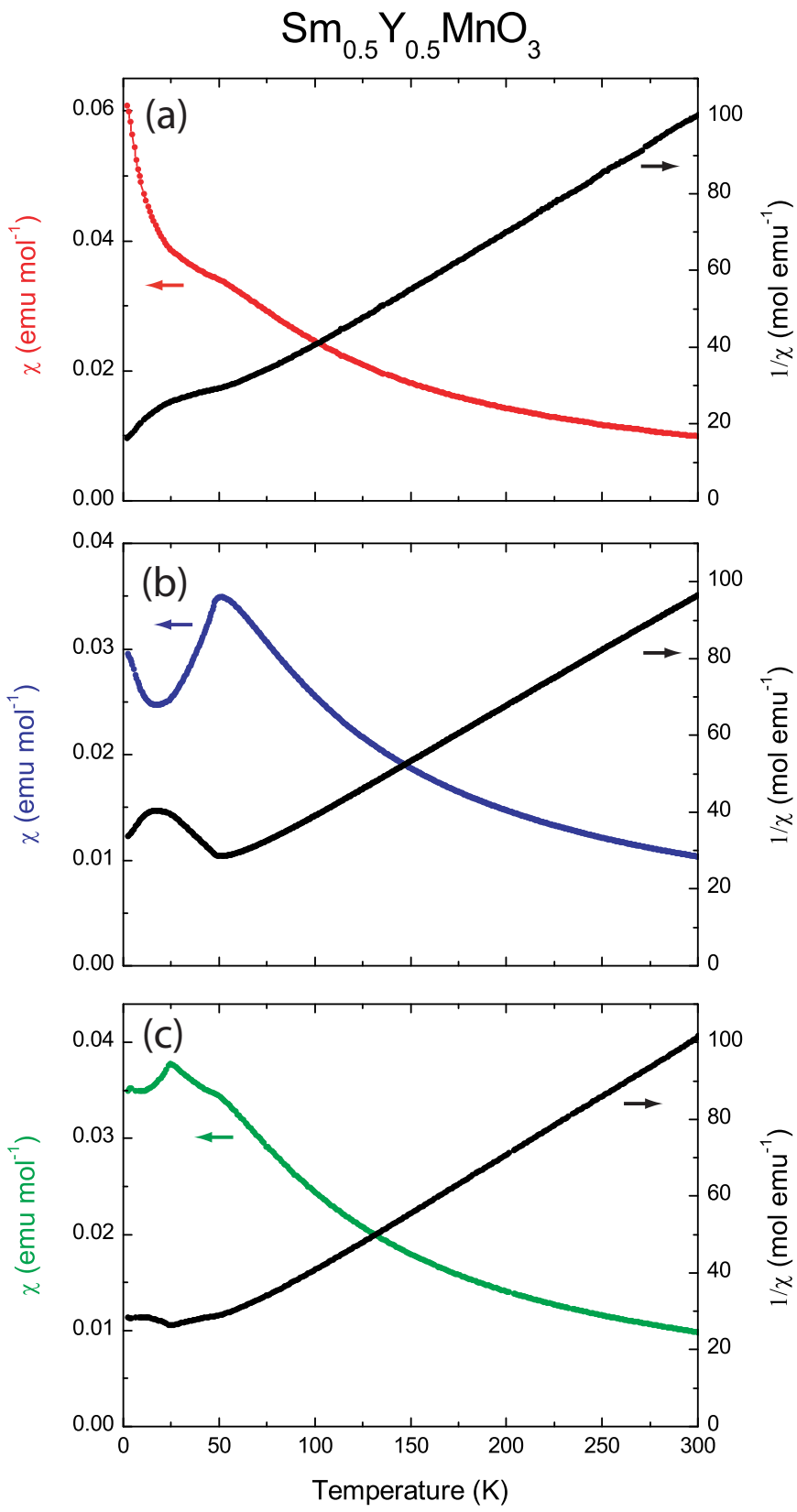

Figure 4.16: Field cooled magnetic susceptibility and inverse susceptibility for $Sm_{0.5}Y_{0.5}MnO_3$, along the (a) *a*-, (b) *b*-, and (c) *c*-axis. Measured in an applied magnetic field of 0.5 T

4.2.3 Magnetisation

The magnetisation data for $Sm_{0.6}Y_{0.4}MnO_3$ and $Sm_{0.5}Y_{0.5}MnO_3$ are shown in Figures 4.17 and 4.18, respectively. As with the susceptibility data, there is little qualitative difference between the magnetisation data of the two compounds, but the magnitudes are smaller for $Sm_{0.5}Y_{0.5}MnO_3$, where less Sm is present. A saturation point is not seen along any axis, which is unlike the behaviour of $TbMnO_3$ where there is a saturation of the Tb moments with $H//a$. From Equation 2.7, and the angular momentum values for Sm ($S = 5/2$, $L = 5$, $J = 5/2$), the saturation magnetisation for the Sm ions in $Sm_{0.6}Y_{0.4}MnO_3$ and $Sm_{0.5}Y_{0.5}MnO_3$ were calculated as 0.43 μ_B and 0.36 μ_B, respectively. The saturation magnetisation for the Mn ($J = 2$) ions is 4 μ_B for both compounds. The largest magnetisation responses are seen at 1.5 K with $H//a = 10$ T (the maximum field applied in these measurements), and are ~0.9 μ_B/f.u. for $Sm_{0.6}Y_{0.4}MnO_3$, and ~0.75 μ_B/f.u. for $Sm_{0.5}Y_{0.5}MnO_3$. It is clear that there is a magnetisation response from both the Sm and the Mn sites, since these values are larger than the saturation magnetisation of Sm^{3+} alone. This is expected for an applied magnetic field as large as 10 T. The difference between the maximum values measured for $Sm_{0.6}Y_{0.4}MnO_3$ and $Sm_{0.5}Y_{0.5}MnO_3$ is larger than that expected if the only difference between the compounds was the contribution from the Sm site. It therefore follows that the Y doping has an effect on the magnetisation of the Mn sublattice, as well as the Sm sublattice. This is not surprising, when considering the difference between the magnetic properties of the Mn sublattice in $SmMnO_3$ (A-type antiferromagnet) and $YMnO_3$ (geometrically frustrated antiferromagnet [89]). By comparison, in $TbMnO_3$ the sharp increase in the magnetisation with $H//a$ is understood to be due to the Tb ions (Section 3.3). However, since the magnetic order from individual ions can not be separated for a magnetisation measurement, it is unclear whether the features observed are due to the Sm or Mn moments.

Features are seen in the magnetisation data at 1.5 K with $H//b$ and $H//c$, although they are not as distinct as those in $TbMnO_3$. In order to understand the nature of these features, it is useful to compare the magnetisation data with the magnetic field dependences of the electric properties of $Sm_{0.6}Y_{0.4}MnO_3$ and

$Sm_{0.5}Y_{0.5}MnO_3$ (Sections 4.2.5 and 4.2.6). With $H//c$ over a similar range (0 − 9 T), significant changes are seen in the dielectric constant and polarisation. It is therefore believed that the application of a magnetic field along this direction causes a reorientation of the Mn moments (this is discussed further in Section 4.3). For $H//b$, no significant changes are seen in the temperature dependence of the dielectric constant, implying that a magnetic field applied along this direction does not result in a significant change in the order of the Mn moments.

Since the metamagnetic transitions seen along the b-axis of $TbMnO_3$ are assumed to be due to the Tb moments (Section 3.3) [31], the weaker magnetic moment of Sm (as well as the smaller molar proportion of Sm ions) is thought to be the reason for the less distinct transitions observed for $Sm_{0.6}Y_{0.4}MnO_3$ and $Sm_{0.5}Y_{0.5}MnO_3$. It is a significant result if there is indeed a weaker coupling between the rare earth moments and Mn moments in $Sm_{1-x}Y_xMnO_3$, since the strong coupling between Tb and Mn moments is important to the nature of the magnetoelectric properties in $TbMnO_3$.

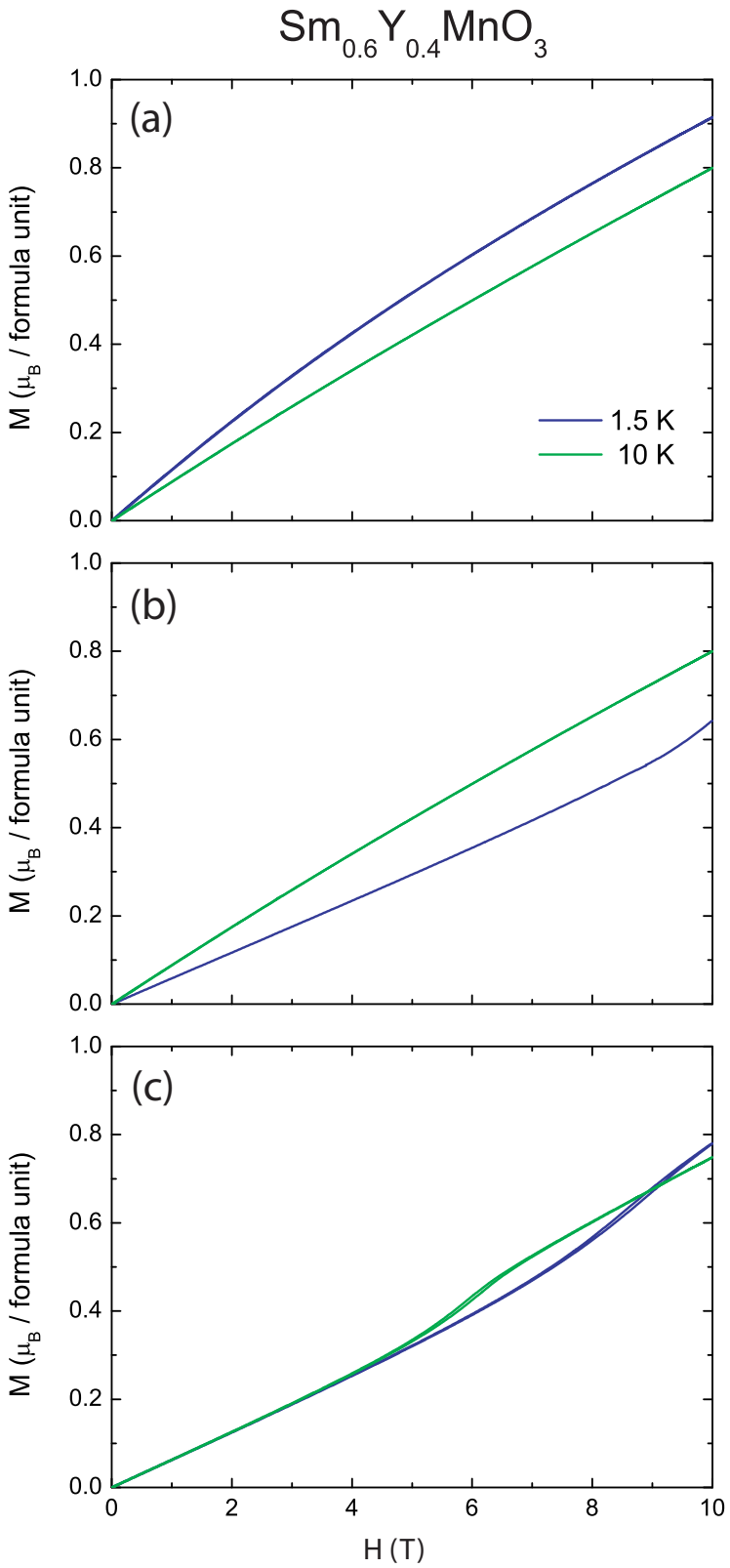

Figure 4.17: Magnetisation versus magnetic field along the (a) *a*-, (b) *b*- and (c) *c*-axis of $Sm_{0.6}Y_{0.4}MnO_3$.

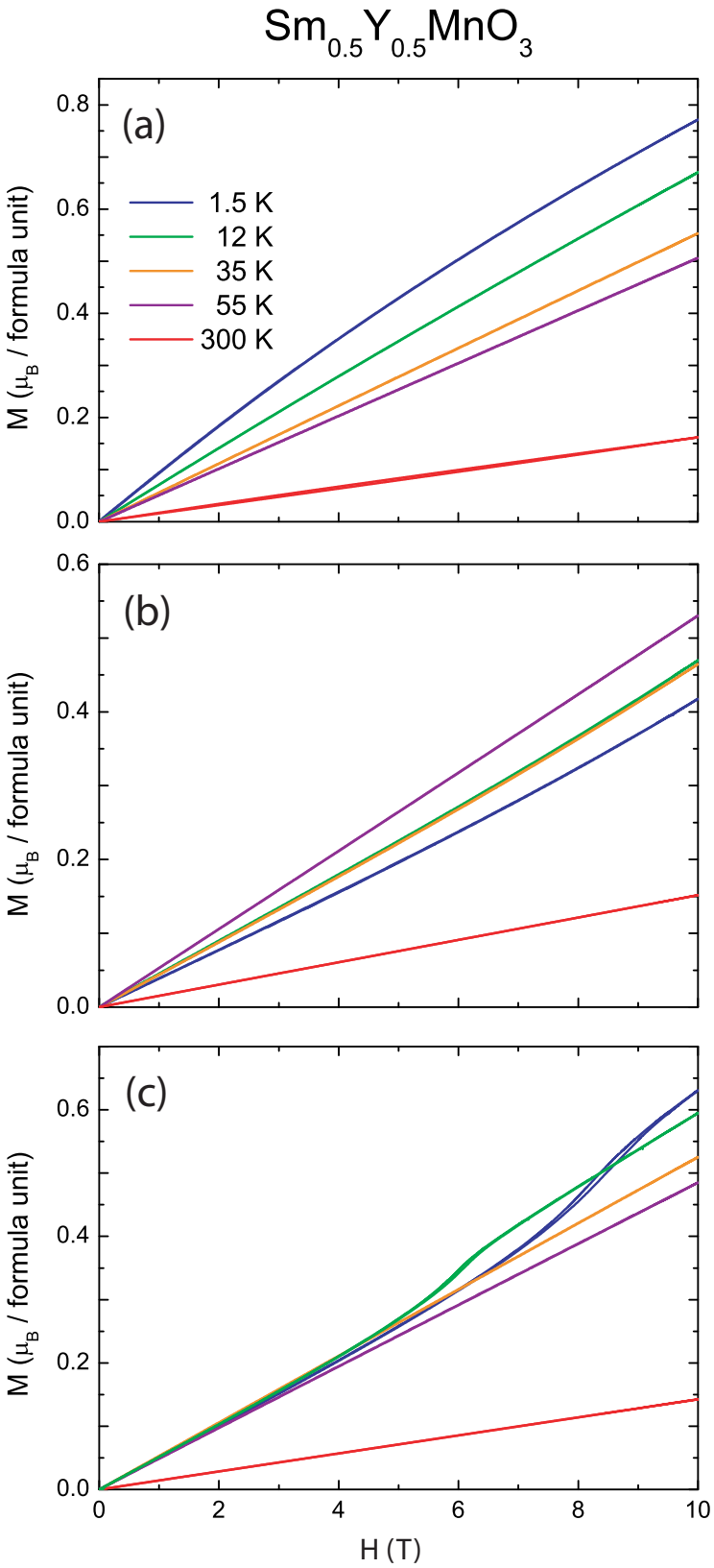

Figure 4.18: Magnetisation versus magnetic field along the (a) *a*-, (b) *b*- and (c) *c*-axis of $Sm_{0.5}Y_{0.5}MnO_3$.

4.2.4 Heat capacity

The heat capacity data for $Sm_{0.6}Y_{0.4}MnO_3$ and $Sm_{0.5}Y_{0.5}MnO_3$ show 3 distinct peaks, corresponding to the features seen in the magnetic susceptibility along the c-axis (Figure 4.19). The respective temperatures at which these features are seen shall from now on be referred to as T_{N1}, T_{N2} and T_{N3}, with $T_{N1} > T_{N2} > T_{N3}$. Similar heat capacity properties are also found in $TbMnO_3$ (Section 3.4 and Ref. [7]). By comparison, the published heat capacity data for $SmMnO_3$ show only one peak, at T_N=58 K, corresponding to the A-type antiferromagnetic ordering of the Mn moments [29]. It is assumed that the peaks at T_{N1} and T_{N2} correspond to ordering temperatures of the Mn^{3+} moments. More detailed experiments (e.g. using neutrons or synchrotron X-ray scattering) are needed to verify the magnetic structure.[1] The peak at T_{N3} is assumed to be due to a low temperature ordering of the Sm moments, by analogy with $TbMnO_3$. This peak is quite broad for both compounds, which implies short-range order between the Sm^{3+} moments (a sharp peak in heat capacity data would be expected if long-range order was present). The peaks at T_{N2} for both compounds are less pronounced than the corresponding peak in $TbMnO_3$.

The magnetic contribution to the heat capacity for both $Sm_{0.6}Y_{0.4}MnO_3$ and $Sm_{0.5}Y_{0.5}MnO_3$ was isolated by subtracting the heat capacity data of a phonon blank compound. $LaGaO_3$ was used as a phonon blank, since it has a similar molecular mass and crystal structure to the $Sm_{1-x}Y_xMnO_3$ compounds, and contains no magnetic ions. To account for the slightly different molecular masses between $LaGaO_3$ and the $Sm_{1-x}Y_xMnO_3$ compounds, the temperature values for the $LaGaO_3$ data were normalised by multiplying by the ratio of the effective Debye temperatures of the two compounds [76]. Equation 3.4 was altered to account for the shared Sm, Y site:

$$\frac{\Theta_D(Sm_{1-x}Y_xMnO_3)}{\Theta_D(LaGaO_3)} = \left[\frac{(M_{La})^{\frac{3}{2}} + (M_{Ga})^{\frac{3}{2}} + 3(M_O)^{\frac{3}{2}}}{(1-x)(M_{Sm})^{\frac{3}{2}} + x(M_Y)^{\frac{3}{2}} + (M_{Mn})^{\frac{3}{2}} + 3(M_O)^{\frac{3}{2}}}\right]^{\frac{1}{3}} \quad (4.2)$$

where Θ_D is the Debye temperature and M is the molecular mass of each atom.

[1] An issue with performing neutron scattering experiments on the $Sm_{1-x}Y_xMnO_3$ compounds is the large neutron absorption cross-section of Sm, as discussed in the following chapter.

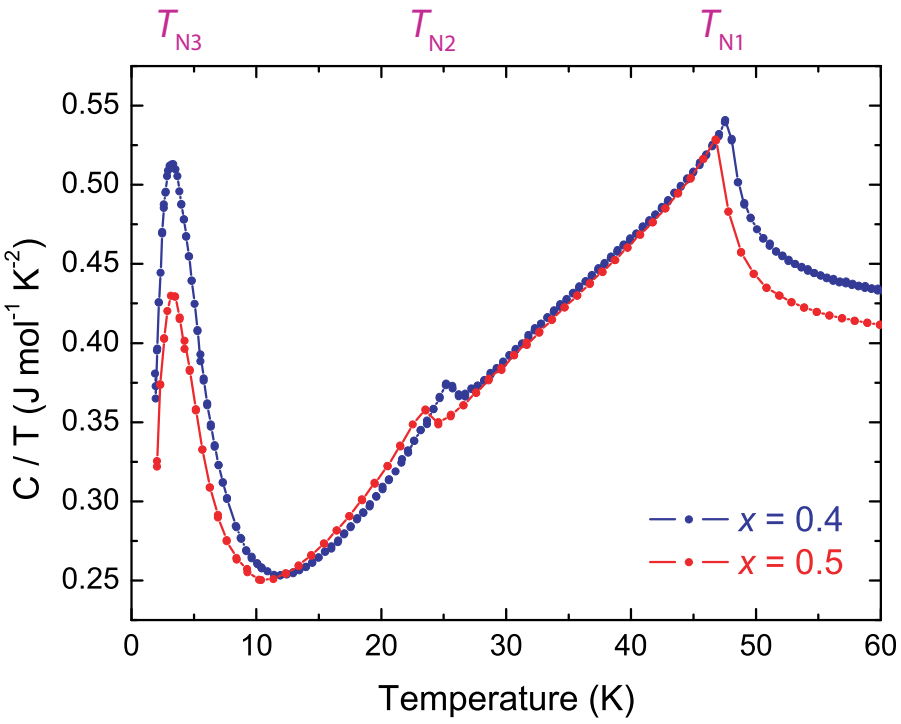

Figure 4.19: Heat capacity/temperature versus temperature for single crystal $Sm_{0.6}Y_{0.4}MnO_3$ and $Sm_{0.5}Y_{0.5}MnO_3$, in zero applied magnetic field

The Debye correction factors for $LaGaO_3$were 1.06 and 1.08 for $Sm_{0.6}Y_{0.4}MnO_3$ and $Sm_{0.5}Y_{0.5}MnO_3$, respectively.[2]. The heat capacity values for $LaGaO_3$ were also scaled by a factor of 1.04 in order to match those of the $Sm_{1-x}Y_xMnO_3$ compounds at high temperature (where only a lattice contribution is expected). It possible that this correction needed to be made for $Sm_{1-x}Y_xMnO_3$ (and not $TbMnO_3$) because the assumption of a similar lattice contribution from $LaGaO_3$ breaks down due to the large difference in molecular mass between La (138.91) and Y (88.906). The correction to the $LaGaO_3$ data only has a small impact on the results presented below. Figure 4.20 shows the lattice subtraction for $Sm_{0.6}Y_{0.4}MnO_3$ and $Sm_{0.5}Y_{0.5}MnO_3$. There is still a finite magnetic heat capacity (C_{mag}) for both compounds up to ~100 K above T_{N1}, as found for $TbMnO_3$ (Figure 3.12), but the magnitude of C_{mag} drops much quicker by comparison.

Integration of the magnetic heat capacity data with respect to temperature gives the magnetic entropy in the system. Prior to integration, the values of C_{mag} corresponding to the overlap between the $Sm_{1-x}Y_xMnO_3$ and $LaGaO_3$ data

[2]The Debye factors are greater than one for the $Sm_{1-x}Y_xMnO_3$ compounds since they have a lower molecular mass than $LaGaO_3$. The opposite is true for $TbMnO_3$

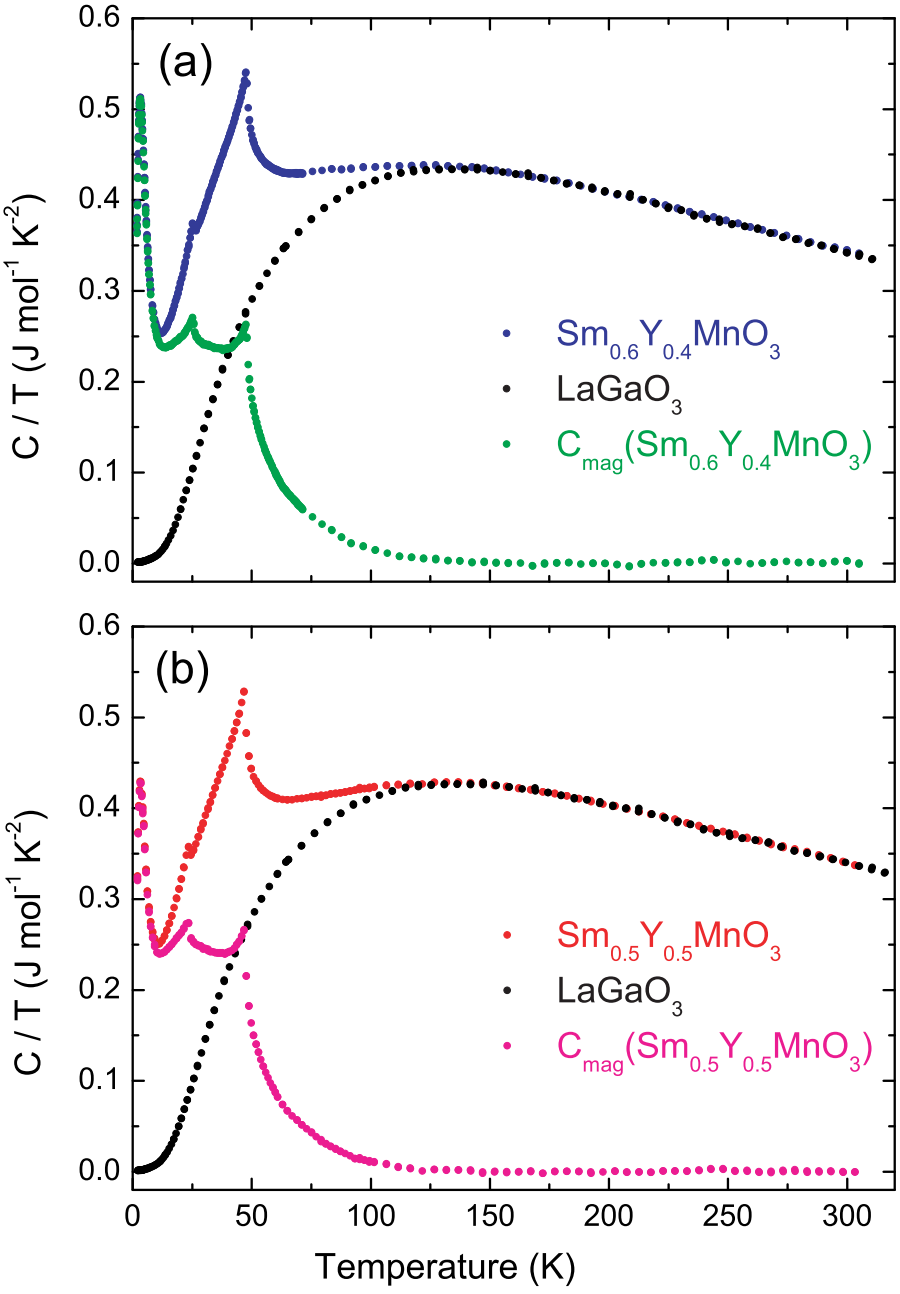

Figure 4.20: Heat capacity data for single crystal (a) $Sm_{0.6}Y_{0.4}MnO_3$ and (b) $Sm_{0.5}Y_{0.5}MnO_3$ and a phonon blank of $LaGaO_3$ in zero applied magnetic field. C_{mag} represents the magnetic heat capacity, calculated as $C(Sm_{1-x}Y_xMnO_3 - C(LaGaO_3)$

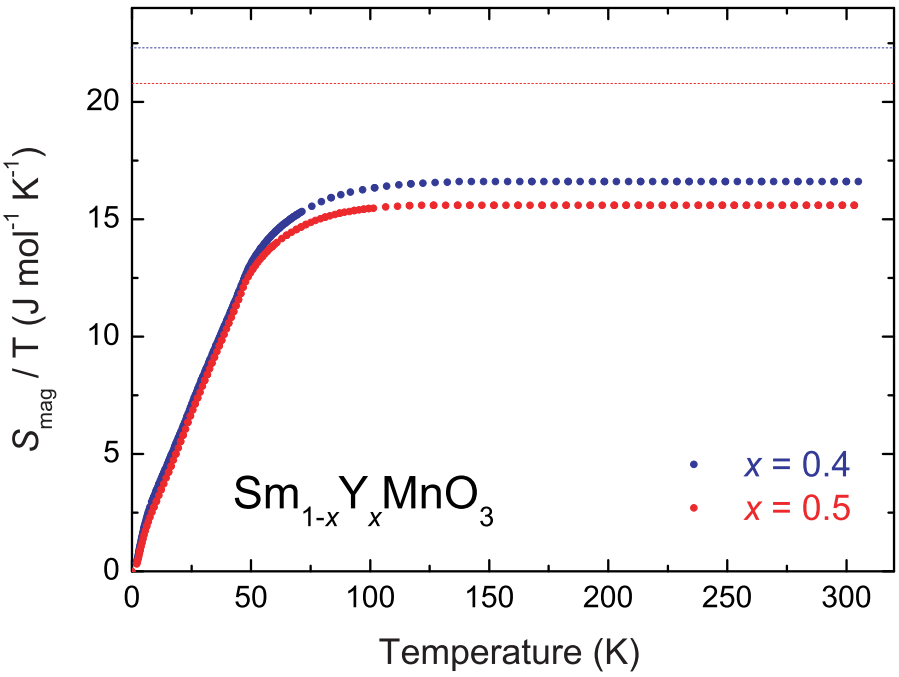

Figure 4.21: Magnetic entropy as a function of temperature for $Sm_{0.6}Y_{0.4}MnO_3$ and $Sm_{0.5}Y_{0.5}MnO_3$. The dotted lines represent the expected total magnetic entropy for each compound

were set to zero. For $Sm_{0.6}Y_{0.4}MnO_3$, C_{mag} was set to zero above 140 K, and for $Sm_{0.5}Y_{0.5}MnO_3$, C_{mag} was set to zero above 125 K. The magnetic entropy data for the $Sm_{1-x}Y_xMnO_3$ compounds are shown in Figure 4.21, reaching maximum values of 16.6 J mol^{-1} K^{-1} for $Sm_{0.6}Y_{0.4}MnO_3$, and 15.6 J mol^{-1} K^{-1} for $Sm_{0.5}Y_{0.5}MnO_3$.

The expected total magnetic entropy for each compound is determined by adapting Equation 2.11:

$$S_{mag}(Sm_{1-x}Y_xMnO_3) = (1-x)R\ln[2J(Sm)+1] + R\ln[2J(Mn)+1] \quad (4.3)$$

where $J(Sm) = 5/2$ and $J(Mn) = 2$. The expected S_{mag} values for $Sm_{0.6}Y_{0.4}MnO_3$ and $Sm_{0.5}Y_{0.5}MnO_3$ are 22.3 J mol^{-1} K^{-1} and 20.8 J mol^{-1} K^{-1}, respectively, as shown by the dotted lines on Figure 4.21. The magnetic entropy measured for each compound is therefore not enough to account for the expected values.

In order to determine the reason for the lower than expected entropy, the peaks in the magnetic heat capacity were separated and integrated individually. For the peak at T_{N3}, a data point was added at zero temperature, zero heat capacity, to include the region beyond the practical measurement range. Integrating this peak

(assumed to be due to the Sm ordering) gives entropy values of 3.6 J mol^{-1} K^{-1} and 3.3 J mol^{-1} K^{-1} for the $Sm_{0.6}Y_{0.4}MnO_3$ and $Sm_{0.5}Y_{0.5}MnO_3$ compounds, respectively. The expected Sm magnetic contributions are 8.9 J mol^{-1} K^{-1} in $Sm_{0.6}Y_{0.4}MnO_3$ and 7.5 J mol^{-1} K^{-1} in $Sm_{0.5}Y_{0.5}MnO_3$, far higher than those measured. Integrating the peaks at T_{N2} and T_{N1} (assumed to be from Mn order) gives $S_{mag} = 13.0$ J mol^{-1} K^{-1} for $Sm_{0.6}Y_{0.4}MnO_3$ and 12.3 J mol^{-1} K^{-1} for $Sm_{0.5}Y_{0.5}MnO_3$, which are reasonably close to the expected value of 13.4 J mol^{-1} K^{-1}.

The observation of a broad peak in the heat capacity data at T_{N3}, and the fact that the magnetic entropy is lower than expected below this temperature give evidence which points towards clustering of Sm atoms, but the data do not provide conclusive proof. Alternative possible explanations are a smaller than expected magnetic moment, or the Sm order is not confined to temperatures below T_{N3}, and that additional Sm magnetic entropy is found at higher temperatures. If this is indeed the case, it would imply that a lower than expected Mn contribution is also present, since the entropy given by the peaks at T_{N1} and T_{N2} could not be solely assigned to Mn order. In $TbMnO_3$, the link between the magnetic order of the Tb moments and the Mn moments is key to the metamagnetic transitions with $H//b$ and the resultant electric polarisation flop. The different behaviour of the Sm moments is therefore interesting when describing the dielectric constant and electric polarisation, and their magnetic field dependence, as discussed in the following sections.

	A (mm^2)	d (mm)
$Sm_{0.6}Y_{0.4}MnO_3$		
$E//a$	6.02	3.56
$E//b$	9.65	2.22
$E//c$	7.90	2.71
$Sm_{0.5}Y_{0.5}MnO_3$		
$E//a$	4.84	0.92
$E//b$	7.08, 3.91*	0.63
$E//c$	5.41	0.91

Table 4.5: Crystal dimensions of $Sm_{0.6}Y_{0.4}MnO_3$ and $Sm_{0.5}Y_{0.5}MnO_3$ used for dielectric measurements (* the crystal piece for $Sm_{0.5}Y_{0.5}MnO_3$ $E//b$ broke in two after the $H//a$ measurement, the $H//b$, c measurements were carried out with the smaller piece).

4.2.5 Dielectric properties

One of the most interesting properties seen in multiferroic materials is the ability to change the direction of the electric polarisation with an applied magnetic field (or vice versa). Such behaviour is key to Type-II multiferroics, therefore it was important to test for the presence of such magnetoelectric coupling in the $Sm_{1-x}Y_xMnO_3$ single crystals. Electric properties measurements were taken with a purpose-built sample insert for a Quantum Design PPMS, as described in Section 2.6. The dielectric constant was measured as a function of temperature for $Sm_{0.6}Y_{0.4}MnO_3$ and $Sm_{0.5}Y_{0.5}MnO_3$ in the presence of magnetic fields up to 9 T. The magnetic and electric fields could each be applied along the three principal crystallographic axes, giving 9 permutations of sample configuration (Figures 4.22 and 4.23).

$Sm_{0.6}Y_{0.4}MnO_3$ and $Sm_{0.5}Y_{0.5}MnO_3$ show very similar dielectric properties, and so are discussed together below. The main differences between the dielectric data for the two compounds are the slightly lower value of T_{N2} for $Sm_{0.5}Y_{0.5}MnO_3$ (as expected from the heat capacity measurements shown in Figure 4.19), and the smaller magnitude of the dielectric constant for $Sm_{0.5}Y_{0.5}MnO_3$ with $E//a$ and $E//b$. It should be noted that the measurements presented for $Sm_{0.5}Y_{0.5}MnO_3$ were with a refined sample preparation method, as detailed in Section 2.8. Three separate single crystal pieces were used for $Sm_{0.5}Y_{0.5}MnO_3$ measurements, whereas one piece was used for $Sm_{0.6}Y_{0.4}MnO_3$. The electrode area, A, and sample thick-

ness, d, for each measurement configuration are shown in Table 4.5.

The dielectric constant as a function of temperature shows large anisotropy between the a, b and c-axes. Features in the dielectric constant develop along the a- and c-axes at T_{N2}, implying a coupling between the magnetic and electric properties (Figure 4.24). The zero-field features are similar to those previously published for $TbMnO_3$ [31], but the behaviour under an applied magnetic field is markedly different, as discussed below.

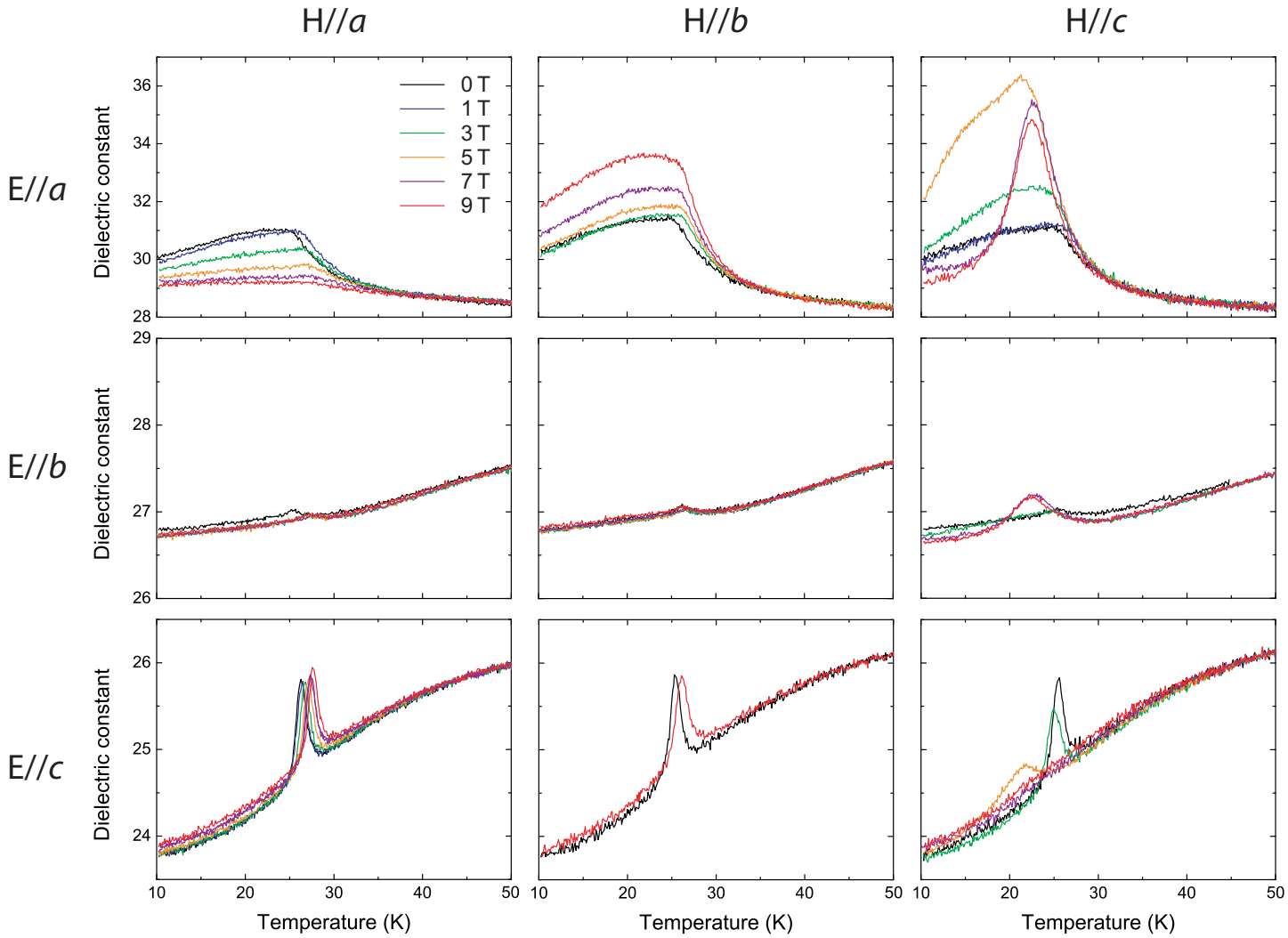

Figure 4.22: Temperature dependence of the dielectric constant of $Sm_{0.6}Y_{0.4}MnO_3$, with electric and magnetic fields applied along the principal crystallographic axes. Measured at 10 kHz.

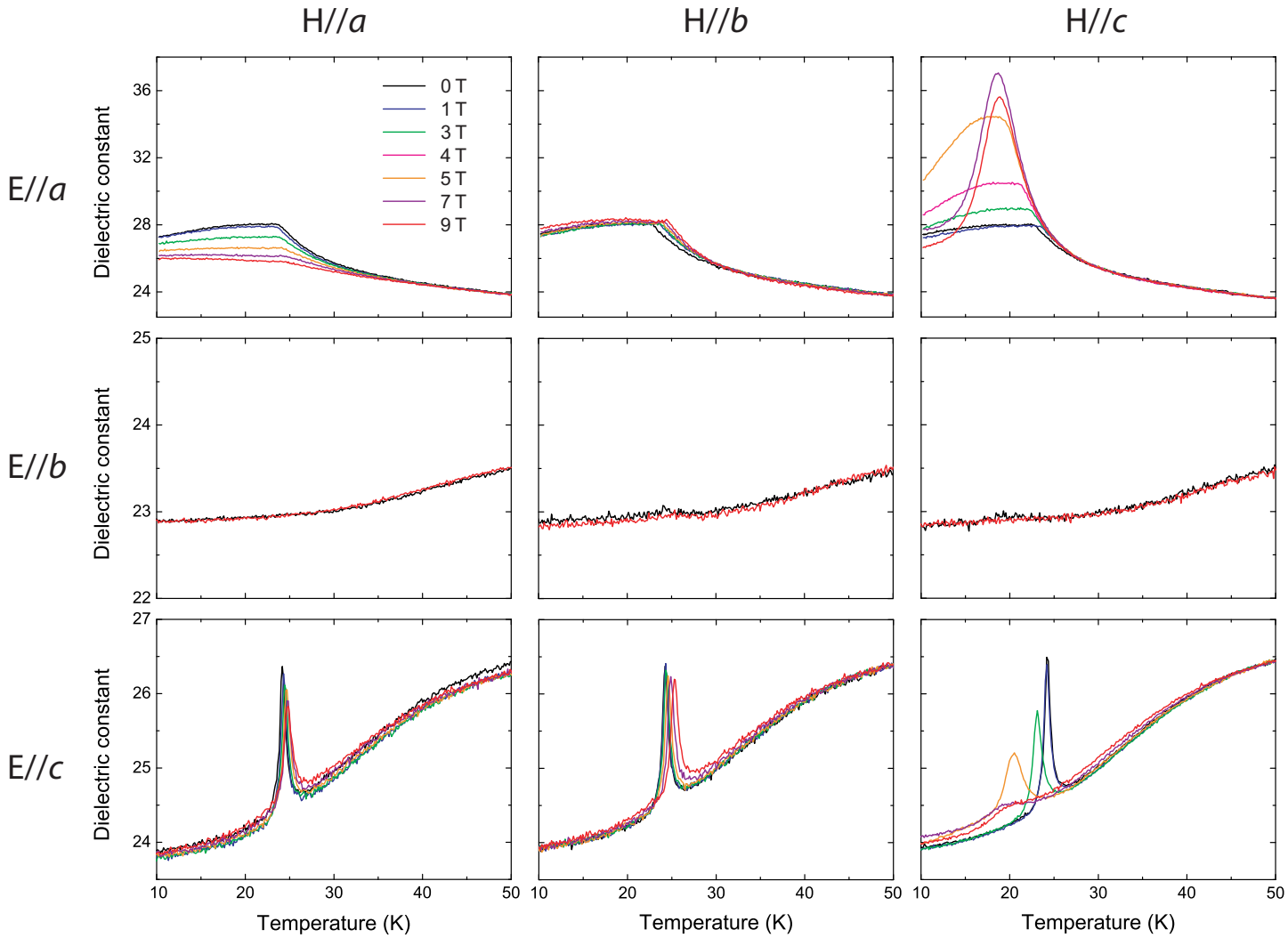

Figure 4.23: Temperature dependence of the dielectric constant of $Sm_{0.5}Y_{0.5}MnO_3$, with electric and magnetic fields applied along the principal crystallographic axes. Measured at 10 kHz.

4.2.5.1 $E//a$

The broad feature in the dielectric constant below T_{N2} is gradually smeared out with increasing $H//a$. No significant change is seen for $H//b$ in $Sm_{0.5}Y_{0.5}MnO_3$, but a steady increase in the size of the feature is seen in $Sm_{0.6}Y_{0.4}MnO_3$. The most interesting behaviour occurs with $H//c$, where the broad feature becomes a more pronounced peak as the magnetic field is increased, with the maximum amplitude occurring around 5 T for $Sm_{0.6}Y_{0.4}MnO_3$ and 7 T for $Sm_{0.5}Y_{0.5}MnO_3$.

4.2.5.2 $E//b$

No features are seen in the dielectric constant along the b-axis for $Sm_{0.5}Y_{0.5}MnO_3$, and only a very small peak is seen for $Sm_{0.6}Y_{0.4}MnO_3$. These features are assumed to be due to a small degree of crystal twinning between the a- and b-axes, which have lattice parameters close to one another in the orthorhombic $RMnO_3$ perovskites. The likelihood of twinning is evidenced by the behaviour of the feature in $E//b$ for $Sm_{0.6}Y_{0.4}MnO_3$ showing a similar response under $H//c$ as for $E//a$. Otherwise, applying a magnetic field up to 9 T along each crystallographic axis causes no change in the dielectric constant in this direction.

4.2.5.3 $E//c$

The sharpest peak in the dielectric constant is measured along the c-axis, and occurs at T_{N2}. No significant changes are seen in this peak when applying a magnetic field parallel to the a- and b-axes, but for a small decrease in the peak magnitude, and shift in temperature of $\sim$2 K with $H = 9$ T. As with $E//a$, the most significant change is seen with $H//c$. As the field is increased, there is a gradual decrease in the peak temperature up to 5 K by 9 T, by which point the peak has been nearly completely suppressed.

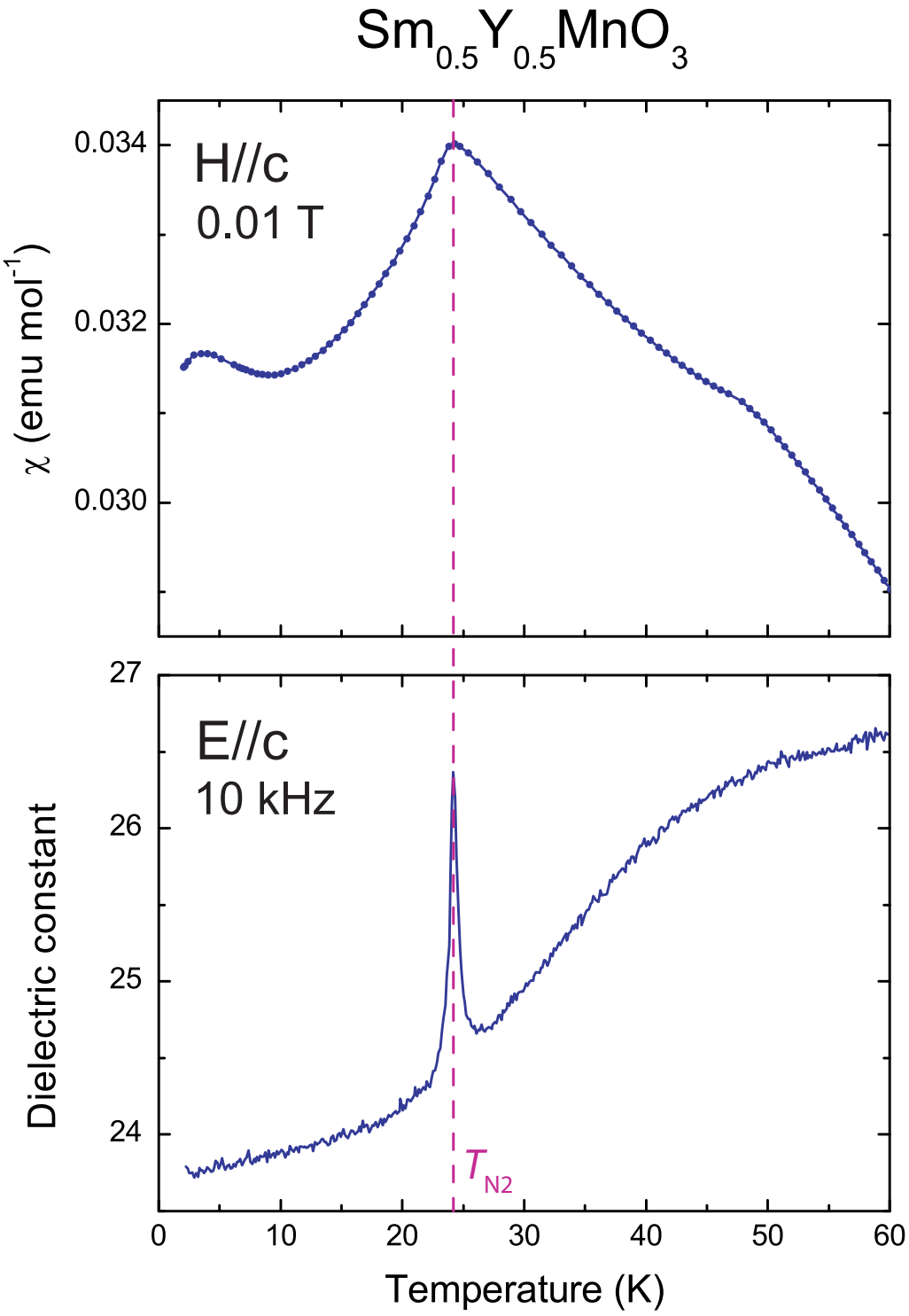

Figure 4.24: Comparison of magnetic and dielectric data as a function of temperature along the c-axis of a $Sm_{0.5}Y_{0.5}MnO_3$ single crystal, showing a coincident phase transition at T_{N2}~24 K

4.2.6 Electric polarisation

Following the study of the magnetic field dependence of the dielectric constant for $Sm_{0.6}Y_{0.4}MnO_3$ and $Sm_{0.5}Y_{0.5}MnO_3$, the next step was to measure the electric polarisation along the *a*- *b*- and *c*-axes. The polarisation was measured using the technique outlined in Section 2.8. Polarisation measurements were also taken with a magnetic field applied along the *c*-axis, since this field direction was found to give the largest changes in the dielectric constant behaviour. Due to the amount of time needed to take measurements of the electric polarisation, magnetic fields were not applied along the other crystal directions. It is important to note that the magnitudes of the polarisation presented below have not been calibrated against a standard material. The pyroelectric current measurement technique is not used for standard ferroelectrics, which exhibit much larger polarisations and have transition temperatures much higher than those of Type-II multiferroics. Since taking the measurements of electric polarisation for $Sm_{0.6}Y_{0.4}MnO_3$, the measurement technique was further refined and improved as detailed in Section 2.8. The data for $Sm_{0.5}Y_{0.5}MnO_3$ shown here represent the slightly improved quality of the data due to the technique refinement.

The zero field electric polarisation data for $Sm_{0.6}Y_{0.4}MnO_3$ are shown in Figure 4.25. It can be seen that a large electric polarisation develops along the *c*-axis, with only small polarisation magnitudes seen along the other two crystal directions. The magnitude of the electric polarisation measured along the *c*-axis is $\sim$160 μC m^{-2} at 10 K. Using the improved measurement technique outlined in Section 2.8, a polarisation of 270 μC m^{-2} was measured at 10 K for $Sm_{0.5}Y_{0.5}MnO_3$ (Figure 4.27).

As with the dielectric constant data, applying a magnetic field along the *c*-axis was found to show significant changes to the polarisation along the *a*- and *c*-axes, with no real change along the *b*-axis (Figure 4.26). The polarisation along the *c*-axis, P_c, was found to greatly decrease with increasing magnetic field, becoming almost zero at 9 T. P_a increased approximately four-fold upon the application of a magnetic field of 9 T along the *c*-direction, although the magnitude is still only 13% of that of P_c at zero field. The temperature dependence of the dielectric con-

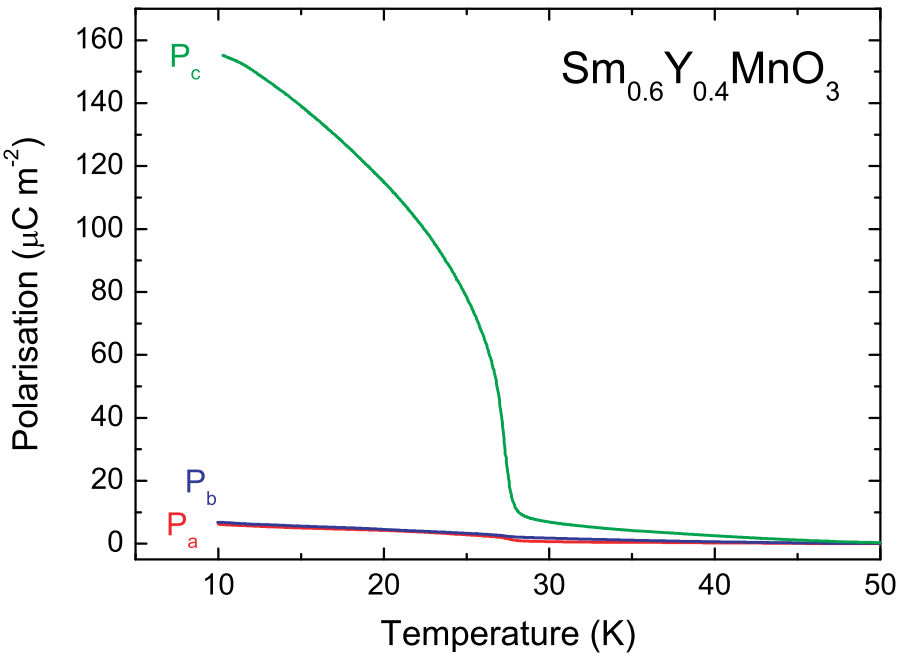

Figure 4.25: Temperature dependence of the electric polarisation of $Sm_{0.6}Y_{0.4}MnO_3$, measured along the principal crystallographic axes in zero magnetic field.

stant and electric polarisation of $Sm_{0.6}Y_{0.4}MnO_3$ and $Sm_{0.5}Y_{0.5}MnO_3$ show very similar properties to those of $TbMnO_3$, with a peak in the dielectric constant and an electric polarisation seen along the c-axis in each compound. The most significant difference between the different materials is the effect of applying magnetic field. In the $Sm_{1-x}Y_xMnO_3$ compounds, the application of a magnetic field along the c-axis causes the greatest change in the electric properties, suppressing both the peak in the dielectric constant and the electric polarisation along the c-axis. By comparison, in $TbMnO_3$ these changes occur with $H//b$. Also, with $E//c$ in $TbMnO_3$ an additional peak appears in the dielectric constant at low temperature - at T_{N3} for 5 T. This peak moves to higher temperatures (towards the peak at T_{N2}) as the magnetic field is increased. If the magnetic order of the Tb moments at T_{N3} is responsible - directly or indirectly - for this additional peak, the lack of such behaviour in $Sm_{0.6}Y_{0.4}MnO_3$ and $Sm_{0.5}Y_{0.5}MnO_3$ can possibly be linked to the absence of a metamagnetic transition with a field applied in this direction (Figures 4.17 and 4.18). The magnitude of the electric polarisation in $Sm_{0.5}Y_{0.5}MnO_3$ is just over 50% of the magnitude of that in $TbMnO_3$ ($\sim$520 μC m^{-2} in Ref. [31]).

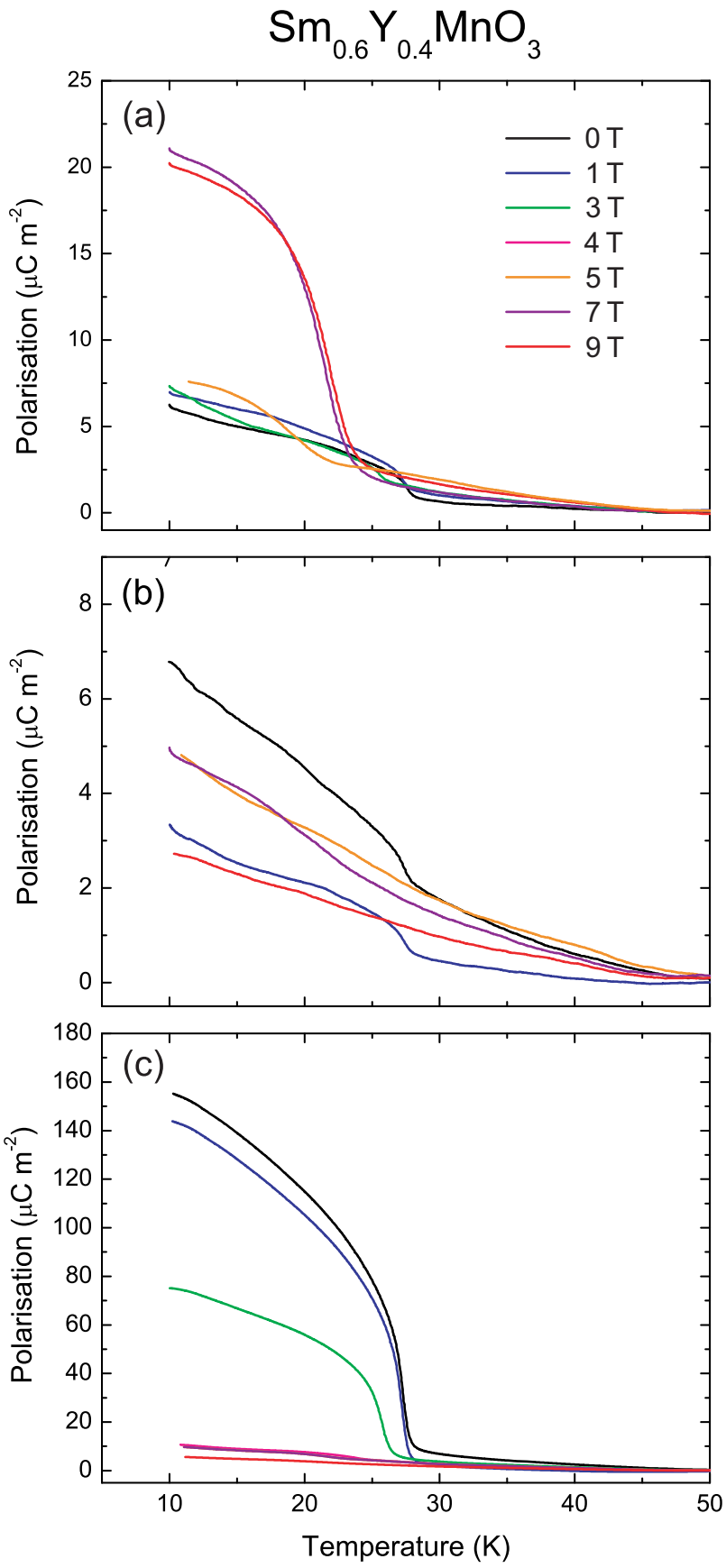

Figure 4.26: Electric polarisation along the (a) *a*-, (b) *b*- and (c) *c*-axis of $Sm_{0.6}Y_{0.4}MnO_3$, with magnetic fields applied parallel to the *c*-axis.

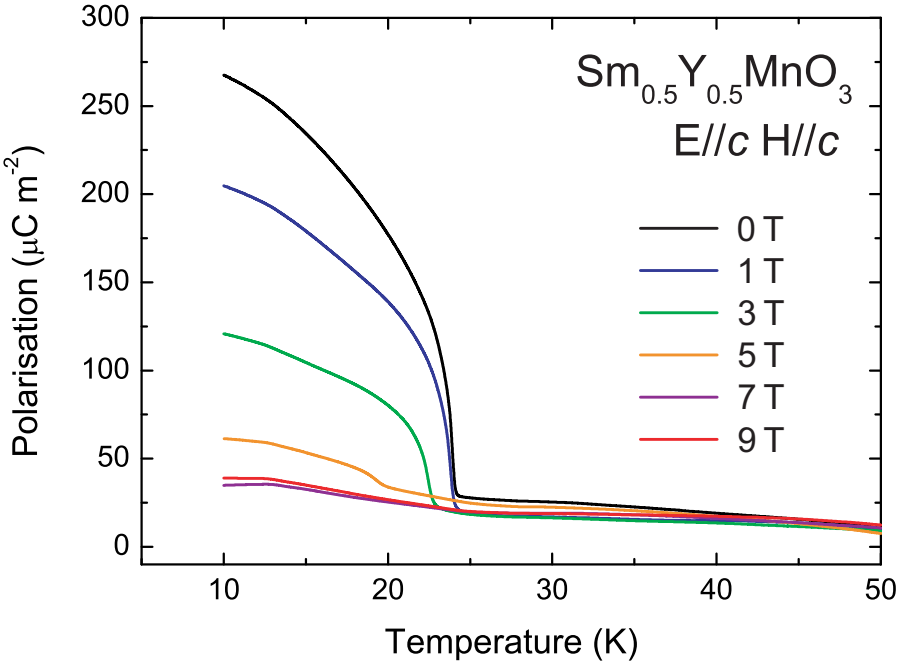

Figure 4.27: Temperature dependence of the electric polarisation along the c-axis of $Sm_{0.5}Y_{0.5}MnO_3$, with magnetic fields applied parallel to the c-axis.

4.3 Discussion

The results obtained for the electric polarisation in zero magnetic field suggest a similar structure of the Mn moments as that found in $TbMnO_3$, i.e. a cycloidal structure with the spins in the b-c plane and propagating along the b-axis. This model would account for the similarities in the susceptibility data between $Sm_{1-x}Y_xMnO_3$ and $TbMnO_3$, and agrees with the theoretical prediction of the polarisation direction given by Equation 1.6. However, bulk crystal data alone are not sufficient to confirm such a magnetic structure model. The magnitude of the electric polarisation measured is ∼50% of that found in $TbMnO_3$ and ∼23% of that in $Eu_{0.6}Y_{0.4}MnO_3$ [31, 59], but 13 times that seen in $Gd_{0.9}Y_{0.1}MnO_3$ [56]. It is not currently known if this difference in magnitude is partly due to the measurement technique.

There is a similar dependence of the electric polarisation on the applied magnetic field seen for $Sm_{0.6}Y_{0.4}MnO_3$ and $Eu_{0.6}Y_{0.4}MnO_3$. The electric polarisation in $Sm_{0.6}Y_{0.4}MnO_3$ is parallel to the c-axis in zero field, and applying the magnetic field parallel to the c-axis causes a suppression of this polarisation. The magnetic field also causes an increase in the electric polarisation along the a-axis to a value

which is ∼13% that of the zero field polarisation along c. Conversely, the electric polarisation in $Eu_{0.6}Y_{0.4}MnO_3$ is parallel to the a-axis in zero field, and applying a magnetic field parallel to the a-axis causes a suppression of this polarisation. The magnetic field also causes an increase in the polarisation along the c-axis to a value which is ∼21% that of the zero field polarisation along a [58].

By analogy with the theory and experimental results discussed in Section 1.6 [32, 34], a polarisation switch from the c- to the a-axis implies that the magnetic state of $Sm_{1-x}Y_xMnO_3$ has been changed. According to the discussion by Mostovoy [35], the magnetic spiral will change orientation under a sufficient magnetic field, with the spins then rotating about the magnetic field direction. Assuming this is the case for $Sm_{0.6}Y_{0.4}MnO_3$ and $Sm_{0.5}Y_{0.5}MnO_3$, a magnetic field applied along the c-axis would cause the spins to rotate about c, i.e. in the a-b plane (illustrated in Figure 4.28). Again referring to Equation 1.6, the result of this magnetic reorientation would be a change in the direction of the electric polarisation to the a-axis. An increase in the polarisation along the a-axis was indeed found with $H//c$, but of a much smaller magnitude than that of the polarisation along the c-axis in zero field. This result suggests two possible outcomes: a magnetic field of 9 T applied along the c-axis is enough to disrupt the b-c cycloid, but not sufficient to completely reorient the spins in the a-c plane; or the switching of the polarisation is strongly dependent on the coupling between the rare earth and the Mn moments in the RMnO$_3$ systems. With regards to the latter case, it is now known that there is a strong coupling between the Tb moments and the Mn moments in $TbMnO_3$ [36, 40, 41], and it is possible that this coupling cannot be replicated in a system such as $Sm_{0.5}Y_{0.5}MnO_3$, which has a smaller magnetic contribution from the rare earth site. In order to determine the precise nature of the magnetic field dependence, neutron diffraction and/or X-ray scattering experiments are required. Another observation made by Mostovoy is that the application of a field along the b-axis should result in an electric polarisation of zero, following the same logic. It is possible that the magnetic fields applied in these measurements were not sufficient to reorient the Mn moments into the a-c plane, and that at higher fields the polarisation could potentially go to zero.

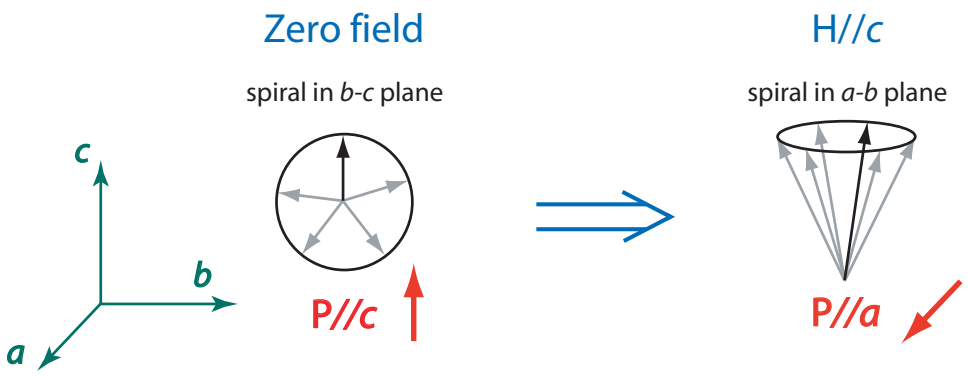

Figure 4.28: Proposed magnetic model for $Sm_{0.6}Y_{0.4}MnO_3$ and $Sm_{0.5}Y_{0.5}MnO_3$, showing the effect on the Mn moments of a magnetic field applied parallel to the c-axis

Mostovoy notes that this model of magnetoelectric behaviour does not apply to $TbMnO_3$, in which a magnetic field applied along the b-axis, rather than the c-axis, causes the polarisation flop. This is attributed to the strongly anisotropic magnetic moment of the Tb ions coupling with the Mn spins. The Tb moments have been found to order along the a-axis at the ferroelectric phase due to magnetic polarisation from the Mn moments [32, 41, 90]. It appears to be the case that a strong magnetic field along the b-axis reorients the Tb moments and changes Mn ordering from a b-c cycloid to an a-b cycloid - with a resultant change in the electric polarisation to the a-axis. The a-b cycloidal order of the Mn spins under $H//b$ was confirmed experimentally by Aliouane *et al.* [36], and indicates a strong magnetic coupling between the Tb and Mn moments. This argument does not appear to apply to the $Sm_{1-x}Y_xMnO_3$ compounds. The Sm^{3+} ions possess a relatively weak magnetic moment (μ_{eff}(Sm)$\sim$1.7 μ_B, μ_{eff}(Tb)$\sim$9.7 μ_B [15]), and due to the Y doping there is proportionally less Sm than Tb in the respective systems. In addition, the introduction of Y on the A-site of the compound will lead to interrupted exchange pathways between the magnetic ions. Therefore, the magnetic order of the Mn spins would not be expected to have such a strong dependence on the Sm moments. If the nature of the electric polarisation in $TbMnO_3$ is strongly dependent on the Tb order, the weak coupling between the Sm and Mn moments could also account for the weaker polarisation seen in $Sm_{1-x}Y_xMnO_3$ compared with that of $TbMnO_3$.

4.4 Conclusion

A detailed study of the bulk magnetic and electric properties of $Sm_{1-x}Y_xMnO_3$ has been presented. Doping $SmMnO_3$ with Y results in large changes to the magnetic properties, with an additional magnetic transition developing at T_{N2}~25 K for $x = 0.4$ and 0.5. This magnetic transition coincides with the onset of an electric polarisation, giving strong evidence for the existence of multiferroicity (Figure 4.29). Initial X-ray studies show the value of the Mn-O-Mn bond angle in $Sm_{1-x}Y_xMnO_3$ moving towards that of $TbMnO_3$ (~145°) with increasing x. The occurrence of local structural distortions in the Mn-O octahedra brought about by the Y doping appear to induce cycloidal magnetic order in $Sm_{1-x}Y_xMnO_3$, thereby giving rise to multiferroic properties. It is proposed that the Mn moments orient in a cycloid in the *b*-*c* plane at T_{N2}, which causes an electric polarisation to develop along the *c*-axis. Comparisons with theoretical predictions and the results found for $TbMnO_3$ appear to confirm this, but the magnetic structure cannot be conclusively deduced without further study.

Proposed phase diagrams for $Sm_{0.5}Y_{0.5}MnO_3$ are shown in Figure 4.30, showing the observed transitions and magnetic/electric phases. These phase diagrams illustrate the different magnetic field dependences of $TbMnO_3$ and $Sm_{0.5}Y_{0.5}MnO_3$.

Investigations of the exact nature of the magnetic order in the $Sm_{1-x}Y_xMnO_3$ compounds are essential in order to understand the magnetoelectric coupling mechanism. As a continuation of this study, powder neutron diffraction and X-ray resonant scattering experiments were carried out on $Sm_{1-x}Y_xMnO_3$, the results of which are presented in the following chapter.

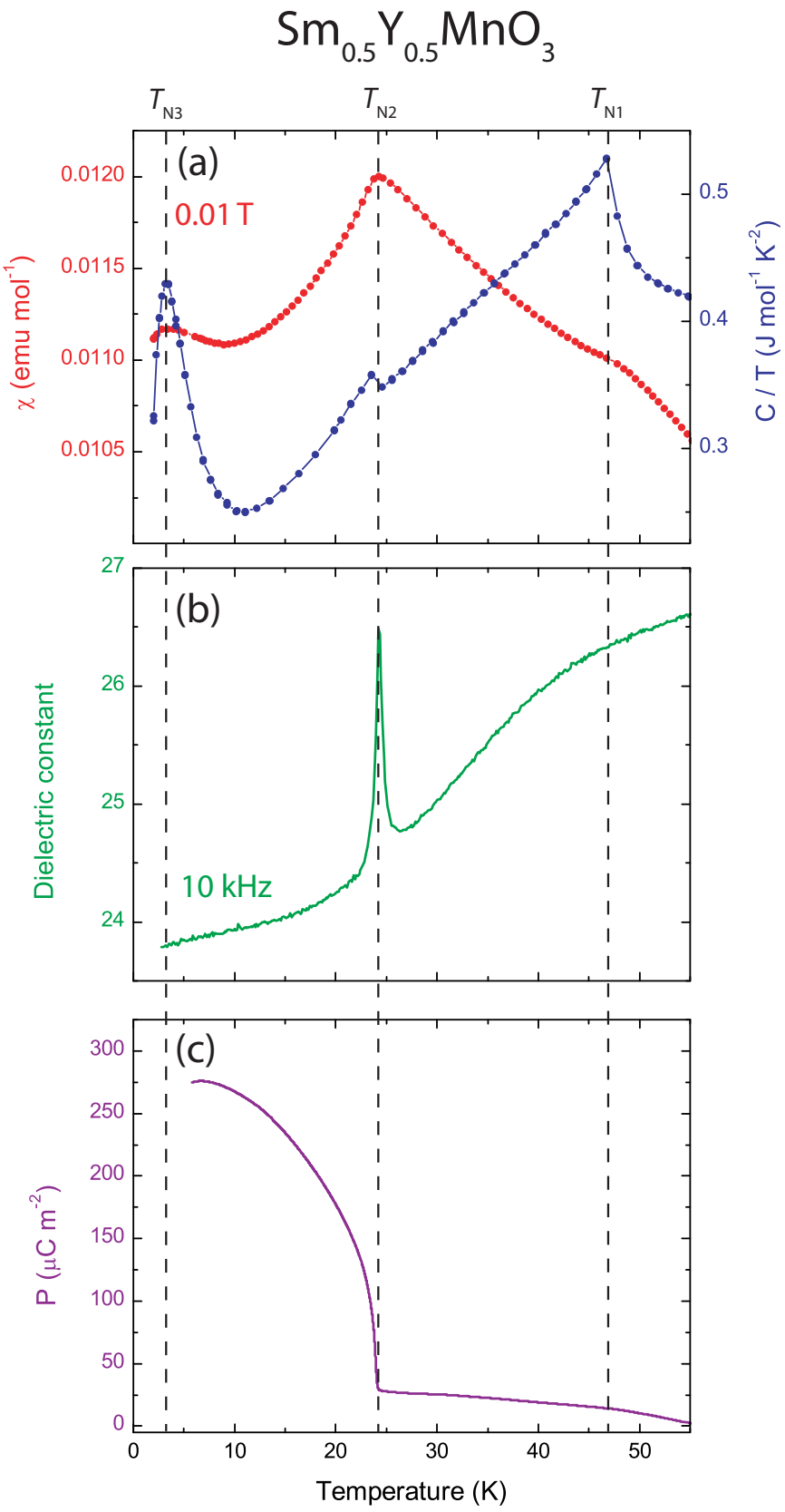

Figure 4.29: Temperature dependence of (a) magnetic susceptibility and heat capacity, (b) dielectric constant, and (c) electric polarisation for single crystal $Sm_{0.5}Y_{0.5}MnO_3$. All data except heat capacity measured along the *c*-axis.

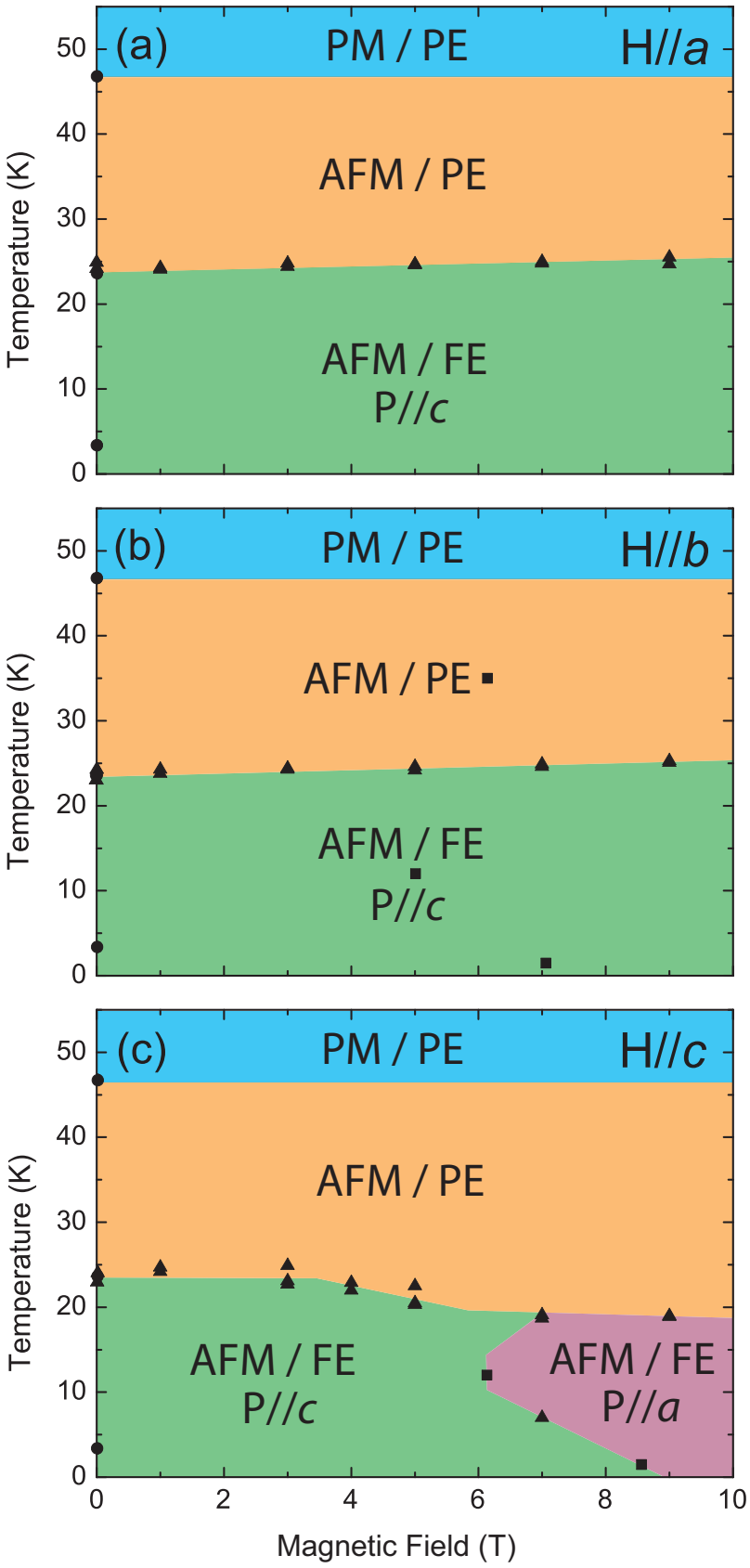

Figure 4.30: Phase diagram of $Sm_{0.5}Y_{0.5}MnO_3$ from this study, with magnetic field applied parallel to the (a) *a*-, (b) *b*- and (c) *c*-axis. Circles, squares and triangles represent transitions in heat capacity, magnetisation and dielectric constant data, respectively. PM = paramagnetic, AFM = antiferromagnetic, PE = paraelectric, FE = ferroelectric.

Chapter 5

Magnetic structure of $Sm_{1-x}Y_xMnO_3$

The interesting coupling between bulk magnetic and ferroelectric behaviour observed in $Sm_{1-x}Y_xMnO_3$ ($x = 0.4$, 0.5) were discussed in the previous chapter. The Y-doping on the Sm site is found to result in a new feature in the magnetic susceptibility and heat capacity, coinciding with a peak in the dielectric constant and electric polarisation along the c-axis. These properties are very similar to those found in $TbMnO_3$ and $DyMnO_3$ (Sections 1.4.2 and 1.4.4). However, applying a magnetic field to $Sm_{1-x}Y_xMnO_3$ has a different result on the electric properties when compared with $TbMnO_3$. In $TbMnO_3$, a cycloidal magnetic ordering of the Mn^{3+} moments induces ferroelectricity by breaking inversion symmetry [32, 34]. Since one of the effects of doping $SmMnO_3$ with Y is to change the Mn-O-Mn bond angle to a value similar to that of the multiferroic RMnO$_3$ compounds, it was important to determine if the Mn magnetic ordering that develops at $\sim$25 K in $Sm_{1-x}Y_xMnO_3$ (as indicated by magnetic susceptibility measurements) is also cycloidal in nature. It is also important to attempt to determine the cause of the magnetoelectric coupling seen in $Sm_{1-x}Y_xMnO_3$, and compare it with $TbMnO_3$. Two experiments were carried out with the aim of determining the magnetic structure of $Sm_{1-x}Y_xMnO_3$, one using neutron diffraction on the GEM instrument at ISIS, UK, and another using X-ray resonant scattering on the XMaS beamline at the European Synchrotron Radiation Facility (ESRF), France.

5.1 Neutron scattering from $SmMnO_3$ and $Sm_{0.6}Y_{0.4}MnO_3$

5.1.1 The GEM beamline (ISIS)

The GEneral Materials instrument is a neutron diffractometer which is used to determine the crystal structure and magnetic structure of materials, as well as performing structural studies on disordered materials such as glasses and amorphous metals [91]. GEM can detect scattered neutrons over a large range of scattering angles, with high resolution. Since magnetic Bragg peaks can be detected with GEM, the instrument can be used to observe changes in the magnetic structure of a sample brought about by changes in temperature or applied magnetic field.

The layout of the GEM diffractometer can be seen in Figures 5.1 and 5.2. There is a long incident path of 17 m, allowing the flight path and time-of-flight to be well defined. Before reaching the sample, the beam is collimated and a series of choppers define an incident wavelength range (typically 0.05 to 3.40 Å). The sample sits inside an evacuated sample tank surrounded by the detector banks. There are 8 banks of detectors on GEM, which allow a wide range of scattering angle, 2θ to be covered. This results in a large observable range of scattering vector Q, due to the relation $Q = 4\pi \sin\theta/\lambda$. The banks contain ZnS/^{6}Li scintillator detectors which are narrow in width, allowing a high Q resolution.

5.1.2 Experimental methods

The natural isotope of samarium is highly neutron absorbing, with an absorption cross section, σ_a of 5922(56) barns for thermal neutrons [92]. It is not practical to carry out a neutron diffraction experiment with compounds containing this isotope due to the extremely long counting times required to acquire a sufficient signal to noise ratio. Instead, an isotope enriched Sm_2O_3 starting powder containing ^{154}Sm ($\sigma_a = 8.4$ barns) was used to prepare samples of $SmMnO_3$ and $Sm_{0.6}Y_{0.4}MnO_3$ for work on GEM. Polycrystalline samples were prepared, since the cost of the isotope enriched samarium oxide meant that it was not possible to purchase enough for single crystal synthesis. The preparation procedure for these samples is given in Table 5.1.

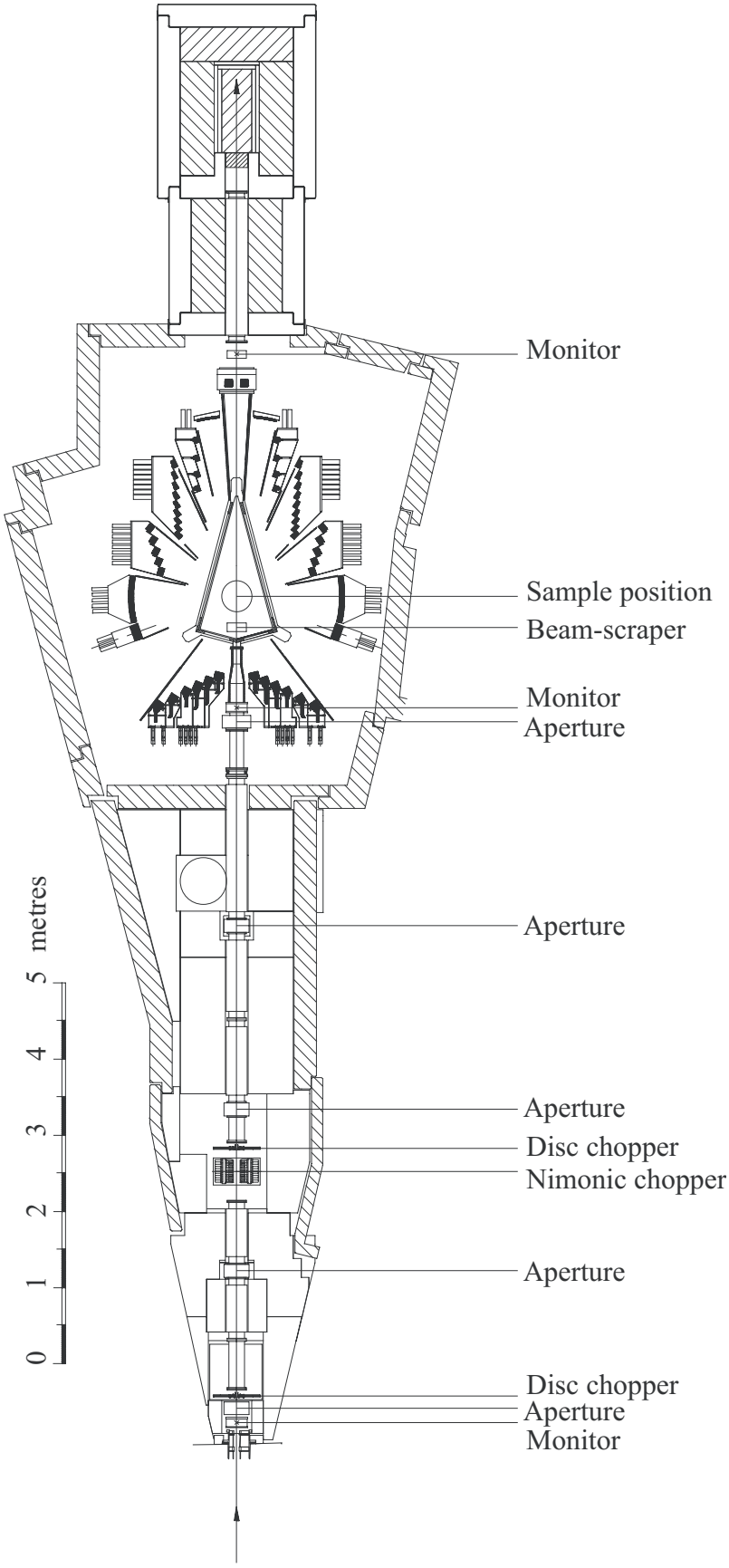

Figure 5.1: Schematic diagram of the GEM diffractometer [91].

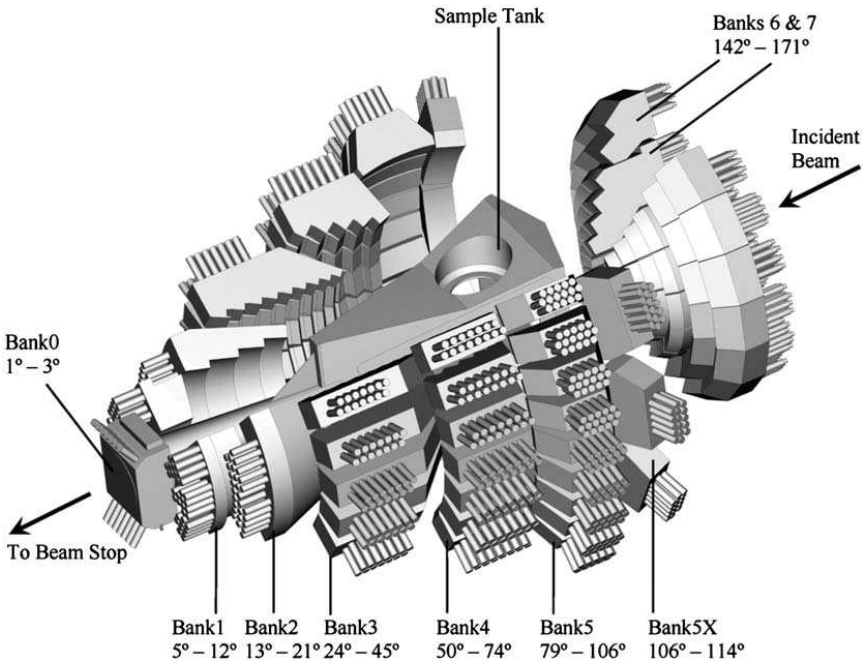

Figure 5.2: The arrangement of the detector banks on the GEM diffractometer [91].

To observe the temperature dependence of the magnetic order in $SmMnO_3$ and $Sm_{0.6}Y_{0.4}MnO_3$, diffraction scans were taken with GEM on ^{154}Sm isotope enriched powders, at a range of temperatures both below and above the respective magnetic transition temperatures of the two compounds. For $SmMnO_3$, scans were taken from base temperature (1.5 K) to 65 K, at intervals of 10 K (intervals of 4 K around $T_N \sim 58$ K). For $Sm_{0.6}Y_{0.4}MnO_3$, scans were taken from 1.5 K to 60 K, in intervals of 1.5 K. Longer scans with improved statistics were also taken at one temperature point in each different magnetic phase, including base temperature (1.5 K) and room temperature (300 K).

Rietveld refinement of the nuclear and magnetic structure of the two compounds was carried out using WinPLOTR in the FullProf Suite of programs [68, 69]. The diffraction data from banks 3, 4 and 5 were refined together, since these banks gave data which had the best balance between Q-resolution and count rate [91].

5.1.3 $SmMnO_3$ results

A comparison of the diffraction patterns obtained at 1.5 K and 300 K for $SmMnO_3$ can be seen in Figure 5.3. Since the 300 K data is far above the magnetic transition

Heating	Temperature (°C)	Duration (hours)	Comments
1	1100	4	(Y_2O_3 preheat)
2	1100	12	Sm_2O_3 (+ Y_2O_3) + MnO_2 mixture
3	1400	24	Sm_2O_3 (+ Y_2O_3) + MnO_2 mixture
4	1400	12	Sm_2O_3 (+ Y_2O_3) + MnO_2 mixture

Table 5.1: Sample heating procedure for synthesis of ^{154}Sm-enriched $SmMnO_3$ and $Sm_{0.6}Y_{0.4}MnO_3$. Comments in parentheses apply to the $Sm_{0.6}Y_{0.4}MnO_3$ compound only.

temperature, only nuclear Bragg peaks are seen. A Rietveld refinement of the 300 K pattern was carried out using the orthorhombic P*bnm* space group as a basis, the results of which can be seen in Table 5.2. The average Mn-O-Mn bond angle, ⟨Mn-O-Mn⟩, was calculated from a weighted average of the Mn-O1-Mn (×2) and the Mn-O2-Mn (×4) angles (this weighting is due to the arrangement of the oxygen octahedra in the crystal, as illustrated in Figure 4.5). The Mn-O-Mn bond angles determined from the fit to the data for $SmMnO_3$ are consistent with those published by Kimura *et al*. [29].[1] with an average value of 147.76(2)°. The lattice parameters and atomic positions determined for $SmMnO_3$ are similar to those published by Chen *et al*. (from refined XRD data) [82]. For comparison, the Mn-O-Mn bond angle of multiferroic $TbMnO_3$ was found to be 145.26(4)° by Alonso *et al* [83].

At 1.5 K, additional peaks are present in the diffraction pattern (most noticeably at ∼7.5 Å), which correspond to the magnetic order in $SmMnO_3$. The order in $SmMnO_3$ has been proposed by Kimura *et al*. to be that of an *A*-type antiferromagnet [29], so this model was used as a starting point for refinement of the magnetic structure. A good fit to the data was found for an *A*-type commensurate order with the spins oriented along the *b*-axis, as shown in Figure 5.4. The magnetic *R*-factors for the fits at 1.5 K were 1.06, 3.14 and 3.12, for banks 3, 4 and 5 respectively. An illustration of the *A*-type magnetic order proposed for $SmMnO_3$ is shown in Figure 5.6. This magnetic model was then used to fit the magnetic Bragg peaks as a function of temperature. The temperature dependence of the magnetic moment (Figure 5.5), shows the system has zero net magnetic moment

[1]The value of ϕ for $SmMnO_3$ given by Kimura *et al*. was interpolated from the values of the other members of the $RMnO_3$ series, taken from Ref. [83].

		$SmMnO_3$		$Sm_{0.6}Y_{0.4}MnO_3$	
		1.5 K	300 K	1.5 K	300 K
a (Å)		5.3584(6)	5.3548(6)	5.3118(5)	5.3141(5)
b (Å)		5.7959(6)	5.8131(7)	5.8290(6)	5.8432(5)
c (Å)		7.4608(8)	7.4771(9)	7.4047(7)	7.4219(7)
V (Å^3)		231.71(4)	232.75(5)	229.27(4)	230.46(4)
Sm/Y	4c (x y $\frac{1}{4}$)				
x		0.98588(19)	0.98531(19)	0.98397(16)	0.98383(13)
y		0.07339(14)	0.07426(13)	0.07870(11)	0.07918(9)
B (Å^2)		0.338(19)	0.60(2)	0.170(15)	0.385(15)
Mn	4b ($\frac{1}{2}$ 0 0)				
B (Å^2)		-0.01(3)	0.11(3)	0.03(3)	0.19(2)
O1	4c (x y $\frac{1}{4}$)				
x		0.0949(2)	0.0951(2)	0.10196(19)	0.10210(15)
y		0.4736(2)	0.4734(2)	0.46910(18)	0.46846(15)
B (Å^2)		0.22(2)	0.40(3)	0.23(2)	0.399(19)
O2	8d (x y z)				
x		0.70725(17)	0.70766(18)	0.70454(15)	0.70490(12)
y		0.32114(16)	0.32176(16)	0.32497(13)	0.32540(11)
z		0.04729(12)	0.04736(12)	0.05004(10)	0.05023(8)
B (Å^2)		0.242(16)	0.442(19)	0.232(14)	0.414(13)
Mn-O1-Mn, ϕ_1 (×2)		148.294(3)	148.209(3)	145.729(2)	145.676(2)
Mn-O2-Mn, ϕ_2 (×4)		147.59(5)	147.53(5)	145.92(4)	145.84(3)
$\langle\phi\rangle$		147.82(2)	147.76(2)	145.86(1)	145.79(1)
R_{wp}		5.28	3.74	6.76	4.50
		5.89	4.29	5.03	4.15
		6.63	4.59	5.42	4.55
Bragg R-factor		3.14	4.22	2.20	2.23
		3.53	5.92	2.27	2.15
		3.88	4.87	2.37	2.26
Magnetic R-factor		1.06	-	7.10	-
		3.14	-	3.98	-
		3.12	-	5.03	-

Table 5.2: Refined unit cell, atomic position and thermal parameters for $SmMnO_3$ and $Sm_{0.6}Y_{0.4}MnO_3$ (space group Pbnm for both compounds), where B is the isotropic temperature factor. The three values for each reliability factor are from the refinement of the data from banks 3, 4 and 5, respectively.

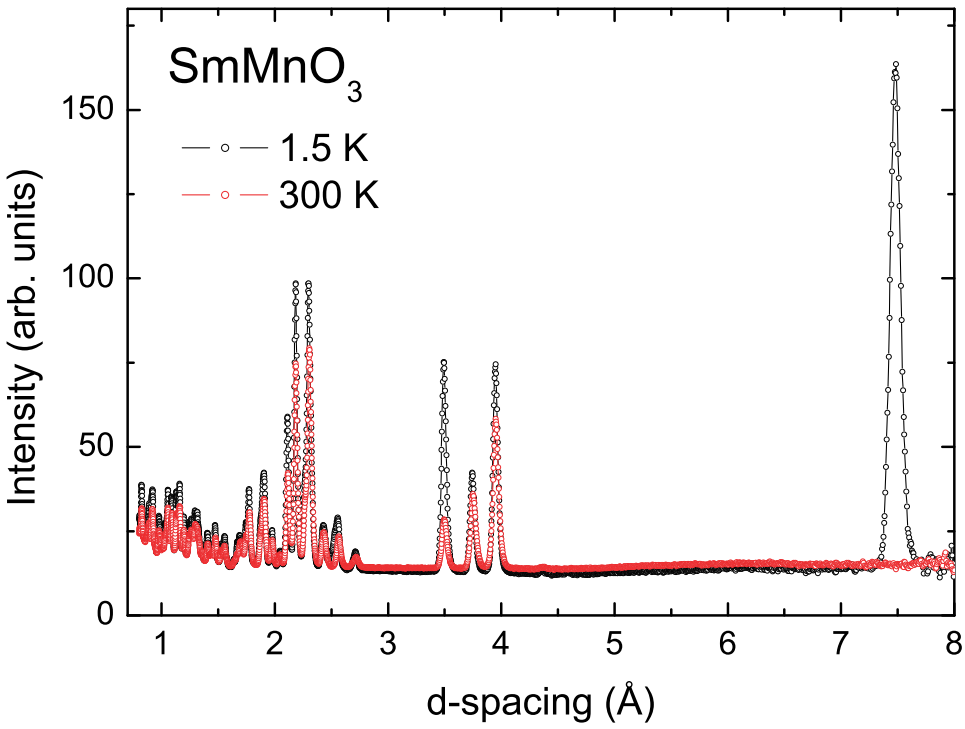

Figure 5.3: GEM diffraction patterns from bank 3 for $SmMnO_3$, taken at 1.5 K and 300 K

(i.e. is in the paramagnetic state) at ∼57 K, as implied by the susceptibility data shown in Figure 4.12. The values for the magnetic moment are fixed to zero at temperatures when magnetic Bragg peaks can no longer be seen in the diffraction patterns. As expected, the magnetic moment value increases with decreasing temperature, as the magnetic disorder due to thermal energy is reduced.

5.1.4 $Sm_{0.6}Y_{0.4}MnO_3$ results

As with $SmMnO_3$, the crystal structure of $Sm_{0.6}Y_{0.4}MnO_3$ was fitted to an orthorhombically distorted perovskite structure represented by the space group P*bnm*. As can be seen in Table 5.2, the *a* and *c* lattice parameters are smaller as a result of the Y doping, whilst the *b* lattice parameter is larger. Also, the atomic positions are shifted, with a change in the tilting of the MnO_6 octahedra. This is quantified by the ⟨Mn-O-Mn⟩ bond angle of 145.79(1)° seen for $Sm_{0.6}Y_{0.4}MnO_3$, a value very close to that of $TbMnO_3$ and thus in the bond angle range shown by the shaded region in Figure 1.20.

It can be seen from Figure 5.7 that the magnetic peaks present at 1.5 K in $Sm_{0.6}Y_{0.4}MnO_3$ are different to those found in $SmMnO_3$. In order to model the

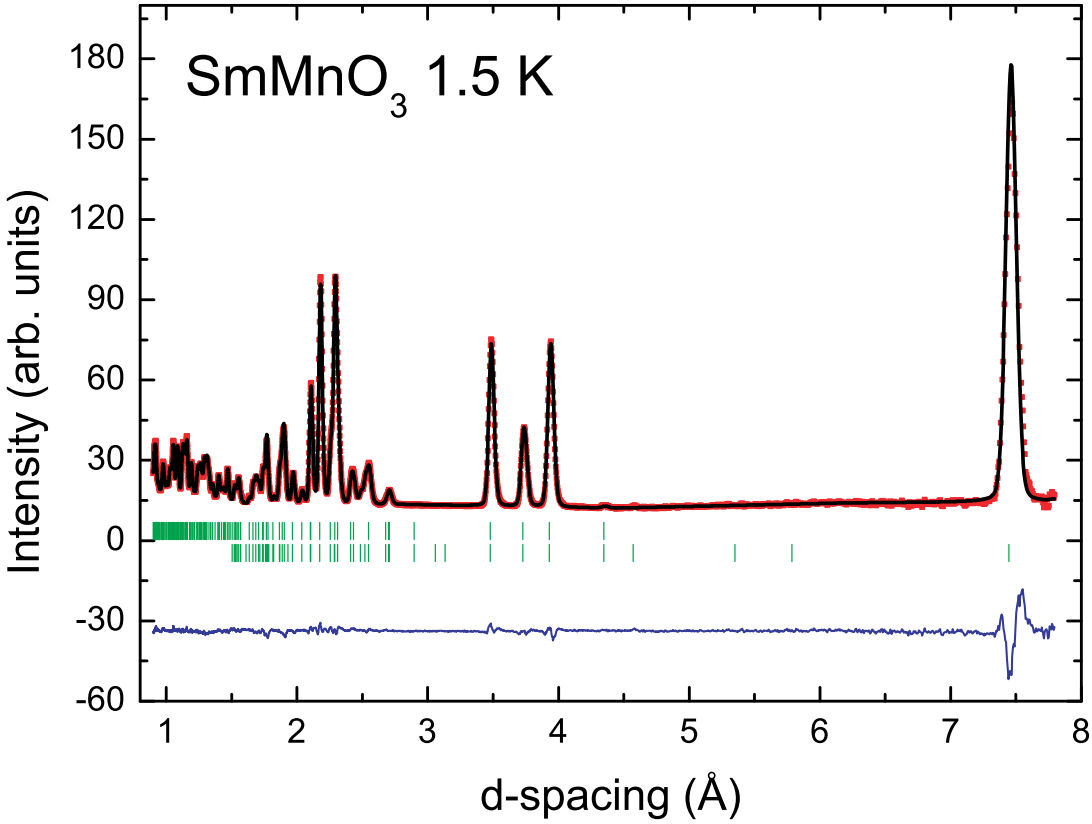

Figure 5.4: Fitted data for $SmMnO_3$ at 1.5 K, from bank 3 of GEM. The red points shows the data, the black line is the fit to the data, and the blue line underneath shows the difference between the two. The upper and lower green ticks represent nuclear and magnetic Bragg reflections, respectively.

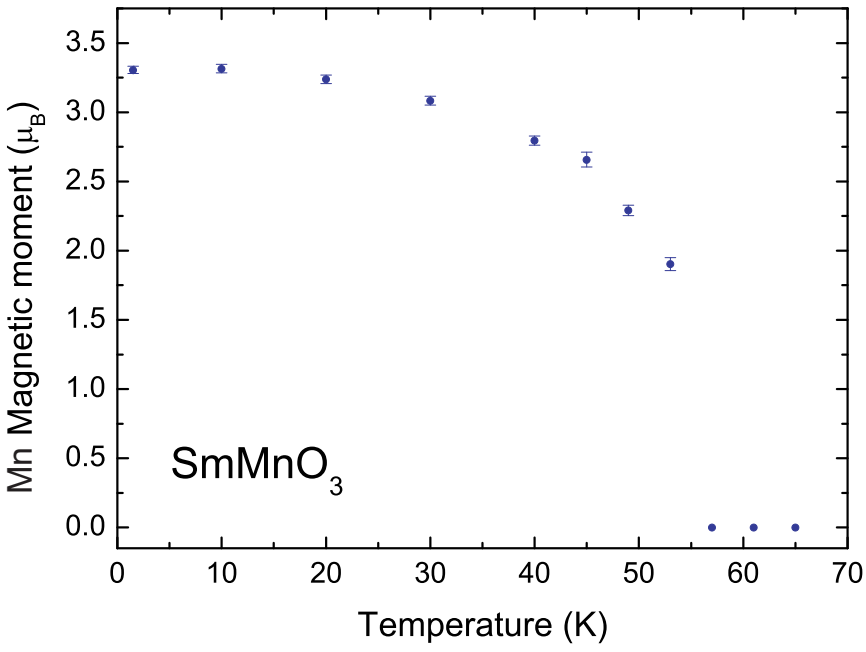

Figure 5.5: Temperature dependence of the Mn magnetic moment magnitude in $SmMnO_3$, along the *b*-axis.

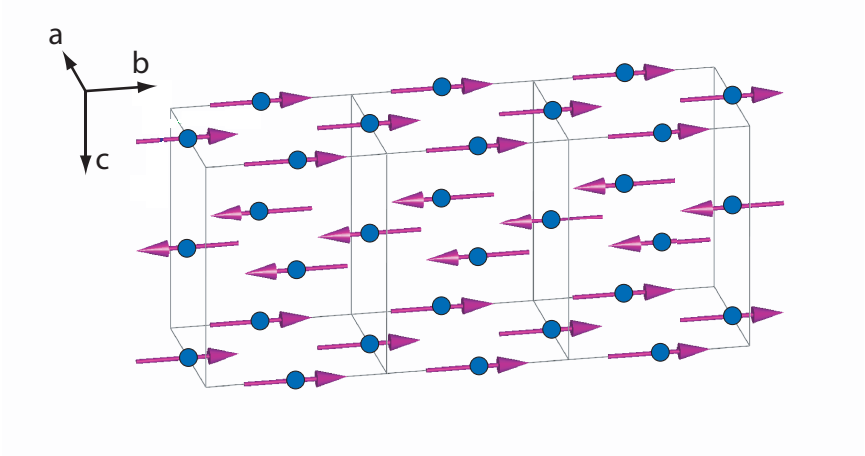

Figure 5.6: The *A*-type magnetic order proposed for the Mn moments in $SmMnO_3$.

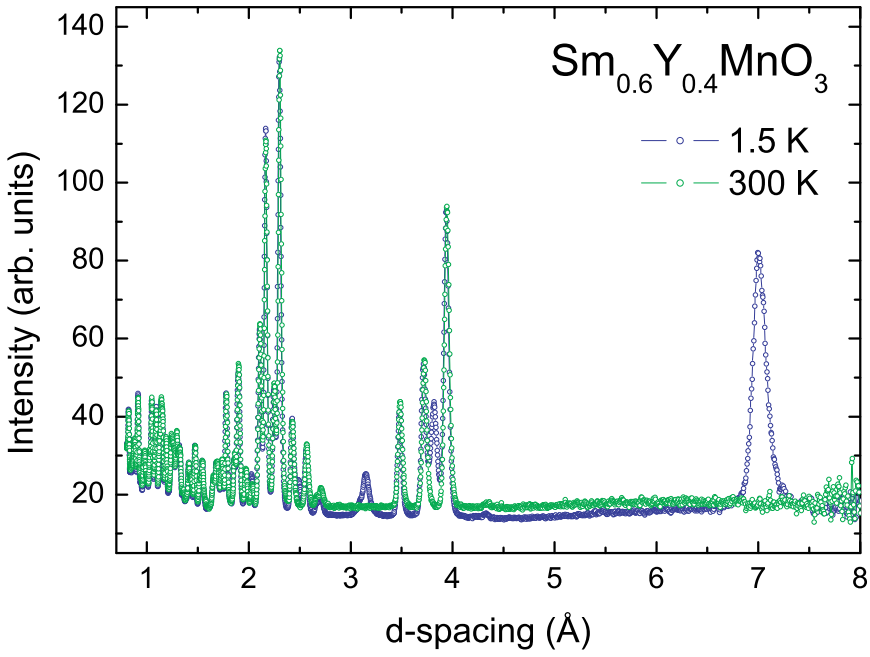

Figure 5.7: GEM diffraction patterns from bank 3 for $Sm_{0.6}Y_{0.4}MnO_3$, taken at 1.5 K and 300 K

data, the magnetic structure of $TbMnO_3$ was used as a template. At the ferroelectric phase transition in $TbMnO_3$, the magnetic ordering of the Mn^{3+} moments changes from an incommensurate sinusoidal ordering propagating along the b-axis to a cycloidal ordering, with the spins rotating in the b-c plane 1.6. A description of how Fullprof models such a magnetic structure is given in the following section, followed by the results of the fit for $Sm_{0.6}Y_{0.4}MnO_3$.

5.1.5 $Sm_{0.6}Y_{0.4}MnO_3$ magnetic structure model

Each lattice point in a crystal structure can be described by the crystallographic vector $\mathbf{R}$:

$$\mathbf{R} = x\mathbf{a} + y\mathbf{b} + z\mathbf{c} \tag{5.1}$$

where $\mathbf{a}$, $\mathbf{b}$ and $\mathbf{c}$ are the crystal cell vectors and x, y and z are integers. The refinement in Fullprof treats the magnetic structure of a compound as being made up of a Fourier series of magnetic moments, μ. For an atom j in a unit cell l, this Fourier series is given as

$$\mu_{lj} = \sum_k S_{\mathbf{k}j} \exp\left[-2\pi i \mathbf{k}\cdot\mathbf{R}_l\right] \tag{5.2}$$

where $\mathbf{k}$ is the magnetic propagation vector. The Fourier component of the magnetic moment on atom j is given by $S_{\mathbf{k}j}$:

$$S_{\mathbf{k}_j} = \frac{1}{2}\left[m_{1j}\mathbf{u}_j + i m_{2j}\mathbf{v}_j\right] \exp\left[-2\pi i \phi_{\mathbf{k}_j}\right] \tag{5.3}$$

where $\mathbf{u}_j$ and $\mathbf{v}_j$ are orthogonal unit vectors of the magnetic moment and ϕ is the magnetic phase factor.

The values m_{1j} and m_{2j} define the nature of the magnetic order. For example, if $m_{2j} = 0$, the magnetic structure is sinusoidal, with an amplitude of m_{1j} and a periodicity given by the propagation vector. If m_{2j} is non-zero, a complex component is introduced, causing the spins to rotate in a helix/cycloid. The rotation of the spins is inside a cylindrical envelope for $m_{2j} = m_{1j}$, and an ellipsoidal envelope for all other values.

The magnetic structure of $Sm_{0.6}Y_{0.4}MnO_3$ below the first magnetic transition temperature, $T_{N1}\sim$50 K was refined by assuming a sinusoidal Mn^{3+} order propagating along the b-axis - a magnetic moment μ_b. Refinements were also carried

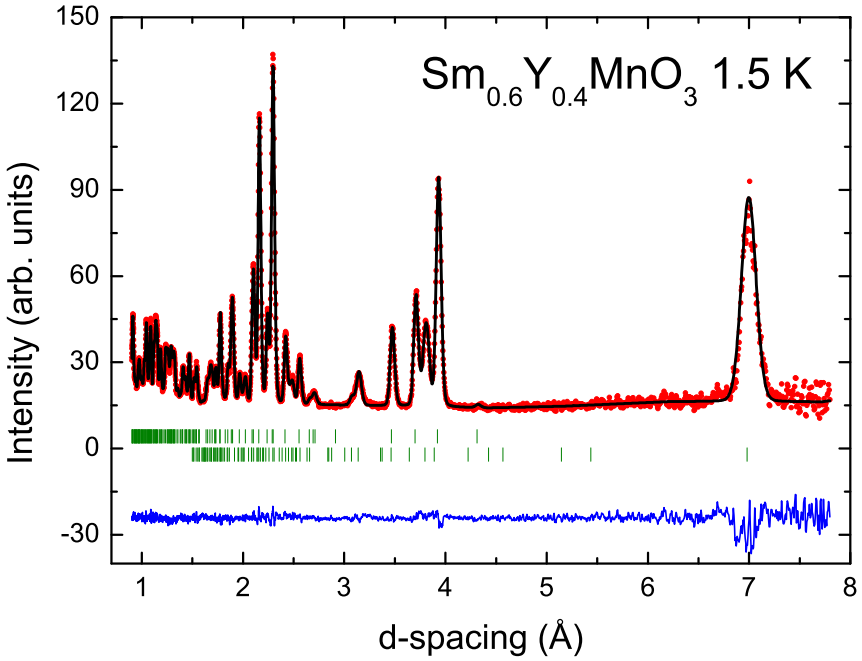

Figure 5.8: Fitted data for $Sm_{0.6}Y_{0.4}MnO_3$ at 1.5 K, from bank 3 of GEM. The red points shows the data, the black line is the fit to the data, and the blue line underneath shows the difference between the two. The upper and lower green ticks represent nuclear and magnetic Bragg reflections, respectively.

out using a model with an additional imaginary term to represent cycloidal order, propagating along the b-axis with the spins rotating in the b-c plane - the magnetic moment is then given by $\mu_b + i\mu_c$. This imaginary component along c was added to the data taken below T_{N2}. Good fits were found to the data using this model, with magnetic R-factors at 1.5 K of 7.10, 3.98 and 5.03 for banks 3, 4 and 5, respectively. The fit to the data at 1.5 K is shown in Figure 5.8.

The cycloidal magnetic structure can be represented by an elliptical envelope inside which the Mn magnetic moments rotate (Figure 5.9), along with a propagation vector which describes the period of rotation with respect to the crystal structure. The temperature dependence of the Mn magnetic moment is shown in Figure 5.10(a), showing the onset of cycloidal order at T_{N2}~27 K in the form of a moment component along the c-axis. This behaviour is very similar to that reported for $TbMnO_3$ [7, 32]. The development of the elliptical envelope is also illustrated in Figure 5.11.

The variation of the magnetic propagation vector with temperature is shown in

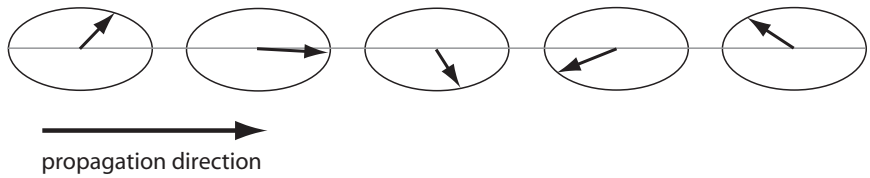

Figure 5.9: Illustration of the elliptical envelope which describes cycloidal magnetic order.

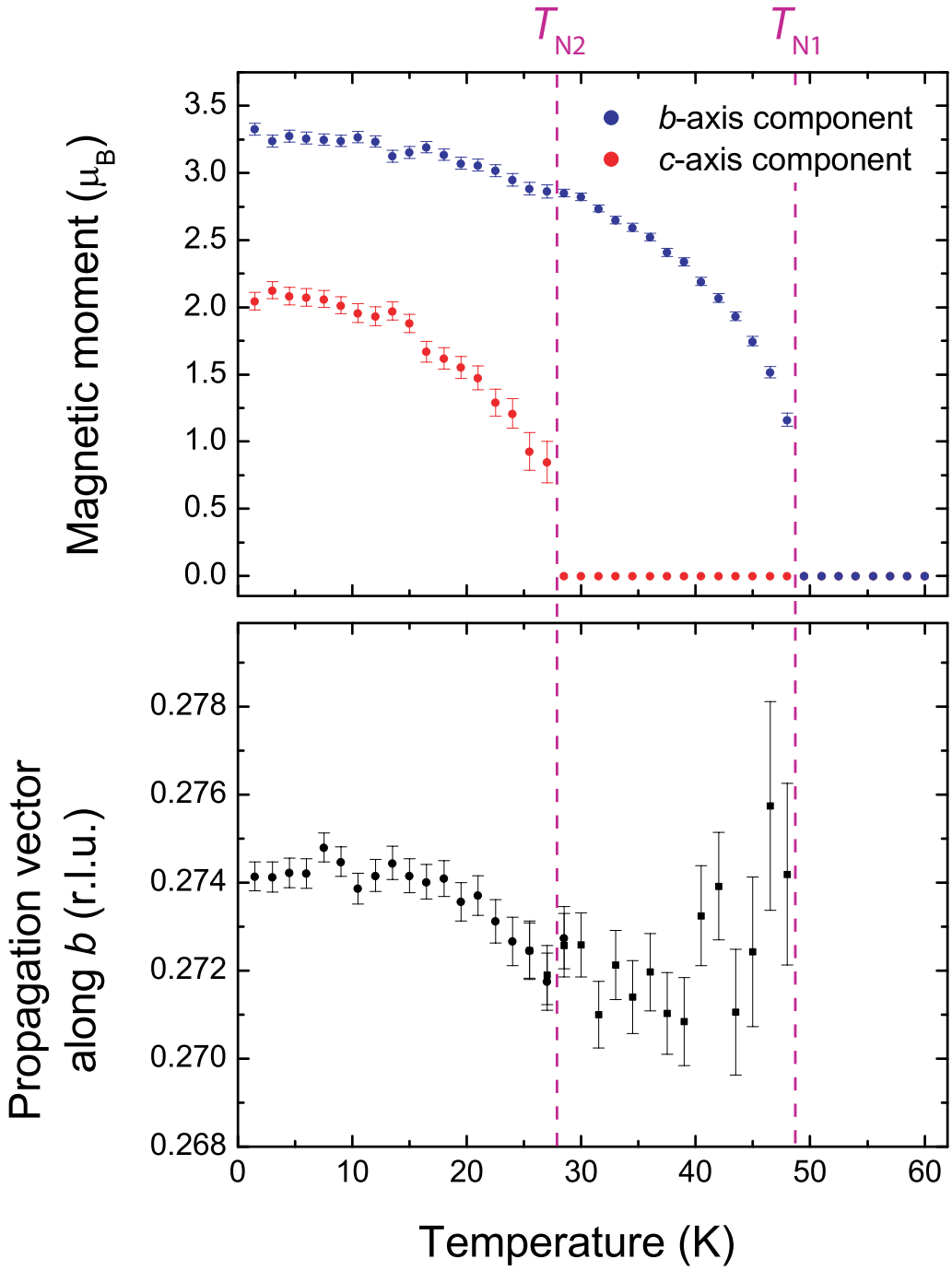

Figure 5.10: (a) Temperature dependence of the *b*-axis and *c*-axis components of the Mn magnetic moment for $Sm_{0.6}Y_{0.4}MnO_3$. (b) Temperature dependence of the propagation vector along the *b*-axis.

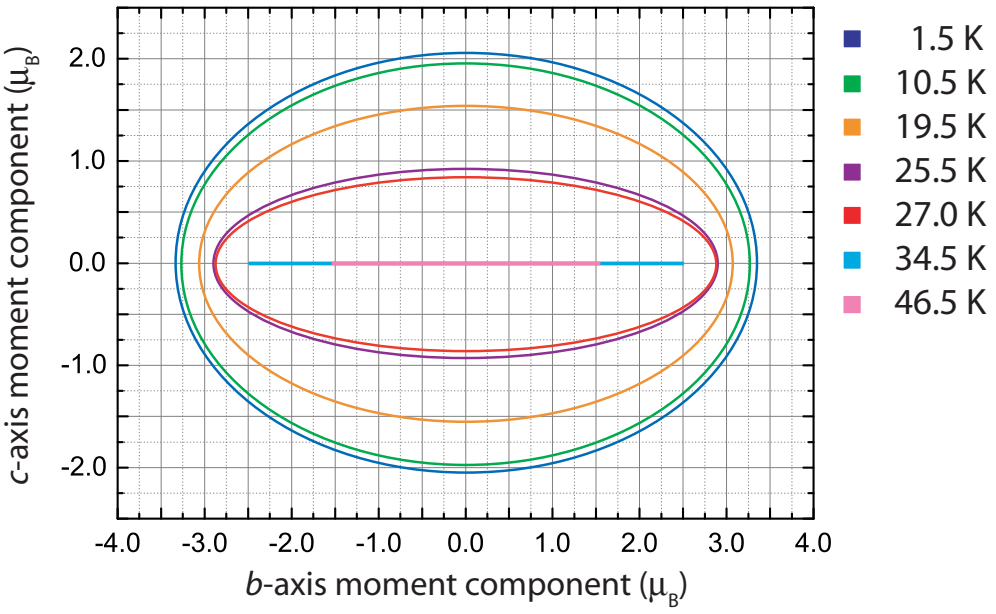

Figure 5.11: Temperature variation of the envelope describing the Mn cycloidal magnetic order in $Sm_{0.6}Y_{0.4}MnO_3$. The flat lines along the *b*-direction for T>27 K represent collinear sinusoidal order.

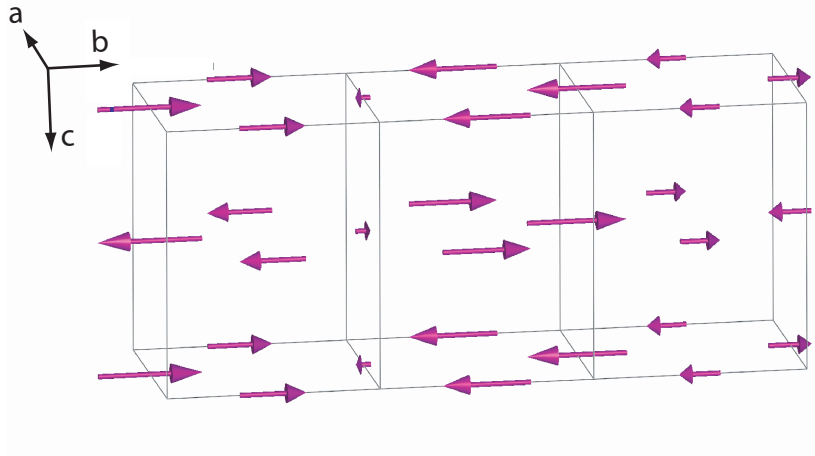

Figure 5.12: The sinusoidal magnetic order proposed for $Sm_{0.6}Y_{0.4}MnO_3$ between 50 K and 27 K, with the propagation and amplitude modulation both along the *b*-axis.

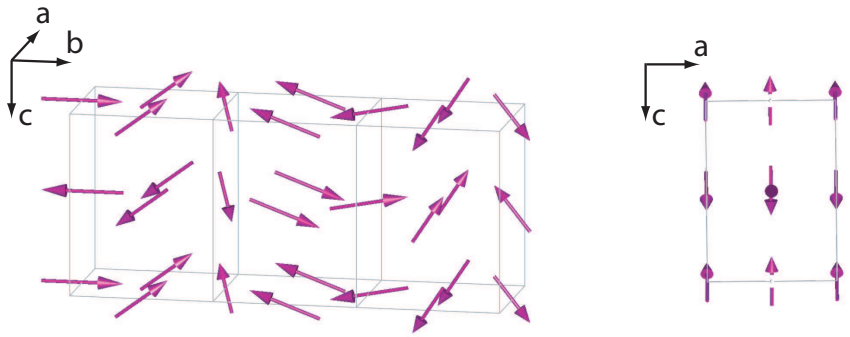

Figure 5.13: The cycloidal magnetic order proposed for $Sm_{0.6}Y_{0.4}MnO_3$ below 27 K. The Mn^{3+} moments rotate in the *b*-*c* plane and propagate along the *b*-axis, with a propagation vector of approximately 0.274 $Å^{-1}$ at 1.5 K.

Figure 5.10(b). The model is set with the magnetic propagation along the *b*-axis, as with $TbMnO_3$. Below the ferroelectric transition temperature the value of the propagation vector increases slightly from ∼0.272 $Å^{-1}$ at 30 K to ∼0.274 $Å^{-1}$ at 1.5 K. The behaviour of the propagation vector for $TbMnO_3$ reported by Kenzelmann *et al.* [32] is different, with a large drop in magnitude from ∼0.287 to 0.276 $Å^{-1}$ between 40 and 30 K, with a slight gradual increase with decreasing temperature up to ∼0.2768 at 2 K.

It should be noted that equivalent fits are obtained for the $Sm_{0.6}Y_{0.4}MnO_3$ data by instead using a real component along both the *b*- and *c*-axes, i.e. $\mu_b + \mu_c$. The spin structure in this case would be a sinusoidal order along *b* which is canted towards the *c*-axis. The two models cannot be differentiated with neutron diffraction data on a powder sample, but by analogy the model of $TbMnO_3$ is assumed. A single crystal sample would be needed to more decisively state the magnetic structure with neutron diffraction, a practical issue due to the cost of sufficient isotope-enriched Sm for crystal growth. The effect of magnetic order of the Sm ions has been neglected from this analysis for the following reasons: the magnetic moment of the Sm^{3+} ions is relatively small ($\mu_{\text{eff}}(Mn^{3+})$=4.82 μ_B, $\mu_{\text{eff}}(Sm^{3+})$=1.74 μ_B), coupled with the weaker contribution due to Y dilution on the *A*-site of the compound; and the fits are of good quality without accounting for Sm order.

5.1.6 Conclusion

In conclusion, the results of the powder neutron diffraction experiment on $SmMnO_3$ and $Sm_{0.6}Y_{0.4}MnO_3$ show that Y doping causes a significant change in the Mn-O-Mn bond angle, moving it towards the value found in the multiferroic $RMnO_3$ compounds. The doping also results in a change in the magnetic structure from the *A*-type antiferromagnetic order seen in $SmMnO_3$. It is proposed that the magnetic order of the Mn moments has two phases: an incommensurate sinusoidal phase below T_{N1}, and a cycloid in the *b*-*c* plane below T_{N2}. If this is the correct magnetic structure, it is similar to that seen in $TbMnO_3$. The data provide further evidence that the Mn-O-Mn bond angle plays a very important role in the

cycloidal magnetic ordering of the Mn^{3+} moments which results in ferroelectric polarisation.

In the following sections, an experiment utilising X-ray resonant scattering (XRS) on single crystal $Sm_{0.5}Y_{0.5}MnO_3$ is presented. The aim of this experiment was also to learn more about the magnetic structure of the $Sm_{1-x}Y_xMnO_3$ compounds, using a complementary technique to neutron scattering.

5.2 X-ray resonant scattering from $Sm_{0.5}Y_{0.5}MnO_3$

5.2.1 The XMaS beamline (ESRF), and experimental setup

The XRS study presented in this thesis was carried out at the XMaS (X-ray Magnetic Scattering) beamline, which is located at the European Synchrotron Radiation Facility (ESRF) in Grenoble, France [93]. XMaS is a bending magnet source and offers an X-ray photon energy range of 2.3 keV - 15 keV, a range that spans the M-edges of the actinide elements and the L-edges of the lanthanides (rare earths).

The experimental layouts of the optics and experimental hutches of XMaS are shown in Figures 5.14 and 5.15, respectively. The incident beam energy (wavelength) is selected by a double crystal monochromator situated in the optics hutch, and a toroidal mirror subsequently focuses the beam such that a high incident flux can be provided to a small sample area (at the centre of rotation of the diffractometer, Figure 5.15). The focused beam spot size at the sample position is 0.8 mm (vertical) × 0.4 mm (horizontal). The harmonic rejection mirrors (Figure 5.15) were used in the study on $Sm_{0.5}Y_{0.5}MnO_3$ to ensure that the beam arriving at the sample position contained just one energy (wavelength, λ) component, i.e. any higher energy components that emerged from the monochromator and then reflected off the toroidal mirror (e.g., $\lambda/2$) were rejected.

Since antiferromagnetic order in $Sm_{0.5}Y_{0.5}MnO_3$ occurs at low temperature (∼47 K), the XRS study was conducted using a Joule-Thomson (J-T) cryostat

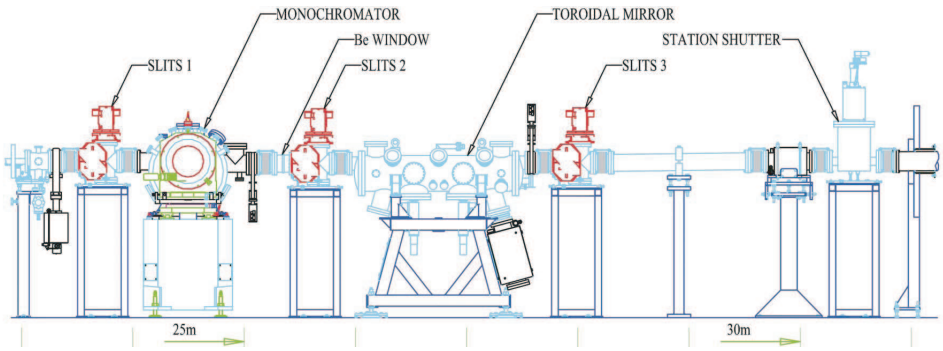

Figure 5.14: Schematic view of the incident beam optics on the XMaS beamline. Bottom scale shows distance from the X-ray source. Taken from Brown *et al.* [93]

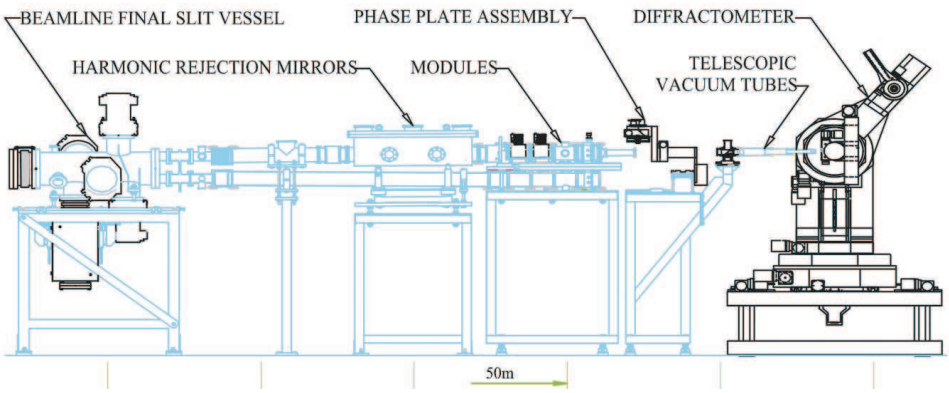

Figure 5.15: Schematic view of the beam conditioning in the experimental hutch on the XMaS beamline (note that the phase-plate was not used in the XRS experiment presented in this thesis). Bottom scale shows distance from the X-ray source. Taken from Brown *et al*. [93].

(base temperature 1.7 K) mounted on the diffractometer (Figure 5.15). The cryostat has beryllium windows through which the incident and scattered beams can pass (beryllium has a low atomic number and, hence, a low X-ray absorption coefficient). The cryostat mount of the XMaS diffractometer is equipped with an *xyz* translation stage, allowing micrometer-precision sample positioning with respect to the incident X-ray beam.

In the present XRS study, a vertical scattering geometry was used. The sample mount used gave the option to switch to a horizontal geometry during the investigation. However, the drawback of the mount was that it prevented the measurement of the azimuthal dependence of the XRS (the measurement of the scattering as a function of rotation, ψ, of the sample about the scattering vector), since over certain ranges of ψ the sample mount blocked the incident and/or scattered beam.

Since the incident beam was horizontally (linearly) polarised (in the plane of orbit of the electrons passing through the bending magnet), the use of a vertical scattering plane implied a σ polarised incident beam (see above) during the XRS study. In order to analyse the (linear) polarisation state(s) of the scattered photons following XRS, a polarisation analyser assembly was mounted on the diffractometer. The assembly comprises two rotation circles, one associated with the analyzer Bragg angle (θ_{CA}, as described above) and the other allowing the analyzer crystal and detector to be simultaneously rotated (by an angle, η) about

the direction of the scattered beam, $\mathbf{k}'$, emerging from the sample. By rotating η such that the detector pointed toward the analyser crystal along a direction parallel to the σ' (π') vector, the σ' (π') component was not diffracted (was filtered out) by the analyser crystal. It was therefore possible to analyse the $\sigma \rightarrow \sigma$' or $\sigma \rightarrow \pi$' channels (as described in Section 2.10.4) during the XMaS experiment. The example of the $\sigma \rightarrow \pi$' setup is shown in Figure 5.16.

5.2.2 Previous XRS studies on $TbMnO_3$

An experiment to further understand the magnetic structure of the $Sm_{1-x}Y_xMnO_3$ compounds was carried out on the XMaS beamline at the ESRF (Section 5.2.1), using X-ray resonant scattering. Before presenting the results of this study, a brief summary of the results of scattering experiments aimed at determining the magnetic structure of $TbMnO_3$ (a well-studied type-II multiferroic compound) is given. These studies will later be referred to when discussing the XRS results for $Sm_{0.5}Y_{0.5}MnO_3$.

As with $TbMnO_3$, the multiferroic state appearing in $Sm_{0.5}Y_{0.5}MnO_3$ coincides with a second antiferromagnetic phase transition seen in magnetic susceptibility measurements (Section 4.2.2). The temperature for the transition, $T_{N2} \sim 24$ K, is very close to T_{N2} in $TbMnO_3$. The magnetic susceptibility results provide initial evidence to suggest similar antiferromagnetic behaviour in the two systems and, hence, a similar mechanism for multiferroic behaviour. In neutron scattering studies, $TbMnO_3$ has been found to show four different types of magnetic satellite reflection, which correspond to four different classifications of magnetic structure, referred to as *A*-, *F*-, *G*- and *C*-type structures. These magnetic reflections are classified by their Miller indices, i.e. their h, k and l values (*A*-type: $h + k =$ even, $l =$ odd, *F*-type: $h + k =$ even, $l =$ even, *G*-type: $h + k =$ odd, $l =$ odd, *C*-type: $h + k =$ odd, $l =$ even). Contrasting reports have been published on the magnetic satellite peak types observed in $TbMnO_3$. The initial powder neutron study by Quezel *et al*. [28] found predominantly *A*-type magnetic peaks, with weak *G*-type peaks and no *C*- or *F*-type reflections. This result was later reproduced by Blasco *et al*. [75], again using the technique of neutron powder diffraction. Kajimoto *et al*. [94] found peaks corresponding to *A*-, *G*-, *F*- and *C*-type order in a neutron diffraction experiment on single crystal $TbMnO_3$. A large increase in the intensity of the *G*-, *F*-, and *C*-type peaks was measured below the magnetic ordering temperature which coincides with the ferroelectric order (at $T_{N2} \sim 27$ K). Kajimoto *et al*. attributed the *A*- and *G*-type peaks to magnetic order along the *b*-axis, but the analysis of the *F*- and *C*-type peaks was only able to conclude that moments were ordered along either the *a*- or *c*-axis. Kenzelmann *et al*. [32]

found that only A-type peaks exist in the magnetic phase above T_{N2}, confirming the existence of a sinusoidal phase with the moments aligned along the b-axis.

Thus in all of the above neutron diffraction studies, signals were observed at A-type satellite positions $(h,k \pm q,l)$, characterized by $h + k =$ even and $l =$ odd. The incommensurate wavevector, denoted by q, was found to be approximately 0.28 reciprocal lattice units (rlu). Signals at the C-, F- and G-type satellite positions (associated with the same value of q but different odd/even permutations of h, k and l) were also observed in some *but not all* of these studies [94]. As discussed in Section 1.6, the link between ferroelectricity and the magnetic structure in $TbMnO_3$ was determined by Kenzelmann *et al.* [32]. By analysing neutron diffraction intensities of the A-type satellite reflections as a function of scattering vector, Q, Kenzelmann *et al.* concluded that the antiferromagnetic ordering in the multiferroic phase of $TbMnO_3$ corresponds to Mn^{3+} moments arranging in a b-c cycloid.

Several investigations have used XRS to study the magnetic structure of $TbMnO_3$ [41, 90, 95]. An important study was carried out recently by Wilkins *et al.* [41], using soft X-ray energies corresponding to the Tb $M_{4,5}$ and Mn $L_{2,3}$ absorption edges. The experiment included an analysis of the dependence of the Mn L_2 edge XRS intensity at the F-type satellite position $(0,q,0)$ as a function of sample azimuth rotation, ψ, about the scattering vector, as well as the ψ-dependence of second harmonic satellites at $(0,2q,0)$ and $(0,1-2q,0)$ (an F- and C-type position, respectively). Wilkins *et al.* discovered evidence for a modified version of the magnetic structure determined by Kenzelmann *et al.*. It was concluded that the A-, F- and C-type satellite reflections can be assigned to one, coherent antiferromagnetic structure, represented by a b-c cycloid canted in the a-axis direction.

An important conclusion of Wilkins *et al.* is that it is not necessary to invoke the idea of different antiferromagnetic (structural) domains existing in $TbMnO_3$ in order to explain the observation of satellite types (i.e, the C- and F-type) in addition to the A-type. However, it should be noted that the G-type satellite reflection is not yet explained by the model of Wilkins *et al.*. It appears that further progress needs to be made in order to fully understand the different ob-

servations made in scattering studies on $TbMnO_3$. For example, Kajimoto *et al.* [94] observed *A*-, *G*-, *F*- and *C*-type magnetic reflections in a single crystal neutron diffraction study on $TbMnO_3$, whereas Kenzelmann *et al.* [32] observed only *A*-type reflections.

Given the observation of similar anomalies in the magnetic susceptibility for $TbMnO_3$ and $Sm_{0.5}Y_{0.5}MnO_3$, i.e. a higher temperature feature at T_{N1} and a lower temperature feature at T_{N2}, one might expect the appearance of similar AFM structures in $Sm_{0.5}Y_{0.5}MnO_3$ as those indicated by the scattering studies on $TbMnO_3$ discussed above. If this is the case, the features would correspond to a sinusoidal antiferromagnetic structure at $T_{N2} < T < T_{N1}$and a cycloidal type structure at $T < T_{N2}$. The XRS results on $Sm_{1-x}Y_xMnO_3$ presented below (alongside the neutron scattering results given in the first half of this chapter) are suggestive of a magnetic ordering similar to that of $TbMnO_3$. However, given that $Sm_{1-x}Y_xMnO_3$ is a new multiferroic system, the magnetic structural information available from scattering experiments on this material is largely incomplete in comparison to the information available on $TbMnO_3$ (the information on $Sm_{1-x}Y_xMnO_3$ is limited to that presented in this thesis). Wilkins *et al.* showed *soft* X-ray resonant scattering to be a powerful tool in determining the magnetic structure of $TbMnO_3$. Traditionally, however, this technique is used following an XRS study in the *hard* X-ray energy regime, which is less of a technically challenging technique than soft XRS, due to X-ray absorption considerations. In the case of $TbMnO_3$, studies at a rare-earth L edge (performed separately by Mannix *et al.* [90] and Voigt *et al.* [95]) preceded the soft XRS study of Wilkins *et al.*. Similarly, the XRS results presented below on $Sm_{1-x}Y_xMnO_3$ were obtained at a rare-earth L edge - the Sm L_2 edge. The L_2 edge was used rather than the L_3 edge because it is known from the XRS literature that for light rare-earth systems the L_2 edge resonant signals are stronger than L_3 signals [71, 96]. Since Tb is a heavier rare-earth element, the Tb L_3 edge was used for the hard XRS studies of $TbMnO_3$ [90, 95].

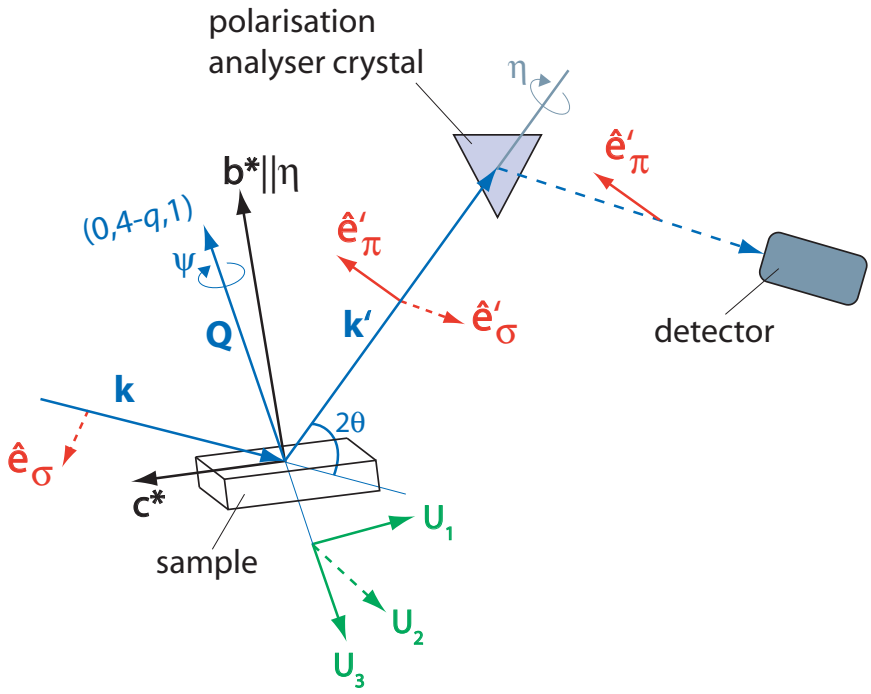

Figure 5.16: X-ray scattering set-up from a $Sm_{0.5}Y_{0.5}MnO_3$ crystal for the experiment at XMaS (sample surface area ~10 mm^2). The reference azimuth ($\psi = 0$) has the c-axis in the scattering plane. In this case, the sample is orientated to give an A-type (0,4-q,1) satellite reflection. Scattering is in the plane of the page, dotted lines refer to directions perpendicular to the page.

5.2.3 Experimental methods

As discussed in Section 5.1.2, a problem with performing neutron scattering experiments on $Sm_{1-x}Y_xMnO_3$ compounds is the large neutron absorption cross-section of Sm, meaning that isotope-enriched Sm is required. Employing X-ray scattering avoids the issue of prohibitively high probe attenuation by the sample, allowing the use of the (much cheaper) natural isotope of Sm and meaning that single crystal samples could be used. The experiment on XMaS used a piece of $Sm_{0.5}Y_{0.5}MnO_3$ single crystal.[2] The crystal was oriented and cut into a cuboid with the b-axis perpendicular to the X-ray scattering surface, and the a- and c-axes perpendicular to the adjacent faces (Figure 5.16). The scattering surface was polished to a 0.25 μm finish using diamond lubricant.

The incident energy was tuned to the Sm L_2 edge (~7.32 keV). A gold (Au)

[2]The original aim was for both $Sm_{0.6}Y_{0.4}MnO_3$ (which was the composition used for the experiment at GEM, Section 5.1.4) and $Sm_{0.5}Y_{0.5}MnO_3$ to be studied at XMaS, but due to time constraints this was not possible. The magnetic structures of the two compositions are not expected to be drastically different from one another, from observation of the magnetic and electric properties presented in the previous chapter.

Type	$h+k$	l	reflection
A	even	odd	(0, 4-q, 1)
F	even	even	(0, 4-q, 0)
G	odd	odd	(0, 3+q, 1)
C	odd	even	(0, 3+q, 1)

Table 5.3: Magnetic satellite reflection positions measured for $Sm_{0.5}Y_{0.5}MnO_3$

crystal with a surface normal parallel to the [111] crystallographic axis was used as the polarisation analyser. For X-rays of an energy tuned to the Sm L2 edge (7.323 keV), the Bragg angle of the Au (222) reflection (θ_{CA}) is very close to 45°. The leakage factor measured with the Au (222) analyser on the (0,4,1) Bragg reflection was approximately 1%. This value is typical of leakage factors measured on XMaS.

Since the bulk magnetic and electric properties of $Sm_{0.5}Y_{0.5}MnO_3$ showed very similar properties to those of $TbMnO_3$, a similar experimental setup was used as that of Mannix *et al.*, who previously performed an XRS experiment on $TbMnO_3$ at the Tb L_3 edge, using the XMaS beamline [90]. The sample was aligned such that the azimuthal angle (as defined in Figure 2.14) was zero when the c-axis was oriented parallel to the (vertical) scattering plane. A search was conducted for A, F, G and C-type peaks at satellite positions (h,$k \pm q$,l), where q is an incommensurate wavevector. Scans were taken with varying q to search for the existence of peaks due to incommensurate magnetic order. The h, k and l values for the different peak positions that were searched for are listed in Table 5.3.

5.2.4 $Sm_{0.5}Y_{0.5}MnO_3$ results

Sm L_2 XRS was observed in $Sm_{0.5}Y_{0.5}MnO_3$ in the multiferroic phase ($T < T_{N2} \sim 24$ K) at the A-, C-, F-, and G-type satellite positions listed in Table 5.3, and associated with an incommensurate wavevector $q \sim 0.31$ rlu. This wavevector is similar to that found for the ordering of the Mn 3d magnetic moments in $TbMnO_3$ ($q_{Mn} \sim 0.28$ rlu [32, 90]). The energy dependence of the Sm L_2 XRS signal at the A-type (0,4-q,1) satellite position, measured at 1.7 K, is shown in Figure 5.17. These data were measured in the $\sigma \rightarrow \pi'$ channel, and are representative of the Sm L_2 resonance also found at the F, C and G-type positions (at base

temperature). The fluorescence (green line) measurement is also shown in Figure 5.17 (this measurement was taken with the polarisation analyser crystal removed and at a diffractometer setting corresponding to a position in reciprocal space close to that of the A-type satellite, to ensure a similar beam penetration depth into the sample as during the satellite measurement).

The similarity between the positions of the peak in the XRS and the white line (peak) in the fluorescence in Figure 5.17 is indicative of an E1 ($2p_{1/2} \rightarrow 5d$) resonant process. The absence of any XRS in the $\sigma \rightarrow \sigma$ channel, over a range of ψ values, is further indication of E1 XRS. It is therefore understood that the Sm L_2 edge resonant scattering is sensitive only to spin polarisation in the $5d$ band of Sm. This is a similar situation to that in XRS studies at the Tb L_3 edge of $TbMnO_3$ [90, 95], i.e. in those studies the XRS mechanism was understood to only involve vacant states in the $5d$ band of Tb. Based on the $TbMnO_3$ XRS studies on the Tb L_3 edge [90, 95], and the Tb $M_{4,5}$ edge [41, 97] XRS studies on $TbMnO_3$, it is possible that below T_{N2} in $Sm_{0.5}Y_{0.5}MnO_3$, the Sm L_2 edge E1 XRS signal is due to spin polarisation of the $5d$ band produced by the Sm $4f$ moments, which are ordered magnetically in the same configuration as the Mn $3d$ moments. This is discussed in more detail in the following subsection.

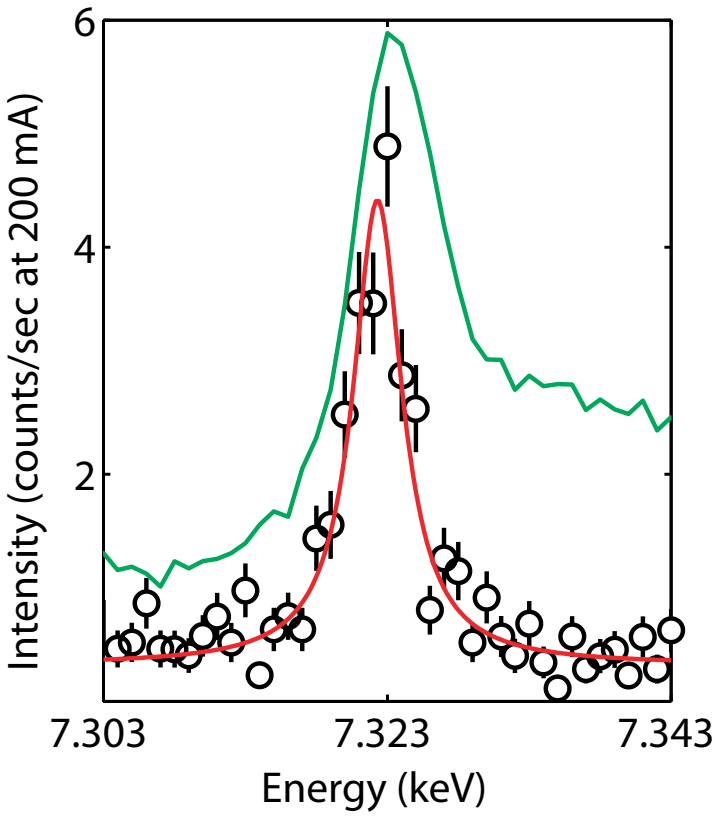

Figure 5.17: Scattering intensity at (0,4-q,1) as a function of incident X-ray energy in the $\sigma \rightarrow \pi'$ channel. The energy is tuned across the Sm L_2 absorption edge (7.323 keV). The data were collected at 20 sec/point, and are monitor corrected. The red line is a Lorentzian fit to the data. The green line is a measurement of the Sm L_2 fluorescence, scaled to the $\sigma \rightarrow \pi'$ resonance.

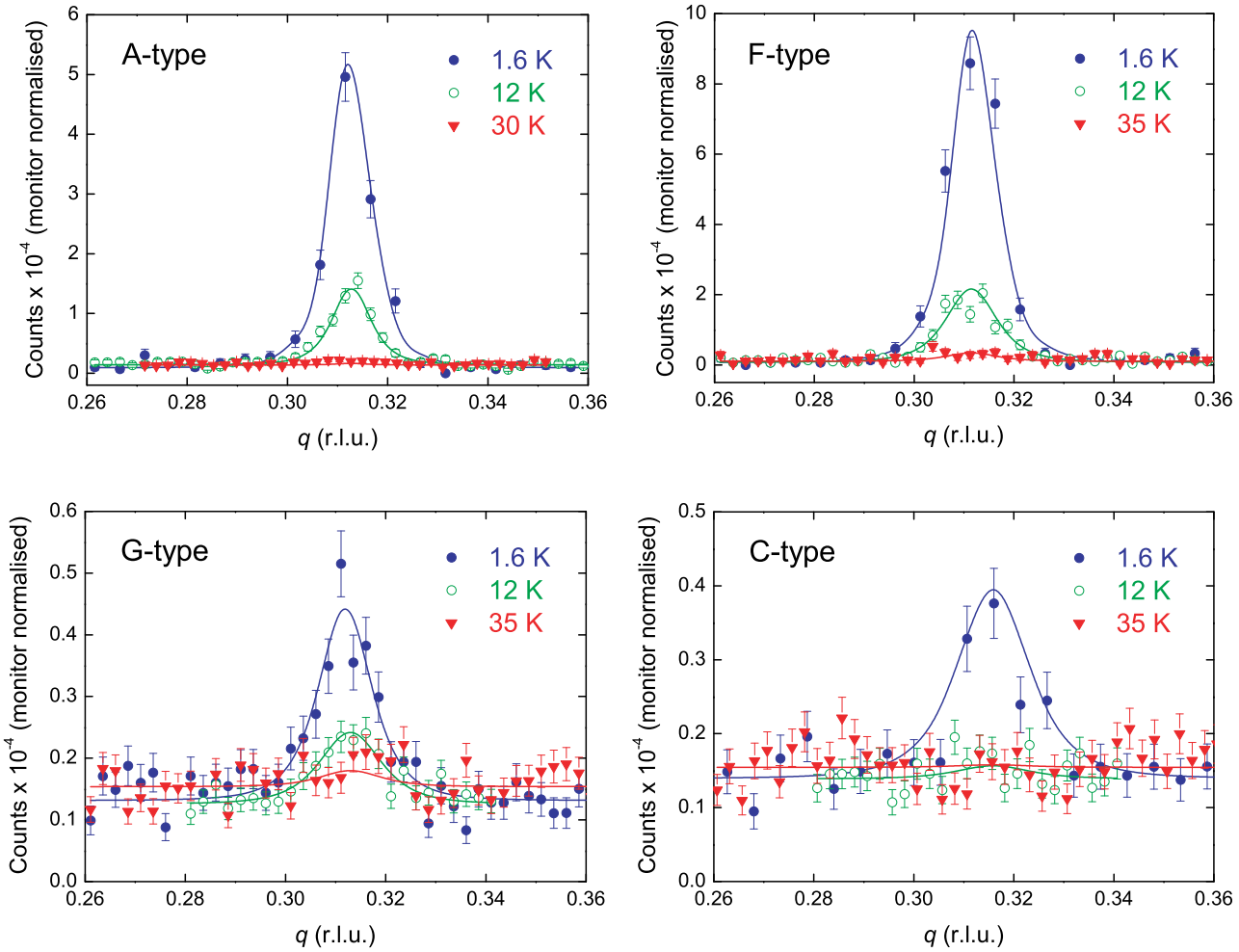

Figure 5.18: Magnetic peak types measured for $Sm_{0.5}Y_{0.5}MnO_3$ at XMaS, at temperatures in each magnetic phase. Data taken in the $\sigma \rightarrow \pi$' channel at the Sm L_2 absorption edge.

Figure 5.18 shows the XRS signal for the *A*-, *F*-, *C*- and *G*-type peaks measured in this experiment, at 1.6 K, 12 K and 35 K. The lowest two temperatures correspond to the proposed cycloidal magnetic ordering phase of $Sm_{0.5}Y_{0.5}MnO_3$, and 35 K is in the proposed collinear sinusoidal order phase. In the XRS and neutron scattering experiments conducted on $TbMnO_3$, the *A*-type satellite reflection was always present, meaning this reflection is unambiguously linked with antiferromagnetic ordering. Based on this, a detailed temperature dependence of the *A*-type peak for $Sm_{0.5}Y_{0.5}MnO_3$ was conducted, with scans taken from 1.6 K to 30 K in increments of 1-2 K. The temperature dependence of the integrated intensities of the *A*-type peaks are shown in Figure 5.19. Although detailed temperature dependences were not carried out for the other peak types (due to time constraints), the intensities of the other peak types at 1.6 K, 12 K and 35 K are also shown, for comparison. It can be seen that the *F*-type peak intensity is approximately twice as large as that of the *A*-type peak across the temperature range, and approximately ten times larger than the *C* and *G*-type peaks. All peak types were observed at the base temperature of 1.6 K. The *C*-type peak disappears at ∼12 K, and the *A*-type peak appears to go to zero at approximately T_{N2} ∼24 K. The *F* and *G*-type peaks persist until some point between 12 K and 35 K, but more data points are needed to determine the temperature more accurately.

The experiment was concluded with a search for independent Sm magnetic order, again at the Sm L_2 edge. An Sm incommensurate wavevector approximately equal to that of Tb in $TbMnO_3$ was assumed, i.e. $q_{Sm} \sim q_{Tb} \sim 0.42$ rlu [90]. No magnetic satellite peaks were found at the positions expected for Sm order.

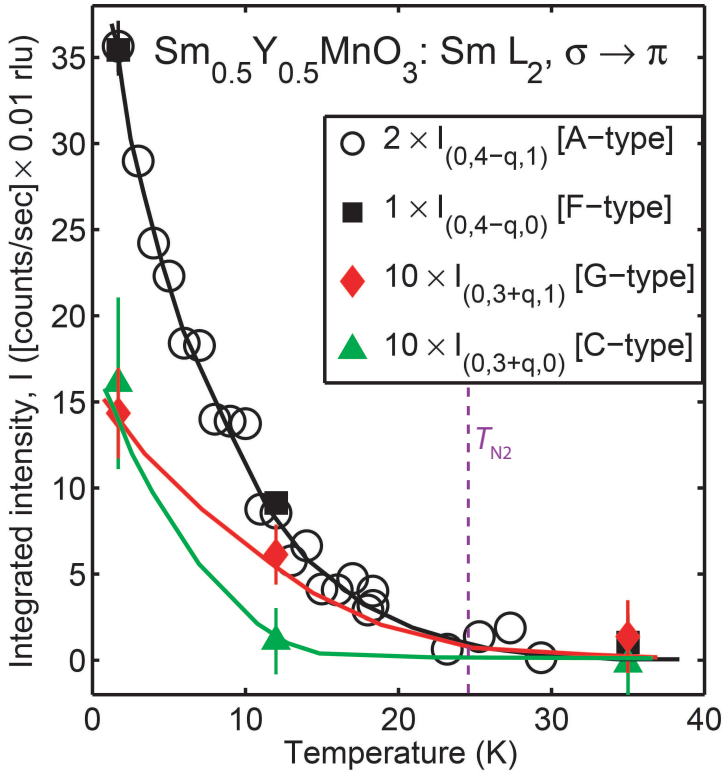

Figure 5.19: Temperature dependence of the integrated intensities of the different magnetic satellite reflections observed in $Sm_{0.5}Y_{0.5}MnO_3$, measured in the $\sigma \rightarrow \pi$' channel at the Sm L_2 absorption edge. Solid lines are guides to the eye. The vertical dashed line represents the magnetic transition temperature, T_{N2}, which corresponds to the onset of multiferroic order.

5.2.5 Discussion

At the time the XMaS experiment was conducted on $Sm_{0.5}Y_{0.5}MnO_3$, the interpretation of the different magnetic peak types observed in $TbMnO_3$ was that they were from different magnetic domains within the sample [90]. Since then, the magnetic structure has been refined by Wilkins *et al.* to give a more complex model which allows for each peak type, and is consistent with the results and predictions of Kenzelmann *et al.* [32, 41]. In this model, the Mn moments in the collinear sinusoidal phase are slightly canted in the *c*-direction, and in the *b*-*c* cycloidal phase, the moments are tilted into the *a*-axis. It was also found that the Tb $4f$ band shows magnetic order coinciding with the Mn cycloidal phase transition [41, 97], countering earlier arguments that the Tb moments were not ordered until below 7 K. There is clearly a strong link between the Tb and Mn magnetic order in this cycloidal/ferroelectric phase, as shown by the unexpected behaviour of the electric polarisation under an applied magnetic field [35] (Section 4.3).

The results of several X-ray scattering experiments were utilised in order to give an accurate picture of the magnetic structure of $TbMnO_3$, including detailed azimuthal scans of the different peak types, measurements at the K, and L-edges Mn and the K, L and M-edges of Tb, and non-resonant scattering [41, 90, 97]. Since we have only conducted one XRS experiment on $Sm_{0.5}Y_{0.5}MnO_3$, limited information is available. Therefore, it is not yet possible to directly deduce the full details of the magnetic structure of $Sm_{0.5}Y_{0.5}MnO_3$, however we can still infer possible behaviour by comparison with the results published for $TbMnO_3$.

It is not possible to directly infer the magnetic structure of the Mn moments from the XMaS data. A search for the Mn K edge was carried out during the XMaS study, however, this proved unsuccessful. Since the energy range available at XMaS (2.3 keV - 15 keV) does not cover the Mn $L_{2,3}$ edges (Mn $L_2 = 0.650$ keV, Mn $L_3 = 0.639$ keV), a study of (soft) XRS at these edges could not be performed. The possible transitions from the Mn K edge are

$1s \rightarrow 4p$ - Dipole (E1) transition

$1s \rightarrow 3d$ - Quadrupole (E2) transition

The $4p$ band polarisation is weak, resulting in a low dipole (E1) XRS amplitude at the Mn K edge. Although the $3d$ band shows stronger polarisation, quadrupolar transitions are statistically (quantum mechanically) less likely events than dipole transitions, meaning there is also a low XRS amplitude for quadrupole (E2) transitions. It could be possible to overcome the problem of low K edge XRS signal intensity with an insertion device beamline (such as ID20), which has a higher beam intensity, or by tuning the X-ray to soft energies. The latter method allows resonances at the Mn $L_{2,3}$ edges, meaning that the $3d$ state can be observed via dipole transitions.

Although measurements were taken at the Sm L_2 edge, it is still possible to obtain information about Mn ordering. For example, in a magnetic system containing two magnetic ions 'A' and 'B', the ordering of the 'A' ions can magnetically polarise the 'B' ions. This can happen since the 'B' ions experience internal magnetic fields due to the ordering of the 'A' ions (dipolar interaction between the 'A' and 'B' magnetic moments). In this case, measurements of the magnetic properties of the 'B' atoms would indirectly uncover information about the magnetic properties of the 'A' ions. Electronic orbitals in an ion can also be polarised due to the magnetisation of other orbitals in the same ion. For example, a magnetic $4f$ band in Sm can potentially polarise the unoccupied $5d$ level. Possible transitions from the Sm L_2 edge are

$2p_{\frac{1}{2}} \rightarrow 5d$ - Dipole (E1) transition
$2p_{\frac{1}{2}} \rightarrow 4f$ - Quadrupole (E2) transition

The magnetic order from Sm^{3+} ions is due to the partially filled $4f$ level, but from the XMaS results it seems that we did not probe this energy band since we detected no evidence of quadrupolar transitions. The energy scans measured only show single peaks; quadrupolar interactions would occur slightly lower in energy than dipole transitions (of the order of a few eV), meaning a split peak would be expected if any E2 transitions were measured. Also, we only measure reso-

nant scattering in the $\sigma \rightarrow \pi'$ channel and not in $\sigma \rightarrow \sigma'$. This is as expected for dipole transitions, where the $\sigma \rightarrow \sigma'$ component of the matrix is zero. For quadrupole transitions, a finite signal in $\sigma \rightarrow \sigma'$ is expected, with the first order term (analogous to Equation 2.32) dependent on the out of plane (z_2) component of the magnetic moment [74]. If we assume the moments were aligned in the diffraction (b-c) plane with our experimental set-up, an E2 signal would only be found in $\sigma \rightarrow \sigma'$ upon significantly changing (by more than ∼20 to 30 degrees) the azimuth angle, which would produce components of the magnetic moments out of plane. The study of the $\sigma \rightarrow \sigma'$ channel as a function of azimuth angle conducted at XMaS did not reveal any ($\sigma \rightarrow \sigma'$) XRS signal, however, the study was only conducted over a limited angle range ($\Delta\psi \sim \pm$ 30 degrees; subsequent changes in ψ resulted in shadowing by the sample mount).

In order to directly probe the $4f$ state of Sm using dipolar transitions, "soft" X-rays would be needed, such as in the experiment conducted by Wilkins *et al.* on $TbMnO_3$ [41]. Specifically, by studying at the $M_{4,5}$ edges of Sm (∼1.7keV), dipole transitions from the $3d$ to the $4f$ levels (as observed by Wilkins *et al.*) can be probed. Nonetheless, our study at the Sm L_2 edge, which has revealed XRS due to transitions to the $5d$ band of Sm provides valuable preliminary information on the magnetic structure of $Sm_{0.5}Y_{0.5}MnO_3$, since, by comparison with the XRS studies (both soft and hard) on $TbMnO_3$, we can conclude that the antiferromagnetic configuration (hence magnetic satellite reflections) associated with the polarisation of the Sm $5d$ band is representative of the magnetic order associated with the ($4f$) Sm and ($3d$) Mn magnetic moments.

In the following two subsections, a discussion of the Sm L_2 XRS in the two different temperature regimes, $T_{N2} < T < T_{N1}$ and $T < T_{N2}$, is made.

5.2.5.1 $T_{N2} < T < T_{N1}$

At the Sm L_2 edge, very weak peaks are seen in the $\sigma \rightarrow \pi'$ channel corresponding to A- and F-type satellite positions in the temperature range $T_{N2} < T < T_{N1}$ (Figure 5.18). By comparison, in $TbMnO_3$ an F-type satellite is seen at the Tb L_3 edge, but not at the Tb M_4 or M_5 edges, where no order is reported [41, 90, 97]. Since

the L_3 edge probes the $5d$ states and the $M_{4,5}$ edges probe the $4f$ states of Tb, these results can be explained as being due to a polarisation of the Tb $5d$ band due to the collinear sinusoidal ordering of the Mn ions. Since a weak signal is seen in the same temperature range for $Sm_{0.5}Y_{0.5}MnO_3$, it is proposed that this is due to a polarisation of the Sm $5d$ band by an ordering of the Mn moments analogous with $TbMnO_3$.

5.2.5.2 $T < T_{N2}$

In the temperature range $T < T_{N2}$ for $Sm_{0.5}Y_{0.5}MnO_3$, one observes a gradual increase in the intensity of the A-, F-, G- and C-type peaks with decreasing temperature, although a detailed temperature dependence was only taken for the A-type peak. In $TbMnO_3$, a resonant signal appears below T_{N2} at the Tb M_4 edge at A-type satellite positions, and at the M_5 edge at A- and C-type satellite positions, demonstrating that the $4f$ magnetic moments of Tb are ordered and strongly linked to the Mn cycloidal order in this phase [41, 97]. The sudden increase in the XRS signals in $Sm_{0.5}Y_{0.5}MnO_3$ at the Sm L_2 edge therefore points towards a similar process, with the Sm $4f$ band being influenced by a cycloidal order of the Mn moments, causing a polarisation of the Sm $5d$ states.

Since the $M_{4,5}$ edges of Sm (in the soft X-ray regime) were not studied in this experiment, and no evidence was found of satellite reflections corresponding to independent Sm ordering (i.e. at a different value of q), we can not directly infer order of the Sm moments. Further XRS experiments are needed to more completely understand the magnetic structure of $Sm_{0.5}Y_{0.5}MnO_3$.

5.3 Conclusion

The experiments presented in this chapter utilised neutron diffraction on polycrystalline $Sm_{0.6}Y_{0.4}MnO_3$ (^{154}Sm isotope enriched) and X-ray resonant scattering on single crystal $Sm_{0.5}Y_{0.5}MnO_3$. These experiments provide evidence that points towards magnetic ordering of the Mn^{3+} moments which is similar to that observed in $TbMnO_3$, that is, a sinusoidal collinear order along the b-axis in the region $T_{N2} < T < T_{N1}$ (24 K $< T <$ 47 K), and a cycloidal order in the b-c plane below T_{N2}. If this model is indeed the case, it agrees well with the results presented in Chapter 4, as discussed in Section 4.3. In particular, the existence of a b-c cycloid alongside the observation of an electric polarisation developing along the c-axis at the same temperature agrees with the model of Kenzelmann *et al.* and Katsura *et al.* (Section 1.6) [32, 34]. This would also be a significant result with regards to the effect of Y doping in $SmMnO_3$, which exhibits simple A-type antiferromagnetic order. One point of note is the slight discrepancy found between the incommensurate wavevector, q, measured in the two experiments. At base temperature, the neutron diffraction experiment measured $q \sim 0.274$ rlu for $Sm_{0.6}Y_{0.4}MnO_3$, and the XRS experiment measured $q \sim 0.31$ rlu for $Sm_{0.5}Y_{0.5}MnO_3$. This discrepancy is possibly due to the different sample compositions, and the planned future XRS experiments may shed further light on this issue (single crystal $Sm_{0.6}Y_{0.4}MnO_3$ has also been prepared for XRS experiments).

The crystal structure determination of $SmMnO_3$ and $Sm_{0.6}Y_{0.4}MnO_3$ from the neutron powder experiment at GEM confirm that the Mn-O-Mn bond angle, ϕ decreases due to Y doping, as expected [30, 64]. In $Sm_{0.6}Y_{0.4}MnO_3$, ϕ is 145.79(1)° at room temperature, close to the value reported for $TbMnO_3$ of ∼145.4° [30]. By comparison, ϕ for $SmMnO_3$ was found to be 147.76(2)° at room temperature. This result provides strong evidence that tuning ϕ allows control of the magnetic - and therefore multiferroic - properties in the rare earth manganite systems.

It should, however, be noted that the results presented in this chapter provide only preliminary information on the magnetic structure, and more experiments are required in order to arrive at a complete picture of the magnetic ordering. Nu-

merous complementary neutron scattering and XRS studies have been carried out on single crystal $TbMnO_3$, meaning that the magnetic structure has been refined over a period of time, whereas experiments carried out on the $Sm_{1-x}Y_xMnO_3$ compounds are limited to those presented in this chapter. Due to the neutron scattering experiment being carried out on a polycrystalline sample, and the non-straightforward nature of the magnetic order, a different magnetic model can be fitted to the data for $T < T_{N2}$ (that of a canted sinusoidal order, rather than a cycloidal order, see Section 5.1.4). It would be beneficial to conduct a neutron scattering study on single crystal $Sm_{1-x}Y_xMnO_3$, but due to the strongly neutron-absorbing nature of Sm this is not practical. The key to further understanding the magnetic structure of the $Sm_{1-x}Y_xMnO_3$ compounds therefore appears to be further XRS experiments. The azimuthal dependence of the *A*-, *F*-, *C*- and *G*-type satellite reflections, may shed more light on the orientation of the magnetic moments present below T_{N2}. Also, the use of soft X-rays could be used to directly probe the $4f$ band of Sm and the $3d$ band of Mn via dipole (E1) XRS.

Chapter 6

Magnetoelectric properties of $Gd_{1-x}Y_xMnO_3$

Subsequent to the studies on the $Sm_{1-x}Y_xMnO_3$ compounds, a similar approach was adopted to $GdMnO_3$. $GdMnO_3$ only exhibits a small electric polarisation in the absence of an external field, but an applied magnetic field along the *b*-axis gradually increases the polarisation magnitude (Figure 1.17) [31]. The polarisation develops parallel to the *a*-axis, rather than the *c*-axis as seen in $TbMnO_3$, $DyMnO_3$ and the $Sm_{1-x}Y_xMnO_3$ series.

The reason for the different magnetoelectric behaviour seen in $GdMnO_3$ is not clear. Kimura *et al*. suggest a link to the position of $GdMnO_3$ in the magnetic phase diagram for the $RMnO_3$ series (Figure 1.20) [31] - i.e. the larger Mn-O-Mn bond angle, ϕ (the reported value of ϕ for $GdMnO_3$ is $\sim$146.2° [29, 30]). The connection between ϕ and the occurrence of a ferroelectric polarisation, has been shown for $Sm_{1-x}Y_xMnO_3$ in the previous chapters. It is also proposed that the magnetic properties of the rare earth atoms play a crucial role in inducing the cycloidal magnetic ordering of the Mn^{3+} moments, and that the large magnetic anisotropy found in Tb and Dy is an important factor in their multiferroic behaviour. Feyerherm *et al*. [39] found that in $DyMnO_3$, the ordering of the Dy^{3+} moments is induced by the Mn^{3+} ordering and, in turn, enhances the ferroelectric polarisation by a factor of three. They also propose that in $GdMnO_3$, a magnetic field applied parallel to the *b*-axis causes an ordering of the Gd^{3+} moments which stabilises the cycloidal Mn^{3+} ordering and so induces the observed electric

polarisation. Due to the high neutron absorption cross sections of Dy and Gd, experiments done to date to observe the magnetic structure have been carried out using synchrotron X-ray diffraction.

In order to further understand the magnetoelectric behaviour of $GdMnO_3$, and to build on the results obtained for $Sm_{1-x}Y_xMnO_3$, a similar approach of doping with Y at the rare earth site has been applied, with the aim of inducing changes in the magnetoelectric properties. Ivanov *et al.* [56] first published results for $Gd_{0.9}Y_{0.1}MnO_3$ in 2006, showing that doping with Y induces a spontaneous electric polarisation (i.e. in zero applied magnetic field). The magnitude of the spontaneous polarisation measured along the *c*-axis of $Gd_{0.9}Y_{0.1}MnO_3$ ($\sim$20 μCm^{-2}) is small compared with that seen in $TbMnO_3$ ($\sim$800 μCm^{-2}). The data on the polarisation were limited to one plot as a function of magnetic field, and no data were reported on the magnetic structure or the Mn-O-Mn bond angle of the new compound.

The following data are from preliminary measurements on polycrystalline samples, taken with the aim of building upon the results of Ivanov *et al.* to further understand the conditions necessary for multiferroicity in the $RMnO_3$ series.

6.1 $Gd_{1-x}Y_xMnO_3$

6.1.1 Sample preparation

Polycrystalline samples of $Gd_{1-x}Y_xMnO_3$ (x = 0.1-0.5) were synthesised by reacting together stoichiometric ratios of Gd_2O_3, Y_2O_3 and MnO_2 powders. The procedure used for heating the powders is given in Table 6.1. Pellets were pressed and sintered for magnetic and dielectric measurements, as with the $Sm_{1-x}Y_xMnO_3$ (Section 4.1.1). Both Gd_2O_3 and Y_2O_3 are hygroscopic, and so these powders were heated prior to mixing with the MnO_2 powder.

6.1.2 X-ray diffraction

Powder X-ray diffraction was used to check the phase formation of the prepared $Gd_{1-x}Y_xMnO_3$ compounds. X-ray diffraction was carried out using a Philips PW1720 X-ray generator, with a counting time of 2 s/step in 0.02° increments.

Heating	Temperature (°C)	Duration (hours)	Comments
1	1100	4	Gd_2O_3 and Y_2O_3 preheat
2	1100	12	$Gd_{1-x}Y_xMnO_3$ powder
3	1400	24	$Gd_{1-x}Y_xMnO_3$ powder
4	1400	12	$Gd_{1-x}Y_xMnO_3$ pellets

Table 6.1: Sample heating procedure for $Gd_{1-x}Y_xMnO_3$ ($x = 0.1$-0.5)

For $x = 0.1$-0.4, single phase compounds were formed, with X-ray patterns similar to that published for $GdMnO_3$ (Figure 6.1) [98]. For $x = 0.5$, additional peaks were seen in the diffraction pattern, corresponding to pure $YMnO_3$ [84].

High quality powder X-ray diffraction data were taken for $Gd_{0.8}Y_{0.2}MnO_3$ using a Panalytical X'Pert Pro multipurpose X-ray diffraction system, shown in Figure 6.2. A Rietveld refinement of these data was performed with Topas Academic [85], giving the crystal structure information shown in Table 6.2. As discussed in Section 4.1.2, powder X-ray diffraction data do not give as accurate bond angle values as neutron diffraction.

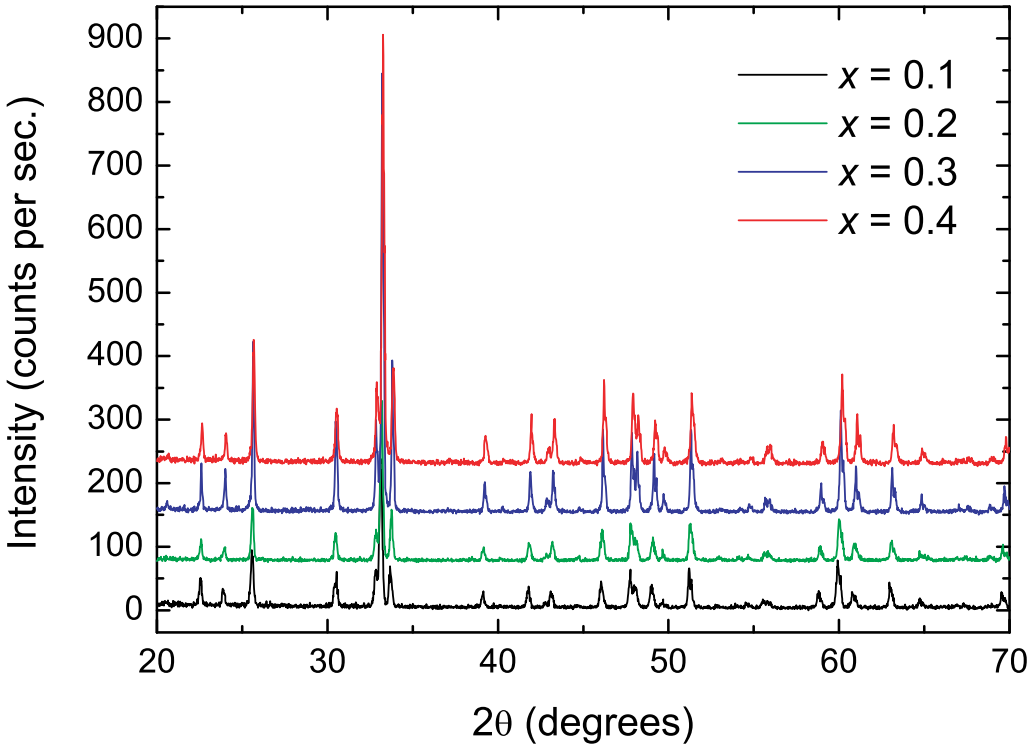

Figure 6.1: Powder X-ray diffraction patterns for $Gd_{1-x}Y_xMnO_3$ ($x = 0.1$-0.4).

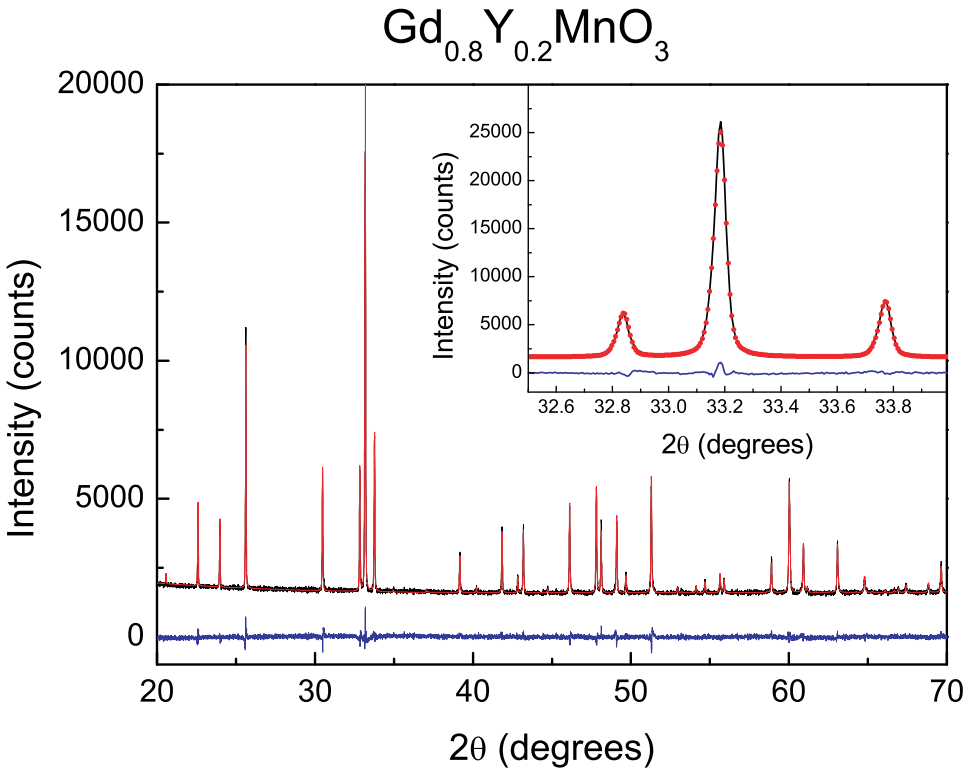

Figure 6.2: X-ray diffraction pattern for polycrystalline $GdMnO_3$, taken with a Panalytical X'Pert Pro multipurpose X-ray diffraction system. The red line shows the observed data, the black line is the fit to the data using Topas Academic, and the blue line is the difference between the two. Inset: close up of the fit in the region of the high intensity peaks, for detail.

	$Gd_{0.8}Y_{0.2}MnO_3$
a (Å)	5.30621(3)
b (Å)	5.86297(3)
c (Å)	7.41768(4)
V (Å^3)	230.765(2)
Mn-O1-Mn, ϕ_1 (×2)	142.9(3)°
Mn-O2-Mn, ϕ_2 (×4)	145.5(3)°
⟨Mn-O-Mn⟩	144.6(3)°
Reliability factors	
R_p(%)	2.223
R_{wp}(%)	2.851
R_{exp}(%)	2.358
χ^2	1.209

Table 6.2: Lattice parameters and Mn-O-Mn bond angles for $Gd_{0.8}Y_{0.2}MnO_3$ (space group Pbnm), from refined powder X-ray diffraction data

6.1.3 Magnetic properties

Magnetic susceptibility versus temperature data for $Gd_{1-x}Y_xMnO_3$ x = 0.1-0.4 are shown in Figure 6.3. As with the $Sm_{1-x}Y_xMnO_3$ compounds, the addition of Y at the rare earth site causes a suppression of the susceptibility - x = 0.4 has a value of χ at 2 K which is under 40% of the magnitude of x = 0.1. This is to be expected, since the large effective moment of Gd (7.94 μ_B) is suppressed by the Y substitution. There are no features apparent in the susceptibility data for any composition. This is in contrast to $Sm_{1-x}Y_xMnO_3$, where a slight feature developed in the magnetic susceptibility at ∼20 K as x was increased.

6.1.4 Dielectric properties

The dielectric constant versus temperature data for $Gd_{1-x}Y_xMnO_3$ (x = 0.1-0.4) were taken for samples cut from sintered polycrystalline pellets, with the pellet piece sizes given in Table 6.3. Sample contacts were made by coating opposing faces of the pellets with silver paint, and connections were made as described in Section 2.6.

The results of the dielectric constant measurements are shown in Figure 6.4. A peak in the dielectric constant is seen for each composition, and the application of a magnetic field of 9 T causes the peak to shift towards higher temperature and

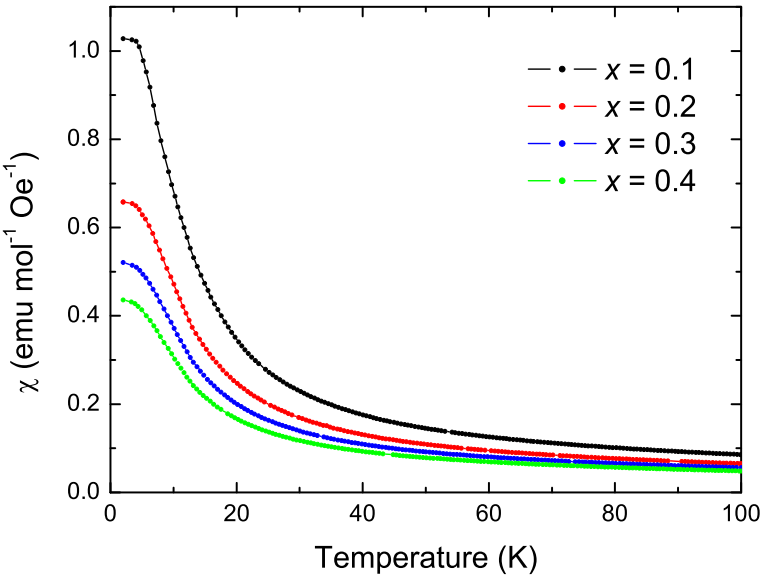

Figure 6.3: Zero-field cooled magnetic susceptibility versus temperature for polycrystalline $Gd_{1-x}Y_xMnO_3$, taken in an applied field of 0.01 T

decrease slightly in magnitude for $x = 0.2$ and 0.4. For $x = 0.3$, the application of a magnetic field appears to cause the magnitude of the peak in the dielectric constant to increase, but the zero field peak is below the temperature range of the measurement. By comparison, a peak in the dielectric constant of single crystal $GdMnO_3$ has been reported by Kimura *et al.*, along the *a*- and *c*-axes [31]. The peak in $GdMnO_3$ occurs at ∼24 K, with the peak temperature shown to increase with an applied magnetic field along any direction. Changes in the magnitude of the peak in the dielectric constant for $GdMnO_3$ are seen with H//*c* - a decrease in the peak size along the *a*-axis and an increase along the *c*-axis. No explanation is given by Kimura *et al.* for this behaviour.

The data for the $x = 0.3$ pellet is a lot noisier than that seen for the other compositions. From observation of the different sample dimensions used, it appears that this is due to the relatively large thickness of the pellet used for the measurement, since the area is larger than those of the $x = 0.1$ and 0.2 compositions and smaller than the $x = 0.4$ compound. It is also possible that an inferior electrical contact was made with the pellet.

x	Pellet thickness (mm)	Pellet area (mm^2)
0.1	1.02	14.10
0.2	1.01	15.52
0.3	1.25	20.98
0.4	0.98	34.62
0.5	1.02	28.21

Table 6.3: $Gd_{1-x}Y_xMnO_3$ pellet dimensions for dielectric measurements (cuboid pieces)

The dependence on the peak in the dielectric constant with an applied magnetic field shows that there is magnetoelectric coupling in the $Gd_{1-x}Y_xMnO_3$ compounds as in $GdMnO_3$. Unlike $Sm_{1-x}Y_xMnO_3$ (polycrystalline and single crystal samples), there is no feature in the magnetic susceptibility that corresponds to the peak in the dielectric constant. Since the magnetic susceptibility data taken were for a polycrystalline sample, it is possible that an oriented single crystal of $Gd_{1-x}Y_xMnO_3$ may show distinct features in the susceptibility, just as was seen for $Sm_{1-x}Y_xMnO_3$. Single crystals of $Gd_{1-x}Y_xMnO_3$ would also allow measurements of the magnetic and dielectric anisotropy of the compounds, as well as polarisation measurements to observe ferroelectric properties. The magnitude of the polarisation would show whether or not doping with Y causes an increase in the magnetoelectric effect in $Gd_{1-x}Y_xMnO_3$.

Due to time limitations, it was not possible to prepare and orient single crystal compounds of the $Gd_{1-x}Y_xMnO_3$ series for magnetic and electric properties measurements for this thesis.

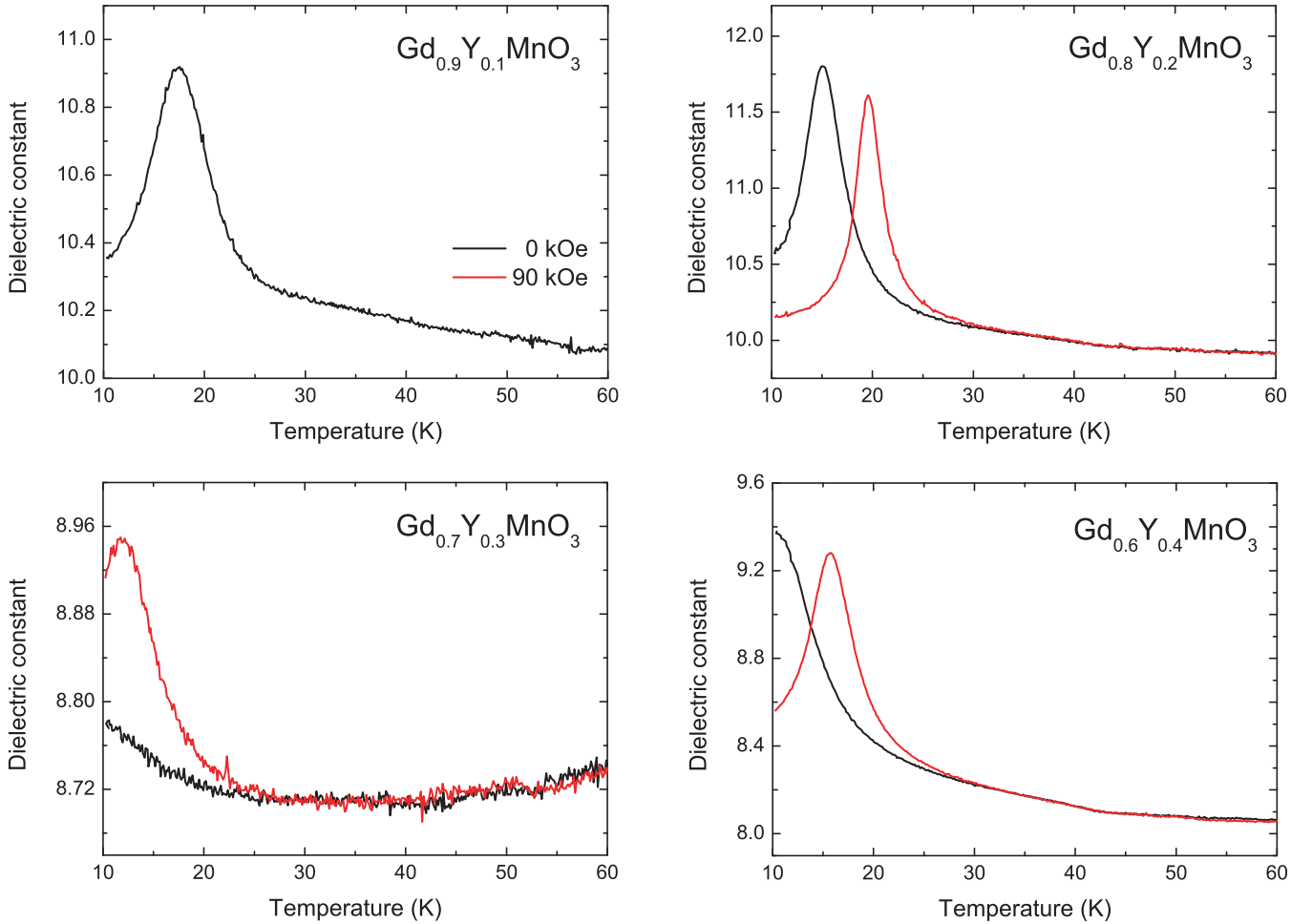

Figure 6.4: Dielectric constant versus temperature for polycrystalline $Gd_{1-x}Y_xMnO_3$ ($x = 0.1$-0.4), measured at 10 kHz.

6.2 $Gd_{1-x}Lu_xMnO_3$

Another approach to altering the multiferroic properties of $GdMnO_3$ was to dope with lutetium. Like Y^{3+}, Lu^{3+} has a smaller ionic radius than that of Gd, and so again the aim of doping on the Gd site was to alter the crystal parameters of the compound. Lu is the last member of the lanthanide series, and therefore Lu^{3+} has a full $4f$ shell ($4f^{14}$) and carries no magnetic moment. This means that Lu is a suitable dopant, since (as with Y) there are no additional magnetic interactions between the Mn^{3+} moments and the A-site moments to consider.

6.2.1 Sample preparation

Polycrystalline samples of $Gd_{1-x}Lu_xMnO_3$ ($x = 0.3$ - 0.5) were synthesised by reacting together stoichiometric ratios of Gd_2O_3, Lu_2O_3 and MnO_2 powders. These doping levels were chosen as a starting point, since magnetoelectric coupling was present in both $Sm_{1-x}Y_xMnO_3$ and $Gd_{1-x}Y_xMnO_3$ around $x = 0.4$. The procedure used for heating the powders is given in Table 6.4. Pellets were pressed and sintered to be used for magnetic and dielectric measurements.

Heating	Temperature (°C)	Duration (hours)	Comments
1	1100	4	Gd_2O_3 preheat
2	1100	12	Gd_2O_3, Lu_2O_3 and MnO_2 mixture
3	1400	24	Gd_2O_3, Lu_2O_3 and MnO_2 mixture
4	1400	12	powder and pellets

Table 6.4: Sample heating procedure for $Gd_{1-x}Lu_xMnO_3$ ($x = 0.3 - 0.5$)

6.2.2 X-ray diffraction

X-ray diffraction was carried out on $Gd_{1-x}Lu_xMnO_3$ ($x = 0.3-0.5$) using a Philips PW1720 X-ray generator, with a step size of 0.02° and a counting time of 2 seconds per step. The results of the measurements are shown in figure 6.5. It can be seen that even for the lowest doping level ($x = 0.3$), there are clear peaks which do not appear in the $GdMnO_3$ diffraction pattern. These peaks can be matched to

hexagonal phase $LuMnO_3$ [84], showing that the compounds did not form as single phases.

6.3 Conclusion

We have shown that single phase $Gd_{1-x}Y_xMnO_3$ can be prepared for $x = 0.1$-0.4, but $Gd_{1-x}Lu_xMnO_3$ is multi-phase for any amount of Lu doping. The dielectric behaviour of the $Gd_{1-x}Y_xMnO_3$ compounds show similar properties to the parent compound up to $x = 0.4$. For each compound, the dielectric constant is shifted under an applied magnetic field of 9 T, showing that magnetoelectric coupling is present for each of these compounds. The bond angle for $Gd_{0.8}Y_{0.2}MnO_3$ was found from powder X-ray diffraction to be $144.6(3)^\circ$. This result provides further evidence that altering the Mn-O-Mn bond angle of the $RMnO_3$ series provides a method of controlling the magnetic order, and that this angle is therefore a crucial factor for the existence of a multiferroic state.

Further work into the $Gd_{1-x}Y_xMnO_3$ and $Gd_{1-x}Lu_xMnO_3$ compounds is currently being undertaken by the Superconductivity and Magnetism group at Warwick. Post-doctoral research assistant Da-Qian Liao has successfully grown single crystal samples of $Gd_{1-x}Y_xMnO_3$, and magnetic, dielectric and electric polarisation measurements have been measured. Also, $Gd_{1-x}Lu_xMnO_3$ was found to be single phase for $x = 0.1$-0.2, and also showed interesting magnetoelectric properties. Papers detailing the magnetoelectric properties of polycrystalline and single crystal $Gd_{1-x}Y_xMnO_3$ and $Gd_{1-x}Lu_xMnO_3$ are currently in preparation.

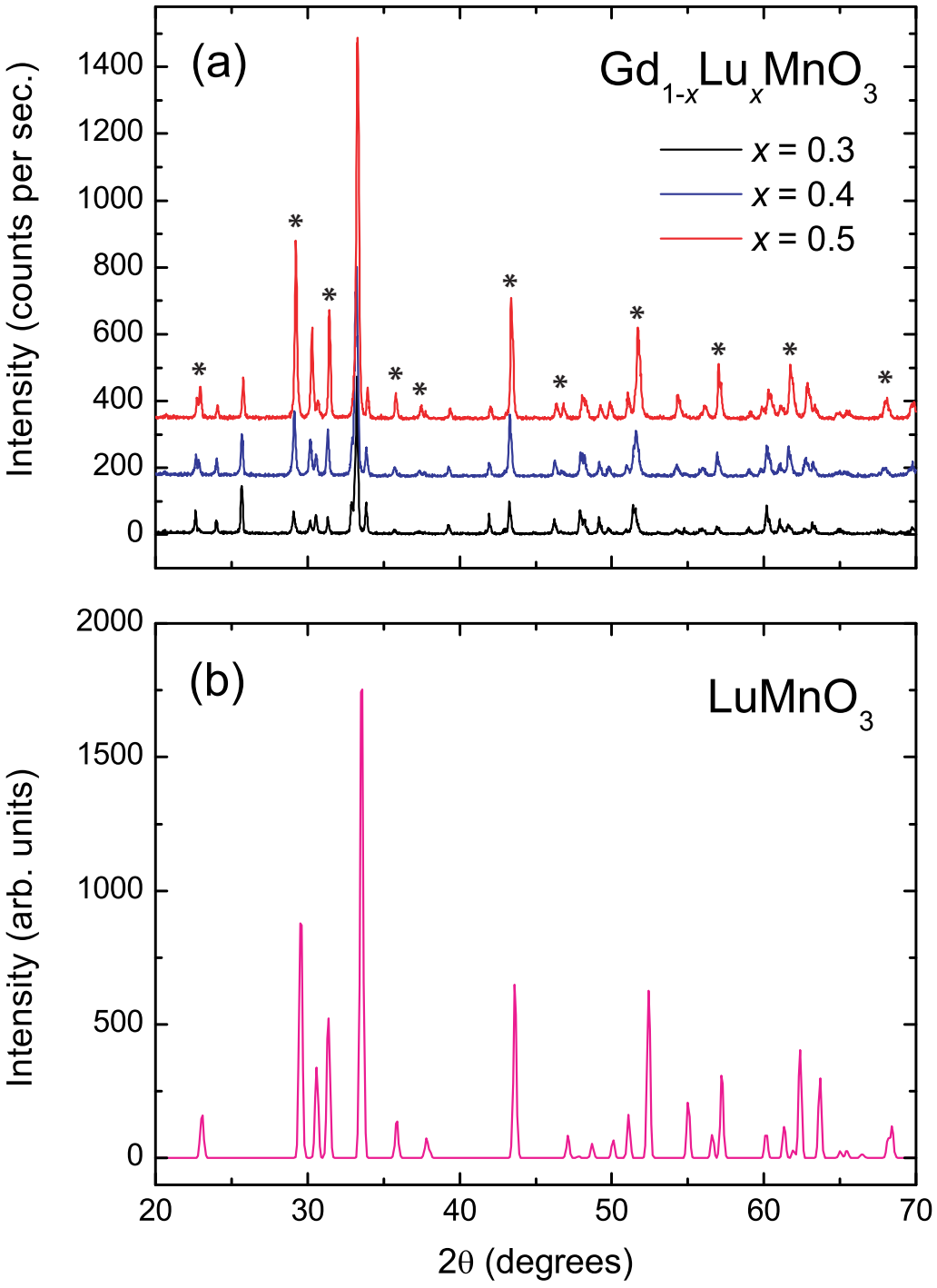

Figure 6.5: (a) Powder X-ray diffraction patterns for $Gd_{1-x}Lu_xMnO_3$ ($x = 0.3 - 0.5$), with peaks due to $LuMnO_3$ marked by asterisks. (b) A reference XRD pattern of $LuMnO_3$ [84].

Chapter 7

Conclusions

Research into multiferroics has been highly active in the years following the discoveries of strong magnetoelectric coupling in 2003 [7–9]. Throughout the course of this Ph.D. (2006-2010) the number of papers on the topic has greatly increased, with ∼1350 publications in this time period compared to 281 beforehand. A great deal of progress has been made into understanding the fundamental causes of multiferroic behaviour, and developing multiferroics for technological applications.

The majority of research into the understanding of type-II multiferroic behaviour (where magnetism and ferroelectricity show a strong coupling) has focused on $TbMnO_3$. As discussed in Section 1.6, a cycloidal ordering of the Mn^{3+} moments breaks inversion symmetry and causes an electric polarisation to develop. It was proposed by several groups that this non-collinear Mn order was related to the crystal structure (specifically the Mn-O-Mn bond angle, ϕ) and the magnetic interaction between the Tb^{3+} and Mn^{3+} moments [29, 30, 63].

The initial work carried out for this thesis used $TbMnO_3$ as a compound to confirm the procedure for single crystal synthesis, and to test for reproducibility of the published magnetoelectric properties. Additional work to that in the literature was also carried out on $TbMnO_3$. Single crystal magnetic susceptibility was measured to 400 K along each principal crystallographic direction, showing that $TbMnO_3$ does not follow Curie-Weiss behaviour until temperatures far above T_N (over 200 K above T_N in the case of $H//c$). This behaviour is proposed to be due to crystal field effects, but no information on the crystal field levels of $TbMnO_3$ is present in the literature. Also previously unreported was the heat capacity of

$TbMnO_3$ under an applied magnetic field. The peak corresponding to the Tb^{3+} order becomes smeared out with increasing $H//a$, corresponding with the saturation point seen in the magnetisation data. Entropy analysis of $TbMnO_3$ was conducted by subtracting the heat capacity data of a phonon blank of $LaGaO_3$. It was found that magnetic entropy is still present in $TbMnO_3$ up to ∼150 K, over 100 K above T_N. The temperature at which no magnetic entropy remains in $TbMnO_3$ coincides with the onset of Curie-Weiss behaviour in the magnetic susceptibility, providing further evidence for crystal field effects. The total entropy measured was significantly lower than expected, implying that a better fit to the lattice contribution than that given by $LaGaO_3$ is required.

$TbMnO_3$ was used to standardise measurements of the dielectric constant and electric polarisation as a function of temperature (reproduced from Kimura *et al.* [7]), using a new measurement system developed for this project. The method for sample preparation and measurement of these properties was refined using the published data on $TbMnO_3$ as a reference, allowing higher quality dielectric and polarisation data to be measured for further samples.

A new multiferroic compound, $Sm_{1-x}Y_xMnO_3$ ($x = 0.4, 0.5$), was developed, following on from the work on $R_{1-x}Y_xMnO_3$ ($R =$ Eu, Gd) in the literature [56–59]. The magnetic properties of polycrystalline $Sm_{0.6}Y_{0.4}MnO_3$ and $Sm_{0.5}Y_{0.5}MnO_3$ were found to be significantly different to those of the parent compound, with an additional feature in the susceptibility data at ∼25 K for these compounds. A peak in the dielectric constant coinciding with the magnetic feature was also found for $x = 0.4, 0.5$. Single crystals of $Sm_{1-x}Y_xMnO_3$ ($x = 0, 0.4, 0.5$) were synthesised, and evidence of a strong magnetic field dependence on the dielectric constant was found. Measurements of the electric polarisation were made by using the pyroelectric current method, refined using $TbMnO_3$ as a standard. It was found that the electric polarisation develops along the c-axis of $Sm_{0.6}Y_{0.4}MnO_3$ and $Sm_{0.5}Y_{0.5}MnO_3$. The application of a magnetic field along the c-axis causes a complete suppression of this polarisation, with a simultaneous increase along the a-axis.

The magnetic and electric properties of $Sm_{1-x}Y_xMnO_3$ show many similarities

with those of $TbMnO_3$, such as large magnetic anisotropy, and an electric polarisation occurring along the c-axis coincident with a magnetic transition. The magnetic susceptibility of $Sm_{1-x}Y_xMnO_3$ shows Curie-Weiss behaviour above ~110 K, with good agreement between the measured and expected magnetic moment. Features are seen in the dielectric constant along the a- and c-axis at $T_{N2} = 25$ K which are similar in zero magnetic field to the same crystal directions in $TbMnO_3$. However, the behaviour of the magnetisation, dielectric constant and electric polarisation show different behaviour under an applied magnetic field in $Sm_{1-x}Y_xMnO_3$ and $TbMnO_3$. This is believed to be related to the magnetic interaction between the Sm^{3+} moments and the Mn^{3+} moments. In $TbMnO_3$, the Tb^{3+} moments are aligned parallel to the a-axis in the Mn^{3+} cycloidal phase. A metamagnetic transition occurs when applying a magnetic field parallel to the b-axis which is thought to correspond to a reorientation of the Tb^{3+} moments [31], with a corresponding switch of the Mn^{3+} cycloid to the a-b plane and a polarisation flop from the c-axis to the a-axis [36]. In $Sm_{0.6}Y_{0.4}MnO_3$ and $Sm_{0.5}Y_{0.5}MnO_3$, no such metamagnetic transitions were seen along the a-, b- or c-axis. The electric polarisation in $Sm_{1-x}Y_xMnO_3$ was suppressed along the c-axis with $H//c$, but only a small increase in the polarisation along the a-axis was found. This behaviour implied a weaker coupling between the rare earth moments and the Mn^{3+} moments in $Sm_{1-x}Y_xMnO_3$ to that in $TbMnO_3$, most likely due to the weaker magnetic moment of Sm^{3+}, coupled with the A-site dilution with Y.

Neutron diffraction and X-ray resonant scattering (XRS) experiments conducted on $Sm_{1-x}Y_xMnO_3$ have provided evidence for a magnetic model of the Mn^{3+} moments similar to that of $TbMnO_3$, i.e. a collinear sinusoidal order along the b-axis for $T_{N2} < T < T_{N1}$, and a cycloidal order in the b-c plane for $T < T_{N2}$ (as illustrated in Figure 7.1). This model agrees with the theoretical predictions (and experimental results for $TbMnO_3$ and $DyMnO_3$) for a polarisation along the c-axis [32, 34, 35]. The crystal structures of $SmMnO_3$ and $Sm_{0.6}Y_{0.4}MnO_3$ were measured using neutron diffraction, showing that ϕ is altered from 147.76(2)° to 145.79(1)° by doping with Y. When comparing with the values of ϕ for other members of the rare earth manganite series (Table 7.1), there is a clear link between ϕ

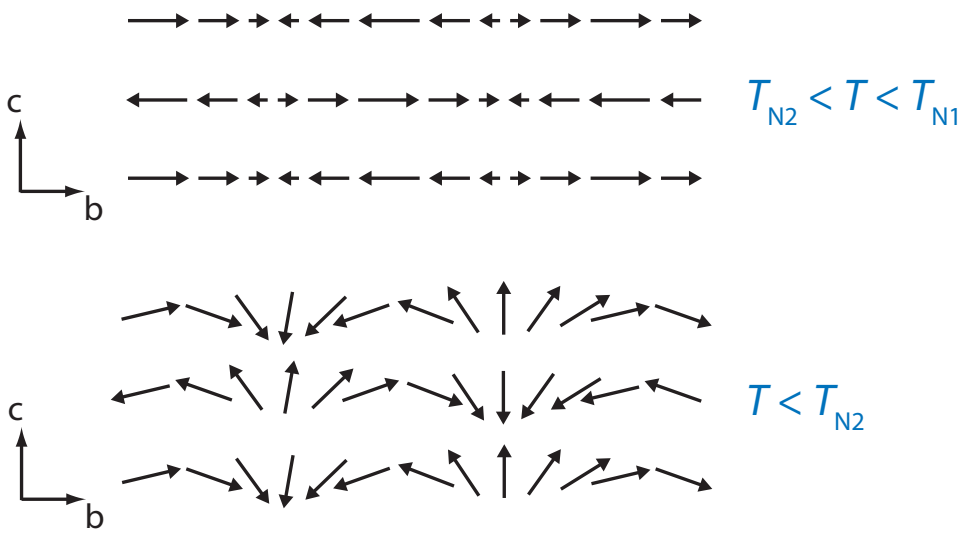

Figure 7.1: Illustration of the proposed magnetic order of the Mn^{3+} moments in $Sm_{0.6}Y_{0.4}MnO_3$ and $Sm_{0.5}Y_{0.5}MnO_3$, based on neutron diffraction and XRS data.

and the existence of multiferroic properties, explicitly confirming previous proposals [29, 30]. Thus, it has been shown that doping with non-magnetic Y provides a way of altering the magnetic properties of a system and causing multiferroic behaviour. Table 7.1 shows a comparison of the electric polarisation and magnetoelectric properties exhibited by $TbMnO_3$, $Eu_{0.6}Y_{0.4}MnO_3$ and $Sm_{0.5}Y_{0.5}MnO_3$. Although $Sm_{0.5}Y_{0.5}MnO_3$ has a relatively small electric polarisation, the values for each compound are much lower than those found in ferroelectric materials with practical applications. For example, $PbTiO_3$ has a room temperature spontaneous polarisation of $\sim$60 μC cm^{-2} (600 000 μC m^{-2}) [24]. It is interesting to note that the polarisation flop occurs with a magnetic field applied along a different crystallographic direction for each of the three multiferroic compounds. For $Sm_{0.5}Y_{0.5}MnO_3$ and $Eu_{0.6}Y_{0.4}MnO_3$, a magnetic field applied along the same direction as that of the electric polarisation causes the flop. This can be understood from the interpretation of Mostovoy [35], discussed in Section 4.3 and illustrated for $Sm_{0.5}Y_{0.5}MnO_3$ in Figure 4.28. This result also agrees with the proposal of Yamasaki *et al*. that the Mn spins in $Eu_{0.6}Y_{0.4}MnO_3$ propagate along the *b*-direction in an *a*-*b* cycloid in zero magnetic field, and a *b*-*c* cycloid under an applied magnetic field (from Equation 1.6, $\mathbf{P}_{H=0} \propto \mathbf{b}\times[\mathbf{a}\times\mathbf{b}] \propto \mathbf{a}$, $\mathbf{P}_{H//a} \propto \mathbf{b}\times[\mathbf{b}\times\mathbf{c}] \propto \mathbf{c}$). It therefore seems that the Mn moments behave in a similar manner under an applied magnetic field for both $Sm_{0.5}Y_{0.5}MnO_3$ and $Eu_{0.6}Y_{0.4}MnO_3$, and are not strongly

	$TbMnO_3$	$Eu_{0.6}Y_{0.4}MnO_3$	$Sm_{0.5}Y_{0.5}MnO_3$
P magnitude (μC m^{-2})	600	1200	275
P direction	c-axis	a-axis	c-axis
P flop due to	$H//b$	$H//a$	$H//c$
P flop direction	a-axis	c-axis	a-axis

Table 7.1: Comparison of the electric polarisation, and magnetoelectric coupling exhibited by $TbMnO_3$ [7, 31], $Eu_{0.6}Y_{0.4}MnO_3$ [58] and $Sm_{0.5}Y_{0.5}MnO_3$ (this work).

(or at all) influenced by magnetism from the rare earth site in the ferroelectric regime, unlike $TbMnO_3$ and $DyMnO_3$.

In order to better understand the magnetoelectric behaviour of $Sm_{1-x}Y_xMnO_3$, there are several possible experiments that could be conducted in the future. Outlined below are some experiments that would help to answer questions raised by the data presented in Chapters 4 and 5.

The heat capacity data obtained for $Sm_{0.6}Y_{0.4}MnO_3$ and $Sm_{0.5}Y_{0.5}MnO_3$ provide evidence for a possible clustering of Sm atoms, i.e. the atoms are not evenly spread throughout the crystal. A local probe such as extended X-ray absorption fine structure (EXAFS) could be used to prove or disprove this proposal. In order to understand the results of the magnetic entropy analysis of $Sm_{0.6}Y_{0.4}MnO_3$ and $Sm_{0.5}Y_{0.5}MnO_3$ (Section 4.2.4), it would be useful to measure the crystal field levels of these compounds. Such measurements could also shed further light on the effect of Y doping.

Due to the limited neutron diffraction and XRS data available at present on the $Sm_{1-x}Y_xMnO_3$ compounds (currently, the work is limited to that presented in this thesis), the results presented in Chapter 5 provide only preliminary information on the magnetic structure of $Sm_{0.6}Y_{0.4}MnO_3$ and $Sm_{0.5}Y_{0.5}MnO_3$, and more experiments are required in order to arrive at a complete picture of the magnetic ordering. Although single crystal neutron scattering experiments are commonly used for this purpose, this is not a practical approach with $Sm_{1-x}Y_xMnO_3$ for two main reasons. Most importantly, the neutron absorption cross section of Sm is very large, therefore making single crystal specimens of $Sm_{1-x}Y_xMnO_3$ for neutron scattering experiments would require isotope-enriched Sm in large amounts, leading to high costs. Since crystal growth is not guaranteed to work each time,

this makes this approach particularly unfeasible. Also, isolating a sufficiently large single crystal piece could prove difficult since the boules were prone to breaking into small pieces after crystal growth. To gain a clearer picture of the magnetic structure of $Sm_{1-x}Y_xMnO_3$, the best approach seems to be further XRS experiments. X-ray scattering requires small sample pieces and the absorption cross section is not a factor.

A follow-up to the experiment conducted at XMaS (Section 5.2.2) has been proposed and accepted, and will take place in early 2011. This experiment will aim to complete the work that was not finished in the initial experiment due to time constraints, in particular gaining more information on the azimuthal dependences to learn more about the orientation of the magnetic moments. Now that interesting results have been found using XRS, it will also be easier to apply for beam time on a more high demand instrument such as ID20 at the ESRF. ID20 has a higher beam intensity than XMaS, which would allow us to probe the Mn K edge. Soft XRS experiments are needed to directly probe the $3d$ states of Mn and the $4f$ states of Sm (the states which are responsible for magnetic order in the respective atoms), following a similar approach to that used in Refs [41] and [97]. Suitable beamlines for such soft XRS experiments are ID08 at the ESRF, or I10 (BLADE) at the Diamond Light Source, UK. The latter beamline is due to begin accepting users for experiments from December 2010. It should be noted that using soft X-rays is not always the best initial approach when studying a new system, since the Q-range of measurements is limited, and the measurements are more sensitive to sample surface quality. It is more common for hard X-ray experiments (using, for example, XMaS or ID20) to be used to gain an initial picture of the system, before following up with soft X-ray experiments.

Magnetoelectric coupling was also demonstrated in $Gd_{1-x}Y_xMnO_3$ (x = 0.1-0.4), in polycrystalline form. $GdMnO_3$ has a weak electric polarisation which is increased by the application of a magnetic field [31]. The Mn-O-Mn bond angle was found to decrease from ~146.2° in $GdMnO_3$ [29] to a value of 144.6(3)° in $Gd_{0.8}Y_{0.2}MnO_3$. This new bond angle is close to that of $TbMnO_3$, so the expected result of Y doping is to induce a zero magnetic field electric polarisation

Compound	ϕ (degrees)	ME coupling	Source
$NdMnO_3$	~149.5	No	Ref. [64]
$SmMnO_3$	147.76(2)	No	This work
$Nd_{0.55}Y_{0.45}MnO_3$	~147.0	Yes	Ref. [64]
$GdMnO_3$	~146.2	Yes	Ref. [30]
$Sm_{0.6}Y_{0.4}MnO_3$	145.79(1)	Yes	This work
$TbMnO_3$	~145.4	Yes	Ref. [30]
$DyMnO_3$	~144.7	Yes	Ref. [30]
$Gd_{0.8}Y_{0.2}MnO_3$	144.6(3)	Yes	This work

Table 7.2: Comparison of the room temperature bond angles and the existence of magnetoelectric (ME) coupling in the rare earth manganite compounds.

in the $Gd_{1-x}Y_xMnO_3$ compounds. Further work is currently being carried out at the University of Warwick on the $Gd_{1-x}Y_xMnO_3$ compounds, and also the $Gd_{1-x}Lu_xMnO_3$ series, which were found to be single phase for compositions (x = 0-0.2). Table 7.2 shows a summary of the Mn-O-Mn bond angles for members of the rare earth manganites, determined by this study and reports in the literature. A clear link can be seen between ϕ and the existence of magnetoelectric coupling.

The discovery of multiferroic properties in the $R_{1-x}Y_xMnO_3$ compounds has shed further light on the nature of the magnetic order which leads to ferroelectric polarisation. This magnetoelectric coupling is still not fully understood, and remains a challenge for future research. Another common trend in multiferroics research is in the area of technological applications, such as data storage media and data reading devices (Section 1.7.1). Composite materials are the most likely candidates for such applications. Although work into technological applications is still at an initial stage, this seems to be an exciting future direction for research into multiferroics.

Bibliography

[1] Schmid, H. *Ferroelectrics* **162**, 317 (1994).

[2] Fiebig, M. *Journal of Physics D: Applied Physics* **38**, R123 (2005).

[3] Spaldin, N. A. and Fiebig, M. *Science* **309**, 391 (2005).

[4] Ramesh, R. and Spaldin, N. A. *Nature Materials* **6**, 21 (2007).

[5] Cheong, S.-W. and Mostovoy, M. *Nature Materials* **6**, 13 (2007).

[6] Khomskii, D. *Physics* **2**, 20 (2009).

[7] Kimura, T., Goto, T., Shintani, H., Ishizaka, K., Arima, T., and Tokura, Y. *Nature* **426**, 55 (2003).

[8] Wang, J., Neaton, J. B., Zheng, H., Nagarajan, V., Ogale, S. B., Liu, B., Viehland, D., Vaithyanathan, V., Schlom, D. G., Waghmare, U. V., Spaldin, N. A., Rabe, K. M., Wuttig, M., and Ramesh, R. *Science* **299**, 1719 (2003).

[9] Hur, N., Park, S., Sharma, P. A., Ahn, J. S., Guha, S., and Cheong, S.-W. *Nature* **429**, 392 (2004).

[10] Merz, W. J. *Physical Review* **76**, 1221 (1949).

[11] Merz, W. J. *Physical Review* **91**, 513 (1953).

[12] Van Aken, B. B., Palstra, T. T., Filippetti, A., and Spaldin, N. A. *Nature Materials* **3**, 164 (2004).

[13] Portengen, T., Östreich, T., and Sham, L. J. *Physical Review B* **54**, 17452 (1996).

[14] Ikeda, N., Ohsumi, H., Ohwada, K., Ishii, K., Inami, T., Kakurai, K., Murakami, Y., Yoshii, K., Mori, S., Horibe, Y., and Kito, H. *Nature* **436**, 1136 (2005).

[15] Blundell, S. *Magnetism in Condensed Matter*. Oxford University Press, (2001).

[16] Eerenstein, W., Mathur, N. D., and Scott, J. F. *Nature* **442**, 759 (2006).

[17] Folen, V. J., Rado, G. T., and Stalder, E. W. *Physical Review Letters* **6**, 607 (1961).

[18] Rado, G. T. and Folen, V. J. *Physical Review Letters* **7**, 310 (1961).

[19] Brown, W. F., Hornreich, R. M., and Shtrikman, S. *Physical Review* **168**, 574 (1968).

[20] Hill, N. A. *Journal of Physical Chemistry B* **104**, 6694 (2000).

[21] Cohen, R. E. *Nature* **358**, 136 (1992).

[22] Moreau, J., Michel, C., Gerson, R., and James, W. *Journal of Physics and Chemistry of Solids* **32**, 1315 (1971).

[23] Teague, J. R., Gerson, R., and James, W. J. *Solid State Communications* **8**, 1073 (1970).

[24] Remeika, J. and Glass, A. *Materials Research Bulletin* **5**, 37 (1970).

[25] Zhao, T., Scholl, A., Zavaliche, F., Lee, K., Barry, M., Doran, A., Cruz, M. P., Chu, Y. H., Ederer, C., Spaldin, N. A., Das, R. R., Kim, D. M., Baek, S. H., Eom, C. B., and Ramesh, R. *Nature Materials* **5**, 823 (2006).

[26] Chu, Y.-H., He, Q., Yang, C.-H., Yu, P., Martin, L. W., Shafer, P., and Ramesh, R. *Nano Letters* **9**(4), 1726 (2009).

[27] Balke, N., Choudhury, S., Jesse, S., Huijben, M., Chu, Y. H., Baddorf, A. P., Chen, L. Q., Ramesh, R., and Kalinin, S. V. *Nature Nanotechnology* **4**, 868 (2009).

[28] Quezel, S., Tcheou, F., Rossat-Mignod, J., Quezel, G., and Roudaut, E. *Physica B+C* **86-88**, 916 (1977).

[29] Kimura, T., Ishihara, S., Shintani, H., Arima, T., Takahashi, K. T., Ishizaka, K., and Tokura, Y. *Physical Review B* **68**, 060403 (2003).

[30] Goto, T., Kimura, T., Lawes, G., Ramirez, A. P., and Tokura, Y. *Physical Review Letters* **92**, 257201 (2004).

[31] Kimura, T., Lawes, G., Goto, T., Tokura, Y., and Ramirez, A. P. *Physical Review B* **71**, 224425 (2005).

[32] Kenzelmann, M., Harris, A. B., Jonas, S., Broholm, C., Schefer, J., Kim, S. B., Zhang, C. L., Cheong, S.-W., Vajk, O. P., and Lynn, J. W. *Physical Review Letters* **95**, 087206 (2005).

[33] Lawes, G., Harris, A. B., Kimura, T., Rogado, N., Cava, R. J., Aharony, A., Entin-Wohlman, O., Yildirim, T., Kenzelmann, M., Broholm, C., and Ramirez, A. P. *Physical Review Letters* **95**, 087205 (2005).

[34] Katsura, H., Nagaosa, N., and Balatsky, A. V. *Physical Review Letters* **95**, 057205 (2005).

[35] Mostovoy, M. *Physical Review Letters* **96**, 067601 (2006).

[36] Aliouane, N., Schmalzl, K., Senff, D., Maljuk, A., Prokeš, K., Braden, M., and Argyriou, D. N. *Physical Review Letters* **102**, 207205 (2009).

[37] Sergienko, I. A., Şen, C., and Dagotto, E. *Physical Review Letters* **97**, 227204 (2006).

[38] Sergienko, I. A. and Dagotto, E. *Physical Review B* **73**, 094434 (2006).

[39] Feyerherm, R., Dudzik, E., Wolter, A. U. B., Valencia, S., Prokhnenko, O., Maljuk, A., Landsgesell, S., Aliouane, N., Bouchenoire, L., Brown, S., and Argyriou, D. N. *Physical Review B* **79**, 134426 (2009).

[40] Fabrizi, F., Walker, H. C., Paolasini, L., de Bergevin, F., Boothroyd, A. T., Prabhakaran, D., and McMorrow, D. F. *Physical Review Letters* **102**, 237205 (2009).

[41] Wilkins, S. B., Forrest, T. R., Beale, T. A. W., Bland, S. R., Walker, H. C., Mannix, D., Yakhou, F., Prabhakaran, D., Boothroyd, A. T., Hill, J. P., Hatton, P. D., and McMorrow, D. F. *Physical Review Letters* **103**, 207602 (2009).

[42] Zavaliche, F., Zheng, H., Mohaddes-Ardabili, L., Yang, S. Y., Zhan, Q., Shafer, P., Reilly, E., Chopdekar, R., Jia, Y., Wright, P., Schlom, D. G., Suzuki, Y., and Ramesh, R. *Nano Letters* **5**, 1793 (2005).

[43] Vopsaroiu, M., Blackburn, J., and Cain, M. G. *Journal of Physics D: Applied Physics* **40**, 5027 (2007).

[44] Zhang, Y., Li, Z., Deng, C., Ma, J., Lin, Y., and Nan, C.-W. *Applied Physics Letters* **92**, 152510 (2008).

[45] Murakami, M., Chang, K.-S., Aronova, M. A., Lin, C.-L., Yu, M. H., Simpers, J. H., Wuttig, M., Takeuchi, I., Gao, C., Hu, B., Lofland, S. E., Knauss, L. A., and Bendersky, L. A. *Applied Physics Letters* **87**, 112901 (2005).

[46] Wu, X., Cai, W., Kan, Y., Yang, P., Liu, Y., Bo, H., Lu, X., and Zhu, J. *Ferroelectrics* **380**, 48 (2009).

[47] Zheng, H., Wang, J., Lofland, S. E., Ma, Z., Mohaddes-Ardabili, L., Zhao, T., Salamanca-Riba, L., Shinde, S. R., Ogale, S. B., Bai, F., Viehland, D., Jia, Y., Schlom, D. G., Wuttig, M., Roytburd, A., and Ramesh, R. *Science*

303, 661 (2004).

[48] Wollan, E. O. and Koehler, W. C. *Physical Review* **100**, 545 (1955).

[49] Vajk, O. P., Kenzelmann, M., Lynn, J. W., Kim, S. B., and Cheong, S.-W. *Physical Review Letters* **94**, 087601 (2005).

[50] Lottermoser, T., Lonkai, T., Amann, U., Hohlwein, D., Ihringer, J., and Fiebig, M. *Nature* **430**, 541 (2004).

[51] Hur, N., Jeong, I. K., Hundley, M. F., Kim, S. B., and Cheong, S.-W. *Physical Review B* **79**, 134120 (2009).

[52] Sahu, J. R., Ghosh, A., Sundaresan, A., and Rao, C. *Materials Research Bulletin* **44**, 2123 (2009).

[53] Rubi, D., Venkatesan, S., Kooi, B. J., De Hosson, J. T. M., Palstra, T. T. M., and Noheda, B. *Physical Review B* **78**, 020408 (2008).

[54] Van Aken, B. B. and Palstra, T. T. M. *Physical Review B* **69**, 134113 (2004).

[55] Fiebig, M., Lottermoser, T., Frohlich, D., Goltsev, A. V., and Pisarev, R. V. *Nature* **419**, 818 (2002).

[56] Ivanov, V. Y., Mukhin, A. A., Travkin, V. D., Prokhorov, A. S., Popov, Y. F., Kadomtseva, A. M., Vorob'ev, G. P., Kamilov, K. I., and Balbashov, A. M. *Physica Status Solidi B* **243**, 107 (2006).

[57] Hemberger, J., Schrettle, F., Pimenov, A., Lunkenheimer, P., Ivanov, V. Y., Mukhin, A. A., Balbashov, A. M., and Loidl, A. *Physical Review B* **75**, 035118 (2007).

[58] Noda, K., Akaki, M., Kikuchi, T., Akahoshi, D., and Kuwahara, H. *50th Annual Conference on Magnetism and Magnetic Materials* **99**(8), 08S905 (2006).

[59] Yamasaki, Y., Miyasaka, S., Goto, T., Sagayama, H., Arima, T., and Tokura, Y. *Physical Review B* **76**, 184418 (2007).

[60] Pimenov, A., Loidl, A., Mukhin, A. A., Travkin, V. D., Ivanov, V. Y., and Balbashov, A. M. *Physical Review B* **77**, 014438 (2008).

[61] Moreira, J. A., Almeida, A., Ferreira, W. S., Araújo, J. E., Pereira, A. M., Chaves, M. R., Kreisel, J., Vilela, S. M. F., and Tavares, P. B. *Physical Review B* **81**, 054447 (2010).

[62] Issing, S., Fuchs, F., Ziereis, C., Batke, E., Pimenov, A., Ivanov, Y. V., and

Mukhin, A. A. *The European Physical Journal B - Condensed Matter and Complex Systems* **73**, 353 (2010).

[63] Prokhnenko, O., Feyerherm, R., Dudzik, E., Landsgesell, S., Aliouane, N., Chapon, L. C., and Argyriou, D. N. *Physical Review Letters* **98**, 057206 (2007).

[64] Landsgesell, S., Maljuk, A., Hansen, T. C., Prokhnenko, O., Aliouane, N., and Argyriou, D. N. *Physical Review B* **80**, 014412 (2009).

[65] Landsgesell, S. *Emerging Magneto-Electric Properties in Orthorhombic $NdYMnO_3$*. PhD thesis, Helmholtz-Zentrum Berlin, (2010).

[66] Inomata, A. and Kohn, K. *Journal of Physics: Condensed Matter* **8**, 2673 (1996).

[67] Squires, G. L. *Introduction to the Theory of Thermal Neutron Scattering*. Dover Publications, Inc., (1978).

[68] Rodríguez-Carvajal, J. Satellite Meeting on Powder Diffraction of the XV IUCr Congress, 127, (1990).

[69] Rodríguez-Carvajal, J. *Physica B: Condensed Matter* **192**, 55 (1993).

[70] Hannon, J. P., Trammell, G. T., Blume, M., and Gibbs, D. *Physical Review Letters* **61**, 1245 (1988).

[71] Lovesey, S. and Collins, S. *X-ray Scattering and Absorption by Magnetic Materials*. Oxford University Press, (1997).

[72] Als-Nielsen, J. and McMorrow, D. *Elements of Modern X-Ray Physics*. John Wiley & Sons Ltd, (2001).

[73] Gibbs, D., Harshman, D. R., Isaacs, E. D., McWhan, D. B., Mills, D., and Vettier, C. *Physical Review Letters* **61**, 1241 (1988).

[74] Hill, J. P. and McMorrow, D. F. *Acta Crystallographica Section A* **520**, 236 (1996).

[75] Blasco, J., Ritter, C., García, J., de Teresa, J. M., Pérez-Cacho, J., and Ibarra, M. R. *Physical Review B* **62**, 5609 (2000).

[76] Bouvier, M., Lethuillier, P., and Schmitt, D. *Physical Review B* **43**, 13137 (1991).

[77] Gopal, E. S. R. *Specific Heats at Low Temperatures*. Heywood Books, (1966).

[78] Scurlock, R. G. and Stevens, W. N. R. *Proceedings of the Physical Society* **86**, 331 (1965).

[79] Li, Y., Graham, R. G., Ross, J. W., McCausland, M. A. H., Bunbury, D. S. P., Cao, L., shu Kong, L., and gen Shen, B. *Journal of Physics: Condensed Matter* **8**, 1059 (1996).

[80] Drain, L. E. *Proceedings of the Physical Society* **88**, 111 (1966).

[81] Campbell, I. A., Allsop, A. L., and Stone, N. J. *Journal of Physics F: Metal Physics* **8**, L235 (1978).

[82] Chen, Y., Yuan, H., Li, G., Tian, G., and Feng, S. *Journal of Crystal Growth* **305**, 242 (2007).

[83] Alonso, J. A., Martínez-Lope, M. J., Casáis, M. T., and Fernández-Díaz, M. T. *Inorganic Chemistry* **39**, 917 (2000).

[84] Katsufuji, T., Masaki, M., Machida, A., Moritomo, M., Kato, K., Nishibori, E., Takata, M., Sakata, M., Ohoyama, K., Kitazawa, K., and Takagi, H. *Physical Review B* **66**, 134434 (2002).

[85] Coelho, A. (2004). http://www.topas-academic.net.

[86] Ivanov, V. Y., Mukhin, A. A., Prokhorov, A. S., and Balbashov, A. M. *Physica Status Solidi B* **236**(2), 445 (2003).

[87] Mukhin, A. A., Ivanov, V. Y., Travkin, V. D., Prokhorov, A. S., Balbashov, A. M., Hemberger, J., and Loidl, A. *Journal of Magnetism and Magnetic Materials* **272**, 96 (2004).

[88] Nekvasil, V., Jandl, S., Mukhin, A. A., Ivanov, V. Y., and Balbashov, A. M. *Proceedings of the 53rd Annual Conference on Magnetism and Magnetic Materials* **105**(7), 07E113 (2009).

[89] Brown, P. J. and Chatterji, T. *Journal of Physics: Condensed Matter* **18**, 10085 (2006).

[90] Mannix, D., McMorrow, D. F., Ewings, R. A., Boothroyd, A. T., Prabhakaran, D., Joly, Y., Janousova, B., Mazzoli, C., Paolasini, L., and Wilkins, S. B. *Physical Review B* **76**, 184420 (2007).

[91] Hannon, A. C. *Nuclear Instruments and Methods in Physics Research A* **551**, 88 (2005).

[92] Sears, V. F. *Neutron News* **3**, 26 (1992).

[93] Brown, S. D., Bouchenoire, L., Bowyer, D., Kervin, J., Laundy, D., Longfield, M. J., Mannix, D., Paul, D. F., Stunault, A., Thompson, P., Cooper, M. J., Lucas, C. A., and Stirling, W. G. *Journal of Synchrotron Radiation* **8**, 1172 (2001).

[94] Kajimoto, R., Yoshizawa, H., Shintani, H., Kimura, T., and Tokura, Y. *Physical Review B* **70**, 012401 (2004).

[95] Voigt, J., Persson, J., Kim, J. W., Bihlmayer, G., and Brückel, T. *Physical Review B* **76**, 104431 (2007).

[96] Adriano, C., Lora-Serrano, R., Giles, C., de Bergevin, F., Lang, J. C., Srajer, G., Mazzoli, C., Paolasini, L., and Pagliuso, P. G. *Physical Review B* **76**, 104515 (2007).

[97] Forrest, T. R., Bland, S. R., Wilkins, S. B., Walker, H. C., Beale, T. A. W., Hatton, P. D., Prabhakaran, D., Boothroyd, A. T., Mannix, D., Yakhou, F., and McMorrow, D. F. *Journal of Physics: Condensed Matter* **20**, 422205 (2008).

[98] Mori, T., Kamegashira, N., Aoki, K., Shishido, T., and Fukuda, T. *Materials Letters* **54**, 238 (2002).